ABS/POLYAMIDE-6 BLENDS, THEIR SHORT GLASS FIBER COMPOSITES AND ORGANOCLAY BASED NANOCOMPOSITES: PROCESSING AND CHARACTERIZATION

A THESIS SUBMITTED TO
THE GRADUATE SCHOOL OF NATURAL AND APPLIED SCIENCES
OF
MIDDLE EAST TECHNICAL UNIVERSITY

BY

GÜRALP ÖZKOÇ

IN PARTIAL FULFILLMENT OF THE REQUIREMENTS
FOR
THE DEGREE OF DOCTOR OF PHILOSOPHY
IN
POLYMER SCIENCE AND TECHNOLOGY

FEBRUARY 2007

Approval of the Graduate School of Natural and Applied Sciences

Prof. Dr. Canan Özgen
Director

I certify that this thesis satisfies all the requirements as a thesis for the degree of Doctor of Philosophy.

Assoc. Prof. Dr. Göknur Bayram
Head of Department

This is to certify that we have read this thesis and that in our opinion it is fully adequate, in scope and quality, as a thesis and for the degree of Doctor of Philosophy.

Prof. Dr. Erdal Bayramlı Co-Supervisor	Assoc. Prof. Dr. Göknur Bayram Supervisor

Examining Committee Members

Prof. Dr. Ülkü Yılmazer (METU, CHE) ______________________________

Assoc. Prof. Dr. Göknur Bayram (METU, CHE) ______________________________

Prof. Dr. Cevdet Kaynak (METU, METE) ______________________________

Prof. Dr. Teoman Tinçer (METU, CHEM) ______________________________

Prof. Dr. S. Ali Tuncel (Hacettepe Unv., CHE) ______________________________

I hereby declare that all information in this document has been obtained and presented in accordance with academic rules and ethical conduct. I also declare that, as required by these rules and conduct, I have fully cited and referenced all material and results that are not original to this work.

Name, Last name: Güralp Özkoç
Signature:

ABSTRACT

ABS/POLYAMIDE-6 BLENDS, THEIR SHORT GLASS FIBER COMPOSITES AND ORGANOCLAY BASED NANOCOMPOSITES: PROCESSING AND CHARACTERIZATION

Özkoç, Güralp
Ph.D., Department of Polymer Science and Technology
Supervisor: Assoc. Prof. Dr. Göknur Bayram
Co-Supervisor: Prof. Dr. Erdal Bayramlı

February 2007, 310 pages

The objective of this study is to process and characterize the compatibilized blends of acrylonitrile-butadiene-styrene (ABS) and polyamide-6 (PA6) using olefin based reactive copolymers and subsequently to utilize this blend as a matrix material in short glass fiber (SGF) reinforced composites and organoclay based nanocomposites by applying melt processing technique. In this context, commercially available epoxydized and maleated olefinic copolymers, ethylene-methyl acrylate-glycidyl methacrylate (EMA-GMA) and ethylene-n butyl acrylate-carbon monoxide-maleic anhydride (EnBACO-MAH) were used as compatibilizers at different ratios. Compatibilizing performance of these two olefinic polymers was investigated through blend morphologies, thermal and mechanical properties as a function of blend composition and compatibilizer loading level. Incorporation of compatibilizer resulted in a fine morphology with reduced dispersed particle size. At 5 % EnBACO-MAH, the toughness was observed to be the highest among the blends produced.

SGF reinforced ABS and ABS/PA6 blends were prepared with twin screw extrusion. The effects of SGF concentration and extrusion process conditions on the fiber length distribution, mechanical properties and morphologies of the composites were examined. The most compatible organosilane type was designated from interfacial tension and short beam flexural tests, to promote adhesion of SGF to both ABS and PA6. Increasing amount of PA6 in the polymer matrix improved the strength, stiffness and also toughness of the composites. Effects of compatibilizer content and ABS/PA6 ratio on the morphology and mechanical properties of 30% SGF reinforced ABS/PA6 blends were investigated. The most striking result of the study was the improvement in the impact strength of the SGF/ABS/PA6 composite with the additions of compatibilizer.

Melt intercalation method was applied to produce ABS/PA6 blends based organoclay nanocomposites. The effects of process conditions and material parameters on the morphology of blends, dispersibility of nanoparticles and mechanical properties were investigated. To improve mixing, the screws of the extruder were modified. Processing with co-rotation yielded finer blend morphology than processing with counter-rotation. Clays were selectively exfoliated in PA6 phase and agglomerated at the interface of ABS/PA6. High level of exfoliation was obtained with increasing PA6 content and with screw speed in co-rotation mode. Screw modification improved the dispersion of clay platelets in the matrix.

Keywords: ABS/Polyamide-6 Blends, Compatibilization, Short Glass Fiber Composites, Organoclay Nanocomposite

ÖZ

ABS/POLİAMİD-6 KARIŞIMLARI, BU KARIŞIMLARIN KISA CAM ELYAF KOMPOZİTLERİ VE ORGANOKİL BAZLI NANOKOMPOZİTLERİ:
ÜRETİMİ VE KARAKTERİZASYONU

Özkoç, Güralp
Doktora, Polimer Bilimi ve Teknolojisi Bölümü
Tez Yöneticisi: Doç. Dr. Göknur Bayram
Ortak Tez Yöneticisi: Prof. Dr. Erdal Bayramlı

Şubat 2007, 310 sayfa

Bu çalışmanın amacı, olefin bazlı reaktif kopolimer kullanarak uyumlaştırılmış akrilonitril-stiren-bütadien (ABS) ve poliamid-6 (PA6) karışımlarını üretmek ve karakterize etmek, ardından eriyik işleme tekniklerini uygulayarak bu karışımları matris malzemesi olarak kısa cam elyaf (KCE) kompozitlerinde ve organokil nanokompozitlerinde kullanmaktır. Bu çerçevede, ticari olarak bulunabilen epoksili ve maleatlı olefin bazlı kopolimerler, etilen-metil akrilat-glisidil metakrilat (EMA-GMA) ve etilen-n bütil akrilat-karbonmonoksit-maleik anhidrit (EnBACO-MAH), farklı oranlarda uyumlaştırıcı olarak kullanıldı. Bu iki olefin bazlı polimerin uyumlaştırma performansı karışım morfolojileri, termal ve mekanik özellikler yoluyla karışım kompozisyonunun ve uyumlaştırıcı yükleme oranının bir fonksiyonu olarak incelendi. Uyumlaştırıcı eklenmesi küçük faz boyutlu bir morfoloji ve indirgenmiş dağılmış parçacık boyutu ile neticelendi. Üretilen karışımlar arasında en yüksek tokluk 5 % EnBACO-MAH'de gözlendi.

KCE takviyeli ABS ve ABS/PA6 karışımları çift burgulu ekstrüder ile hazırlandı. KCE konsantrasyonunun ve ekstrüder süreç koşullarının kompozitlerin elyaf boyut dağılımına, mekanik özelliklerine ve morfolojilerine olan etkileri incelendi. KCE'ların hem ABS hem de PA6'ya yapışmalarını arttırmak için en uygun organosilan türü yüzeyler arası gerilimlerden ve kısa çubuk bükme testlerinden belirlendi. Mekanik test sonuçları matristeki PA6 oranının arttırılmasının kompozitlerin dayanımını, pekliğini ve ayrıca tokluğunu da geliştirdiğini gösterdi. %30 KCE ile takviye edilmiş ABS/PA6 kompozitlerinin morfoloji ve mekanik özelliklerine uyumlaştırıcı miktarı ve ABS/PA6 oranının etkileri araştırıldı. Çalışmanın en çarpıcı sonucu uyumlaştırıcı etkisi ile KCE/ABS/PA6 kompozitlerinin darbe dayanımlarındaki gelişme idi.

ABS/PA6 karışımı bazlı organokil nanokompozitlerini üretmek için eriyik halde interkalasyon metodu uygulandı. Süreç koşullarının ve malzeme parametrelerinin karışım morfolojilerine, nanoparçacıkların dağılabilirliğine ve mekanik özelliklere olan etkileri incelendi. Karışmayı geliştirmek için ektrüder vidaları modifiye edildi. Aynı yönde dönüşlü burgu ile işleme zıt yönde dönüşlü burgu ile işlemeden daha küçük boyutlarda bir karışım morfolojisi sağladı. Killer seçimli olarak PA6 fazında dağıldı ve ABS/PA6 arafazında topaklandı. Yüksek derecede delaminasyon, artan PA6 miktarında ve aynı yöndeki burgu hızında elde edildi. Burgu modifikasyonu matris içerisinde kil tabakalarının dağılımlarını geliştirdi.

Anahtar Kelimeler: ABS/Poliamid-6 Karışımları, Uyumlaştırma, Kısa Cam Elyaf Kompozitleri, Organokil Nanokompozitleri

To the memory of Sarı Tarihçi…

ACKNOWLEDGEMENTS

I would like to express my gratitude to my supervisor Assoc. Prof. Dr. Göknur Bayram for her support and guidance during my research. Her challenging approach in publication and presentation of the researches has profoundly influenced me. I am very grateful to my co-supervisor Prof. Dr. Erdal Bayramlı for his guidance, valuable advice throughout this study, for sharing his industry related experiences and opening his laboratory in which I feel like at home. His approach in solving problems will sure help me in my future academic life.

I would like to express my sincerely acknowledgements to Prof. Dr. Ülkü Yılmazer and Prof. Dr. Cevdet Kaynak for their fruitful discussions during the progress of my study. It was a pleasing honor for me to work with them. I am very grateful to Dr. Cevdet Öztin, Prof. Dr. Teoman Tinçer and Prof. Dr. Güngör Gündüz for giving me every opportunity to use the instruments and other facilities in their laboratories.

My sincere appreciation goes to Seha Tirkeş from Department of Chemistry for his assistance in FTIR experiments and valuable comments and to Dr. Gaye Çakal for her help in fiber length measurements. I also thank technicians Osman Yaslıtaş and Salih Sarıkaya from Department of Chemistry and Adil Demir from Department of Chemical Engineering for their help in the laboratory and machine-shop.

The companies Cam Elyaf A.Ş., Emaş Plastik, Dupont Inc., Tekno Polimer, and DSM Xplore are greatly acknowledged for providing materials and for their cooperation.

I also wish to extend my acknowledgements and sincere thanks to Martin Quaedflieg, the Global Sales Manager of DSM Xplore, and Leon Rijks, the General Manager of Technical Service in DSM Research for giving me the opportunity to

work in DSM Research and to implement my ideas to a commercial product. During the period of my internship, they had taught me how to stand on my own legs. I would like to express my gratitude to them once more.

I could not have finished my studies without supports of my friends. I would like to thank my side partners Mehmet Doğan, Ümit Tayfun, Yasin Kanbur, Ali Sinan Dike and Fuat Çankaya, my coworkers Mert Kılınç, Işıl Işık, Özcan Köysüren, Sertan Yeşil and the other friends who are graduated from our Polymer Research Group. My colleagues in PST-502 Laboratory, Olcay Mert and Elif Vargün, deserve to be acknowledged because of their understanding when I was too busy with my thesis. Special thanks go to the administrative staff of Department of Chemistry for their helps without any expectations.

I would also like to thank to Faculty Development Program (ÖYP) for the financial support during my thesis and Kocaeli University for providing me the opportunity of working and studying in METU.

I am grateful to all my family, my mother, my father, my brother and my grand mother for their endless support and belief in me. This thesis could not be written without love, patient and understanding of my fiancé S. Özge Keskin. Her presence will strengthen me forever.

Last but not the least, I dedicate this dissertation to the memory of my grand father Salih Ercan, alias “Sarı Tarihçi”, my first “teacher”, who enlarged my vision about science of life...

TABLE OF CONTENTS

CHAPTER

LIST OF TABLES

LIST OF FIGURES

CHAPTER 1

INTRODUCTION

There are few scientific explorations in modern age that have had greater influence on humankind than those gathered in the field of polymer science and technology. The discovery of new polymerization techniques and therefore new polymers, together with evident advances in the theory and application of polymeric materials at the beginning of this century, helped to initiate a materials reform. However, at the onset of new century the technical and economical issues restrict the innovation of new polymers for specific applications. Thus, scientists have focused on the improvement of the properties of current polymers by mixing with other polymers to produce 'polymer blends' or by mixing with inorganic fillers to produce 'polymer composites' at a reasonably low cost.

Blending of polymers to obtain a unique property offers a powerful way of combining performance and economy using existing materials. As a consequence of this, the science and technology of polymer blending has become an important way of product development for both academy and industry. Basic issues that have influence on the physical properties of blends include interfacial behavior i.e. physical and chemical interactions between the components at the interface and phase morphology, which designate the issues of compatibility. It should be emphasized that great majority of several hundred scientific papers published on polymer blends are about compatibility and compatibility related properties. Thus, it is clear that compatibilization is the principle issue in polymer blends.

Compatibilization generally means improvement of properties of the blends and involves an additive which has some interfacial activity. It improves the interfacial adhesion and affects the phase morphology of the blend system. Two approaches are proved to be successful in compatibilization [1]. In first approach, a graft or a block copolymer which is chemically similar to the blend components is incorporated during melt processing. The second approach, which is the one used in this study involves the formation of in-situ graft or block copolymer during melt processing through covalent bonds. This method is usually preferred when one of the components includes reactive sites such as amine, epoxy, anhydride, etc.

The blends of polyamide-6 (PA6) with acrylonitrile-butadiene-styrene (ABS) terpolymer have gained commercial interest because of relatively low cost of ABS and its contribution to the blend's dimensional stability, processability, surface quality of molded products and high toughness. Due to the highly polar structure of the PA6, the simple blends of PA6 with ABS yield poor physical properties because of incompatibility arising from coarse and instable morphology and lack of interfacial adhesion [2]. There is great interest to compatibilize ABS/PA6 blends using compatibilizers which are capable of reacting with amine and/or acid end groups of PA6 and miscible with styrene-acrylonitrile (SAN) copolymer phase of ABS [1-12]. The studies reported in the literature have shown that maleated styrenic polymers such as styrene-maleic anhydride (SMA) [11], styrene-co-acrylonitrile-graft-maleic anhydride (SAN-MA) [5-7] or maleated acrylic polymers due to the miscibility of acrylics with SAN of ABS such as maleated poly(methyl methacrylate) (MMA-MA) [11], imidized acrylics (IA) [4-6] were utilized to compatibilize the ABS/PA6 blends.

In the studies on the compatibilization of ABS/PA6, the toughness of the blends which is the leading property of ABS/PA6 was controlled by dispersion morphology of ABS particles and the toughness of the ABS itself which depends on the butadiene content of ABS. In the current study, different than the literature, commercially available epoxydized and maleated 'olefinic copolymers', ethylene-methyl acrylate-glycidyl methacrylate (EMA-GMA) and ethylene-n butyl acrylate-carbon monoxide-maleic anhydride (EnBACO-MAH) were utilized as the compatibilizers for ABS/PA6 blends. Epoxy and maleic anhydride groups in the structure of these copolymers are responsible for the in-situ reaction with end-groups of PA6; MA and nBA are responsible for the miscibility with SAN [13-18] phase of ABS and most importantly, ethylene chains act as 'tougheners' (impact modifiers) because of their relatively low glass transition temperatures. Furthermore, most of the studies reported in the literature have basically focused on the blends in which PA6 is the continuous phase and ABS is the dispersed phase, so called impact toughened PA6. However, in the current study, it was aimed to compare the properties of PA6/ABS blends in which either ABS or PA6 is continuous, or both are continuous to enlighten this lacking. Thus, the effects of compatibilizer type (i.e maleated or epoxydized olefinic copolymers) and content on blend morphologies, fracture toughness, mechanical, dynamic mechanical and thermal properties as the function of blend composition were investigated. For the forthcoming parts of the study, the best functioning compatibilizer type and the amount were determined for ABS/PA6 systems among the compatibilizers examined here.

Another route to improved properties of current polymers is the incorporation of rigid, high aspect ratio particles, in the form of fibers or platelets, into the polymer matrix. The resulting 'polymer composite' will have improved physical properties. The incorporation of fibrous glass is known to improve the properties of the thermoplastic materials by applying traditional processes such as extrusion and injection molding [19-22]. It is well known that the mechanical properties of fiber filled polymeric composites are governed by both individual properties of fiber and by the physicochemical interactions of the polymer/fiber interphase [23-27]. Interphase is a region intermediate to two (usually solid) phases in contact, the composition and/or structure and/or properties of which may be variable across the region and which also may differ from the composition and structure or properties of either of the contacting phases [28]. The interactions at the polymer/filler interphase can be related to changes in the microstructure of the polymer at vicinity of fibers and the surface properties of fibers leading to development of interphase.

An effective interface can be obtained if there exists sufficient bonding between constituents. Silane coupling agents, which are generally applied to the surface of inorganic fillers, are well known and most widely used interfacial agents to bind the glass fibers to the polymeric matrices [29]. However, because of the lack of functional groups of polymers to allow reaction at the interface, silane coupling agents are incapable to bind the fibers to polymers. One of the well-known solutions to this problem is the introduction of new functional groups externally to the polymer. It has been reported by the many researchers that to constitute polarity or acidity to a non-polar matrix, great variety of acidic additives including acrylic acid, methacrylic acid, maleic acid and their anhydrides have been used to enhance the adhesion between glass fibers and polymers [30]. The most commonly applied process is the melt blending of reactive species, especially through reactive extrusion [31]. The previous studies showed that incorporation of short glass fibers (SGF) to the ABS results in an improvement in tensile strength and modulus, on the other hand a drastic decrease in toughness. Microscopic studies showed a lack of adhesion between ABS and glass fibers [1, 32, 33]. Furthermore, the compatible silane coupling agent type to promote adhesion at the GF/ABS interphase is lacking in the literature.

In this research as one of the objectives, to solve the interfacial adhesion problem and reduction in toughness in ABS/SGF composites, blending of ABS with PA6 was carried out. Therefore, the most compatible silane coupling agent type among the organosilanes examined for ABS/PA6/SGF composites were determined, and the effects of ABS/PA6 ratio, SGF loading level, compatibilizer content and processing conditions such as screw speed and barrel temperature in the extrusion were examined.

Over the last two decades, a new term has entered the materials science terminology. This developing technology, termed polymer nanocomposites, uses new type fillers that are capable of reinforcing the matrix polymer at the nano-scale level. Organically modified layered silicate (OMLS) based nanocomposites have developed extensively since Toyota Research first discovered by polymerizing caprolactam in the presence of clays [34-37], however, nanocomposites have been produced by melt mixing using conventional processing devices [38-40]. In these melt processes, by dispersing the 1 nm thick, high aspect ratio, aluminosilicate sheets of OMLSs in a polymer matrix, the physical properties such as stiffness and strength, solvent and UV resistance, gas barrier properties, dimensional stability, and flame retardancy can be enhanced at extremely low filler concentrations ($\leq$10 % by volume).

In general, OMLS based nanocomposites are divided into three general types: conventional composites, in which the clay acts as normal filler; intercalated nanocomposites, in which a small amount of polymer enters into the clay layers; and exfoliated nanocomposites, in which the clay layers are fully dispersed in a continuous polymer matrix. The last structure is important, because a great improvement in properties is achieved even at very low clay concentrations [42]. The degree of exfoliation is highly dependent on the type of organic modifier to enhance compatibility between clay and polymer matrix to promote diffusion of polymer into clay platelets together with the processing conditions such as the intensity of shear in the mixing, the processing temperature and the residence time distribution (or amount of backflow) [43-46].

Recently, the research in polymer nanocomposites has built up towards the preparation of polymer blends based nanocomposites to combine the synergistic effects of polymer blending and polymer nanocomposites. One of the applied methods is the impact modified-polymer-clay ternary nanocomposite systems to improve the toughness of the final material by incorporation a rubbery polymer. The recent examples from the literature are the nanocomposites based on PA6/ethylene-propylene rubber (EPR) [47], PA6/ethylene-co-propylene maleated rubber [48], PA6/maleated styrene-butylene-co-ethylene-styrene elastomer [49], PA6/maleated ethylene-methylacrylate blends [50]. Other method is the preparation of nanocomposites based on blends of an engineering plastic with a commodity plastic or blends of two engineering plastics, such as PA6/polypropylene [51], polycarbonate/polypropylene [52], PA6/poly(phenylene oxide) [53], polymethylmethacrylate/polystyrene [54]. One of the aims of the current study is to process and characterize the compatibilized ABS/PA6 blends based nanocomposites due to their potential commercial importance.

For the production of the nanocomposites, a mini-twin screw batch extruder was utilized as the processing device. Due to time and cost effectiveness of these mini-devices, they are frequently used in material research and development activities in nanocomposites. However, the effects of processing conditions for lab-scale mixers on the properties of nanocomposites have not been studied using a blend based organoclay nanocomposite; therefore, in this study it was also aimed to explore the effects of micro-compounding process conditions such as screw speed, screw rotation-mode (i.e. co- or counter-rotation) and mixing time as a function of blend composition and clay loading in ABS/PA6 blends based organoclay nanocomposites. Furthermore, it was also aimed to modify the screws of the micro-compounder to improve mix-ability of the device.

In the light of objectives stated above, this dissertation is partitioned into three main parts. In the first part, the compatibilization of ABS/PA6 blends is taken in hand in terms of compatibilizer type and blend composition. In the second part, SGF reinforcement of ABS and ABS/PA6 are investigated by considering the effects of SGF surface chemistry, SGF content, ABS/PA6 ratio, compatibilization and twin-screw extrusion conditions on the performance of composites. In the third and final part of the study, compatibilized ABS/PA6 blends were utilized as the matrix material for organoclay based nanocomposites. The influence of blend compositions, clay loading level and processing conditions were examined.

CHAPTER 2

BACKGROUND

2.1 Polymer Blends

Mixing of two or more polymers at different chemical composition is an effective way of combining performance and economic relationships using existing materials [55]. As a result, the area of polymer blends has become an important research topic for both academy and industry. Fundamental issues that affect the properties of blends include equilibrium phase and interfacial behavior, physical and chemical interactions between the components, phase morphology, and rheology, all of which are related to the issues of compatibility [55]. One of the most important way of polymer blending is the incorporation of an elastomeric phase in a rigid matrix to enhance mechanical toughness [55].

The physical properties of a blend depend on the degree of miscibility between the components. Fully-miscible blends generally represent the simplest case. For amorphous polymers, most properties follow some additive relationship; thus miscible blends are similar to random copolymers in this regard [56]. The glass-transition temperature, and hence the softening point, is generally a monotonic function of composition, but maxima have been observed in strongly interacting systems [56]. As a rule, most mechanical properties follow nearly linear relations with composition in such systems, but exceptions are known [57-62].

For blends where the components form separate phases, properties depend on the arrangement of these phases in between and the nature of the interface (i.e. interfacial reactions and strength) between the phases. Immiscible blends behave like composite materials in many respects. Properties like softening temperature, modulus, permeation, etc, are dominated by the properties of the component that forms the continuous phase [59]. Failure properties, especially those related to ductility, e.g, elongation at break and impact strength, often depend on the dimensions of the phases and the degree of interfacial adhesion between the components [55].

The nature of the interface is related to the thermodynamic interaction between the components [63], which then governs morphology generation in the melt via interfacial tension, and adhesion in the solid state via the thickness of the interfacial zone and the degree to which chains from the two phases entangle. When the thermodynamic affinity is very low, the blend can exhibit a degree of toughness well below that of either component and is regarded as incompatible. Improvement of this property response is often called compatibilization and approaches to this important aspect of blend technology are described in the forthcoming part. When the interaction between phases is good enough, additive properties may be obtained without compatibilization. The PC-SAN interface [63] seems to be such a case and forms the basis of commercial PC-ABS blends.

2.1.1 Compatibilization

Incompatible blends have little commercial value because of the deficiencies in ductility-related properties such as impact resistance, elongation at break, and strength at break. This overall response is usually related to the lack of interfacial adhesion between the phases in immiscible systems and to poor control of morphology [55]. Two general methods are used to overcome these problems: copolymer addition and reactive compatibilization. Both methods seek to place a block or graft copolymer at these interfaces. This lowers interfacial tension, retards coalescence of domains and improves the adhesion, all of which improves dispersion and reduces domain size. Retarding coalescence leads to a more stable morphology and lessens the dependence of blend performance on processing history.

2.1.1.1 Copolymer Addition

Addition of block or graft copolymers to improve the mechanical properties of immiscible polymer blends has been used since the mid-1970s with varying degrees of success. Studies have shown that interfacial adhesion [64] and mechanical compatibility [55] can be improved by the addition of appropriate block and graft copolymers. In their simplest forms, the copolymers have block or graft segments that are chemically identical to those in the respective phases, although non-identical segments, which are miscible or partially miscible in the respective phases, are also effective [55]. The principle of compatibilization by block or graft copolymers is shown in Figure 2.1. The compatibilizer acting in fact like a "surfactant" and will preferably migrate at the interface to reduce surface tension. Red blocks are compatible with polymer A (matrix) and blue blocks are compatible with polymer B (dispersed phase). The consequence will be a better interfacial adhesion and better dispersion [65].

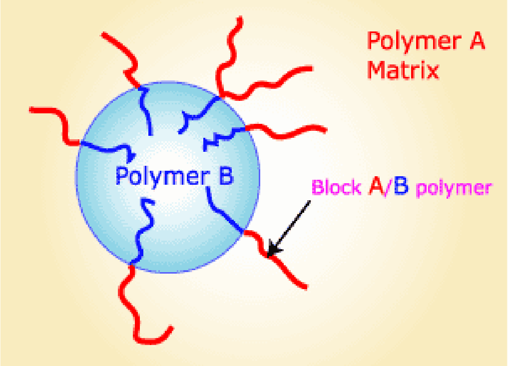

Figure 2.1 Compatibilization by Block Copolymers

Like a surfactant, block-copolymers have also the tendency to create miscelles. The amount of compatibilizer is generally high (sometimes more than 5%). Moreover, there are not too many block-copolymers commercially available for all polymers and they are generally expensive [65].
As little as 0.5–2.0% of diblock [66] can be sufficient to achieve uniform and stable phase dispersion with most of the copolymer at the interface. Diblocks are thought to be the most efficient interfacial agents, but triblock and graft copolymers are also useful [55].

2.1.1.2 Reactive Compatibilization

Polymers with functional groups such as anhydride, carboxylic acid, amine, hydroxyl, epoxy, etc. have been utilized in reactive compatibilization. These groups can react by means of condensation chemistry to give block or graft copolymers whose constituent chains are joined by ester, amide, and imide linkages during the melt-blending process. In the specific case of rubber-toughened polyamides, the naturally occurring functional end groups, e.g. the primary amine ends or carboxylic acid ends, of the polyamide provide the needed reaction capability. The other functionalized polymer can be a maleic anhydride-modified rubber. During melt mixing, reactions at the interface produce a nylon-grafted rubber phase with significantly reduced dispersed rubber particle size. Alternatively, small amounts of polymers containing reactive functionality can be added to one of the phases to produce the reaction [66]. For instance, various polymers miscible with SAN and reactive with amine groups have been added to ABS to affect reactive compatibilization of polyamide–ABS blends; therefore, system shows reductions in domain size of up to a factor of 100 as a result of such reactions [12, 67, 68].

The principle of action is to react at the interface to create "in-situ grafted block copolymer” by reaction between functional groups of the different polymers (see Figure 2.2). The functionalized copolymer is miscible with the matrix and can react with functional groups of the dispersed phase. The advantages are adjustable reactivity, high efficiency and generally lower cost than block copolymers [65].

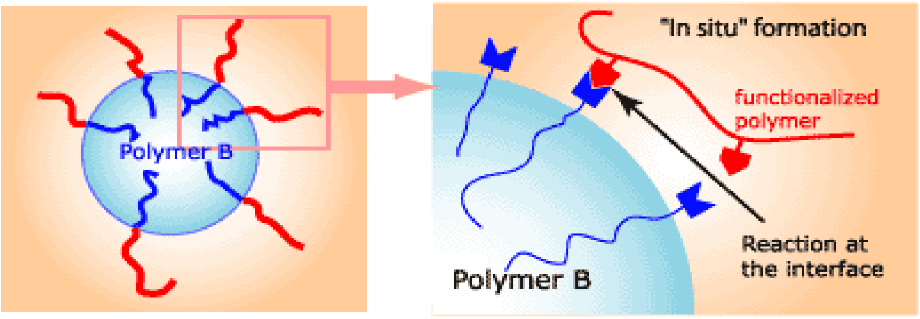

Figure 2.2 Compatibilization by reactive copolymers

In maleated polymers, the reactive monomer is generally maleic anhydride. Maleated polymers are most widely known family of functionalized polymers used as compatibilizer and adhesion promoters. They can be prepared directly by polymerization or by modification during compounding (this process is called reactive extrusion). Anhydride groups can react with amine groups, epoxy groups and eventually alcohol groups. The following scheme shows the example of reaction between a maleated polymer and -NH_2 end groups of polyamides such as Nylon 6,6 or Nylon 6 in order to compatibilize PA/polyolefin blends.

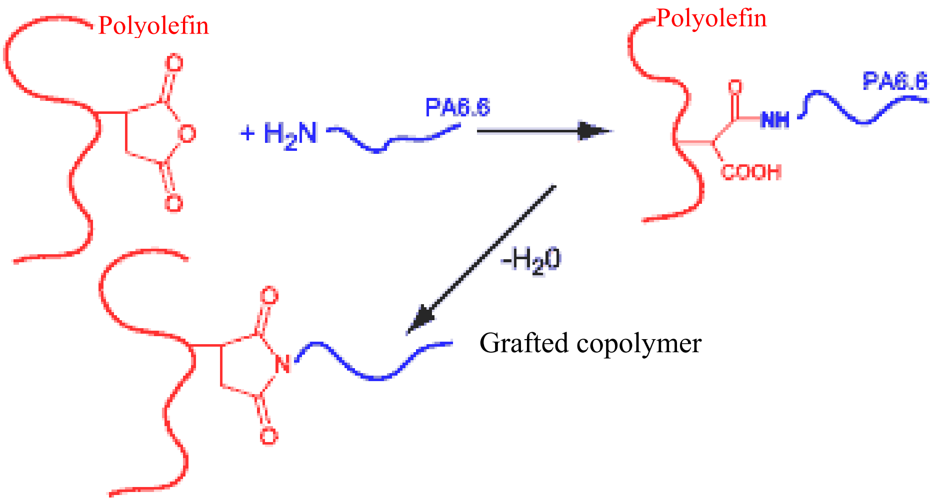

Figure 2.3 Reaction scheme of a maleated olefin with a polyamide

In the group of epoxydized polymers, they are generally modified by glycidyl methacrylate. They are very reactive with amine, anhydride, acid, alcohol groups. They are recommended to compatibilize polyesters (PET, PBT) and olefinic polymers or elastomers according a mechanism below:

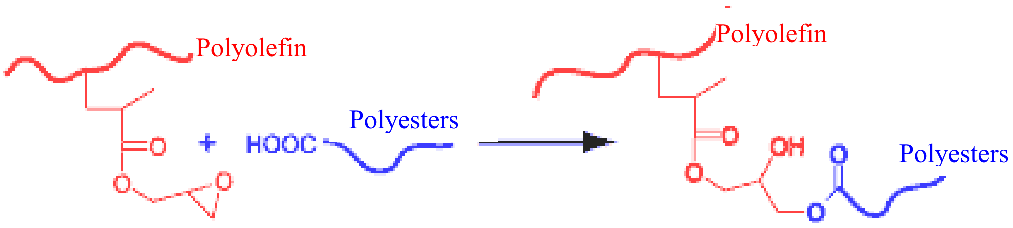

Figure 2.4 Reaction scheme of an epoxydized olefin with a polyester

2.2 ABS, Polyamide-6 and ABS/Polyamide-6 Blends

2.2.1 Acrylonitrile–Butadiene–Styrene (ABS) Terpolymer

Acrylonitrile–butadiene–styrene (ABS) terpolymers are composed of elastomer, which is polybutadiene, dispersed as a grafted particulate phase in a thermoplastic matrix of styrene and acrylonitrile copolymer (SAN). The presence of SAN grafted onto the elastomeric component, usually polybutadiene or a butadiene copolymer, compatibilizes the rubber with the SAN component (see micrograph showing structure of ABS in Figure 2.5). Property advantages provided by this graft terpolymer include excellent toughness, good dimensional stability, good processibility, and chemical resistance. The system is structurally complex. This allows considerable versatility in the tailoring of properties to meet specific product requirements. Consequently, research and development in ABS systems is currently active [69].

The proportions of monomers can vary from 15% to 35% acrylonitrile, 5% to 30% butadiene and 40% to 60% styrene. The result is a long chain of polybutadiene criss-crossed with shorter chains of poly(styrene-co-acrylonitrile). Numerous grades of ABS can be produced for high heat and flame-retardant, static dissipative or high impact requirements. Good chemical resistance combined with the relatively low water absorption (<1%) results in high resistance to staining agents. Antioxidants improve oxidative stability [69].

In manufacturing, grafting is achieved by the free-radical copolymerization of styrene and acrylonitrile monomers. The three commercial processes for manufacturing ABS are emulsion, mass, and mass-suspension [69]. ABS is sold as an unpigmented product for on-line coloring using color concentrates during molding, or as precolored pellets. ABS can be processed by compression and injection molding, extrusion, calendering, and blow-molding. Post-processing operations include cold forming, painting, and adhesive bonding. As a “bridge” polymer between commodity plastics and higher performance engineering thermoplastics, ABS has become the most selling engineering thermoplastic in the world [69].

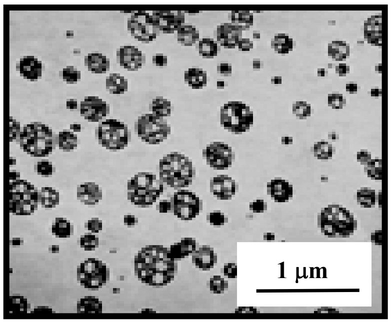

Figure 2.5 Microstructure of ABS (black and grey parts are polybutadiene and SAN matrix, respectively) [69]

Toughness is a primary consideration in the selection of ABS for many applications. ABS is structured to dissipate the energy of an impact through shear and dilational modes of deformation. Upon impact, the particulate rubber phase promotes both the initiation and termination of crazes. Crazes are regions of considerable strength that contain both voids and polymer fibrils oriented in the stress direction. Crazes are terminated by mutual interference or are stopped by other rubber particles, thereby dissipating energy without the formation of a crack, which would lead to failure [70].

Good thermal stability plus shear thinning allow wide flexibility in viscosity control for a variety of processing methods. ABS exhibits non-Newtonian viscosity behavior. For example, raising the shear rate one decade from 100 s^{-1} to 1000 s^{-1} (typical in-mold shear rates) reduces the viscosity by 75% on a general-purpose injection-molding grade. Raising melt temperature can also reduce viscosity;

typically increasing the melt temperature 20-30°C within the allowable processing range reduces the melt viscosity about 30% [71].

Its broad property balance and wide processing window has allowed ABS to become the largest selling engineering thermoplastic as mentioned on the previous pages. Table 2.1 summarizes the production capacities of some ABS producers in 2005.

Table 2.1 The production capacities of some ABS producers in 2005 [72]

PRODUCER	CAPACITY (million pounds/year)
Bayer, Addyston, Ohio	450
Diamond Polymers, Akron, Ohio	50
Dow, Allyn's Point, Conn.	55
Dow, Hanging Rock, Ohio	140
Dow, Midland, Mich.	195
GE Plastics, Bay St. Louis, Miss.	280
GE Plastics, Ottawa, Ill.	475
GE Plastics, Washington, W.Va.	160

2.2.2 Polyamide-6 (PA6)

PA6, was first discovered in 1899, is a tough, white translucent, semi-crystalline solid, melts at a relatively lower temperature with respect to other engineering plastics. Nylon-6 is produced commercially from caprolactam by ring opening polymerization (see Figure 2.6), which is the industrially most important lactam [69].

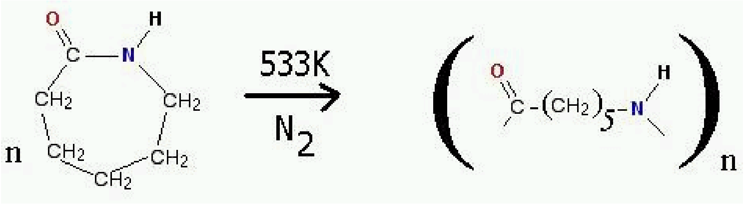

Figure 2.6 Ring opening polymerization of ε-caprolactam

The PA6 is produced from caprolactam in the presence of water. The reaction is initiated by a hydrolytic ring opening to aminocaproic acid followed by reaction of the amine end with caprolactam, giving ring opening and further addition reactions. The polymerization, which takes place at 240–280°C, can be carried out at atmospheric pressure [69].

Even at elevated temperatures, PA6 retains its shape because of its partially crystalline structure and the strong cohesive forces exerted between the molecules by the hydrogen bonds. PA6 resins are characterized by a combination of high strength, elasticity, and toughness and abrasion resistance. Good mechanical properties are maintained up to 150°C, although a more conservative limit for use is 120°C. Both toughness and flexibility are retained well at low temperatures. The solvent resistance of material is good, but it's strongly hygroscopic. This property positively affects the toughness and elastic behavior of the product while it decreases the elongation at break. The equilibrium moisture content of PA6 is 0.25-0.30 % at atmospheric conditions [69].

2.2.3 ABS/PA6 Blends

Blends of ABS with PA6 are immiscible due to the highly polar structure of polyamide; therefore simple blends of ABS and PA6 do not exhibit desired properties. The widely applied method is utilization of reactive compatibilizers to obtain well-dispersed and stable morphology.

Due to the crystalline structure of linear polyamides with a high melting point, it is preferable to have these resins as the continuous phase. These systems have better heat and solvent resistance than the ones with reversed morphology. However, to preserve the ABS-generated toughness in a wide range of conditions, the ABS phase should also be continuous. Thus, co-continuity of phases has been the preferred morphology of these blends. Such morphology can be achieved by adjusting concentration and the viscosity ratio of the individual components [1]. In these systems compatibilization must stabilize the co-continuity of morphology, and provide an appropriate degree of dispersion. Optimization of the amount and the type of compatibilizer to generate stable co-continuous morphology is the key factor with an appropriate degree of dispersion. Just as in the case of blends with dispersed-drop morphology, so also in systems with co-continuous structures it is the degree of finesse that determines the performance [1].

The advantages of blending ABS with PA6 are primarily to reduce moisture sensitivity, improve toughness and reduce shrinkage and warpage of the latter resin. The ABS/PA6 compatibilized blends combine the intrinsic properties of the semi-crystalline PA6 with those of the amorphous ABS. The materials have good processability and flow, good surface finish (gloss or matte as required), high heat, chemical, oil, wear and abrasion resistance, dimensional stability, low temperature impact strength, reduced moisture sensitivity and economy [1].

The main uses of ABS/PA6 alloys are in the automotive, chemical, electrical, electronics, consumer and sport industries, such as large components for recreational vehicles, snow-mobiles, tractors, lawn and garden equipment, power tool housings, impellers, wheel covers, gears, mirror housings and automobile interior components. The material has also been used in anti-vibration damping structures.

In the literature, the reaction capability of anhydrides with amide groups is seemed to be an efficient solution to compatibilize the ABS/PA6 system. Maleic anhydride grafted polystyrene (SMA) and maleic anhydride grafted poly (styrene-*co*-acrylonitrile) SANMA are widely used [3, 12, 73]. When the chemical structures of these two copolymers are considered, it is seen that while styrenic groups are miscible with ABS, the maleic anhydride groups reacts with amide groups of PA6. The following scheme shows this reaction (Figure 2.7):

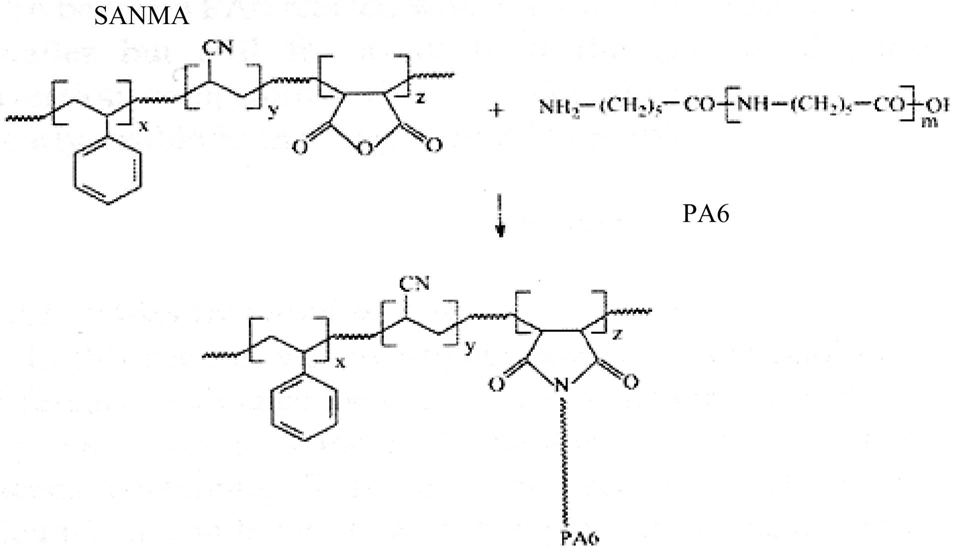

Figure 2.7 Compatibilization reaction between SANMA and PA6

Imidized acrylic polymers are also used to compatibilize ABS/PA6 polymers [2, 16, 74]. Imidized acrylic can be obtained with reactive extrusion of PMMA with methylamine at sufficiently high temperature and pressure. Imidized acrylic polymers have high modulus, tensile strength and heat distortion temperature, which make them attractive candidates for several industrial uses. More recently, the presence of controlled levels of acid and anhydride groups in these polymers has been utilized to generate blends with nylon with a grafting reaction with the amine groups. Depending on their functionality level, these polymers are miscible with SAN phases, which make them potentially useful compatibilizers for polyamide/ABS blends. The main repeat units of imidized acrylic polymers can be seen from the reaction given in Figure 2.8.

$\text{PMMA} + CH_3NH_2 \longrightarrow$

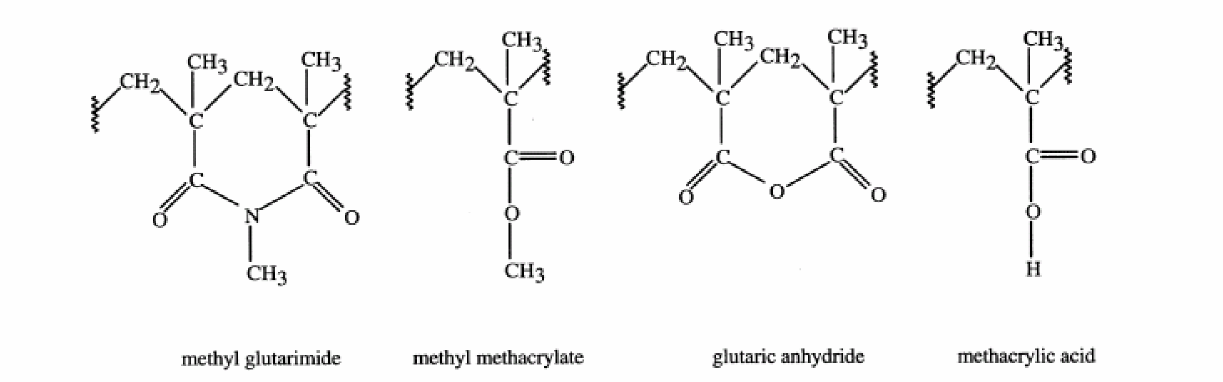

Figure 2.8 Reaction scheme of PMMA and methylamine

Oxazoline groups can also be grafted to a polymer, and this approach has been used to produce reactive polystyrene by Dow Chemical Co. A peroxide-initialized free radical grafting is often used to attach oxazoline groups to a polymer. Recently, another method was proposed for converting the nitrile groups of SAN or nitrile rubber into oxazoline with the aid of a metal salt catalyst in solution at 130 to 140°C or in the compounding equipment at 230 to 240°C in the absence of a solvent. 2-Aminoethanol (AE) and zinc acetate are shown to be an efficient reactant and catalyst, respectively, for this reaction [75]. The nitrile content has a marked influence on the efficiency of the reaction between SAN and AE. It should, therefore, be interesting to explore the reactivity of AE towards a variety of SAN materials with different acrylonitrile contents. The number of available end groups of PA6, which is related to the molecular weight, is also of interest. The possible reactions between oxazoline modified SAN and PA are shown with the given mechanism in Figure 2.9.

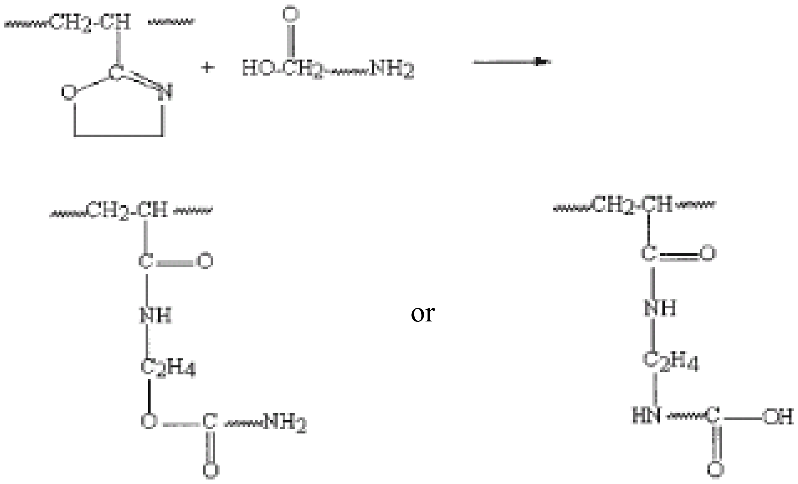

Figure 2.9 Reactions between oxazoline functionalized SAN and PA6

Moreover, acrylic group including anhydride functional polymers, such as poly (methylmethacrylate-*graft*-maleic anhydride) (MMA-MA) and poly(n-butyl acrylate-*graft*-maleic anhydride) (nBA-MA), were used as a compatibilizer due to miscibility of acrylic group with styrenics in order to achieve desired degree of interfacial interactions between PA6 and ABS [76].

Epoxy group is also capable of reacting with acidic end groups of polyamides; therefore, epoxy grafted acrylic or styrenic copolymers can be used to compatibilize ABS and PA6.

In this research, commercially available epoxydized and maleated olefinic copolymers, ethylene-methyl acrylate-glycidyl methacrylate (EMA-GMA) and ethylene-n butyl acrylate-carbon monoxide-maleic anhydride (EnBACO-MAH) were selected as the compatibilizers for ABS/PA6 blends.

2.3 Short Glass Fiber Reinforced Polymeric Composites

A composite is defined as a combination of two or more components, differing in form or composition on a macro-scale with two or more distinct phases having recognizable interfaces between them [77]. Proper combinations of these components into composites give rise to properties that transcend those of constituents, as a result of combined action.

Composites usually consist of a reinforcing material embedded in a matrix. The most effective way to obtain higher strength and improved overall properties is to incorporate dispersed phase into the matrix, which can be an engineering material such as ceramic, metal or polymer. Therefore, it is possible to classify the composites with respect to matrix material. Polymer matrix composites (PMCs), thermoplastic or thermosetting, are one of the important subgroup of composites. The reinforcing component in a composite structure can be discontinuous or continuous, in particulate or fibrous form. The most commonly employed reinforcing component for polymer matrices is short fibers. Usually, materials in fibrous form are much stronger than in any form, which is the basic reason for the ascending of fibrous reinforcements [77]. Because of the higher strength, stiffness and ease of production, glass fibers are very common and widespread. The addition of glass fibers to polymers yields an improvement drastically on the stiffness, strength and the high temperature performance [23].

Glass fibers, which are non-crystalline, may consist of a range of compositions; all of which have certain characteristics in common. There are four main classes of glass fibers used commercially [77]:
i.) A-Glass: High alkaline grade (essentially soda-lime-silica)

ii.) E-Glass: Electrical grade (calcium alumina-borosilicate with low alkali oxide content)

iii.) S-Glass: High strength grade (Magnesium alumina silicate without boron oxide)

iv.) ECR-Glass: modified E-Glass grade for chemical resistance

Fibers from any of these classes can be prepared. E-glass grade fiber is the most widely used one for reinforcement purpose, although S-Glass has the higher strength and modulus. Table 2.2 represents the properties of glass grades.

Table 2.2 Properties of glass fibers from different grades [77]

Material	**Density g/cm^3**	**Tensile Strength (MPa)**	**Elastic Modulus (GPa)**	**Strain to failure (%)**	**Coefficient of thermal expansion (10^{-6}/K)**
E-Glass	2.620	3450	81	4.9	5.0
S-Glass	2.500	3590	89	5.7	5.6
A-Glass	2.500	3050	69	5.7	8.6

Because of several advantages including ease of processing, possibility of obtaining complex shapes, higher strength/density ratio and recycling, short glass fiber (SGF) reinforced thermoplastics are of great interest. It is known that some properties of plastics are improved by the incorporation of SGF by performing economical processing methods such as extrusion and injection molding [78]. The properties of SGF reinforced thermoplastics depend not only on the properties of matrix and fiber alone, but also on

- glass fiber content
- orientation of fibers
- aspect ratio of fibers and its distribution
- fiber/matrix adhesion

2.3.1 Glass Fiber Content

The glass fiber content is normally expressed in terms of volume fraction or weight fraction. The following equation is valid,

$$V_f = \frac{\frac{W_f}{\rho_f}}{\frac{W_f}{\rho_f} + \frac{W_m}{\rho_m}} \tag{2.1}$$

where W and ρ are respectively corresponding to weight fraction and density with subscripts of m and f denoting the matrix and the fiber. The basic theoretical concept to explain the dependence of glass fiber content of any physical property is based on rule of mixtures

$$P_c = P_f V_f + P_m (1 - V_f) \tag{2.2}$$

where P stands for any property (like modulus, density, etc) and V stands for volume fraction with subscripts of m and f denoting the matrix and fiber, respectively. It is obvious from Equation (2.2) that increasing the volume fraction of fibers results in an increase in property of composite. The more realistic theory used for mechanical properties of SGF reinforced systems is:

for $L \geq L_c$,

$$\sigma_c = k\sigma_f V_f \left[1 - \left(\frac{L_c}{2L}\right)\right] + \sigma'_m V_m \tag{2.3a}$$

and for $L < L_c$,

$$\sigma_c = \left(k\tau L V_f / d\right) + \sigma'_m V_m \tag{2.3b}$$

where σ_c is the strength of composite, σ_f is the ultimate strength of fibers, L is the length of fibers, L_c is the critical length of fibers, V_m and V_f are the volume fractions of matrix and fiber, respectively, σ'_m is the tensile stress at break for matrix, k is the orientation factor, d is the diameter and τ is the adhesive bond strength [79].

The practical experiences also showed that increase in fiber volume fraction increases the tensile strength and modulus [80], and each resin has an upper limit of reinforcement where addition of more fiber is not cost effective [81].

2.3.2 Fiber Orientation Distribution (FOD)

It is known that the mechanical properties of SGF reinforced thermoplastics depend critically on the fiber orientation distribution (FOD). In order to obtain high performance injection molded SGF reinforced thermoplastics, it is therefore of greatest importance to study the effects of the FOD, because of the isotropy dependence of final product properties. During extrusion compounding and injection molding processes, progressive changes take place in fiber orientation through the molded component. The changes are related in a complex way to the size and concentration of fibers, rheology of polymer melt, mold cavity design and the processing conditions; therefore, the control of orientation is a very hard work. During processing of short glass fiber reinforced thermoplastics, the polymer melt undergoes either elongational flow or shear flow. An indication of the effects of those flow processes on the fiber orientation is illustrated in Figure 2.10 for simple two-dimensional deformations.

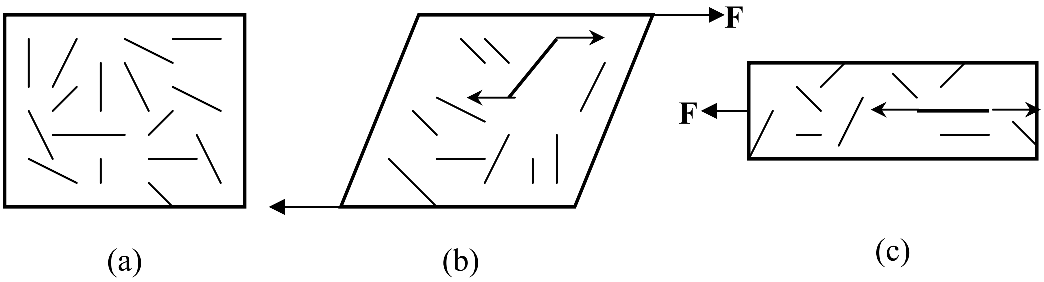

Figure 2.10 Schematic representation of changes in fiber orientation occurring during flow (a) initial random distribution, (b) rotation during shear flow, (c) alignment during elongational flow [82]

The degrees of preferred fiber orientation after processing depend on the flow field and type. The viscosity of the molten matrix affects the final orientation distribution mainly on the way in which the mold fills. Taking the orientation effect into account, the tensile strength of fiber reinforced composites may be calculated by using Equations (2.3a) and (2.3b). In these equations, k-the orientation factor- is unity if there are only continuous fibers present, and 0.33 if randomly oriented short fibers exist. The measurement of fiber orientation and FOD is performed utilizing 2D images [83].

2.3.3 Aspect Ratio of Fibers

Aspect ratio of fibers (length/diameter) is the other factor influenced by process conditions. During the extrusion and injection molding, shear stress exerted by the screw or ram will break the fibers and result finally in a fiber length distribution with an asymmetric character with a tail at long fiber lengths. The number average fiber length is defined as;

$$L_n = \frac{\sum N_i L_i}{\sum N_i} \tag{2.4}$$

where N_i is the number of fibers of lengths L_i.

The improvement in mechanical properties of fiber filled polymer is due to ability of withstanding a higher proportion of the mechanical load than the matrix it replaces. Fibrous filler is required in order to provide sufficient transfer of mechanical load from the matrix to the reinforcement. Such transference can only occur if the fiber length exceeds the critical length. Tensile loads acting on the fibers are zero at the ends and gradually increase to a plateau in the central portion of the fibers. Thus, the parts of the fibers near the ends carry less load then middle section. The sum of the length of the fiber on each end required for the tensile load to reach its plateau or maximum value is often called critical length. In other words, a fiber must have a length of at least critical length to achieve maximum stress in the fiber [84].

Fibers that are shorter than critical length will pull out the matrix under tensile load. For such a case, full load transfer is not realized. At the critical length both the fiber and matrix will fracture along the same failure plane. Additional increase in fiber length will not increase the strength of the composite, since the failure will be the same as that experienced at the critical length, as shown in Figure 2.11 [85].

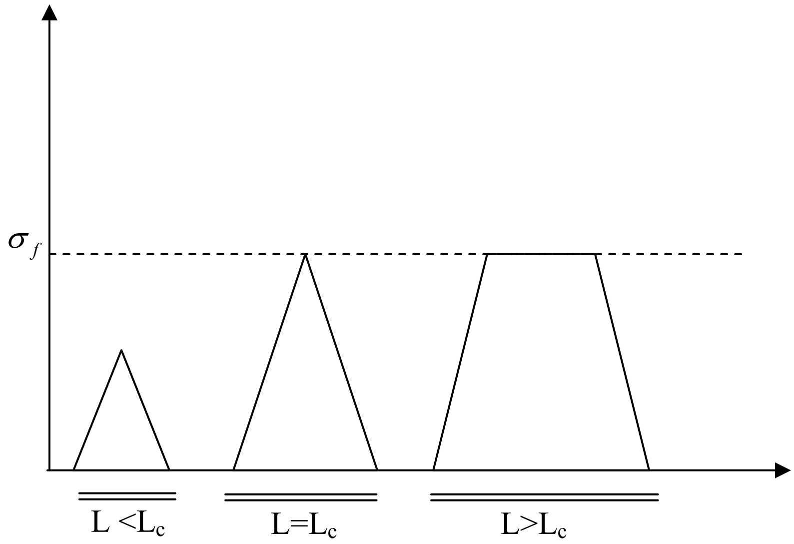

Figure 2.11 Simplified illustration of the variation of tensile strength in SGF reinforced polymers as a function of fiber length [85]

Because the fibers suffer severe damage during compounding and injection molding, their ultimate length is usually only a fraction of its value. The possible causes of fiber fracture during processing are listed as follows [86]:

i.) Fiber/Fiber Interactions: Abrasion of glass surfaces causes the uncontrolled fiber breakage, leading to direct or subsequent fracture because of increased stress concentration at the fiber ends (by increasing number of fiber ends). Breakage may also occur due to bending stress caused by fiber overlap.

ii.) Fiber/Machinery Interactions**:** The wear of the equipment when processing reinforced thermoplastics supports the idea of fiber/machinery interactions being significant factor. This effect is a result from the high shear rate on the moving surfaces.

iii.) Fiber/Matrix Interactions: Viscous forces imparted by the polymer may cause fracture of fibers. In order to avoid this shearing condition, the melt temperatures should be kept as high as tolerable regarding the thermal degradation to reduce the viscosity. For the protection of fibers, the screw speed of the machinery may be lowered.

2.3.4 Fiber/Matrix Adhesion

The mechanical properties of resulting SGF reinforced polymer depend heavily on the nature of the fiber/matrix bonding strength. A strong adhesion generally leads to the best composite properties but there are some exceptional handicaps such as lowering the toughness, increasing the mold shrinkage, etc. Many effective coupling agents that are capable of forming desired medium to established bonding have been identified for polymer matrices [29]. Silane coupling agents are one of the most widely used organic molecules to promote interfacial adhesion.

The need for techniques to bond glass fibers to polymer matrices was recognized since glass fibers were first used as reinforcement [29]. Silane coupling agents are widely used for this purpose today. They are believed to create a bond between many inorganic substrates such as glass, and organic polymers by the scheme shown in Figure 2.12 provided that an appropriate organofunctional group is chosen. The general formula of an organosilane shows two classes of functionality [29].

$$\mathbf{R_n\text{-}Si\text{-}X_{(4-n)}}$$

Figure 2.12 The chemical structure of silane coupling agents

The X group is involved in the reaction with the inorganic substrate. The bond between X and silicon atom in coupling agents is replaced by a bond between the inorganic substrate and the silicon atom. X is a hydrolysable group, typically, alkoxy, amine, or chlorine. The most common alkoxygroups are methoxy and ethoxy, which give methanol and ethanol as by-products during coupling reactions. Since chlorosilanes generate hydrogen chloride as a byproduct during coupling reactions, they are generally utilized less than alkoxysilanes. R is a non-hydrolysable organic radical that possesses a functionality, which enables the coupling agent to bond with organic resins and polymers. Most of the widely used organosilanes have one organic substituent [29].

Appropriate organofunctional groups generally involve a moiety that reacts with the polymer resin to form a chemical bond with the glass substrate and the organic matrix or, alternatively, a strong physical interaction. Typically, the silane coupling agent is provided as a trialkoxysilane, as shown in Figure 2.13, which readily hydrolyzes in the presence of water to form the corresponding silanol, the active agent in the reaction with the glass substrate [29]. These silanol groups can undergo condensations with silanol groups naturally occurring on the glass surface to form a siloxane bond between the glass and silane coupling agent. The result is a functionalized glass surface where the organofunctional group can then react with the polymer matrix if a reactive functionality has been chosen. There is no doubt the simple conceptual scheme described earlier and shown in Figure 2.13 may capture all the events at the fiber–matrix interface.

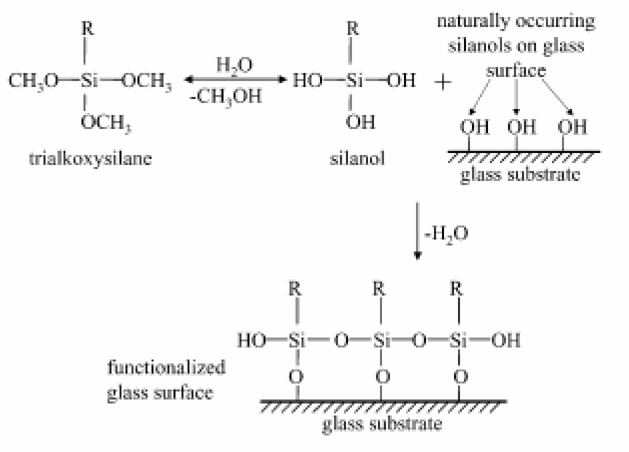

Figure 2.13 Reactions of organosilanes (R and *R are the functionalities of silane coupling agent and polymer, respectively)

The number of reactive sites on a surface area and the type of silane deposition sought, i.e. monolayer, multilayer or bulk, are all factors which can be used in calculating the amount of silane necessary to silylate a surface. Silanes with one hydrolysable group can be utilized to produce surfaces with monolayers of consistent stoichiometry. These materials are more expensive and produce surfaces with less hydrolytic stability. The number of silanols on a surface is varied by thermal history. Optimum deposition of silane with more than one hydrolysable group is defined as the amount necessary to produce a surface of uniform energy. A value defined as the wetting surface describes the area in m^2 per one gram of a silane deposited from solution will cover. In combination with data on the surface area of a siliceous substrate in m^2/g, the amount of silane required for deposition may be calculated. Most composite, adhesive, and coating formulations do not follow any stoichiometry, but simply define optimal concentration by operational success. For most filler, a treatment level of 0.02-1.00% by weight is used [29].

Selection of the appropriate coupling agent is accomplished by empirical evaluation of silanes within predicted categories. Exact prediction of the best silane is extremely difficult. Increased bond strength by utilization of silanes is a result of a complex series of factors - wet out, surface energy, boundary layer absorption, polar adsorption, acid-base interaction, interpenetrating network formation and covalent reaction. Strategies for optimization must take into account the materials on both sides of the interface and their susceptibilities to the various coupling factors. Usually the initial approach is to select a single coupling agent and assume a direct bond between the two materials [29].

For a better understanding of fiber/matrix interphase mechanics, it is necessary to determine the interface strength and possible interactions between polymer and fiber. This is usually carried out by means of contact angle measurements [27, 87, 88] to determine the thermodynamic energy (work) of adhesion and specific mechanical tests on real or model composites to determine the strength of interphase formed between fiber and polymer [89].

2.3.4.1 Work of Adhesion

The method of estimating the thermodynamic adhesion at fiber matrix interphase, which is generally called work of adhesion, from the surface properties of both materials, is a theoretical approach. This thermodynamic model of adhesion is certainly most widely used approach in adhesion science. This theory considers that the adhesive will adhere to the substrate because of interatomic and intermolecular forces established at the interphase, provided that an intimate contact between both materials is achieved [90].

The total surface energy, γ_i^{TOT}, of a given non-metallic material (i) can be considered as being composed of two parts: the Liftshitz-van der Waals (LW), γ_i^{LW}, and the acid-base (AB) component, γ_i^{AB}. The former represents the dispersion forces, dipole-dipole and induction, and the latter represents the short range H-bonding or acid-base interactions. This is written as the sum of the two components,

$$\gamma_i^{TOT} = \gamma_i^{LW} + \gamma_i^{AB} \qquad (2.5)$$

where the acid-base term is a property of one that depends on the mutual interaction of two unlike species, an acid and base. γ_i^{AB} is composed of two surface parameters which are independent of physical presence of another one: γ_i^{+} is the Lewis acid component and γ_i^{-} is the Lewis base component of the surface free energy. These, together, yield the acid-base component of surface free energy, γ_i^{AB}.

$$\gamma_i^{AB} = 2(\gamma_i^{+}\gamma_i^{-})^{1/2} \qquad (2.6)$$

The most characteristic feature of these Lewis acid and base components is that they are not additive although the non-polar ones are. It means that if phase (i) possesses only γ_i^{+} or γ_i^{-}, this component does not participate in the total surface free energy of the phase (i). However, it will interact with the complementary component of phase (j), contacting phase. As a result, the total surface free energy of a phase (i) is

$$\gamma_i^{TOT} = \gamma_i^{LW} + \gamma_i^{AB} = \gamma_i^{LW} + 2(\gamma_i^{+}\gamma_i^{-})^{1/2} \qquad (2.7)$$

The values of γ_i^{AB}, $\gamma_i^{+}$and γ_i^{-} can be determined by using the contact angle θ and "Complete Young Equation" [91],

$$(1+\cos\theta)\gamma_i^{TOT} = 2\,[(\gamma_i^{LW}\gamma_j^{LW})^{1/2} + (\gamma_i^{+}\gamma_j^{-})^{1/2} + (\gamma_i^{-}\gamma_j^{+})^{1/2}\,] \qquad (2.8)$$

The LW component of a solid surfaces (i) can also be found from the contact angle of a non-polar liquid (j), where $\gamma_i^{TOT}=\gamma_j^{LW}$, on the solid surface. In this case Equation (2.8) reduces to,

$$(1+\cos\theta)\gamma_i^{TOT} = 2(\gamma_i^{LW}\gamma_j^{LW})^{1/2} \tag{2.9}$$

As a result, the LW component of a solid surface can be calculated by applying the contact angle of a non-polar liquid on the solid surface in Equation (2.9).

For a bipolar liquid (L) contacting with the solid (S), with surface tension γ_L, acidic and basic surface parameters $\gamma_L^+$and γ_L^-, respectively, and non-polar surface component, γ_L^{LW}, the complete equation to be considered is as follows,

$$(1+\cos\theta_L)\gamma_L^{TOT} = 2\,[(\gamma_L^{LW}\gamma_S^{LW})^{1/2} + (\gamma_L^+\gamma_S^-)^{1/2} + (\gamma_L^-\gamma_S^+)^{1/2}\,] \tag{2.10}$$

which can be constructed to form a set of two simultaneous equation, in terms of the parameters of the solid γ_S^-, γ_S^+ and two advancing contact angles θ_1 and θ_2, which are measured on the solid surface. These two equations can then be simultaneously solved for γ_S^- and γ_S^+ provided that the γ_i^{LW}, $\gamma_i^+$and γ_i^- for the probe liquids are known [47].

Providing the known surface components of the contacting phases (i.e. polymer and fiber), the work of adhesion (W_a) between phase 1 and phase 2 can be calculated from the summation of dispersive and acid/base components by using [92],

$$W_a^{TOT} = W_a^{LW} + W_a^{AB} = 2\,[(\gamma_1^{LW}\gamma_2^{LW})^{1/2} + (\gamma_1^+\gamma_2^-)^{1/2} + (\gamma_1^-\gamma_2^+)^{1/2}] \tag{2.11}$$

2.3.4.2 Interfacial Strength Measurement

Mechanical tests that are most commonly used for determining the strength of fiber/matrix interphase in the field of composites materials are (see Figure 2.14) [89]:

a. Tests on real composites

- Short beam flexural test
- Iosipescus's test
- Transverse and off-axial tensile test

b. Tests on model composites

- Pull-out and micro-droplet tests
- Micro-indentation
- Fragmentation test
- Determination of fiber strain in single fiber composites by Raman spectroscopy

In this study, because of ease of application, short beam flexural test was selected. The measurement is performed applying a three point bending method on a short beam with the span-to-depth ratio chosen to produce interlaminar shear failure. Parallel fibers are oriented in the direction perpendicular to the axis of the supports. From the elastic analysis of bending of beam, the apparent interlaminar shear strength τ_{ILSS} is given by

$$\tau_{ILSS} = 0.75\frac{F}{A} \tag{2.12}$$

where F is the rupture force in Newton (N) and A is the cross-sectional area of the beam [93]. This method is often used in industry to control the desired adhesion level due to its ease.

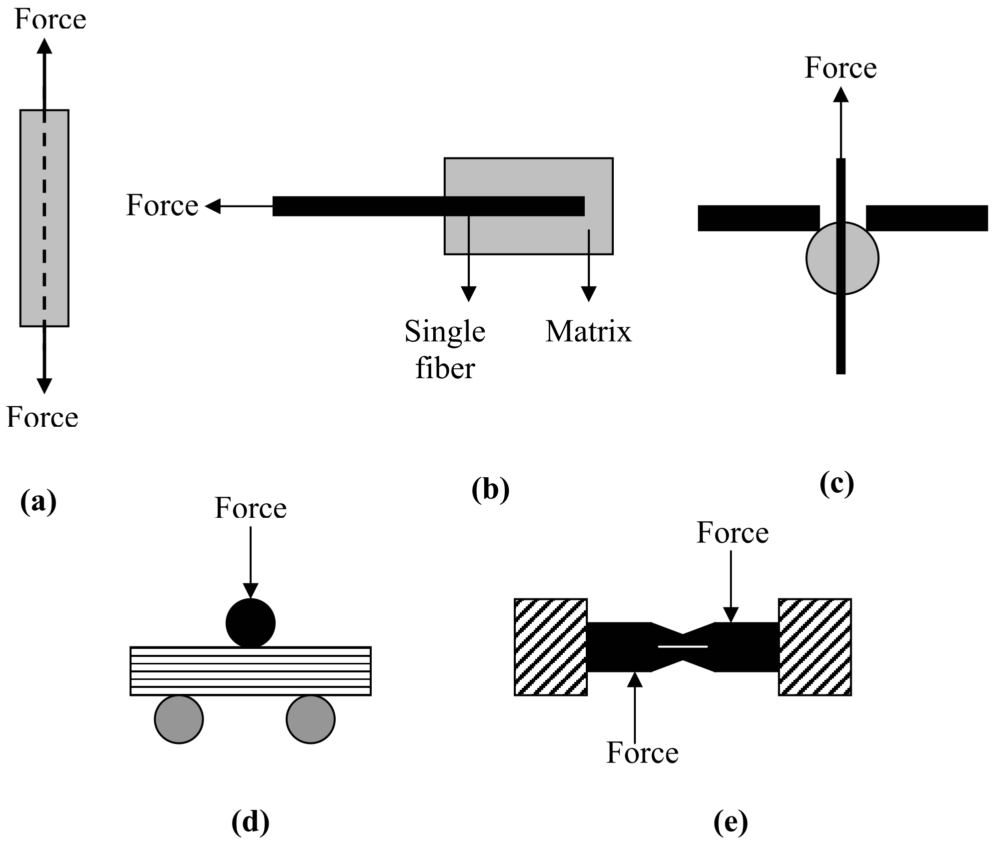

Figure 2.14 Schematic representation of mechanical tests used for determination of interphase strength where, (a). Fragmentation, (b). Pullout, (c). Micro-droplet, (d). Short Beam Flexural Test, (e). Iosipescus's test

This study focuses on the improvement of the fiber/matrix adhesion in ABS/SGF and ABS/PA6/SGF composites by treating fiber surface with a compatible organosilane to promote interfacial interactions of GF/ABS and GF/PA6. Therefore, the adhesion capacities of different coupling agents were examined experimentally. The coupling agent, which exhibited the best adhesion performance, was used for SGFs in compounding experiments with the polymeric matrices (i.e. ABS or ABS/PA6 blends) in the further studies.

2.4 Polymer Layered Silicate Nanocomposites

Composites that exhibit a change in composition and structure over a nanometer length scale have been shown over the last ten years to afford remarkable property enhancements relative to conventionally-scaled composites [94].

Nanocomposites can be considered as solid structures with nanometer-scale dimensional repeat distances between the phases that constitute the structure [95]. This term is commonly used in distinct areas of materials science: ceramics, metals and polymers; but polymers have been the most intriguing and focused subject in nanocomposite technology. There are a number of types of nanocomposites classified by nanofiller dimensionality. Zero dimensional (nanoparticle), one dimensional (nanofiber), two dimensional (nanolayer) and three-dimensional (interpenetrating network) systems can all be imagined [96].

Polymer layered silicate nanocomposites are two dimensional systems, consisting of silicate layers of nanometer thickness with high aspect ratio (30-10000) and surface area dispersed in a polymer matrix. Although the history of polymer layered silicate nanocomposites dates back to 1950’s, it was not until Toyota researchers began a detailed examination that pioneered revival of these materials [97, 98].

2.4.1 Clays

Clay is a hydrous aluminum silicate in which alkalies or alkaline earths are also present. Clay may be amorphous (allophone), crystalline (kaolinite, hollocite, montmorillonite, vermiculite), mixed-layer type (chlorite) or chain structured (attapulgate). These minerals, which are widely distributed geographically throughout the world, are the natural decomposition products of feldspar, and include kaolins (kaolinite, dickite, nacrite) [99].

Many clays have a sheet like (layered structure), and consist of silicon tetrahedra bonded to alumina octahedra in a variety of ways. A 2:1 ratio of the tetrahedral to the octahedral results in smectite clays, the most common of which is montmorillonite obtained from a rock called bentonite [100].

2.4.1.1 Clay Structure

The montmorillonite crystal lattice consists of 1 nm thin layers, with a central octahedral sheet of alumina fused between two external silica tetrahedral sheets (in such a way, so that the oxygens from the octahedral sheet also belong to the silica tetrahedral) [101]. Isomorphous substitutions of Si_4^+ for Al_3^+ in the tetrahedral lattice and of Al_3^+ for Mg_2^+ in the octahedral sheet, cause an excess of negative charges within the montmorillonite layers. This excess charge is counterbalanced by alkali or alkaline earth cations situated within the layers. This structure is shown in Figure 2.15. Due to the high hdyrophilicity of the clay, water molecules are usually also present between the layers. Stacking of the layers leads to regular van der Waals gaps called interlayers or galleries. The sum of the single layer thickness (9.6 Å) and the interlayer is called d-spacing (basal spacing) [102]. Montmorillonite has very high surface area: about 750 m^2/g, a large aspect ratio: greater than 50, a platelet thickness of 10 Å (1 nm) [102].

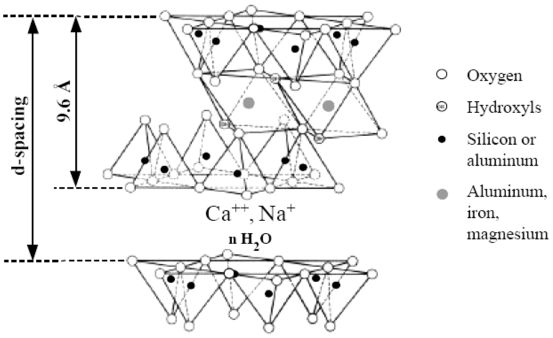

Figure 2.15 Idealized structure of 2:1 layered silicate showing two tetrahedral-site sheets fused to an octahedral-site sheet [102]

2.4.1.2 Cation Exchange Process

Montmorillonite is characterized by a moderate negative surface charge (known as cation exchange capacity, CEC, and expressed in meq/100g). The charge of the layer is not locally constant as it varies from layer to layer and must rather be considered as an average value over the whole crystals. Montmorillonite layers sorb certain cations and keep them in an exchangeable state. These exchangeable cations are usually Na^+, Ca^+, Mg^{+2}, H^+, K^+ and NH_4^+ [102]. One important consequence of the charged nature of clays is that they are generally highly hydrophilic species and therefore naturally incompatible with a wide range of polymer types [102]. In order to render these hydrophilic phyllosilicates organophilic, hydrated cations of the interlayer can be exchanged with cationic surfactants such as alkylammonium or alkylphosphonium (onium). The modified clay (or organoclay) being organophilic, its surface energy is lowered and is more compatible with organic polymers [102]. This process is schematically illustrated in Figure 2.16.

Alkylammonium ions have a general formula $CH_3\text{-}(CH_2)_n\text{-}NH_3^+$ where n is between 1 and 18. The length of the ammonium ions has a strong impact on the resulting structure of a nanocomposite [102].

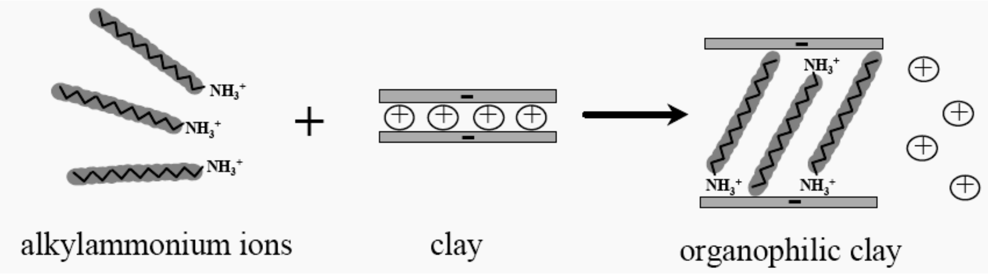

Figure 2.16 The cation-exchange process between alkylammonium ions and cations initially intercalated between the clay layers [102]

2.4.2 Nanocomposite Synthesis Methods

Several strategies can be used to prepare polymer layered silicate nanocomposites. Three methods are mainly used.

2.4.2.1 In-Situ Polymerization

In-situ polymerization was the first method used to synthesize polymer-clay nanocomposites based on polyamide-6. Nowadays it is the conventional process used to synthesize thermoset-clay nanocomposites [102]. The modified layered silicate is swollen by a liquid monomer or a monomer solution. The monomer migrates into the galleries of the layered silicate, so that the polymerization can occur within the intercalated sheets. The polymerization reaction leads to the delamination of the clay [102]. The polymerization reaction can be carried out by heat, radiation or a suitable initiator. This process is schematically illustrated in Figure 2.17.

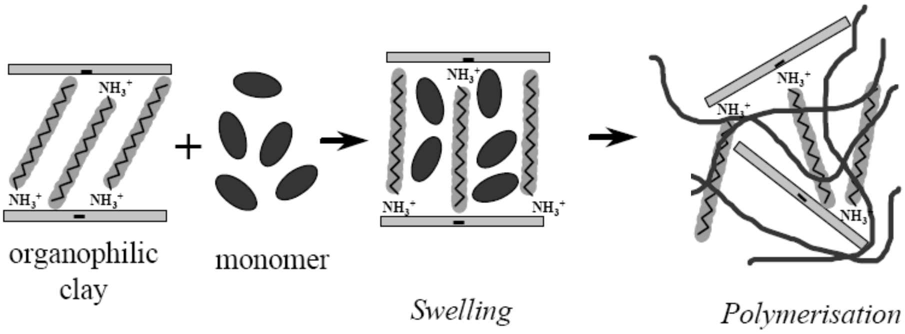

Figure 2.17 Schematic representation of PLS obtained by in situ polymerization [102]

2.4.2.2 Solution Method

It is well known that such layered silicates, owing to the weak forces that stack the layers together can be easily dispersed in an adequate solvent [42]. Then the polymer dissolved in the solvent, is added to the solution and intercalates between the clay layers. The last step consists of removing the solvent by evaporation under vacuum. Nanocomposites, based on untreated clays can also be synthesized using this approach [102]. This process is schematically illustrated in Figure 2.18.

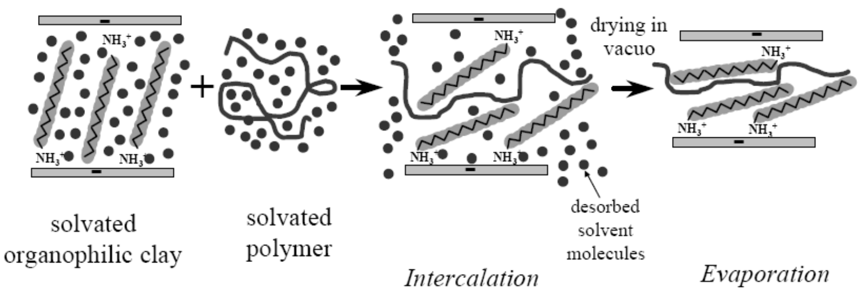

Figure 2.18 Schematic representation of the intercalation of the polymer by the solution approach [102]

2.4.2.3 Melt Intercalation

The layered silicate is mixed with the polymer matrix in the molten state. Under these conditions, if the layer surfaces are sufficiently compatible with the chosen polymer, the polymer can crawl into the interlayer surface to form either an intercalated or an exfoliated nanocomposite. This process is schematically illustrated in Figure 2.19. In this technique, no solvent is required [42]. Due to its great potential in industrial applications, the melt intercalation process has become increasingly popular.

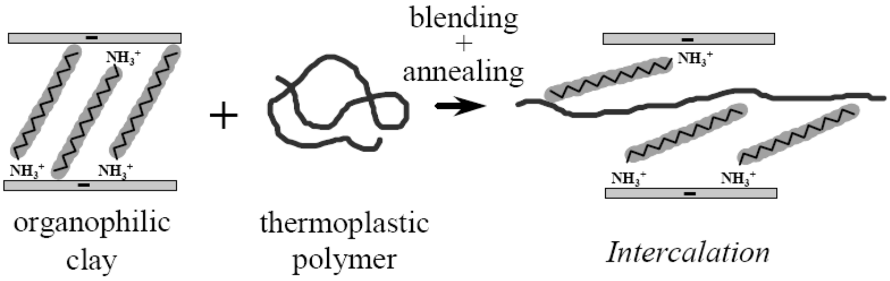

Figure 2.19 Schematic representation of PLS obtained by polymer melt intercalation process [102]

2.4.3 Nanocomposite Structures

The essence of nanotechnology is the ability to work at the molecular level to create large structures with fundamentally new molecular organization [103]. The small size provides that the particles do not create large stress concentrations and leads to an exceptionally large interfacial area [41].

Three main types of composites can be obtained when a layered silicate is dispersed in a polymer matrix. This dominantly depends on the nature of the components used including polymer matrix, layered silicate, and organic cation [104]. The choice of method for making a nanocomposite depends on the final form of the hybrid.

2.4.3.1 Conventional

If the clay particles are dispersed as tactoids in the polymer matrix; i.e. if the clay layers are not separated, a microcomposite structure is obtained. The clay acts as conventional filler in this case (see Figure 2.20) [102].

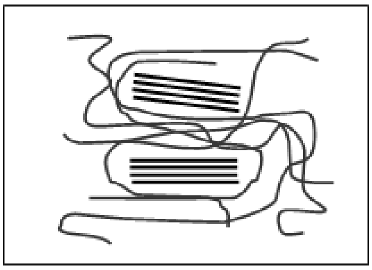

Figure 2.20 Schematic representation of conventional composites with organoclays in polymer matrix

2.4.3.2 Intercalated

In an intercalated system, the polymer swells the galleries of the silicate layers but preserves the stacking of layers [105]. The resulting structure is a multilayered system built up with alternating polymeric and inorganic layers (see Figure 2.21).

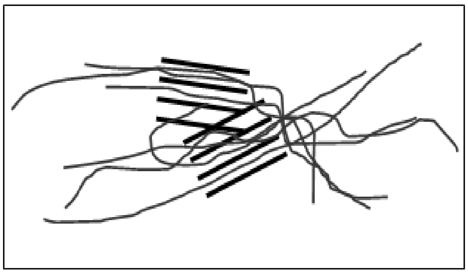

Figure 2.21 Schematic representation of intercalated nanocomposites with organoclays in polymer matrix

2.4.3.3 Exfoliated (Delaminated)

Exfoliated or delaminated structures are obtained when the silicates are completely and uniformly dispersed in the continuous polymer matrix. This structure is of particular interest because it maximizes the polymer-clay interaction surface area (Figure 2.22).

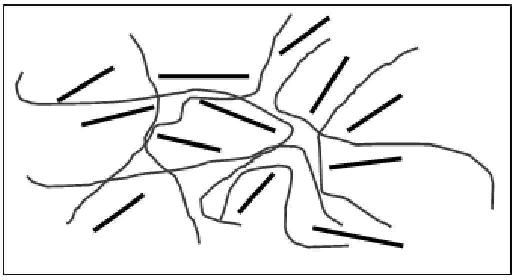

Figure 2.22 Schematic representation of exfoliated nanocomposites with organoclays in polymer matrix

The mechanism leads to exfoliation of the organoclays was proposed by Paul and co-workers [98]. According to this proposal, the organoclay particle at an agglomerate size of 8 microns are broken into silicate stacks by means of shear imposed by processing device (i.e. twin screw extruder). Further shearing of the stacks results in a decrease in the size, but this is not enough to delaminate. Delamination is a process controlled by shear together with the chemical affinity which enforces polymer chains to diffuse between clay layers. Diffusion can be controlled by proper selection of the organoclay and arranging the residence time. If the organoclay and the polymer is compatible and the residence time is enough, then polymer chains diffuse through the clay platelets. Diffusion in combination with shear leads to exfoliation as a result of pealing apart of the platelets. This procedure is illustrated in Figure 2.23.

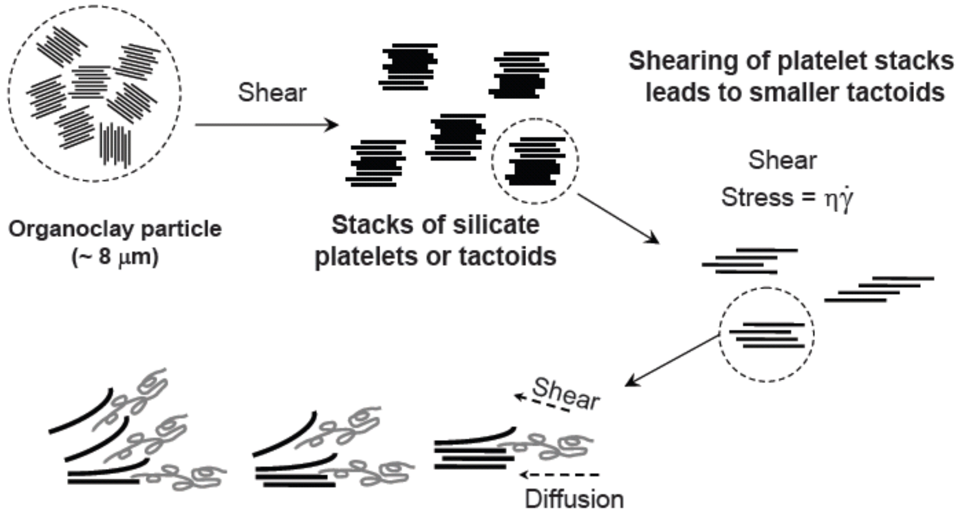

Figure 2.23 Schematic of exfoliation mechanism of organoclays in melt intercalation [98]

2.5 Experimental Techniques

The experimental techniques used to characterize the polymer blends, short glass fiber reinforced polymer composites and organoclay based nanocomposites investigated in this dissertation are discussed here. Some specific experimental methods, such as impact fracture toughness, optical microscopy, tensiometry, Fourier transformation infrared spectroscopy, short beam fracture test and image analysis are discussed in the Experimental part (Chapter 3).

2.5.1 Mechanical Properties

2.5.1.1 Tensile Tests

Standard test method for tensile properties (ASTM D 638M-91a) employs samples of a specified shape, typically a dog-bone [106]. The sample is clamped at one end and pulled at a constant rate of elongation until the center of the specimen fails.

The initial length of a central section contained within the narrow region of the tensile specimen is called the initial gauge length, L_0. During deformation, force F, is measured as a function of elongation at the fixed end by means of a transducer. Usually, the tensile response is plotted as nominal stress σ, versus nominal strain ε,

$$\sigma = F/A_0 \tag{2.13}$$

$$\varepsilon = \Delta L/L_0 \tag{2.14}$$

where A_0 is the original (undeformed) cross-sectional area of the gauge region and ΔL is the change in sample gauge length ($L-L_0$) due to the deformation [106]. Figure 2.24 represents the stress-strain behavior over the entire strain range for a typical polymeric material.

Tensile stress (nominal), σ is the tensile load per unit area of minimum original cross-section, within the gauge boundaries, carried by the test specimen at any given moment. It is expressed in force per unit area, usually megapascals ($MPa = N/mm^2$), (Equation 2.13).

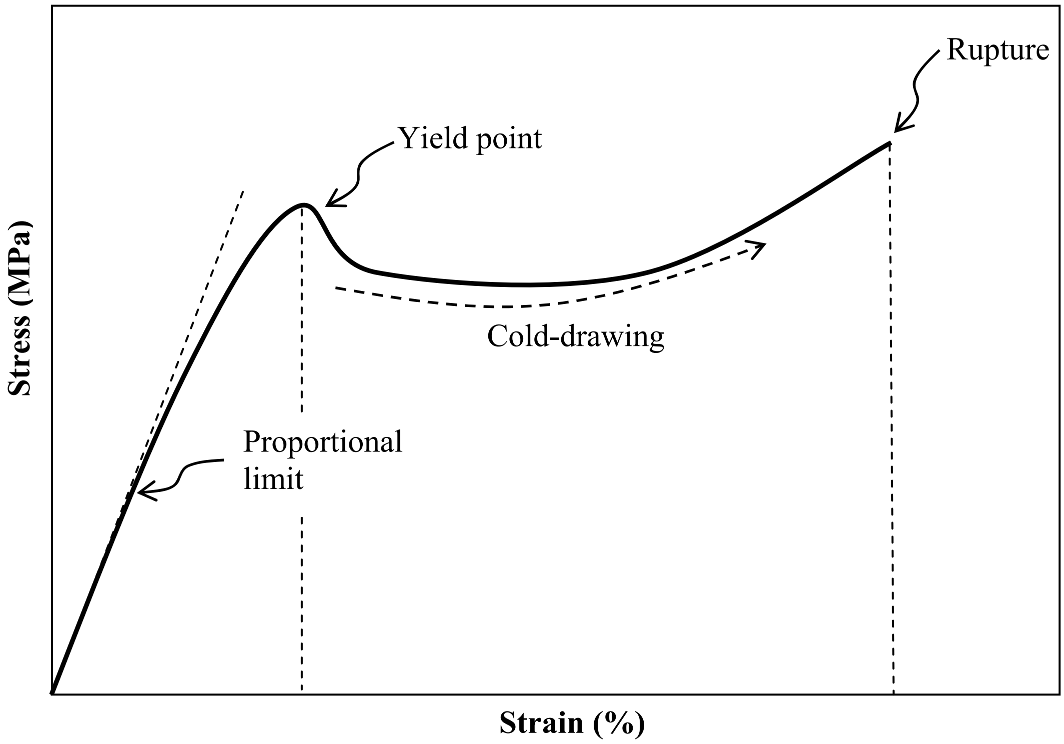

Figure 2.24 Stress-strain behavior over the entire strain range for a typical polymeric material [107]

Tensile strength (nominal), σ_m is the maximum tensile stress sustained by the specimen during a tension test. When the maximum stress occurs at the yield point, it is designated tensile strength at yield. When the maximum stress occurs at break, it is designated tensile strength at break.

Tensile strain, ε is the ratio of the elongation to the gauge length of the test specimen, that is, the change in length per unit of original length. It is expressed as a dimensionless ratio (Equation 2.14).

It is seen in Equation 2.15 that modulus of elasticity, E is the ratio of stress (nominal) to corresponding strain below the proportional limit of a material. It is expressed in force per unit area, usually megapascals. It is also known as elastic modulus or Young's modulus [108].

$$E = \sigma/\varepsilon \tag{2.15}$$

In this study, tensile tests were applied to ABS, PA6, ABS/PA6 blends, their short glass fiber reinforced composites and nanocomposites.

2.5.1.2 Flexural Tests

ASTM D790M-92 test methods cover the determination of flexural properties of unreinforced and reinforced plastics and electrical insulating materials using a three-point or four-point loading system [109].

Three-point loading system utilizes center loading on a simply supported beam [109]. At the point of loading, the top surface of the specimen is placed in a state of compression, whereas the bottom surface is in tension (Figure 2.26). Stress is computed from the specimen thickness, the bending moment and the moment of inertia of the cross-section. The maximum tensile stress exists at the bottom specimen surface directly below the point of load application [110].

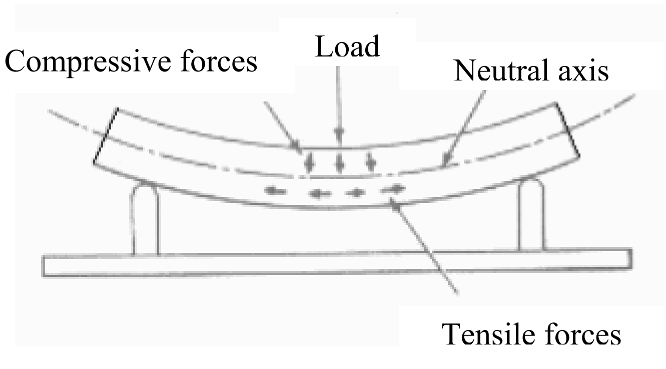

Figure 2.26 The stresses on the sample during flexural testing

Flexural strength is equal to the maximum stress in the outer fibers at the moment of break. It is calculated by the following equation;

$$S = 3PL/2bd^2 \quad (2.16)$$

where S is the stress in the outer fibers at midspan (MPa), P is the load at a given point on the load-deflection curve (N), L is the support span (mm), b is width of beam tested (mm) and d is depth of beam tested (mm).

The maximum strain in the outer fibers occurs at midspan as well, and may be calculated as follows;

$$r = 6Dd/L^2 \quad (2.17)$$

where r is the maximum strain in the outer fibers (mm/mm), D is the maximum deflection of the center of the beam (mm), L is the support span (mm), and d is depth of beam tested (mm).

The tangent modulus of elasticity (flexural modulus) is the ratio, within the elastic limit of stress to corresponding strain and shall be expressed in megapascals. It is calculated by drawing a tangent to the steepest initial straight-line portion of the load-deflection curve and using Equation 2.18.

$$E_B = L^3m/4bd^3 \quad (2.18)$$

where E_B is modulus of elasticity in bending (MPa), L is support span (mm), b is width of beam tested (mm), d is depth of beam tested (mm), and m is slope of the tangent to the initial straight line portion of the load-deflection curve (N/mm) [111].

In this study, flexural tests were applied to short glass fiber reinforced ABS, PA6 and ABS/PA6 blends.

2.5.1.3 Impact Tests

Impact tests measure the energy required for failure when a standard specimen receives a rapid stress loading. The impact strength of a polymer can be measured employing a number of techniques including the Izod and the Charpy tests [112]. For both the Izod and Charpy tests a hammer like weight strikes a specimen and the energy-to-break is determined from the loss in the kinetic energy of the hammer. Other variations include the falling ball or dart test, whereby the energy-to-break is determined from the weight of the ball and the height from which it is dropped.

The most popular impact tests are Izod and Charpy impact tests specified in ASTM D256-92 [113]. In this study, Charpy impact test was applied to the ABS, PA6, ABS/PA6 blends and their short glass fiber reinforced composites in order to determine their impact strengths.

2.5.2 Scanning Electron Microscopy (SEM)

Due to the great depth of focus, relatively simple image interpretation and ease of sample preparation, SEM is the preferred technique for viewing specimen detail at a resolution well exceeding that of the light microscope. The SEM images vividly display the three-dimensional characteristics of the object surface under examination [114].

In SEM analysis, the surface of a specimen to be examined is scanned with an electron beam and the reflected (or back-scattered) beam of electrons is collected, and then displayed at the same scanning rate on a cathode ray tube. The image on the screen, which may be photographed, represents the surface features of the specimen. The surface may or may not be polished and etched, but it must be electrically conductive; a very thin metallic surface coating must be applied to nonconductive materials. Magnifications ranging from 10 to in excess of 50000 diameters are possible [110].

In this study, SEM analysis was conducted to ABS, PA6, ABS/PA6 blends, their short glass fiber reinforced composites and nanocomposites in order to observe their fracture morphologies.

2.5.3 Transmittance Electron Microscopy (TEM)

Transmission electron microscopy (TEM) is an imaging technique whereby a beam of electrons is focused onto a specimen causing an enlarged version to appear on a fluorescent screen or layer of photographic film (see electron microscope), or to be detected by a CCD camera [115].

The wavelength of electrons is dependent on their energy, and so can be tuned by adjustment of accelerating fields, and can be much smaller than that of light, yet they can still interact with the sample due to their electrical charge. Electrons are generated by a process known as thermionic discharge in the same manner as the cathode in a cathode ray tube, or by field emission; they are then accelerated by an electric field and focused by electrical and magnetic fields onto the sample. The electrons can be focused onto the sample providing a resolution far better than is possible with light microscopes, and with improved depth of vision. Details of a sample can be enhanced in light microscopy by the use of stains; similarly with electron microscopy, compounds of heavy metals such as lead or uranium can be used to selectively deposit heavy atoms in the sample and enhance structural detail, the dense electron clouds of the heavy atoms interacting strongly with the electron beam. The electrons can be detected using a photographic film, or fluorescent screen among other technologies [115]. Modern TEMs are often equipped with specimen holders that allow the user to tilt the specimen to a range of angles in order to obtain specific diffraction conditions, and apertures placed below the specimen allow the user to select electrons diffracted in a particular direction [115].

2.5.4 X-Ray Diffraction (XRD)

The method of x-ray diffraction and scattering is one of the oldest and most widely used techniques available for the study of polymer structures. A beam of x-rays incident to a material is partly absorbed and partly scattered, and the rest is transmitted unmodified. The scattering of X-rays occurs as a result of interaction with electrons in the material. The x-rays scattered from different electrons interfere with each other and produce a diffraction pattern that varies with scattering angle. The variation of the scattered and diffracted intensity with angle provides information on the electron density distribution and hence the atomic positions within the material [114]. X-ray diffraction is used to determine the identity of crystalline phases in a multiphase sample and the atomic and molecular structures of single crystals. It can also be used to determine structural details of polymers, fibers, thin films and amorphous solids and to study stress, texture and particle size.

In the spectrum of electromagnetic radiation, x-rays lie between the ultraviolet rays and gamma rays. Those x-rays used for structure analysis have wavelengths λ in the range of 0.05-0.25 nm. Most work on polymers is done with the CuKα emission line, a doublet with an average wavelength equal to 0.154 nm [114].

Figure 2.27 shows the diffraction from two scattering planes (i.e. two consecutive clay layers or other crystallographic planes of the layers themselves) that are separated by a distance d (i.e. interlamellar spacing or d-spacing) and intercept X-rays of wavelength λ at the incident angle Θ. The experimental 2Θ. value is the angle between the diffracted and incoming x-ray waves. The wave normals connect points of identical phase for incident and diffracted waves. Since the direction of d is normal to the planes, and the wave normal is normal to the wavelets, the angles opposite A and B are also Θ. Thus, $\sin\Theta = A/d = B/d$ so that $(A+B) = 2d\sin\Theta$. Thus, a constructive interference occurs when:

$$n\lambda = 2d\sin\Theta \tag{2.19}$$

This equation is known as the Bragg Law. The integer n refers to the degree of the diffraction [114].

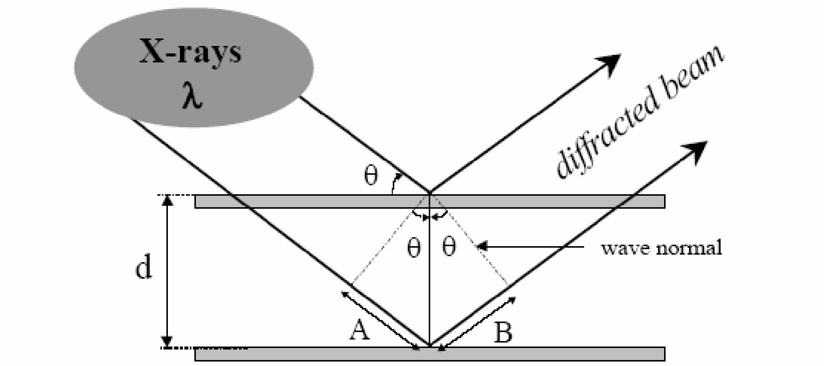

Figure 2.27 Principle of X-Ray diffraction [114]

In this thesis, XRD method was used to measure the basal spacing, which is the distance between the platelets of organoclays, for the characterization of ABS, PA6 and ABS/PA6 blends based nanocomposites. This method helps experimenter to decide the type of the nanocomposites formed, i.e. conventional, intercalated or exfoliated. When XRD pattern of an organically modified clay is considered, usually it gives a sharp characteristic peak which indicates the original basal spacing of the clay (see Figure 2.28-a). If original peak shifts after processing to a lower 2Θ values, it means that the basal spacing increased and intercalated nanocomposites are formed because of the diffusion of the polymer between clay layers by means of the shear [43] (see Figure 2.28-b). If this peak disappears after processing, it means that the clay layers are dispersed into single layers. This is the case of exfoliated nanocomposites (see Figure 2.28-c).

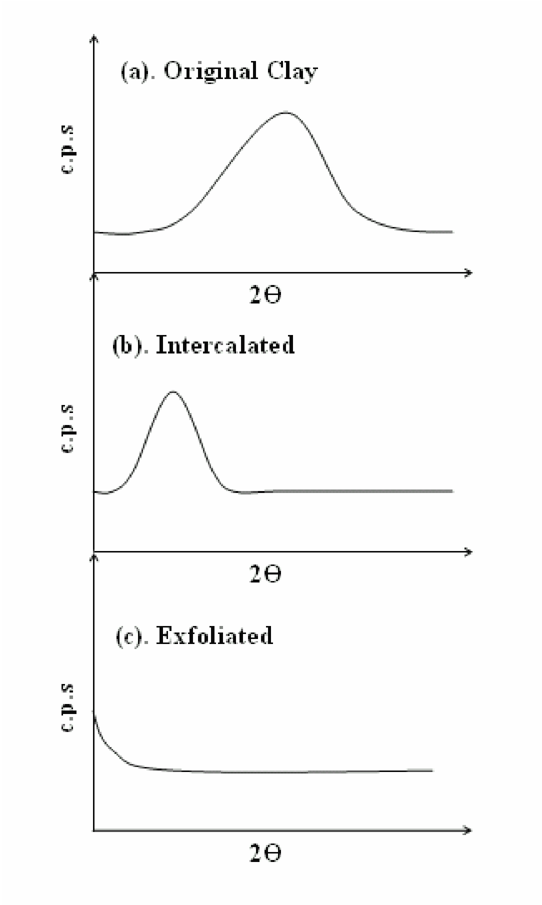

Figure 2.28 Representation of XRD responses of nanocomposites

2.5.5 Melt Flow Index (MFI) Test

The melt index is not an intrinsic or fundamental property of a polymer. It is rather a conventional property of a polymer for expressing important flow characteristics [112]. The melt index, also known as melt flow rate, test measures the rate of extrusion of a thermoplastic material through an orifice of standard diameter under prescribed conditions of temperature and load [116]. The weight of the material extruded during the specified time is the melt index expressed in grams per ten minutes.

2.5.6 Thermal Analysis Methods

2.5.6.1 Differential Scanning Calorimeter (DSC) Analysis

The differential scanning calorimeter (DSC) is the instrument that has dominated the field of thermal analysis in the past decade. The term DSC was coined in 1963 at Perkin-Elmer to describe a new thermal analyzer they had developed [117]. It measures heat flows and temperatures associated with exothermic and endothermic transitions. The ease with which important properties such as transitions, heat capacity, reaction, and crystallization kinetics are characterized has made the DSC widely used in the plastics laboratory [118].

In DSC analysis, two identical small sample pans are instrumented to operate at the same temperature and can be programmed up or down in temperature at the same rate. A sample is placed in one, and the other is left empty. Instrumentation is provided to measure the electrical power necessary to keep the two sample pans at the same temperature. If a temperature is encountered at which the sample undergoes a change of phase or state, more or less power will be needed to keep the sample pan at the same temperature as the reference pan (depending on whether the reaction is exothermic or endothermic). Since power is the value being recorded, the area under the peak is the electrical equivalent of the heat of the reaction. To measure heat capacity in this calorimeter, the sample pan and reference pan are first brought to some temperature and then heated at some constant rate. Since the reference pan is empty, it will require a smaller amount of electrical power to achieve this rate [119].

Some advantages of the differential scanning calorimeter are that relatively short times are required to make a determination and that small sample size is sufficient. The disadvantage is that it is a comparative rather than an absolute method.

DSC is routinely used for investigation, selection, comparison, and end-use performance of materials. It is used in academic, industrial, and government research facilities, as well as quality control and production operations. Material properties measured include glass transitions, melting point, freezing point, boiling point, decomposition point, crystallization, phase changes, melting, crystallization, product stability, cure and cure kinetics, and oxidative stability.

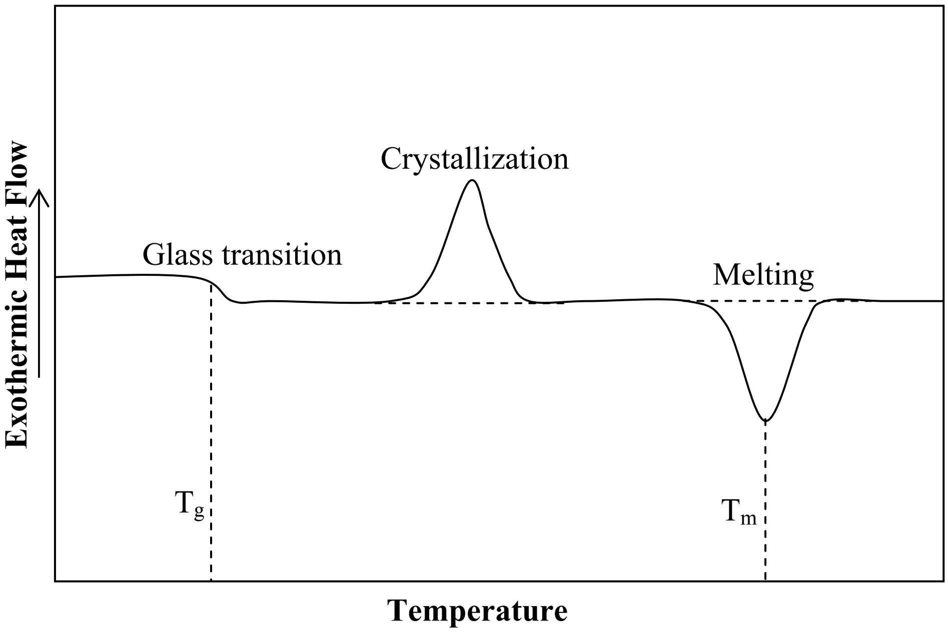

Figure 2.29 Schematic of DSC curve

At T_g, the heat capacity of the sample suddenly increases, requiring more power (relative to the reference) to maintain the temperatures the same. This differential heat flow to the sample (endothermic) causes a drop in the DSC curve (Figure 2.29).

At T_m, the sample crystals want to melt at constant temperature, so a sudden input of large amounts of heat is required to keep the sample temperature even with the reference temperature. This results in the characteristic endothermic melting peak. Crystallization, in which large amounts of heat are given off at constant temperature, gives rise to a similar but exothermic peak. By measuring the net energy flow to or from the sample, heat capacities and heat of fusion can be determined [120].

2.5.6.1 Dynamic Mechanical Analysis (DMA)

Polymeric materials may be subjected to variable loading at a moderately high frequency. In order to study the response of these materials to such variable loading dynamic mechanical analysis (DMA) is carried out. In DMA a low stress is applied to the material in a sinusoidal fashion. For a perfectly elastic material, stress and strain are perfectly in phase since strain is directly proportional to stress. For a perfectly viscous fluid, the strain will lag behind the stress by a phase angle of 90º. For a polymeric material, the response to a variable load is a combination of elastic and viscous responses, i.e. they show elasticity to some extent and also flow to some extent and the strain lags behind the stress by a phase angle. Thus polymeric materials are named viscoelastic. The typical response of stress and strain with time for a polymeric material is shown in Figure 2.30.

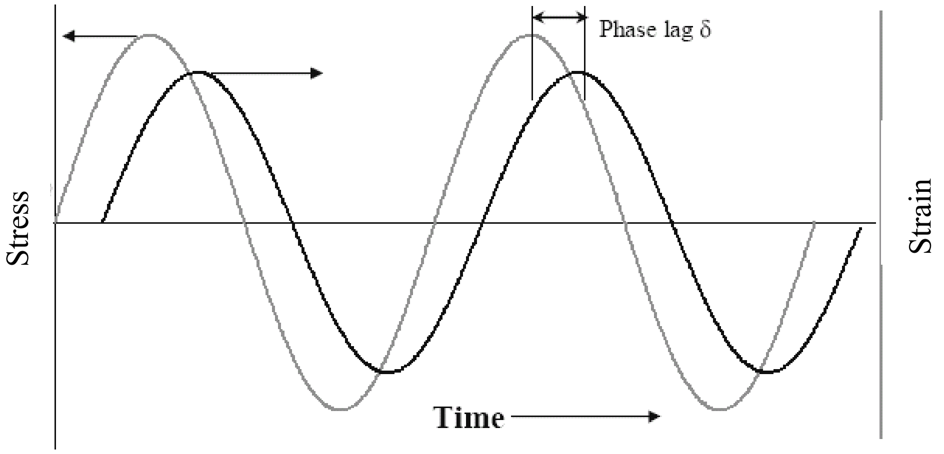

Figure 2.30 Response of stress and strain with time for a typical polycrystalline polymer above T_g

It is seen that for a polymeric material the strain lags behind the stress by some phase angle, δ, between 0º and 90º. This lagging of the strain behind the applied stress can be considered as a damping process [121]. The strain and the stress can be written as follows:

$$\varepsilon = \varepsilon_0 \sin(\omega t) \tag{2.20}$$

$$\sigma = \sigma_0 \sin(\omega t + \delta) = \sigma_0 \sin\omega t * \cos\delta + \sigma_0 \cos\omega t * \sin\delta \tag{2.21}$$

Here, ω and t are frequency and time of measurement, respectively. As seen in Equation (2.21) stress is composed of two components:

- $\sigma_0 \cos\delta$ component which is in-phase with the strain is called as the storage component (elastic component) of stress and the corresponding modulus is called as storage modulus, E'.

- $\sigma_0 \sin\delta$ component which is 90° out of phase with the strain is called as the loss component of stress and the corresponding modulus is called as loss modulus, E".

In terms of the moduli, the stress can be written as

$$\sigma = \varepsilon_0 E'\sin\omega t + \varepsilon_0 E''\cos\omega t \tag{2.22}$$

The phase angle is then given by $\tan\delta = E''/E'$ which is the amount of energy dissipated as heat during the loading/unloading cycle and thus gives a direct measure of the damping effect in the polymer. From the above discussion, it is apparent that for a perfectly elastic material tanδ is zero whereas for a perfectly viscous material tanδ is infinite. Thus in DMA, elastic modulus (E') and loss modulus (E") are calculated by studying the response of the material to a sine wave. These moduli helps to study the ability of the material to store energy (E'), ability to lose energy (E"), and the damping behaviour from the ratio of loss and storage moduli (tanδ) and moreover, the peak point of tanδ vs. temperature gives the T_g of the material [122].

When completely miscible two polymers are blended together, a single T_g is observed. The T_g of the resulting system is located between the T_g's of the parent materials in proportion to the amount of each phase present in the blend. If two polymers are not miscible, then resulting blend exhibits two glass transitions corresponding to those of the parent polymers. Intermediate cases exist where the polymers are partially miscible so that two T_g's are still observed but they are moved towards that of the ideally miscible blend.

2.5.7 Impact Essential Work of Fracture Toughness Method

The toughness of the materials are generally characterized by standard impact tests such as notched/unnotched Izod or Charpy testing according to relevant standard methods. These tests are practical, industry-friendly, the results obtained from these tests are comparable to each other and they do not require any complicated experimental systems. However, the fracture energies obtained by these tests are not a material property and depend on various parameters such as material dimensions, crack geometry and rate of deformation. Moreover, they provide limited information about the fracture behaviour of ductile materials under stress in the presence of a crack [123].

There is a tendency toward the use of methods of fracture mechanics, which are especially designed for metals, in polymer science to characterize the fracture behaviour and fracture toughness [124-131]. The techniques offered by linear elastic fracture mechanics (LEFM) could be utilized for better characterization of these properties, if the condition were well-suited. It needs to be ensured that the test sample must be in a state of plane strain which generally occurs in very thick samples that are difficult to obtain conventional injection molding process in order to satisfy the small scale yield criterion [132, 133]. Recently, *J*-integral method has been proposed to characterize ductile polymeric materials in which plane-strain toughness value can be obtained at relatively low thickness with respect to LEFM [133, 134]. However, this method requires more sophisticated equipments to measure precisely the crack propagation at very slow rate of deformations.

Essential Work of Fracture (EWF) methodology was developed to characterize the fracture toughness of ductile polymers and tough composites in a practical manner. According to this technique, the energy to break a sample was partitioned into an essential work done in the fracture zone to create new surfaces and a non-essential work done in the outer plastic zone [135-140]. The total fracture energy W_f can be written as follows:

$$W_f = W_p + W_e \tag{2.23}$$

where the essential work, W_e, is surface related and non-essential, W_p, is volume related. Equation (2.23) can be expressed in terms of specific energies:

$$W_f = w_e \ell t + w_p \beta \ell^2 t \tag{2.24}$$

where w_e and w_p are specific essential work (energy/area) and specific non-essential work (energy/volume), respectively, ℓ is ligament length, t is sample thickness and β shape factor of plastic zone. A typical sample for EWF analysis is shown in Figure 2.31 and the notch geometry is shown in Figure 2.32. Normalizing Equation (2.24) by ℓt results in:

$$w_f = w_e + w_p \beta \ell \tag{2.25}$$

where w_f is specific total work of fracture (energy/area). If the specific fracture energies of a material is obtained for different ligament lengths, according to Equation (2.25), plots of ℓ versus w_f can yield a straight line with slope of $w_p\beta$ and intercept of w_e. The specific essential work term is a material constant.

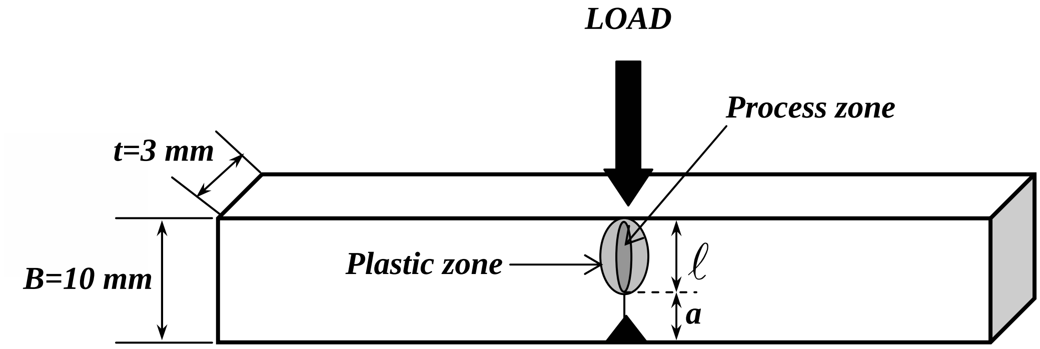

Figure 2.31 Specimen geometry for the impact essential work of fracture method (The term '*a*' is the depth of the notch)

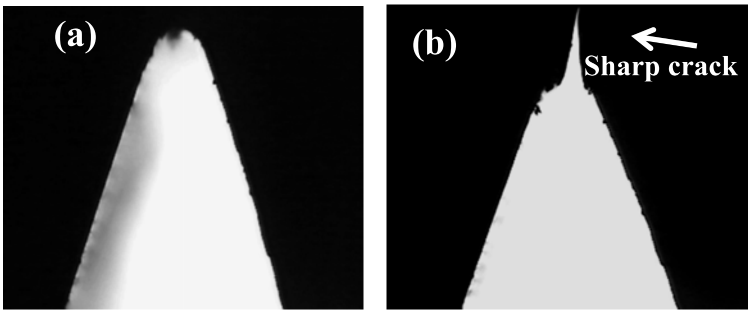

Figure 2.32 Optical micrographs of a.) Notch without pre-crack and b.) Notch with pre-crack

The recently established protocol has stated several important criteria that must be satisfied in order to apply the EWF methodology to evaluate fracture toughness [141]. They are summarized as follows:

i.) The specimen ligament must fully yield prior to fracture initiation.

ii.) The specimen ligament must be proportional to essential work performed in the process zone.

iii.) Size of the outer fracture zone surrounding the fracture ligament must scale with the square of the ligament length.

In addition to that, Mai have recently mentioned that EWF methodology can not be applied if the two halves of the specimen are not separated after testing [142]. The valid range of ligament length under plane stress conditions is given by the condition stated below:

$$(3-5)t \le \ell \le \min(\frac{B}{3}, 2r_p) \tag{2.26}$$

where B is the width of the sample and $2r_p$ is the size of the plastic zone [143-145]. When these conditions are satisfied, EWF methodology that consists of testing specimens with different ligament lengths (ℓ), measuring the area under the Force versus deformation curve to obtain fracture energy (W_f), plotting specific fracture energy (w_f) versus ligament length (ℓ) and evaluating the best linear line performing regression becomes applicable.

The test method which is described here to determine the essential work of fracture of ductile polymers has been used by many researchers and has been incorporated in the European Structural Integrity Society (ESIS) Test Protocol for EWF under quasi-static loading conditions [141-146]. However, once this concept was extended to impact loading conditions, great attention was paid to this method due to its simplicity and useful information that can be drawn out to understand fracture behaviour of polymers, polymer blends and composites under high rate of deformations.

The concept of EWF methodology was proved by many researchers [135-140, 147-160]. The main difference in their approach is interpretation of the terms, loading rate and mode, and sample geometries. Vu-Khanh's Energy Equation [147]:

$$\frac{U}{A} = G_i + \frac{1}{2} T_a A \tag{2.27}$$

where $A = \ell t$ is the area of the ligament, G_i is fracture energy at crack initiation, T_a is tearing modulus. The methodology proposed requires high speed testing of thick samples in bending mode. Recently Kudva et. al. [160] has proposed different nomenclature. Due to the insatisfaction in the yielding criterion in their system, they used the expression given by Equation (2.25).

$$\frac{U}{A} = u_o + u_d \ell \tag{2.28}$$

where U/A is total fracture energy per unit area, ℓ is the ligament length, u_o is the limiting specific fracture energy, u_d is the dissipative energy density. These should be regarded as phenomenological parameters where, in certain cases, $u_o = w_e$ and $u_d = \beta w_p$.

2.6 Polymer Extrusion

This process is used to obtain significant quantities of plastic products in the form of film, sheet, and profiles, but it is also used to produce the plastic pellets that are later used by all the other plastics manufacturing processes. In addition to the shaping of parts by the extrusion process, extrusion is the most efficient and widely used process for melting plastic resin as part of the process of adding or mixing fillers, colorants, and other additives into the molten plastics. Extrusion can be used to shape the part directly after this mixing or an extruder can be used as the melting device that is coupled with other shaping processes.

In normal plastics extrusion, plastics granules or pellets and any other materials to be mixed with them are fed into a hopper attached to the extrusion machine. From the hopper the materials falls through a hole in the top of the extruder onto the extrusion screw. This screw, that turns inside the extruder barrel, conveys the plastic forward into a heated region of the barrel where the combination of external heating and heating from viscous dissipation melts the plastic. The screw moves the molten plastic until it exists through a hole in the end of the extruder barrel to which a die has been attached. The die imparts a shape to the molten plastic stream which is immediately cooled by a water bath [161].

The components of the extruder are, control panel, feeders, screw, barrel and die. The control panel consists of different indicators to control the extrusion process. It is possible to adjust the temperature, screw speed and feeding rate with the control panel. Moreover, pressure of the die, temperature of the zones and torque can be monitored.

The screw is the main part of the extruder which directly affects the performance of the machine. It performs a number functions such as; conveying the plastic pellets, melting the material, conveying the molten material, and mixing the plastic melt to obtain homogeneity. The screw is placed inside the cylinder extruder barrel. It provides the bearing surface where shear is imparted to the plastic granules. The barrel consists of cast or fabricated steel sections and a smooth inner liner, often made of a wear-resistant material. Heating and cooling media surrounds the barrel to keep it at the desired temperatures.

The polymer is shaped in the die zone. The objective of an extrusion die is to distribute the polymer melt in the flow channel in such a way that the material exits from the die with a uniform velocity. The polymer melt is forced through the die by means of the die-head pressure [161]. There are tremendous die design and applications such as compounding, (coloring and blending of melts, additives, and fillers), sheet, film, coatings, pipe, and rod.

Screw extruders are divided into single screw and multi screw extruders. Single screw extruders are generally used for shaping and multi screw extruders are generally used for mixing (compounding).

2.6.1 Twin Screw Extruders

Although twin-screw extruders are used less than single-screw extruders they are widely employed for difficult compounding applications, devolatilization, chemical reaction, and profile extrusion of thermally sensitive materials in the polymer processing industry [161].

The complex flow patterns in twin screw extruders have several advantages, such as good mixing, good heat transfer, large melting capacity, good devolatilization capacity, and good control over stock temperatures [161]. Type of transport in extruder is different in single screw and twin screw extruders. Material transport in single screw extruder is by frictional drag in solid conveying zone and viscous drag in the melt conveying zone. On the other hand, the transport in an intermeshing twin screw extruder is a positive displacement type of transport [161]. There is a tremendous variety of twin screw extruders, with vast differences in design, principle of operation, and field of applications. The twin screw construction substantially increases the number of design variables, such as direction of rotation, intermeshing, non-intermeshing, etc. [161]. There are two different patterns for intermeshing twin screw extruders according to the direction of rotation of the screws: co-rotating, and counter rotating twin screw extruders. Figure 2.33 shows intermeshing co-rotating and counter-rotating twin screws.

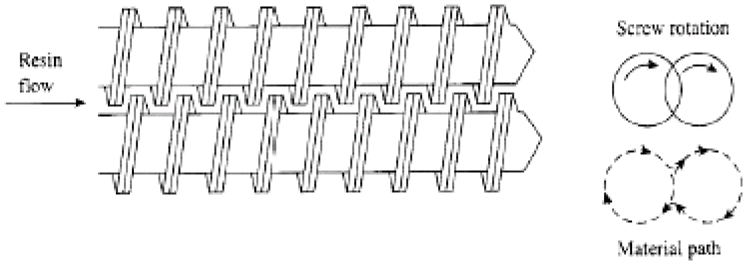

(a) Co-rotating

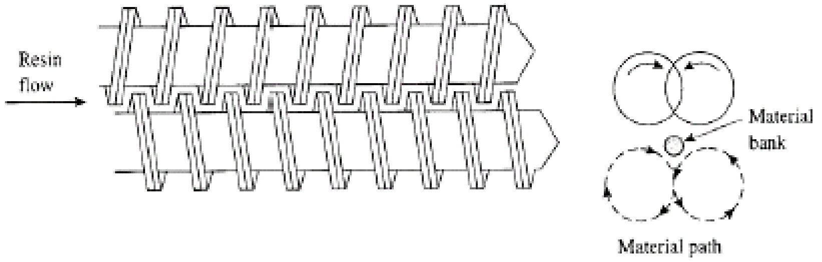

(b) Counter-rotating

Figure 2.33 Intermeshing twin screw extruder (a) Co-rotating and (b) Counter-rotating

Co-rotating twin screw extruders in which both screw rotate in the same direction, are typically used in applications where mixing and compounding need to be accomplished in addition to the molding of the plastic melt. They are highly capable of dispersing small agglomerates such as carbon black or clay [161]. In the other intermeshing type, the screws rotate counter to each other, one rotates clockwise and the other counterclockwise thus it is called counter rotating extruder. In this type, material is brought to the junction of the two screws and a material bank occurs on the top of the junction. Only a small amount of material passes between the screws so the total shear applied to material is lower than the single screw extruders and co-rotating twin screw extruders. Most of the material in the bank along the junction of the screws is simply carried toward the end of the extruder.

Hence, pumping is more efficient in counter-rotating screw systems than in co-rotating systems [161].

2.7 Laboratory Scale Mixing Devices

Laboratory-scale mixing devices, which serve as cost and time efficient research facilities, provide possibilities of processing a few grams of material and they have the capability of continuous or batch processing with the same thermal environment as a conventional extruder [162, 163]. It enables researchers to use these micro-devices as a fast screening tool in the field of polymer based nanocomposite development [162-168]. There are few number of studies focused on the design and mixing behaviour of these small scale mixing devices. Walia et al. compared the mixing efficiency of a batch mixer and mini-compounder during preparation of poly(methyl methacrylate)/polystyrene blends [165]. They reported that from distributive mixing point of view, the micro-compounder mixed similarly to the batch mixer under favourable mixing conditions, on the other hand micro-compounder performed less favourably compared to batch mixer under challenging mixing conditions. Maric et al. investigated the mixing-ability of the laboratory mixing devices (i.e batch mixer, twin screw mini compounder, a lab-scale conventional twin screw extruder and a minimixer mixing by the help of steel balls) in polystyrene/poly(dimethyl siloxane) blends [169]. It was concluded in their study that the twin screw extruder resulted in the finest particle size among the others. The other mixing equipments lead to similar particle sizes. Breuer and coworkers designed and tested a new miniature mixer for specially polymer blends and nanocomposites [170]. Their new mixing device has a capacity of approximately 2 gr of material. The mixer has an asymmetrically designed rotor and it was claimed to support complex flow modes providing dispersive mixing. The tests conducted by the authors showed that small dispersed phase size of polypropylene/polyamide and polystyrene/polypropylene immiscible blends which was superior to the other compared mixing devices such as internal mixers and conventional extruders.

Nanocomposites prepared in this new miniature extruder exhibited well-distribution under high shear conditions.

In this study, a conical mini twin screw extruder (micro-compounder, hereafter) with a recirculation facility was utilized as the processing device for the production of nanocomposites. Beyond the advantages of this device (i.e. cost and time efficient processing), there appear also some potential disadvantages. Completely-flighted screws do not equipped with mixing elements, and consequently can not create complex flow types which are more efficient in dispersive mixing. As a result of similar geometrical design of two screws, the melt conveying characteristics are analogous to each other; therefore, the melt conveying of this twin screw is also similar to that of a single screw extruder if they have the same screw geometry [41, 171]. Addition of a distributive or dispersive mixing element resulting in a better mixing is very well known [172]. Besides, average residence time in this lab-extruder is obviously short, although it has recirculation facility.

2.8 Polymer Mixing

Mixing can be broadly defined as a process to reduce the non-uniformity of a composition. The basic mechanism of mixing is to induce physical relative motion of the ingredients. The convective mixing by laminar flow in polymer melts is the dominant motion type. This is the type of mixing that can be realized in extrusion. The mixing action generally occurs by shear flow and elongational flow. As a consequence of these flow types, two types of mixing can be achieved: distributive and dispersive mixing [172].

Distributive mixing aims to improve the spatial distribution of the components without cohesive resistance playing a role; it is also called simple or extensive mixing. On the other hand, in dispersive mixing, cohesive resistances have to be overcome to achieve finer levels of dispersion; dispersive mixing is also called intensive mixing. The cohesive component can consist of agglomerates where a certain minimum stress level is necessary to rupture the agglomerate. It can also be droplets where minimum stresses are required to overcome the interfacial stresses and deform the droplet to cause break-up [172].

Dispersive mixing, the desired mixing mode in polymer compounding and blending, is usually more difficult to achieve than distributive mixing. Single screw extruders are generally considered to be poor dispersive mixers while twin screw compounding extruders have much better dispersive mixing capability. When the mixing process in co-rotating twin screw extruders is analyzed, it is clear that the main mixing action does not occur in the intermeshing region but in the region between the pushing flight flank and the barrel. This is particularly true when the flight helix angle is large. The reason that twin screw extruders make good dispersive mixers is that the space between the pushing flight flank and the barrel is wedge shaped and thus creates elongational flow as the material is force through the flight clearance. Shear flow is not very efficient in achieving dispersive mixing because particles in the fluid are not only sheared they are also rotated. In elongational flow particles undergo a stretching type of deformation without any rotation; rheologists call this “irrotational flow” (see Figure 2.34) [172].

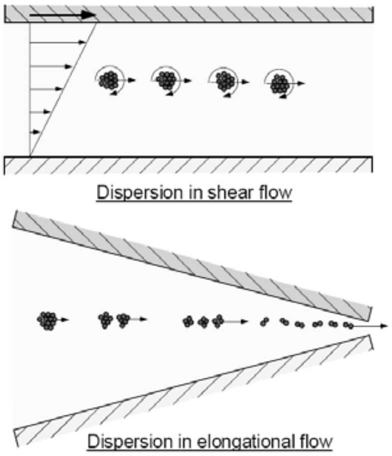

Figure 2.34 Dispersion in shear and elongation [172]

CHAPTER 3

EXPERIMENTAL

Experimental part of this dissertation is divided into three parts. In the first part, the materials and methods used to compatibilize and characterize the acrylonitrile-butadiene-styrene (ABS)/polyamide-6 (PA6) blends are mentioned. In the following part, the materials utilized and experimental procedures followed to prepare short glass fiber reinforced ABS and ABS/PA6 blends are described. In the third part, the details about the materials and the processing methods to produce ABS/PA6 blends based nanocomposites are given.

3.1 Compatibilization of ABS/PA6 Blends

3.1.2 Materials and Processing

The materials used in this study are specified in Table 3.1. Prior to blending, ABS and PA6 pellets were dried in vacuum at 80°C for 12 hours, ethylene-methyl acrylate-glycidyl methacrylate (EMA-GMA) and ethylene-n butyl acrylate-carbon monoxide-maleic anhydride (EnBACO-MAH) were dried at 50°C for 4 hours. The ABS/PA6 ratio were 0/100, 20/80, 50/50, 80/20 and 100/0. The ABS/PA6 part was (100-x) % of the blend, where x is the compatibilizer weight percent in the blend which varied as 0, 5 and 10. ABS/PA6/Compatibilizer batches at prearranged compositions were dry-mixed first, then processed in a co-rotating twin-screw extruder (see Figure 3.1) (Thermoprism TSE 16 TC, L/D=24) at a screw speed of 200 rpm and a barrel temperature profile of 190-230-230-235-240°C. The extrudate was water cooled and chopped into small pellets. The produced pellets were again vacuum-dried at 80°C for 12 hours prior to injection molding. The specimens for mechanical and dynamic mechanical tests were molded by using a laboratory scale injection-molding machine (see Figure 3.2) (Microinjector, Daca Instruments) at a barrel temperature of 230°C and mold temperature of 80°C.

Table 3.1 Specifications of the materials used in the study

Material	*Trade Name and Supplier*	*Specifications*
ABS	Lustran ABS M203FC, Lanxess	Density: 1.05 g/cm^3 MFI (220°C and 10 kg): 32.5 g/10min Standard impact strength, easy flowing
PA6	Teklamid 6, Polyone	Density: 1.13 g/cm^3 MFI (235°C and 2.16 kg): 34.25 g/10min Natural, unfilled, extrusion grade
EMA-GMA	Lotader 8900, Arkema	MFI (190°C, 2.16 kg): 6 g/10min Melting point: 65 °C Acrylic ester: 24 wt% GMA content: 8 wt%
EnBACO-MAH	Fusabond A MG423D, Dupont	MFI (190°C, 2.16 kg): 8 g/10min Melting point: 62 °C MAH content: 16.6 mg KOH/g*

* Determined in our laboratory according to the procedure elsewhere [173].

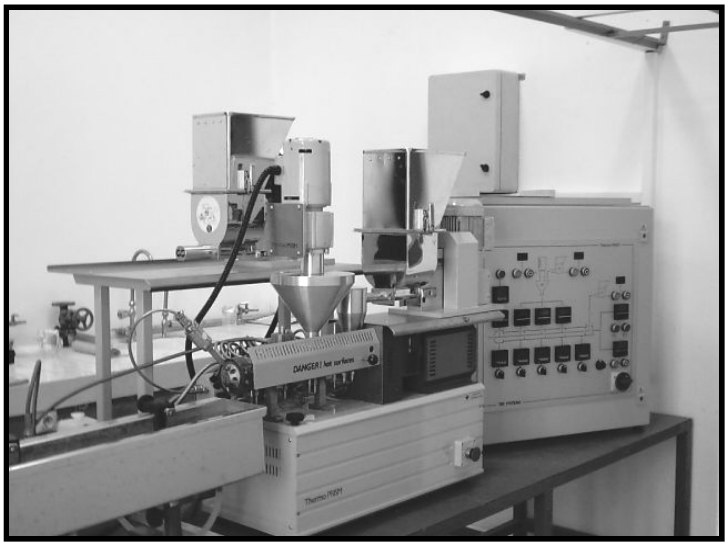

Figure 3.1 A photograph of the twin-screw extruder

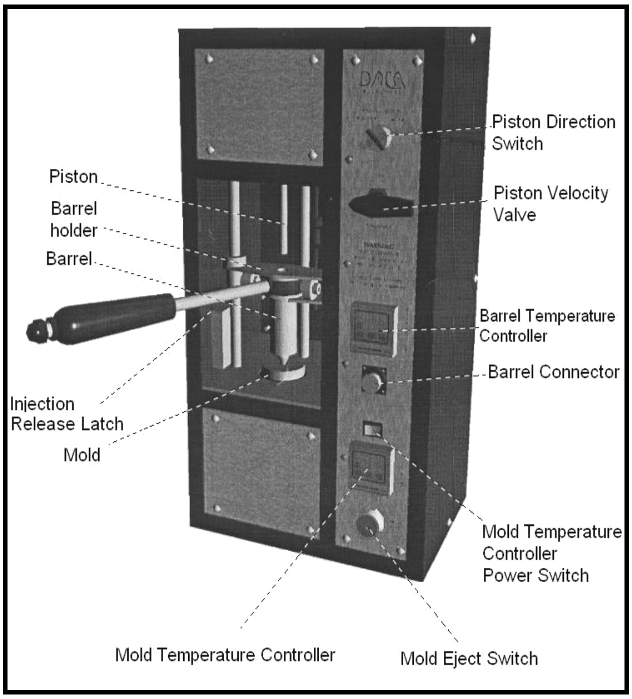

Figure 3.2 Schematic representation of the injection molding machine

3.1.3 Characterization

3.1.3.1 Scanning Electron Microscopy (SEM) and Image Analysis

The cryogenically fractured sample surfaces were analyzed by using a low voltage scanning electron microscopy (SEM) (JEOL JSM-6400) to observe the morphologies of the blends. PA6 and ABS phases were etched by immersing the fracture surfaces in formic acid for 15 minutes and in THF for 60 minutes, respectively. To prevent arcing sample surfaces were coated with gold.

In order to calculate the apparent dispersed particle diameter, the area of the particles was measured automatically using an image analyze software (Image J 1.36, USA). The operating principle of the image analyze software is configured on the basis of color threshold between the particles to be measured and the matrix seen in the micrograph. Once the threshold is created, image analyzer marks particles as ellipsoids and calculates their areas. The color threshold and marking stages of image analysis are shown in Figure 3.3.

By using area of the each particle, their apparent diameters, d_{app}, were calculated using Equation (3.1) by assuming globular particles:

$$d_{app}=2(A/\pi)^{1/2} \tag{3.1}$$

where A is the area of the particle analyzed which was obtained as an output using software. The distribution of d_{app} was obtained by measuring at least 300 particles. The average apparent diameters, $(d_{app})_{avg}$, were calculated using Equation (3.2):

$$(d_{app})_{avg} = (\sum n_i d_i)/(\sum n_i) \tag{3.2}$$

where n is the number of the particle with apparent diameter size, d.

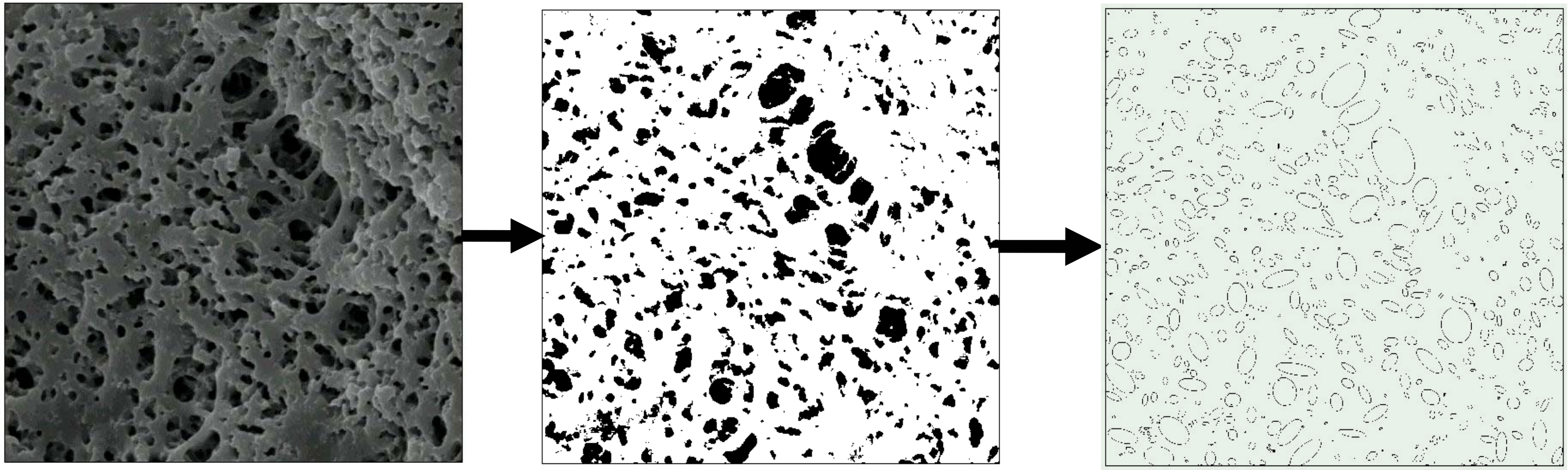

2. Color threshold setting

3. Ellipsoidal particle marking

1. Original SEM micrograph

Figure 3.3 Schematic representations of stages of image analysis

3.1.3.2 Differential Scanning Calorimeter (DSC)

Differential scanning calorimeter (DSC) analyses were carried out by using a Perkin Elmer Diamond DSC at a scanning rate of 10°C/min between 25°C-250°C temperature under N_2 atmosphere. The samples were first heated to 250°C and kept at this temperature for 3 minutes to erase any thermal history, then cooled to room temperature. They were again heated to 250°C as the second heating run.

3.1.3.3 Dynamic Mechanical Analysis (DMA)

Dynamic mechanical analysis (DMA) tests were performed on rectangular samples with the dimensions of 6 mm x 60 mm x 2 mm using Perkin Elmer Pyris Diamond DMA instrument operating in bending mode. Measurements were taken at a frequency of 1 Hz. Temperature was raised from -150°C to 150°C at a scanning rate of 5°C/min.

3.1.3.4 Mechanical Properties

Tensile tests were carried out at room temperature according to ASTM D 658 using Lloyd 30 K universal testing machine. The crosshead speed was 5 mm/min. At least five samples were tested and average results with standard deviations were reported for each type of blend. Charpy impact tests were performed by using a pendulum impact tester of Coesfeld Material Test, according to the ASTM D 256 at room temperature. The notches were machined according to the relevant standard.

3.1.3.5 Impact Essential Work of Fracture Analysis

The extruded and pelletized blends were vacuum-dried at 80°C for 12 hours prior to injection molding. The specimens for impact fracture tests were moulded by using a laboratory scale injection-molding machine (DSM Xplore 12 ml injection molding machine) at a barrel temperature of 230°C and mold temperature of 80°C. All the injected moulded samples were kept in plastic bags at least 24 hour prior to testing.

The notches were first made by forming of a slot with a notcher (Notchvis, Ceast) equipped with a V-shaped knife. Notches were sharpened by tapping a fresh razor blade into the root of the notch. The exact notch lengths were measured under an optical microscopy. To obtain total work of fracture energy, samples were tested with a pendulum type Charpy impact tester (Resil Impactor, Ceast) equipped with an instrumented hammer to measure the force vs displacement during the test. The test speed was 3.5 m/s and the ambient temperature was 25±3 °C. By the help of a data acquisition system (DAS 16000, Ceast), the force versus displacement curves and total fracture energies were obtained.

The notched Charpy impact tests were performed according to ASTM D 256 using samples of 3 mm x 10 mm x 80 mm. Five samples were tested and average values were reported.

The impact fractured sample surfaces were analyzed by using a low voltage scanning electron microscope (SEM) (JEOL JSM-6400) to observe the morphologies of the blends. To prevent arching, samples were coated with a thin layer of gold.

3.1.3.6 Fourier Transformation of Infrared Spectroscopy (FT-IR)

The injection molded tensile bars were peeled by a razor blade to remove the skin part, then the core part was utilized to perform FT-IR Spectroscopy in attenuated total reflectance (ATR) mode using IR-spectrometer (Bruker Optics Tensor Series). The measurement was done at a resolution of 2 cm^{-1} and with 32 scans. The wave length range was 600 - 4000 cm^{-1}.

3.2 Short Glass Fiber Reinforced ABS and ABS/PA6 Blends

3.2.1 Materials

The natural, extrusion grade ABS (Tairilac®) resin used in this study was supplied by EMAŞ Plastik Ltd. Şti. PA6 (Teklamide 6®) used in this study was obtained from Tekno Polimer Ltd. For the preparation of the short glass fiber reinforced ABS/PA6 blends, EnBACO-MAH was used as compatibilizer. The details about this material are given in Table 3.1.

The continuous E-glass fiber strand used in surface free energy measurements was supplied by Cam Elyaf A.Ş. with initial sizing of "styrylsilane/methacrylosilane" coupling agents and "polyester/epoxy" film formers. The chopped E-glass fibers used in processing experiments were also obtained from Cam Elyaf. These fibers were sized with "aminosilane" and "epoxy" film former. Some characteristic properties of glass fibers are given in Table 3.2. Silane coupling agents used during surface modification of glass fibers were represented in Table 3.3.

Table 3.2 Characteristic properties of glass fiber roving

	Continuous Strand	Chopped Strand
Product code	WR 3-1200	PA-1
Coupling type	Styrylsilane/Methacrylosilane	Aminosilane
Film formers	Polyester/Epoxy	Epoxy
Fiber Diameter (μm)	16.0	13
Fiber Length (mm)	Continuous	4.75
Moisture Content (%)	Max. 0.15	Max. 0.15

Table 3.3 Silane coupling agents used in this study

Chemical Structure	Manufacturer	Designation
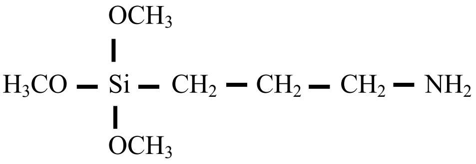 $H_3CO-\overset{OCH_3}{\underset{OCH_3}{Si}}-CH_2-CH_2-CH_2-NH_2$ γ-aminopropyltrimethoxysilane	Aldrich, 97% Lab. scale silicone compound Cat.: 28,177-8	Aminopropylsilane (APS)
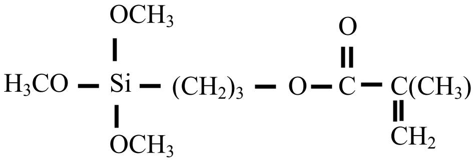 $H_3CO-\overset{OCH_3}{\underset{OCH_3}{Si}}-(CH_2)_3-O-\overset{O}{\overset{\|}{C}}-\underset{CH_2}{\underset{\|}{C}}(CH_3)$ γ-(trimethoxysilyl)propylmethacrylate	Aldrich, 97% Lab. scale silicone compound Cat.: 44,015-9	Methacrylopropylsilane (MPS)
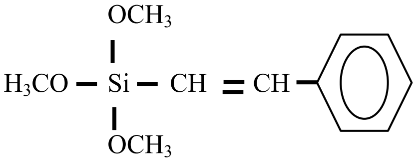 styryltrimethoxysilane 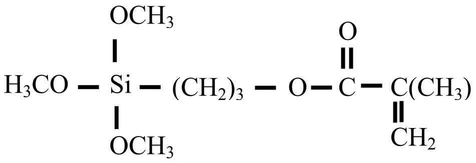 $H_3CO-\overset{OCH_3}{\underset{OCH_3}{Si}}-(CH_2)_3-O-\overset{O}{\overset{\|}{C}}-\underset{CH_2}{\underset{\|}{C}}(CH_3)$ γ-(trimethoxysilyl)propylmethacrylate	A blend of silane compounds was already applied to the glass fiber surfaces by the manufacturer	As Received (REC)

3.2.2 Experimental Procedure

3.2.2.1 Silane treatment

Before new coupling agents were applied onto glass fiber surfaces, initial film formers and couplings had to be removed. The removing was carried out in a furnace by burning off them at approximately 600°C for 30 minutes, then by using a soxhlet apparatus glass fibers were washed with acetone for 1 hour to remove organic degradation deposits.

Firstly, the APS and MPS were dissolved in distilled water to form a 1wt% solution for hydrolysis. The pH of solution was adjusted to 4.5 with acetic acid to catalyze the MPS reaction. For APS, to avoid the possible reaction between amino group and acid, no catalyst was used. Since the MPS is not water soluble, it was dissolved in a solution of 10wt% water in ethanol. After hydrolysis, continuous glass fiber bundles were dipped into the solution and kept for 1 hour to allow formation of silanol bonds with continuous stirring. Then, the solution was removed and glass fibers were washed with water and then with ethanol to remove the physisorbed coupling agents. The fibers were then dried in an oven for 10 minutes at 110° C. To check the amount of coupling agent bonded to the fiber surface, a small sample of fiber was analyzed in TGA (thermo gravimetric analyzer). This measurement indicated that the coupling agent weight fraction on the surface was almost 0.5 %.

3.2.2.2 Contact Angle Measurements

Contact angles were measured tensiometrically using an electronic microbalance (Sartorious Microbalance, M25D) equipped with a motor-driven stage that has vertical displacement capability of 10 mm. Figure 3.4 shows the schematic of the microbalance. The digital signals from the microbalance were recorded. In the case of glass fibers, a single fiber specimen was prepared first, by tapping 1 cm of a 2 cm length of fiber between two pieces of adhesive tape, with about 1 cm of the fiber exposed. The specimen was then placed to the hook of the microbalance. In all experiments a stage velocity of 1 μm/s was used to bring the fiber into contact with the liquid. The force (F) measured by the microbalance was then recorded to calculate the advancing contact angle (θ) by Equation (3.3),

$$F = (P)(\gamma)(\cos\theta) \qquad (3.3)$$

where P is the perimeter of the sample and γ is the surface tension of the probe liquid. Each contact angle measurement was repeated at least three times. Each contact angle measurement was repeated at least three times. After each measurement to specify the perimeter of sample, 0.5 cm of the fiber tip was cut; the remainder was then brought into contact with n-decane, completely wetting liquid.

For the polymeric samples, same procedure was repeated with a tiny, very thin strip-shaped sample with dimensions of 2 mm x 20 mm x 0.2 mm. The samples were prepared with a hot-press at 230°C and 100 bar. Diiodomethane (DIM) was used as the probe liquid for Liftshitz-van der Waals interactions. Ethyleneglycol (EG) and formamide (FA) were used to identify the acid-base interactions between sample and the probe liquid. n-Decane, completely wetting liquid, was used to find the perimeters of the sample. It is assumed that n-decane makes zero angle with the sample. Properties of these probe liquids are given in Table 3.4 [174].

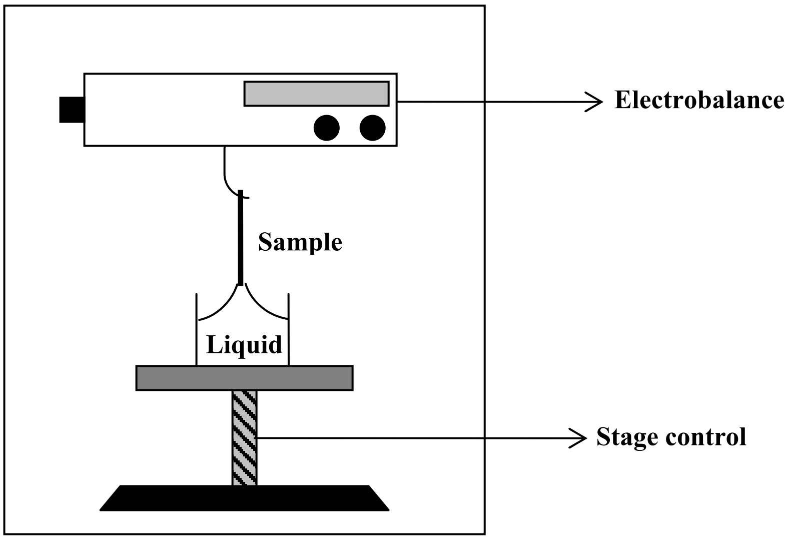

Figure 3.4 Experimental set-up for contact angle measurements

Table 3.4 Surface free energy components of probe liquids, (mN/m)

Surface Tension (mN/m)	DIM	EG	FA	n-Decane
$\gamma^{TOT}{}_{L}$	50.8	58	48	23.83
$\gamma^{LW}{}_{L}$	50.8	39	29	23.83
$\gamma^{AB}{}_{L}$	-	19	19	-
$\gamma^{-}{}_{L}$	-	39.6	39.6	-
$\gamma^{+}{}_{L}$	-	2.3	2.3	-

3.2.2.3 Short Beam Flexural Tests

Inter laminar shear strength (ILSS) was determined according to ASTM D 2344 using the short beam flexural test. Bundles of different silane coupling agent treated glass fibers were embedded into polymer matrix using a hot-press, which is illustrated in Figure 3.5.

The short beams including unidirectional parallel glass fibers at the central position were then cut from the obtained sheets and then tested by using a Lloyd 30 K Universal Testing Machine (see Figure 3.6). The support span to depth ratio used was 5:1 with a corresponding specimen length to depth of 7:1, and crosshead speed was 2.0 mm/min. The force versus displacement curve for each sample was obtained.

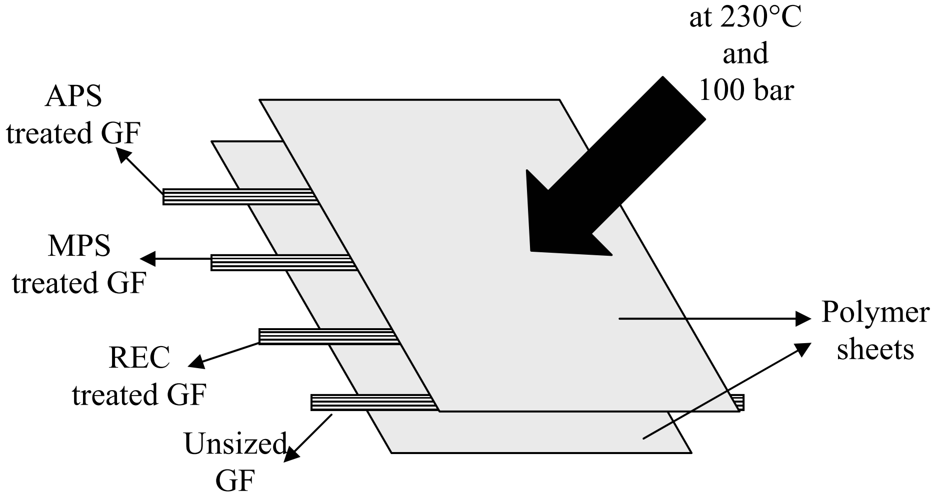

Figure 3.5 The sample preparation for short beam flexural testing

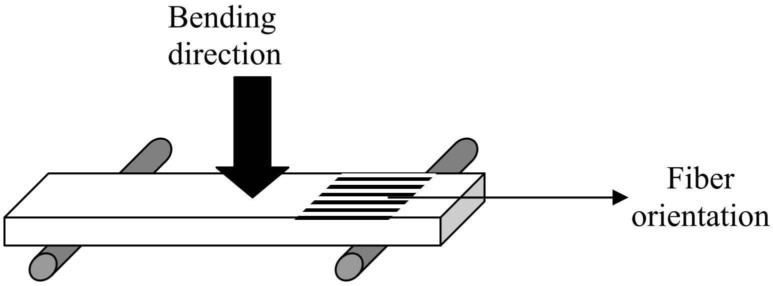

Figure 3.6 The schematic illustration of the short beam flexural testing

3.2.2.4 Processing and Experimental Design

ABS/SGF Composites

Prior to processing, ABS pellets and glass fibers were dried in a vacuum oven for 4 hours at 80°C. Composites containing 10, 20, and 30 wt% short glass fiber were prepared by melt mixing in a co-rotating twin screw extruder (Thermoprism TSE 16 TC, L/D: 24). ABS pellets and glass fibers were fed from main-feeder and side-feeder, respectively. Molten composite obtained from die of the extruder was water cooled and pelletized. The extrusion conditions were arranged for each run as given in Table 3.5. In runs 1, 2, 3 and 4, the effects of short glass fiber loading level; in runs 4, 5, 6 and 7, the effects of screw speed and in runs 6, 8 and 9, the effects of barrel temperature were studied. The specimens for mechanical characterization experiments were molded by using a laboratory scale plunger type injection-molding machine (Microinjector, Daca Instruments) at 230°C of barrel temperature and 80°C of mold temperature.

ABS/PA6/SGF Composites

For the preparation of the blends, ABS and PA6 pellets were dried in vacuum oven at 80°C for 4 hours and 12 hours, respectively, prior to processing. The 10, 20 and 30 by wt % PA6 containing ABS/PA6 batches were processed in a co-rotating twin-screw extruder at screw speed of 200 rpm and barrel temperature profile of 195-230-230-235-240°C. The extrudate was water cooled and chopped into small pellets. The produced ABS/PA6 pellets were vacuum dried again at 80°C for 12 hours. The 30% glass fiber reinforced ABS\PA6 composites were prepared by extrusion at the same operating conditions in the ABS/PA6 blending. The extrudate was again water cooled and chopped into small pellets. The specimens for mechanical characterization experiments were molded by using a laboratory scale plunger type injection-molding machine (Microinjector, Daca Instruments) at 230°C of barrel temperature and 80°C of mold temperature.

Compatibilized ABS/PA6/SGF Composites

For the preparation of the blends, ABS and PA6 pellets were dried in vacuum oven at 80°C for 4 hours and 12 hours, respectively, and compatibilizer (EnBACO-MAH) were dried in vacuum oven at 50°C for 4 hours, prior to processing. The ABS/PA6 ratio were 0/100, 20/80, 50/50, 80/20 and 100/0. The ABS/PA6 part was (100-x) % of the blend, where x is the compatibilizer weight percent in the blend which was 0, 5 and 10. (ABS/PA6)/Compatibilizer batches at prearranged compositions were dry-mixed first, then processed in a co-rotating twin-screw extruder (Thermoprism TSE 16 TC, L/D: 24). The screw speed was 200 rpm and barrel temperature profile was 195-230-230-235-240°C. The extrudate was water cooled and chopped into small pellets. The produced ABS/PA6 pellets were vacuum dried again at 80°C for 12 hours. The 30% glass fiber reinforced ABS\PA6 composites were prepared by extrusion at the same operating conditions in the ABS/PA6 blending. The extrudate was again water cooled and chopped into small pellets. The specimens for mechanical characterization experiments were molded by using a laboratory scale plunger type injection-molding machine (Microinjector, Daca Instruments) at 230°C of barrel temperature and 80°C of mold temperature.

Table 3.5 Experimental conditions

	SGF Content (wt%)	ABS:PA6 ratio in the matrix	Barrel Temperature Profile (feed to die, °C)	Screw Speed (rpm)
Run 1	0	1:0	195-210-210-215-220	100
Run 2	10			
Run 3	20			
Run 4	30			
Run 5	30	1:0	195-210-210-215-220	150
Run 6				200
Run 7				250
Run 8	30	1:0	195-230-230-235-240	200
Run 9			195-250-250-255-260	
Run 10*	30	1:0	195-230-230-235-240	200
Run 11		9:1		
Run 12		8:2		
Run 13		7:3		

*In Run 10 (ABS/30wt%SGF), ABS was first extruded at the given conditions to equalize the thermal history of matrix with runs 11, 12 and 13, then compounded with SGFs at the same processing conditions in the second extrusion step.

3.2.3 Characterization

3.2.3.1 Mechanical Tests

All mechanical tests were carried out at room temperature. At least five samples were tested and average results with standard deviations were reported for each type of composite. Tensile tests were performed on dog-bone specimens according to ASTM D638 by using a Lloyd 30K Universal Testing Machine. Flexural tests were applied according to ASTM D 790 on rectangular specimens of 2 mm x 7.4 mm x 100 mm using the same machine. Charpy impact tests were performed by using a Pendulum Impact Tester of Coesfeld Material Test, according to the ASTM D256 on rectangular specimens of 6 mm x 60 mm x 2 mm.

3.2.3.2 Scanning Electron Microscopy

A low voltage SEM (JEOL JSM-6400) was used to analyze the tensile fractured surfaces of the composites. The specimens were coated with gold to eliminate arcing of the beam.

3.2.3.3 Optical microscopy

About 5 g of randomly selected samples from extruded pellets for each run were placed in a crucible in an oven at 600°C for 30 minutes to remove the polymeric matrix. The glass fibers left were dispersed in water and transferred to the glass slides of microscope. The photographs (see Figure 3.7) obtained from optical microscope (Prior Laboratory Microscope Model B 3000) were analyzed after digital scaling to measure the fiber lengths. A minimum of ten photographs were obtained from each slide, and a population of approximately 400 fibers for each run was taken into account for fiber length distributions. The lengths were measured manually for statistical analysis from the magnified pictures by utilizing calipers with a precision of 0.05 mm, which corresponds to 6.6 microns when photos are considered.

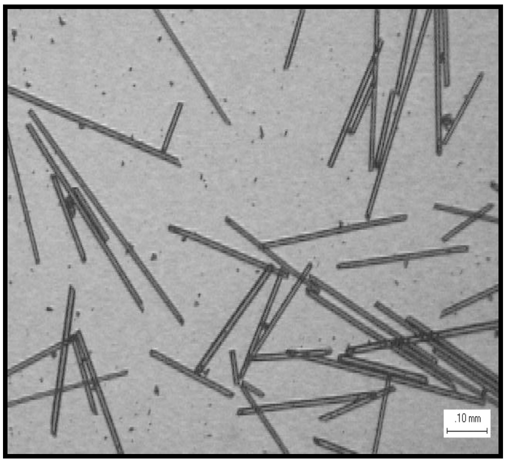

Figure 3.7 A photograph of dispersed fibers under microscope

3.2.3.4 Melt Flow Index (MFI)

Melt flow index values were measured by using an extrusion plastometer (Omega Melt Flow Indexer) according to ASTM D 1238 with 5 kg load and at 230 ^{o}C.

3.3 ABS/PA6 Blends Based Nanocomposites

3.3.1 Materials

The properties of ABS, PA6 and compatibilizer (EnBACO-MAH) are described in Table 3.1. Montmorillonite (Cloisite® 30B, Southern Clay Products Inc.) used was organically modified with methyl, tallow, bis-2-hydroxyethyl, quaternary ammonium by the supplier. The chemical structure of the organic modifier is given in Figure 3.8. Prior to compounding, ABS and PA6 pellets were dried in vacuum at

80°C for 12 hours; EnBACO-MAH was dried at 50°C for 4 hours. The ABS/PA6 ratio were 0/100, 20/80, 50/50, 80/20 and 100/0. The percentage of ABS+PA6 portion of the matrix was 95% and compatibilizer was 5% of the matrix (blends will be named in the order of ABS/PA6/Compatibilizer by giving the ratios, hereafter). Montmorillonite (MMT) amount in the nanocomposite was 1%, 3%, and 5% by weight of the nanocomposites.

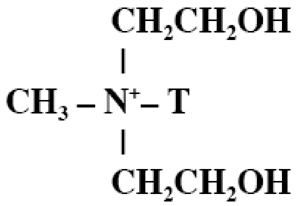

$$CH_3-\overset{\overset{CH_2CH_2OH}{|}}{\underset{\underset{CH_2CH_2OH}{|}}{N^+}}-T$$

Figure 3.8 The chemical structure of the organic modifier of Cloisite 30B (T is tallow: 65% C18, 30%C16, 5%C14)

3.3.2 Microcompounding and Injection Molding

Firstly, (ABS/PA6)/Compatibilizer batches at prearranged compositions were dry-mixed at predefined amounts with a precision of 0.01 g. The mixture was melt compounded in a twin-screw microextruder (15 ml microcompounder®, DSM Xplore). Figure 3.9 shows the whole-laboratory extruder and Figure 3.10 shows the cross-section of the barrel in co-, counter and modified co-rotating modes. The core of this laboratory compounder is formed by a separable, sealed mixing compartment containing two detachable, conical mixing screws. The main drive is continually digitally variable and allows for torque measurement. The processing temperature can be adjusted in three zones separately controlled heating zones and the mixing time can be varied via recirculation of the melt. This laboratory extruder can be operated in both co-rotating and counter-rotating mode by the help of a gear box fixed on the main drive of the machine.

Materials were fed from the top of the microextruder by a specially designed injector type feeder. The screw speed was kept at 30 rpm during feeding. Feeding was taking about 15 seconds. After feeding, the screw speed was increased to operating value. The operating conditions of the microextruder were arranged as screw speeds of 100 or 200 rpm and barrel temperature profile of 235-235-235°C (from top to bottom). At the end of mixing period, the extrudate was taken by changing the position of the valve to guide the polymer to the die.

Materials were injection molded using DSM Xplore 10 ml injection molding machine® to obtain ISO 527-2/5A tensile bars. The injection and holding pressures were set to15 bars. Melt temperature and mould temperature were 235°C and 80°C, respectively.

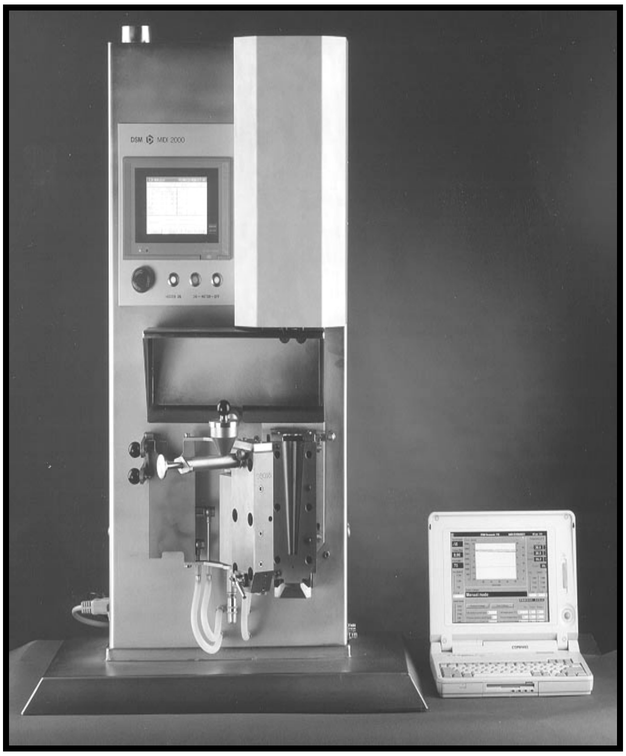

Figure 3.9 The twin-screw conical microcompounder

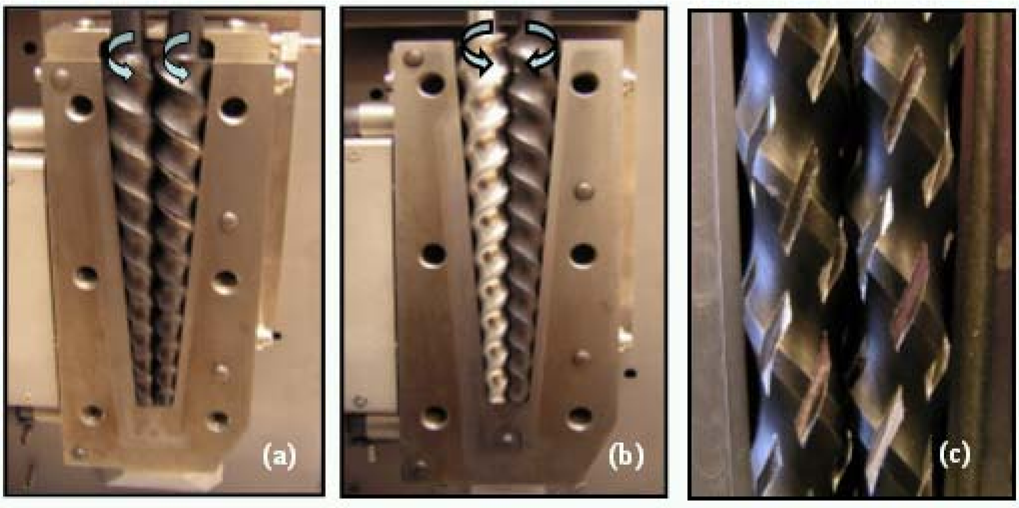

Figure 3.10 The cross-sections of (a) co-rotating (b) counter-rotating and (c) modified co-rotating screw

3.3.3 Characterization

3.3.3.1 X-Ray Analysis

The nanocomposites were analyzed by using a RIGAKU D/MAX 2200/PC X-ray diffractometer on the narrow part of injection moulded tensile bars (see Figure 3.11) except organoclay, which was in powder form, using CuKα (λ=1.54Å) radiation, generated at a voltage of 40 kV and current of 40mA was used as the X-Ray source. The diffraction angle 2θ was scanned from 1^{o} to 10^{o} at a scanning rate of 1^{o}/min. The XRD patterns were used to calculate final d-spacing of the clay galleries by using Bragg's Law.

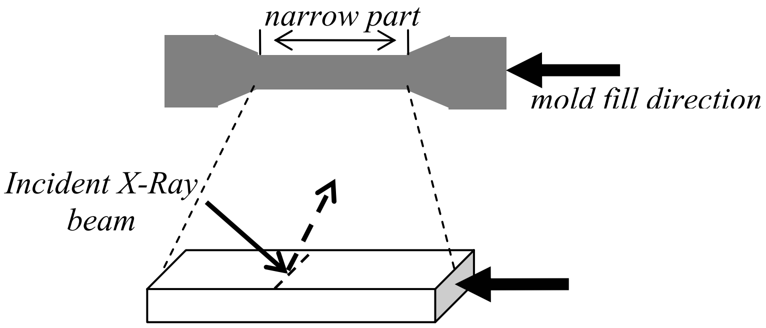

Figure 3.11 Illustration of sample positioning in X-Ray analysis

3.3.3.2 Tensile Testing

Prior to testing, the tensile bars were kept in a desicator in polyethylene bags at least 24 hours. Tensile test were performed on dumbbell-shaped samples according to ASTM D 638 using tensile testing machine (Instron Model 1137) at 23°C. The crosshead speed was 2.5 mm/min. For each experiment, 5 samples were tested. The average results were reported with standard errors.

3.3.3.3 Scanning Electron Microscopy (SEM)

The cryogenically fractured surfaces of injection molded samples were analyzed by using a low voltage SEM (JEOL JSM-6400) to observe the morphologies of the nanocomposites. PA6 and ABS phases were etched by immersing the fracture surfaces in formic acid for 15 minutes and in THF for 60 minutes, respectively, to observe the blend phase morphologies. To prevent arcing, sample surfaces were coated with gold. In order to calculate the apparent dispersed particle diameters, the areas of the particles were measured automatically using image analyzer software (Image J 1.36, USA).

3.3.3.4 Transmission Electron Microscopy (TEM)

Injection molded samples were examined by Transmission Electron Microscope (Philips CM200 TEM) at an acceleration voltage of 120 kV. Ultra thin sections of 70 nm in thickness were cryogenically cut with a diamond knife at a temperature of -100 ºC. All samples are trimmed parallel to the injection molding direction.

The resulting images were analyzed to observe extend of exfoliation and to obtain nano-particle size distribution (see Figure 3.12). Because of the slight variation in the thickness of the ultra-microtomed section, grey shades were appeared on the TEM micrographs and they disturb the clearness of the image and reduce the image quality for the analysis. To make the clay layers, stacks and tactoids much clear and visible [175], selected TEM micrographs (at same magnification) were printed on A4-size papers at photographic quality by using a laser-printer. Then, the particles were traced on transparency films, which were put just on the printed images, with a permanent pen.

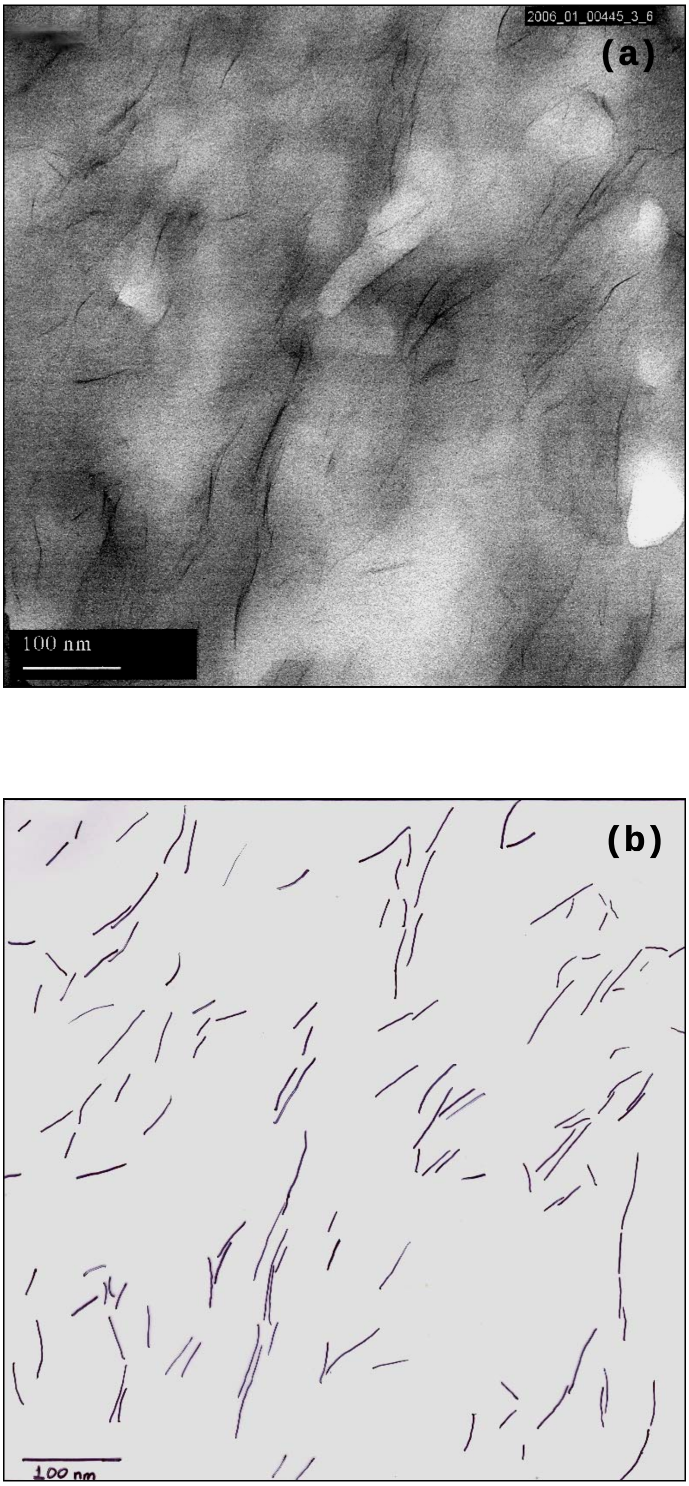

Figure 3.12 Representative pictures showing the stages of image analysis on TEM micrographs: (a) Original TEM micrograph (b) Traced manually and scanned on white background subsequently

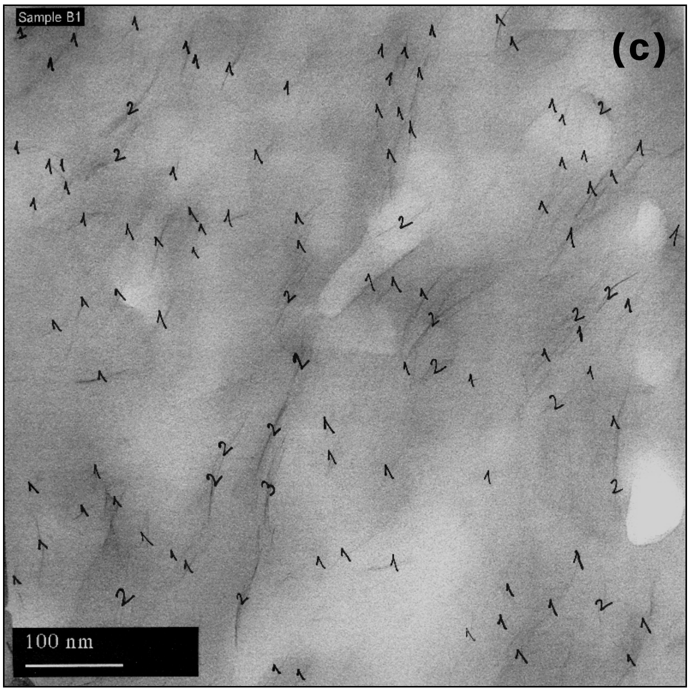

Figure 3.12 (Cont'd) Representative pictures showing the stages of image analysis on TEM micrographs: (c) Number of platelets per particles were marked manually

The resulting transparencies were scanned at 300 dpi resolution on a white background to obtain maximum contrast for image analysis. The scanned images were analyzed using an image analyzer (Scion Image, USA) for automatic particle size distribution using an image analyzer. At least 250 particles were analyzed for each composition. The average particle lengths, L_{avg}, were calculated using Equation (3.4):

$$L_{avg} = (\sum n_i L_i)/(\sum n_i) \tag{3.4}$$

where n is the number of the particle with length, L. This procedure is illustrated in Figure 3.11.

To obtain the average particle thickness, the number of platelets was counted and marked manually on to the print-out of the TEM micrographs; then, they were analyzed statistically to calculate average particle thickness.

CHAPTER 4

RESULTS AND DISCUSSIONS

4.1 Compatibilization of ABS/PA6 Blends

In this part of the dissertation, the results and discussions related to the compatibilization efficiency of olefin based, maleated and epoxydized copolymers in melt compounded ABS/PA6 blends is presented in terms of blend morphologies by SEM and mechanical properties by tensile and impact tests. The potential chemical reactions between functional groups of the compatibilizers and end-groups of PA6 were investigated by FTIR. In the blends, the ABS/PA6 part was (100-x) % of the blend, where x is the compatibilizer weight percent in the blend which varied as 0, 5 and 10. The samples were named in the order of ABS/PA6/Compatibilizer by giving the corresponding compositions and the type of the compatibilizer.

4.1.1 Effects of compatibilizer type and content on the morphologies, mechanical and thermal properties of ABS/PA6/Compatibilizer blends

4.1.1.1 FTIR Analysis

In the current blend system, possible chemical reactions lead to the final morphology and therefore physical properties due to the interactions between maleic anhydride with amine end-group and epoxy group with amide and/or acid end-groups of PA6 for EnBACO-MAH and EMA-GMA, respectively. These reactions are shown in Figures 4.1 and 4.2. These reactions were inspected by performing FTIR spectroscopy analysis on blends compatibilized with EnBACO-

MAH or EMA-GMA copolymers. Since the higher concentration of components was in 50/50/10 blends, FTIR spectroscopy performed on this composition.

The FTIR spectrum for ABS is shown in Figure 4.3. The characteristics peaks located at 756 cm^{-1}, 962 cm^{-1}, 1450 cm^{-1}, 1490 cm^{-1}, 2848 cm^{-1}, 2914 cm^{-1}, 3020 cm^{-1} are associated with -CH- groups. The peaks appeared at 698 cm^{-1} is the phenyl ring vibration in SAN phase. The peaks located at 1022 cm^{-1} and 2231 cm^{-1} stand for -C-H deformation in phenyl ring and -C≡N vibration of SAN phase, respectively. The double bond in butadiene phase of ABS can be characterized from the peak located at 1596 cm^{-1} representing C=C strech vibration. The other peaks and corresponding representations are given in Table A.1 in Appendix A.

The FTIR spectrum for PA6 is shown in Figure 4.4. The peaks at 676 cm^{-1}, 964 cm^{-1}, 1363 cm^{-1}, 1465 cm^{-1}, 2850 cm^{-1}, 2916 cm^{-1} indicated various absorptions of -C-H group. The characteristic peaks of functional groups of PA6 located at 1112 cm^{-1} and 1166 cm^{-1} for C-N stretching vibrations, 1625 cm^{-1} for C=O and 3284 cm^{-1} for O-H vibration in –COOH. All of the peaks seen in FTIR spectrum of PA6 are explained in Table A.2 in Appendix A.

The FTIR spectrum for EnBACO-MAH and EMA-GMA PA6 are shown in Figure 4.5 and 4.6, respectively. The maleic anhydride group and epoxy group have characteristic peaks at 1778 cm^{-1} (C=O stretch vibration) in spectrum of EnBACO-MAH (see Figure 4.5) and at 910 cm^{-1} (oxiarine ring vibration) in spectrum of EMA-GMA (see figure 4.6), respectively. The other FTIR peaks seen in spectra of EnBACO-MAH and EMA-GMA are explained in Tables A.3 and A.4, respectively.

The potential reaction shown in Figure 4.1 indicates that PA6 and EnBACO-MAH forms imide-bonds through reaction of maleic-anhydride and amide group above 120°C. The imide-linkage formed as a result of interfacial grafting reaction can be identified from new peaks appeared at 1770 cm^{-1} (imide carbonyl symmetric stretching), 1705 cm^{-1} (imide carbonyl asymmetric stretching). The peaks appeared at 1731 cm^{-1} (carboxylic C=O streching) and 1710 cm^{-1} (Amide I C=O stretching) indicate that the reaction (a) shown in seen Figure 4.1 also realized.

The grafting between EMA-GMA, which is given in Figure 4.2, occurs through reaction of epoxy ring of compatibilizer with both end groups of polyamide. This reaction can be identified from the disappearing of absorption band of ring vibration of oxiarine group seen at 910 cm^{-1} in spectrum of EMA-GMA in FTIR spectrum from 50/50/10 blend system compatibilized with EMA-GMA (see Figure 4.8).

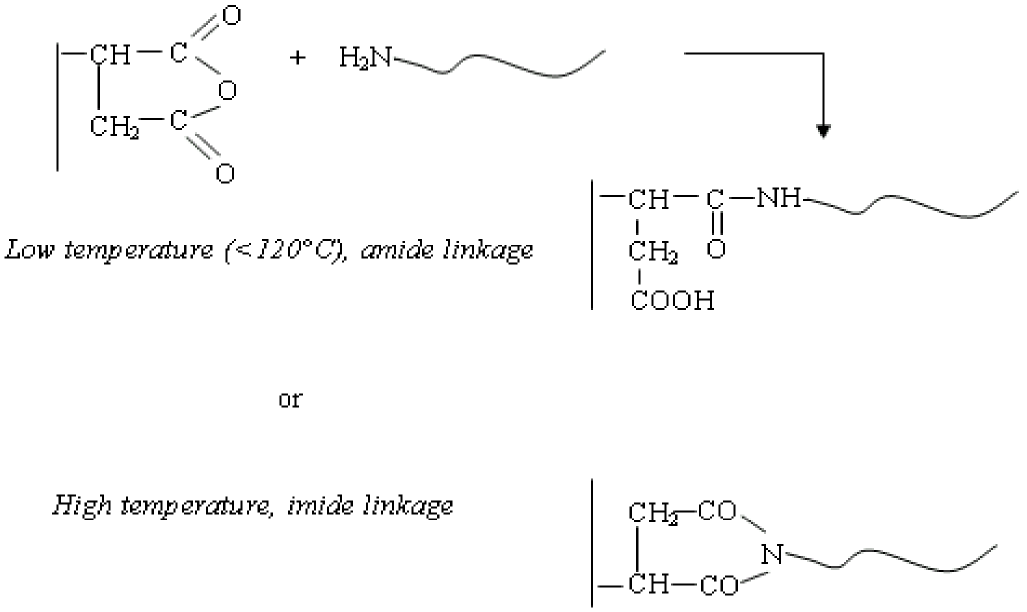

Figure 4.1 Reaction scheme of maleic anhydride group with amide end groups of PA6 [176]

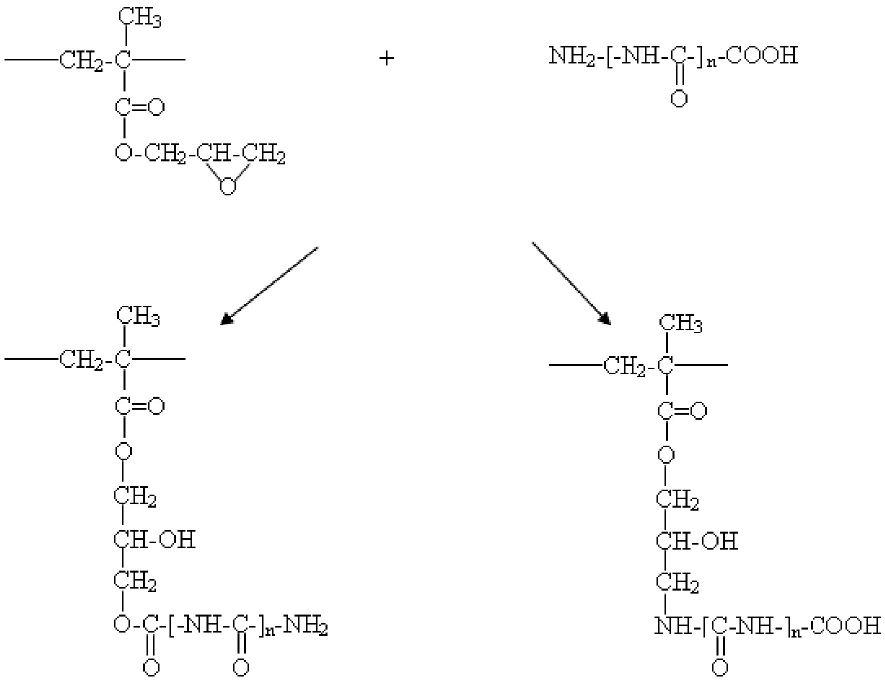

Figure 4.2 Reaction scheme of epoxide group with acid and amide end groups of PA6 [177]

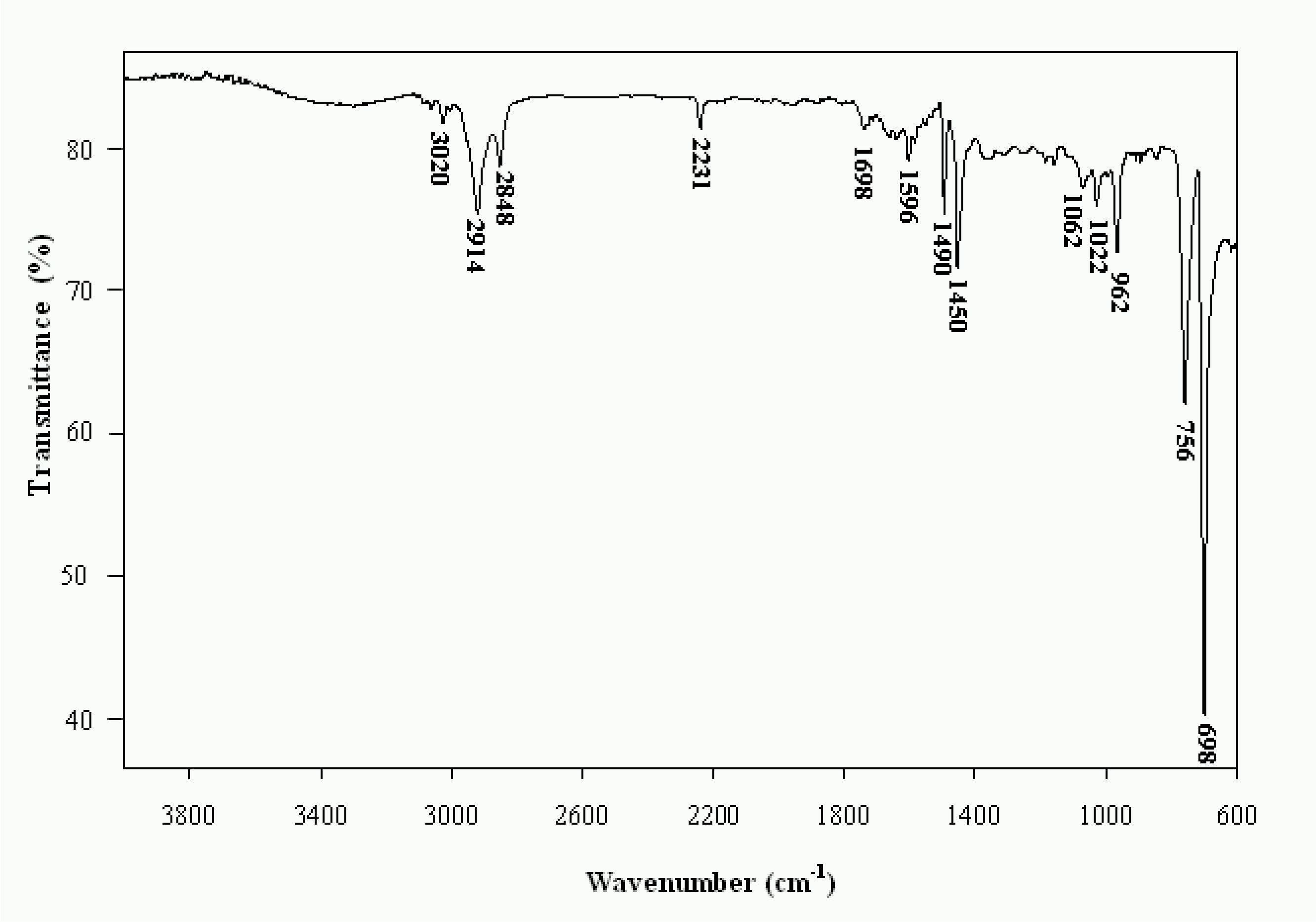

Figure 4.3 ATR-FTIR spectrum of ABS

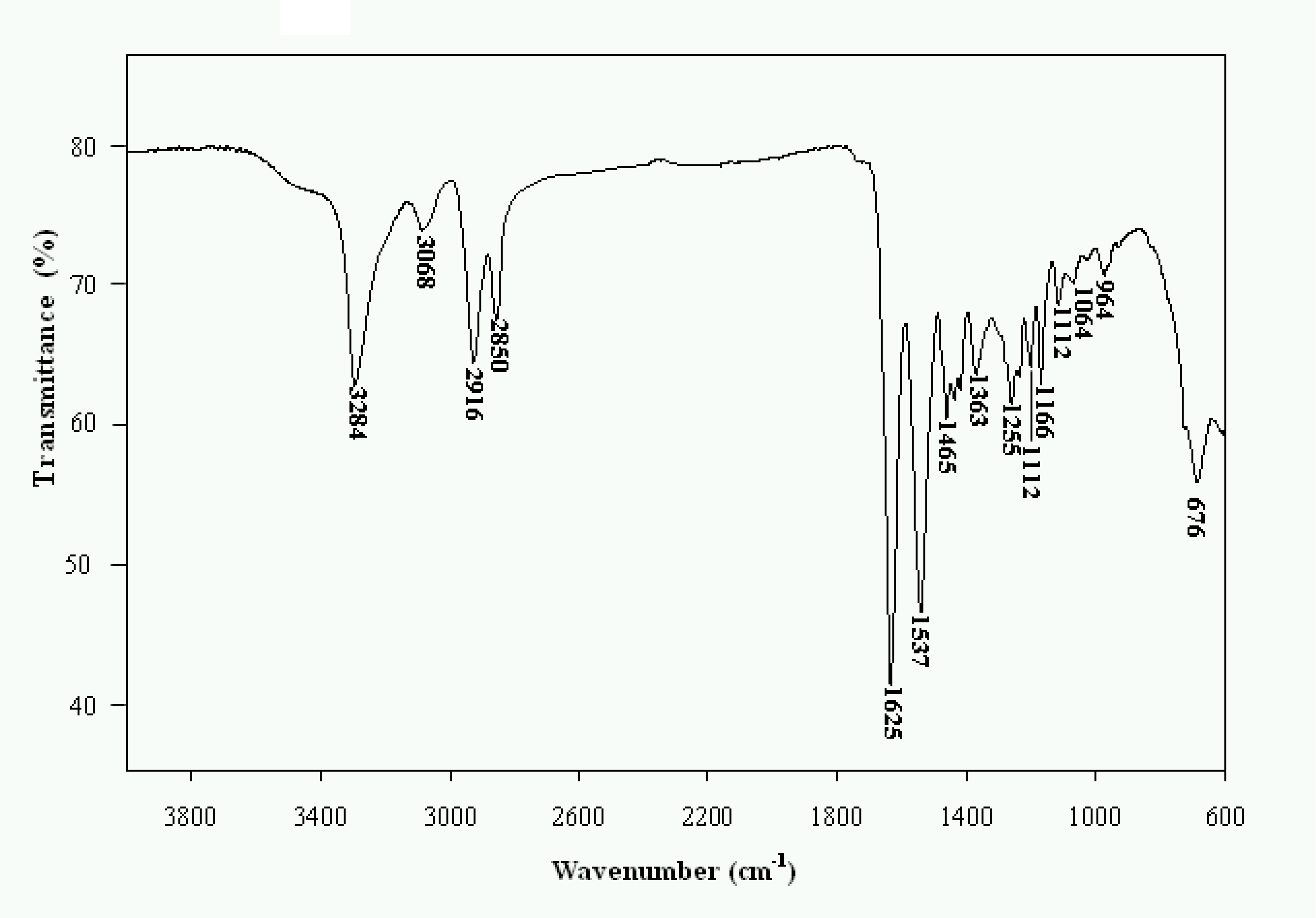
Transmittance (%)
80
70
60
50
40
Wavenumber (cm-1)
3800
3400
3000
2600
2200
1800
1400
1000
600
3284
3068
2916
2850
1625
1537
1465
1363
1255
1166
1112
1112
1064
964
676

Figure 4.4 ATR-FTIR spectrum of PA6

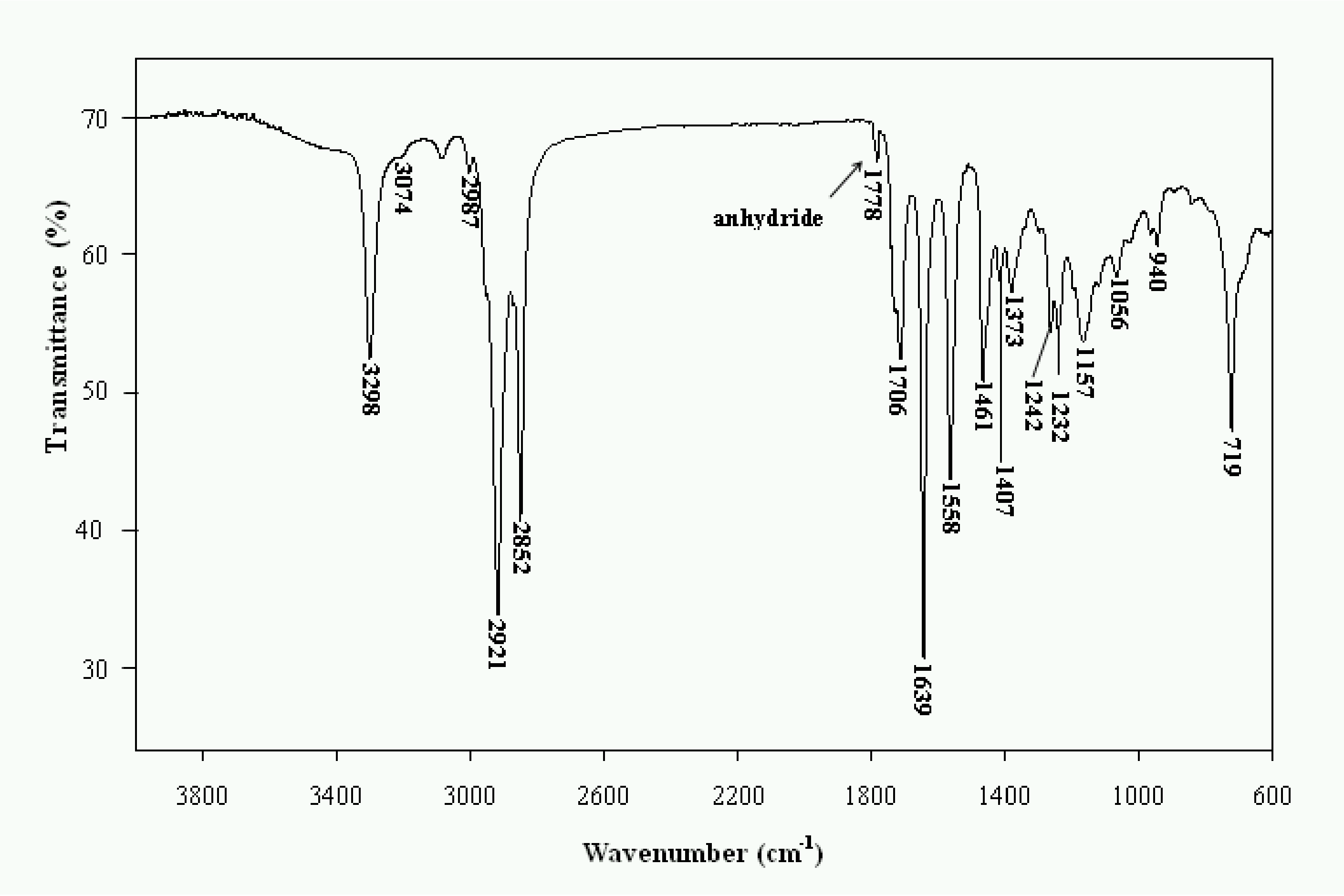

Figure 4.5 ATR-FTIR spectrum of EnBACO-MAH

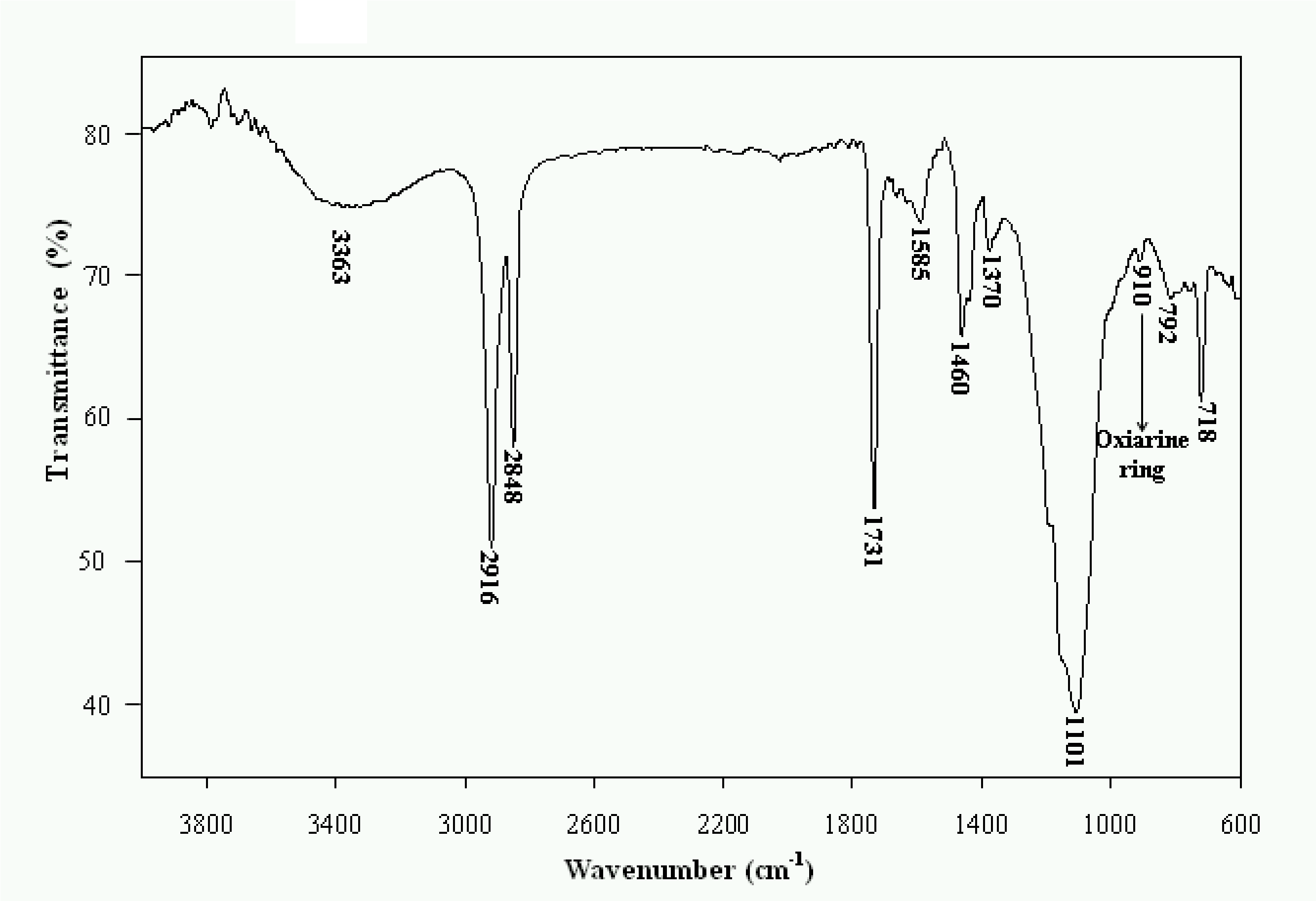

Figure 4.6 ATR-FTIR spectrum of EMA-GMA

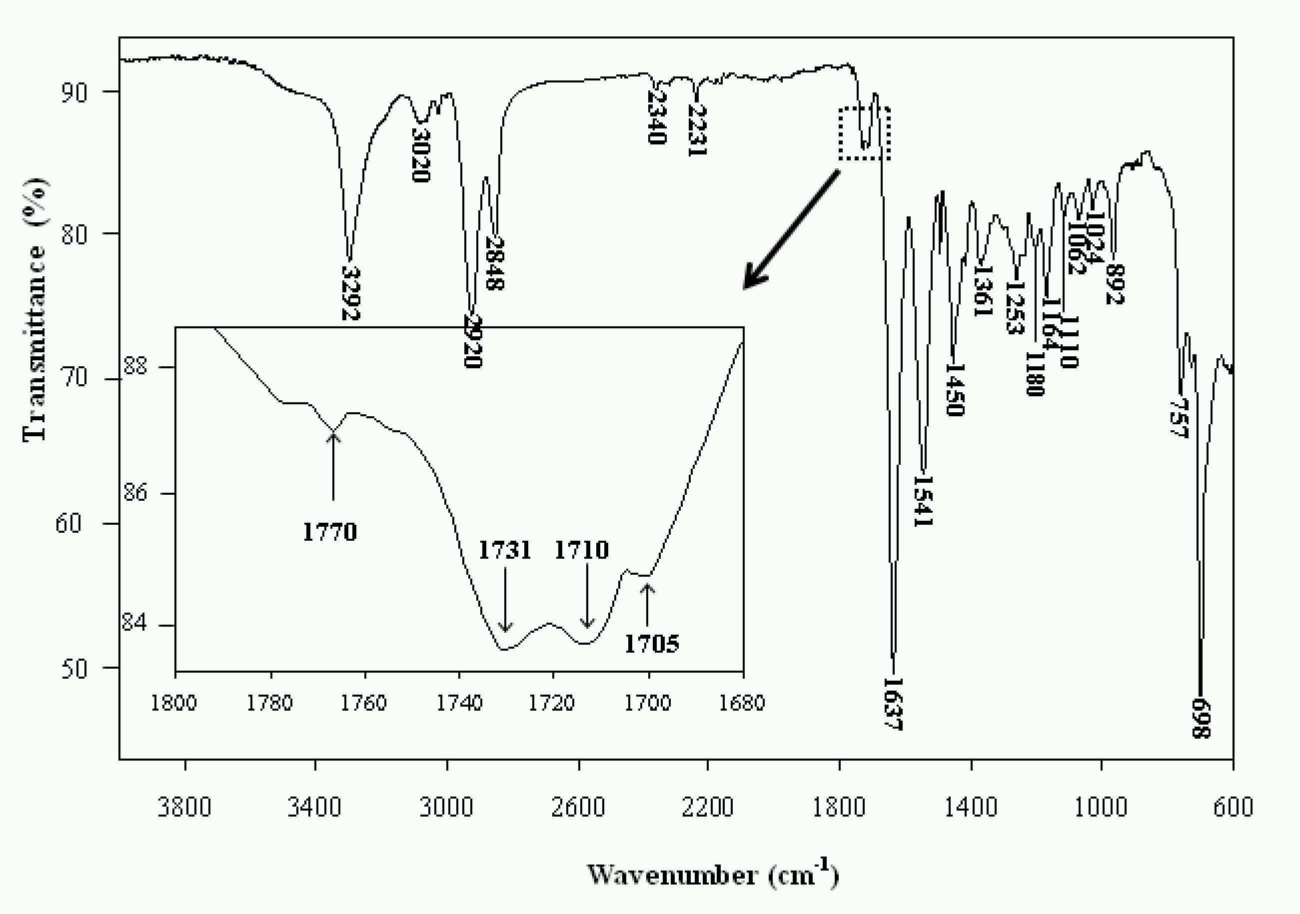

Figure 4.7 ATR-FTIR spectrum of 50/50/10-EnBACO-MAH

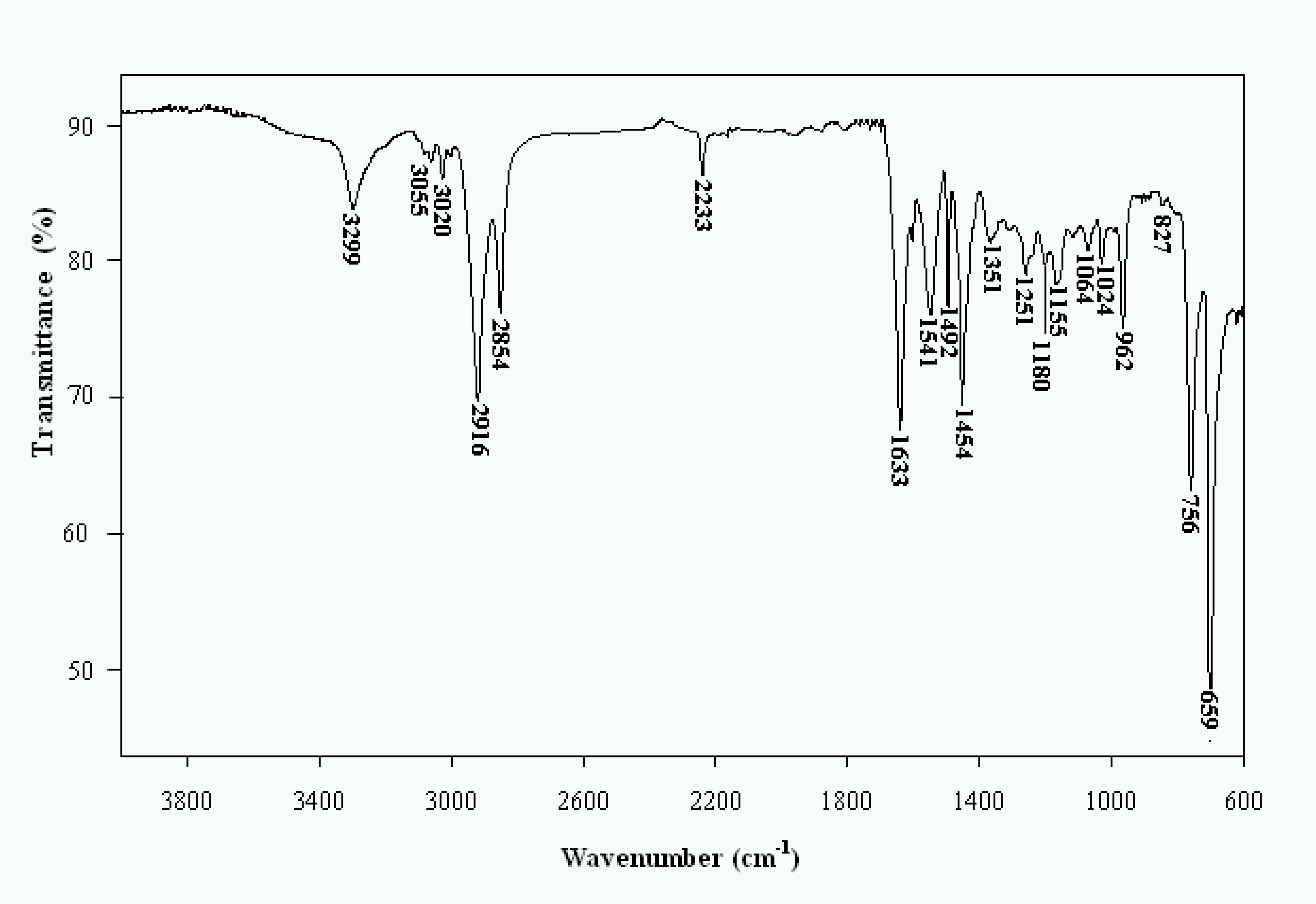

Figure 4.8 ATR-FTIR spectrum of 50/50/10-EMA-GMA

4.1.1.2 Blend Morphologies

The morphologies of ABS/PA6/5%Compatibilizer blend system were examined in terms of blend ratio and compatibilizer type. The SEM micrographs of 80/20/5 blend system as a function of compatibilizer type can be observed in Figure 4.9 (a), (b) and (c), and corresponding distributions of dispersed phase apparent diameters are shown in Figure 4.10. The continuous phase is ABS and the dispersed phase is PA6. The black holes seen in the micrographs are the vacancies left after the removal of PA6 by formic acid extraction. The irregular, coarse ($(d_{app})_{avg}$= 10.1 μ), non-elliptical dispersed morphology of PA6 in ABS matrix in the absence of compatibilizers became a fine ($(d_{app})_{avg}$ =0.44 μ for EnBACO-MAH and $(d_{app})_{avg}$ =1.04 μ for EMA-GMA), elliptical morphology with the addition of compatibilizers (see Figure 4.9 (a)). Incorporation of the compatibilizer reduces the interfacial tension between ABS/PA6 phases that results in a fine dispersion of PA6 in melt state during preparation of blends. Moreover, the addition of compatibilizers reduces the droplet coalescence rates because of steric repulsion [178-180]; therefore, finely dispersed phase morphology with relatively small particles can be obtained in the presence of effective compatibilizers. The SEM micrographs show that EnBACO-MAH has a higher compatibilization capability than EMA-GMA for ABS/PA6 system taking into account the sizes of the dispersed PA6 domains are concerned.

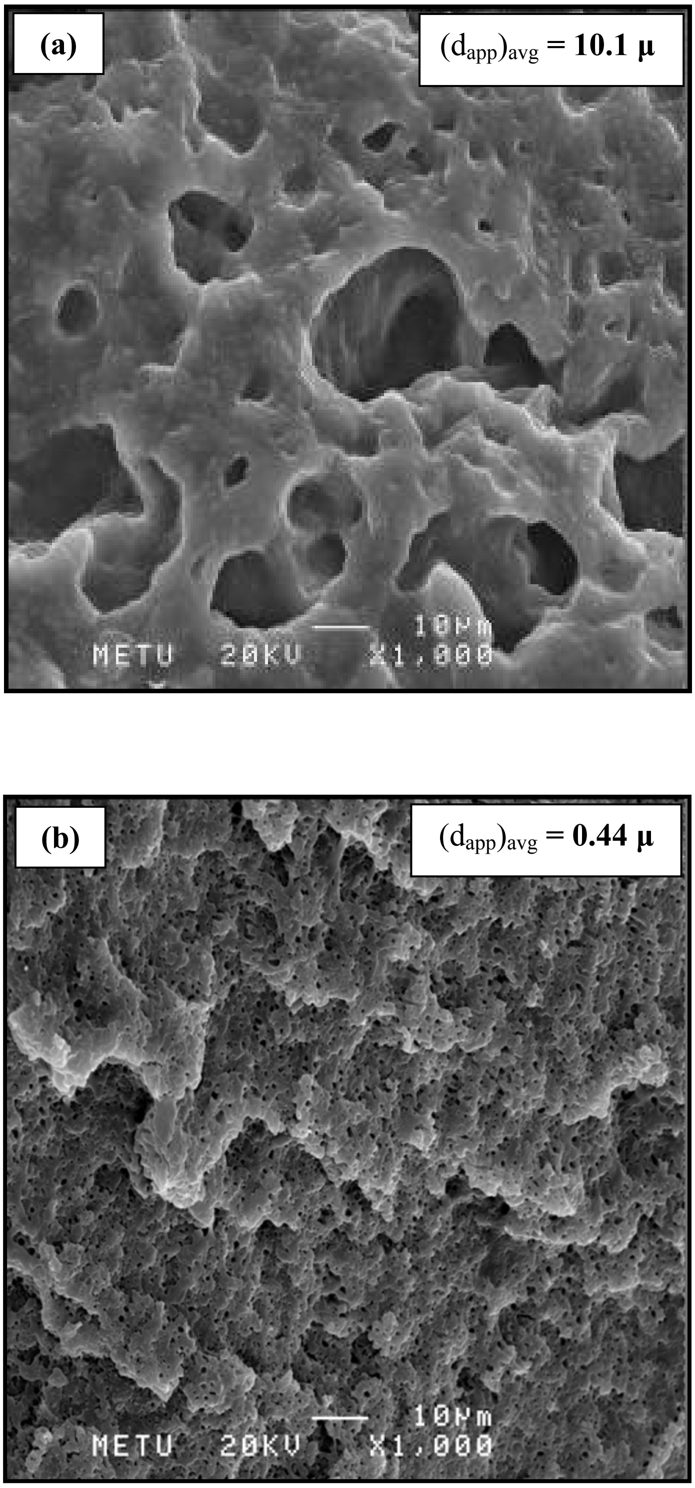

Figure 4.9 SEM micrographs (x 1000) of compatibilized and incompatibilized blends containing 80/20/5 (a) No compatibilizer, (b) EnBACO-MAH (PA6 phase was etched with formic acid)

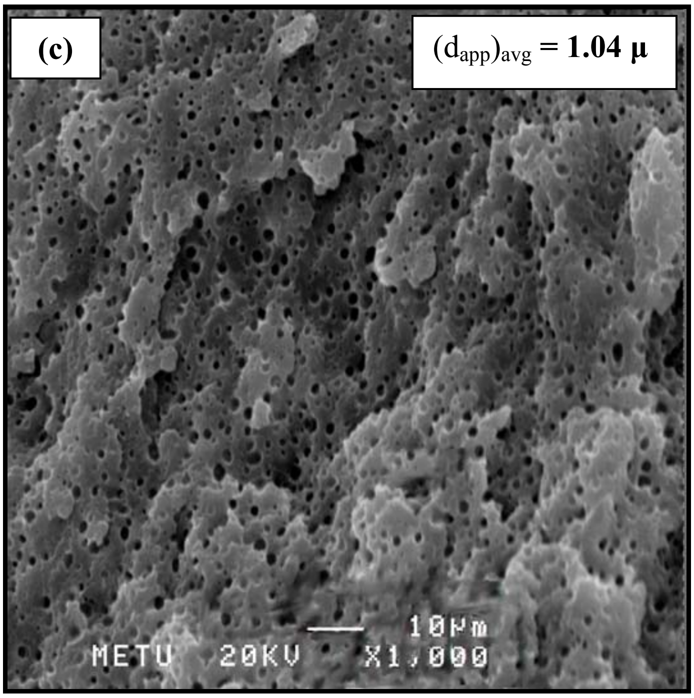

Figure 4.9 (Cont'd) SEM micrographs (x 1000) of compatibilized and incompatibilized blends containing 80/20/5 (c) EMA-GMA (PA6 phase was etched with formic acid)

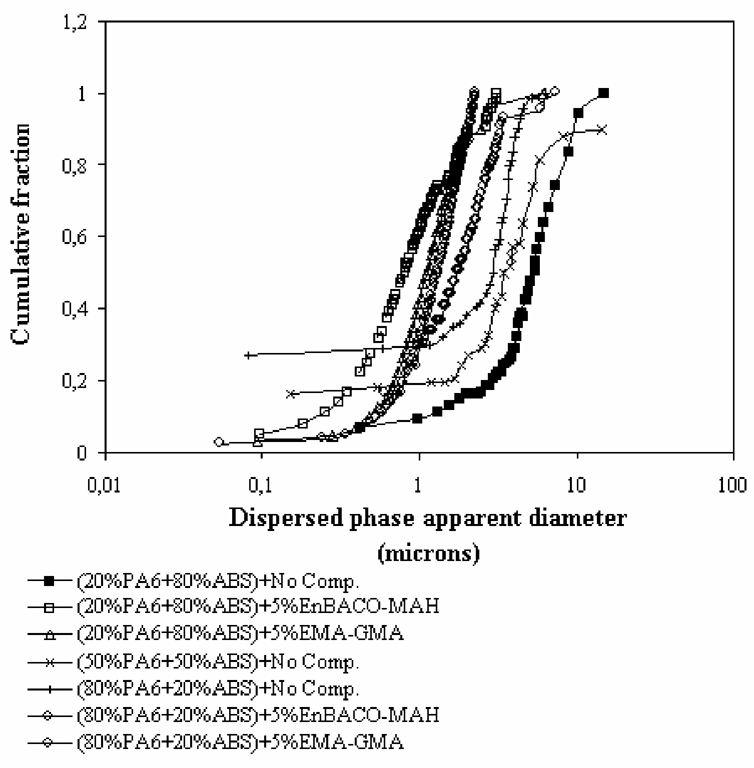

Figure 4.10 Dispersed phase apparent diameter distribution for the compatibilized and incompatibilized ABS/PA6 blend system

The SEM pictures of 50/50/5 system with the two compatibilizers are shown in Figure 4.11 (a), (b) and (c). The holes in the pictures are the vacancies left after the removal of PA6 by formic acid extraction. In the case of no compatibilizer, the discontinuous phase is PA6. This dispersed morphology became co-continuous when compatibilizers were added. The possible reason can be the increased viscosity of PA6 as a result of grafting reactions with the compatibilizers; hence the viscosity ratio of ABS to PA6 becomes close to their volumetric ratio, which is the criterion to obtain co-continuity according to Paul Barlow model [181]. The size of the undulations seen on the surface is different for each compatibilizer type. In the case of EnBACO-MAH, the sizes of the undulations are smaller than that of EMA-GMA.

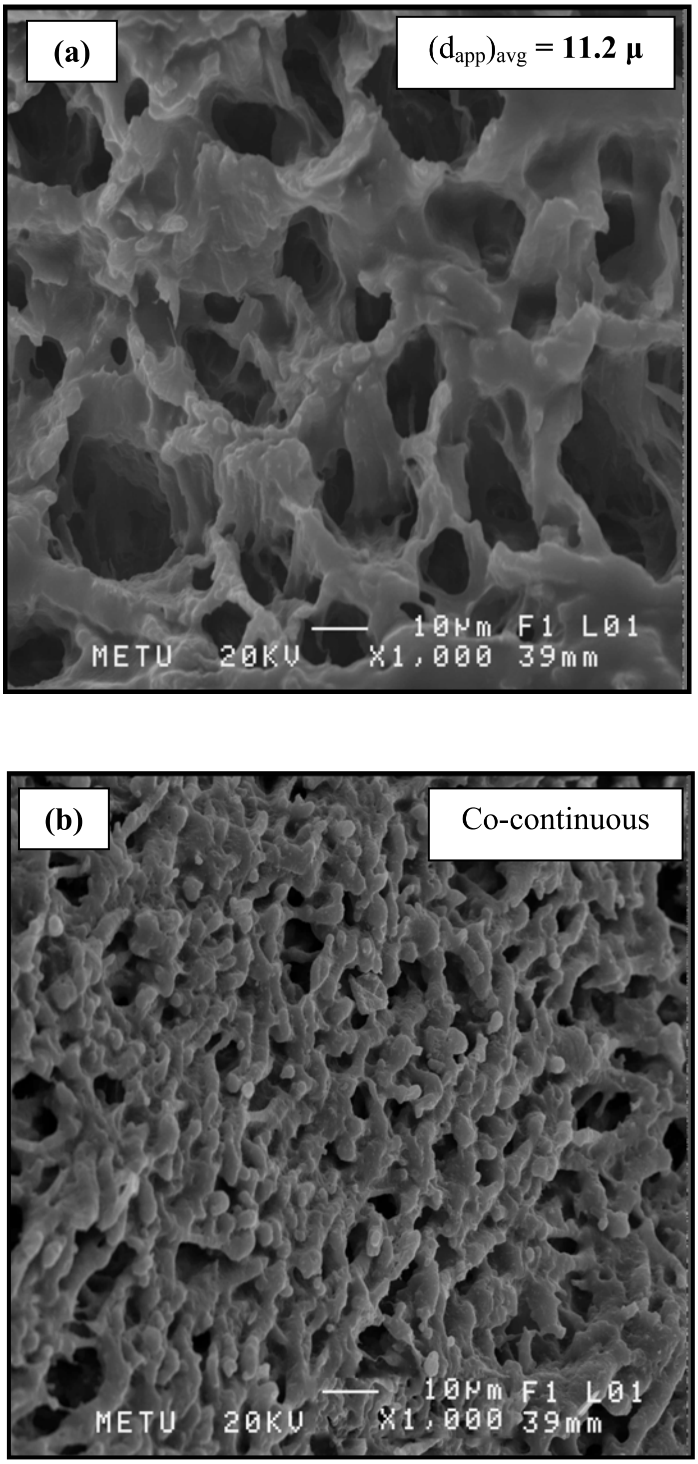

Figure 4.11 SEM micrographs (x 1000) of compatibilized and incompatibilized blends containing 50/50/5 (a) No compatibilizer, (b) E-nBA-MAH (PA6 phase was etched with formic acid)

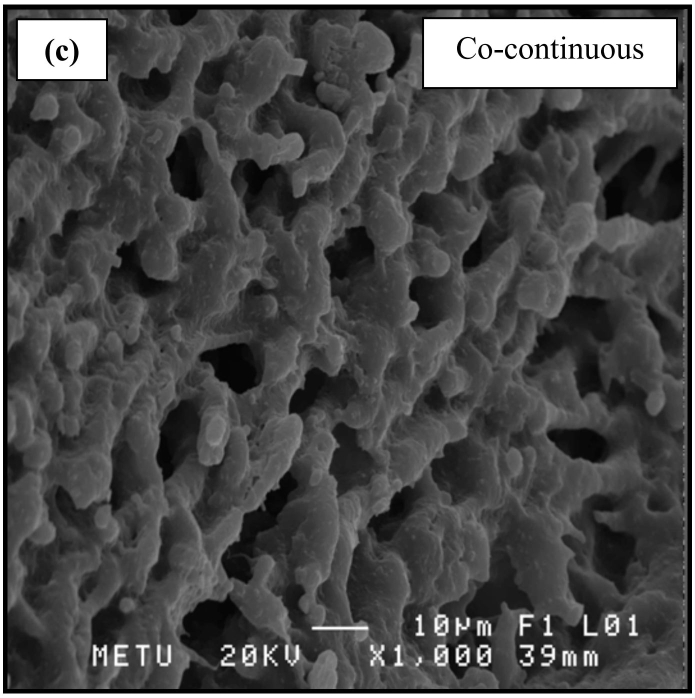

Figure 4.11 (Cont'd) SEM micrographs (x 1000) of compatibilized and incompatibilized blends containing 50/50/5 (c) E-MA-GMA (PA6 phase was etched with formic acid)

For 20/80/5 system, the dispersed ABS domains in the PA6 matrix are seen as black holes left after the removal of ABS by THF extraction (see Figures 4.12 (a), (b) and (c)). The addition of compatibilizers decreased the diameter of ABS domains ($(d_{app})_{avg}$ = 9.97 μ for no compatibilizer, $(d_{app})_{avg}$ = 0.86 μ for EnBACO-MAH and $(d_{app})_{avg}$ = 1.20 μ for EMA-GMA) significantly. The average diameter of the ABS domains in the case of EnBACO-MAH is smaller than that of EMA-GMA.

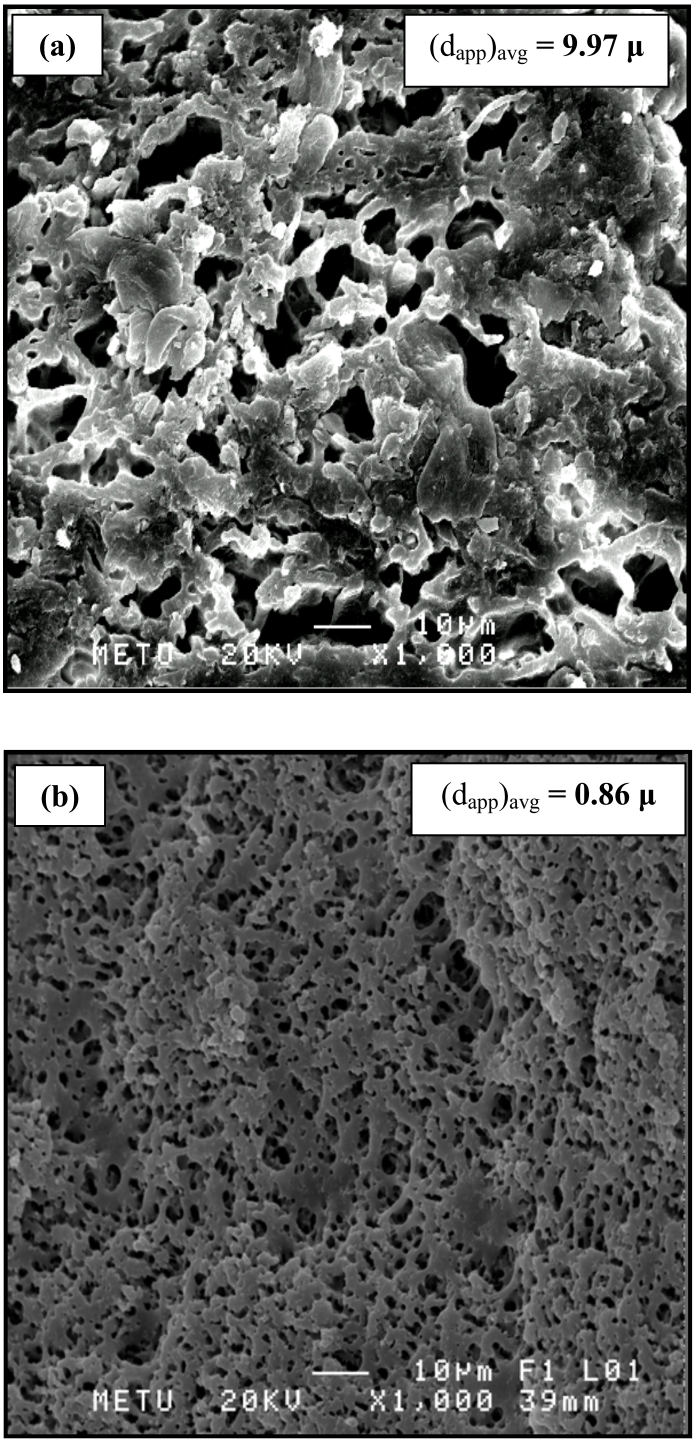

Figure 4.12 SEM micrographs (x 1000) of compatibilized and incompatibilized blends containing 20/80/5 (a) No compatibilizer (b) E-nBA-MAH (ABS phase was etched with THF)

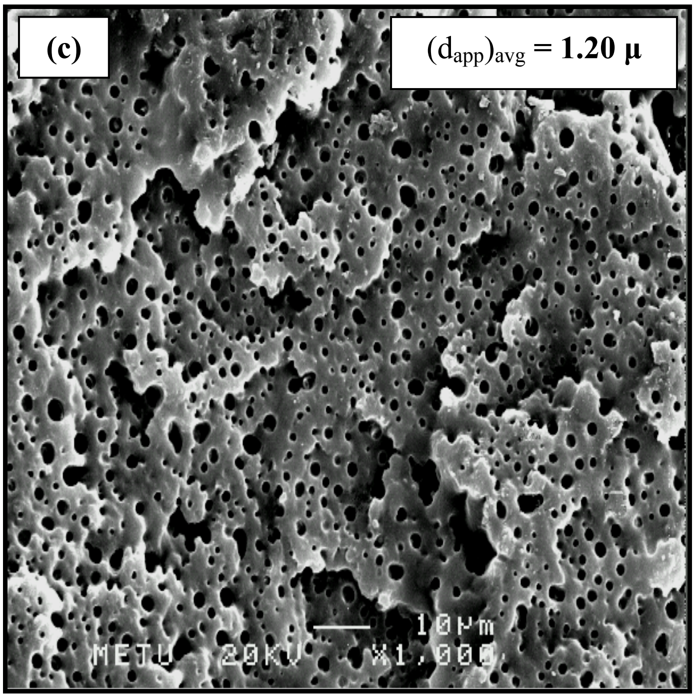

Figure 4.12 (Cont'd) SEM micrographs (x 1000) of compatibilized and incompatibilized blends containing 20/80/5 (c) E-MA-GMA (ABS phase was etched with THF)

When the compatibilization efficiency of these two olefin based copolymers were compared, EnBACO-MAH seemed to be more effective than EMA-GMA copolymer as observed by the smaller dispersed particle apparent diameters of the blend for 80/20 and 20/80 at 5% compatibilizer content. It has been proposed that the final morphology is highly dependent on the topology of grafting [66, 182, 183]. In the case of blends prepared using EMA-GMA, which is difunctional with respect to PA6 (i.e. possible reactions with both amine and acid ends), dense locals of PA6-graft-EMA-GMA with high probability of two point grafting resulting in cross-linking can form in the early stages of extrusion which can hinder further particle break-down in the downstream of extruder [16, 184].

It should also be noted that break-up of the dispersed phase is another process that takes place during melt-compounding which determines the final morphology together with interfacial interactions [184]. It highly depends on the viscosity ratios of matrix. However, in the content of thesis the rheological properties of the materials produced were not measured.

4.1.1.3 Thermal Properties

Differential scanning calorimeter (DSC) was used to examine the melting and crystallization behaviour of the PA6 component in the blends. Melting point (T_m, °C), melting enthalpy (ΔH_f, J/g) and degree of crystallization (X_c, %) were obtained from second heating thermograms and crystallization temperature (T_c) were obtained from cooling thermograms for PA6 phase in the blends. ΔH_f in the second heating thermogram was used for calculation of degree of crystallinity of the PA6 part of the blends using following equation:

$$X_c(\%)=\frac{\Delta H_f}{(F)(\Delta H_f^{\ *})}x100 \tag{4.1}$$

where F is the weight fraction of PA6 in the blend and ΔH_f^* is the extrapolated value of the enthalpy corresponding to the melting of 100% crystalline pure PA6. The DSC thermograms of examined blends are given in Appendix-B.

Table 4.1 shows that, the addition of ABS to the pure PA6 did not affect the melting temperature of the system in the absence of a compatibilizer. However, compatibilized blends exhibited a lower melting temperature with respect to both pure PA6 and incompatibilized 50/50 blend system. Depression in T_m of approximately 2-5°C can be considered as an indication of improved interfacial compatibility of the system with the addition of the compatibilizer [185-188]. Probably the addition of compatibilizers to the ABS/PA6 blends has a negative effect on crystallization of PA6 due to the interfacial interaction and formation of PA6-*graft*-compatibilizer molecules that are less perfect than pure PA6.

Table 4.1 Results of DSC analysis

No	**ABS/PA6/Compatibilizer**	**T_m(°C)**	**ΔH_f (J/g)**	**X_c (%)**	**T_c(°C)**
1	PA6	224.9	65.8	28.6	191.2
2	50/50/No Comp.	224.3	23.4	20.4	187.2
3	50/50/5-EMA-GMA	222.6	22.8	20.9	184.6
4	50/50/10-EMA-GMA	213.9 and 221.6	12.2	11.8	183.5
5	50/50/5-EnBACO-MAH	221.5	22.0	20.1	183.8
6	50/50/10-EnBACO-MAH	214.5 and 220.3	13.2	12.7	182.2
7	80/20/5-EnBACO-MAH	221.3	10.0	22.9	181.8
8	20/80/5-EnBACO-MAH	222.4	36.5	20.8	183.5
9	80/20/5-EMA-GMA	222.4	9.9	22.8	183.2
10	20/80/5-EMA-GMA	222.2	38.4	22.0	183.2

Specific heat of fusion for 100% crystalline PA6 (ΔH_f^*) is 230 J/g [191].

50/50/10-EnBACO-MAH and 50/50/10-EMA-GMA blends exhibited two melting peaks in the second heating thermograms given in Figure 4.13. This result shows that there are two different structures of crystals formed during cooling. At first around 214°C, the major peak shows that the less perfect γ-crystals formed in the cooling step melts. Around 221°C (the minor peak), the more stable α-crystals melt [189]. The small exotherm observed before the major melting peak is the reorganization of the less perfect PA6 crystals. These crystals are the monoclinic γ-crystals of the PA6 [189, 190]. The formation of this structure in the presence of 10% compatibilizer may have resulted from increasing extent of reaction between PA6 and maleic anhydride; so the formation of thermally stable α-crystals is hindered because of this grafting reaction [191, 192]. This phenomenon is also observed from the X_c and T_c, which are lower when compared with other blend systems. The chemical reaction leading to increase in the viscosity of the media can decrease the crystallization rate and crystal growth [191].

The degree of crystallinity of the blends is lower than that of PA6. The presence of the second phase inhibits the crystallization and the crystallization ability of PA6 was detrimentally influenced. This effect can also be observed from T_c values. Addition of the second phase together with a compatibilizer further decreases the crystallization temperature as a result of retardation effect of increasing viscosity due to the compatibilization reactions.

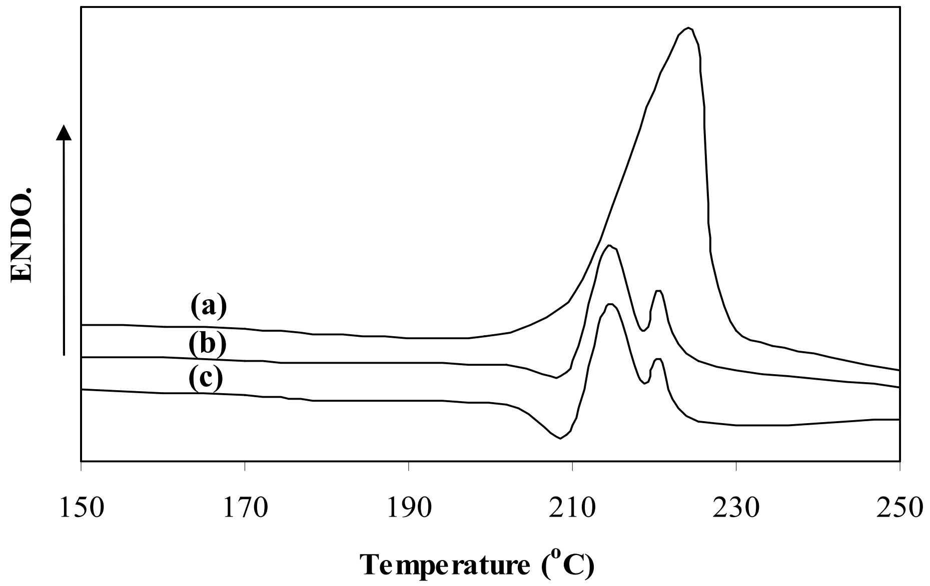

Figure 4.13 Representative thermograms for the melting behaviour of ABS/PA6 blends: (a) 50/50, (b) 50/50/10 EnBACO-MAH, (c) 50/50/10 E-MA-GMA

DMA is used to observe the miscibility of the ABS and PA6 in the presence of the olefin based copolymers. Figure 4.14 shows the DMA curves of some selected blend systems. The peaks at -69.2°C and 110.3°C are the T_gs of the polybutadiene (PB) and poly (styrene-*co*-acrylonitrile) (SAN) phase of ABS, respectively. The T_g peak of PA6 is seen at 34.8°C. When the incompatibilized 50/50 blend system is considered, it is seen that the T_g's of the PB and SAN phase of ABS and PA6 are not shifted. If the phases are immiscible, they exhibit their own T_g after blending [192]. When the compatibilizers were incorporated to the system, the T_g of both SAN and PA6 phases were shifted to the lower values probably due to the lower T_g values of the PA6-g-Compatibilizer molecules. This shows the partial miscibility of phases within each other by the addition of the compatibilizer. With the addition of the compatibilizers, the damping peaks are broadened, and this can be ascribed to the increased length of the interfacial region, probably due to the formation of PA6-

g-Compatibilizer at the interphase [193]. There is no significant effect of the compatibilizer type, compatibilizer content and blend composition in DMA curves.

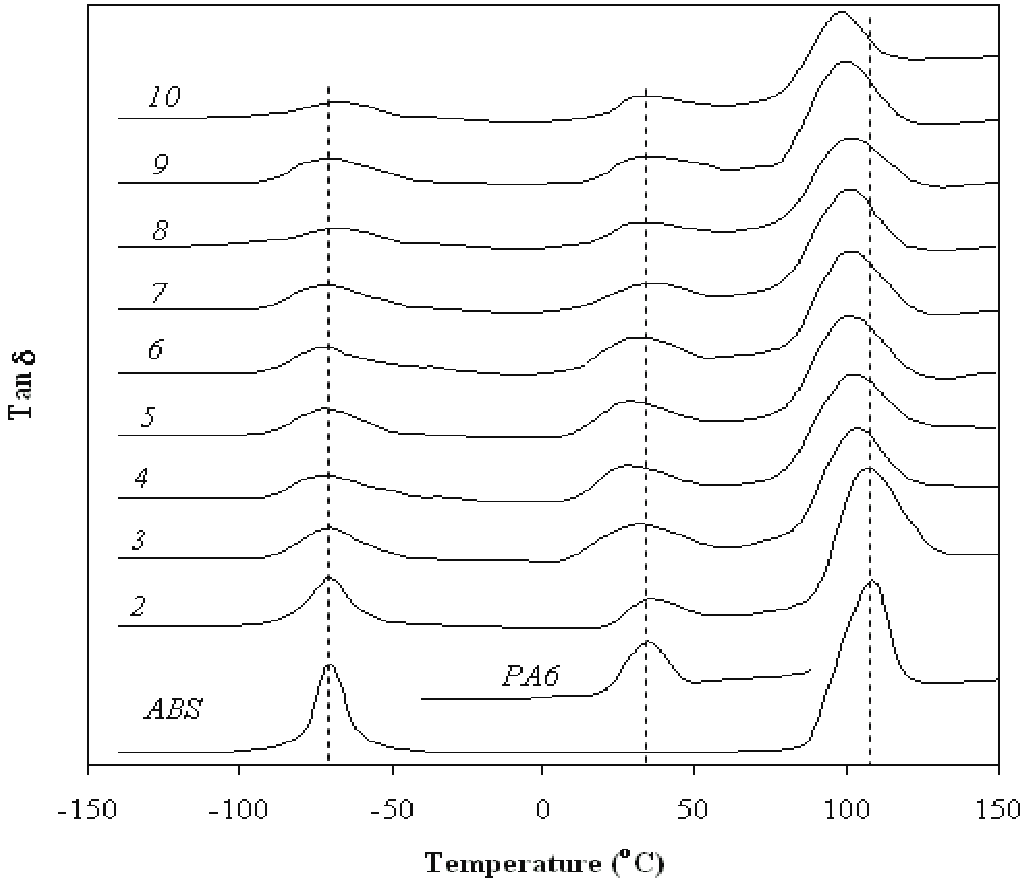

Figure 4.14 Representative Tan δ curves for the blends obtained from DMA analysis (the numbers correspond to the blend system given in Table 4.1)

4.1.1.4 Mechanical Properties

Figure 4.15 shows the variation of yield strength with respect to PA6 and compatibilizer content. In the absence of compatibilizers, an increasing trend is observed after 50% PA6 content. The compatibilized blends containing 80% PA6 have higher strength values compared to other blends due to the continuous PA6 phase. The blends of 20% and 50% PA6 compatibilized with 5% olefinic polymer have higher yield strength values than that of incompatibilized ones owing to the improved adhesion at the interface because of the possible reactions mentioned above. However, the blends of 20% and 50% PA6 compatibilized with 10% olefinic polymer have lower yield strengths. Below the saturation level of compatibilizer, the bonded molecules are located in the interfacial area between the dispersed phase and matrix. When saturation level is exceeded, the compatibilizer forms a weak boundary layer between the ABS and PA6 phases resulting in low yield strength values. Thus, only required amount of compatibilizer is used to improve the miscibility of the components [194]. For the blends containing 80% PA6, the incompatibilized blends exhibit higher yield strengths. When all the yield strength data of tertiary blends are concerned, the strength values measured can not exceed that of neat-PA6 and all of them are greater than the yield strength of neat-ABS.

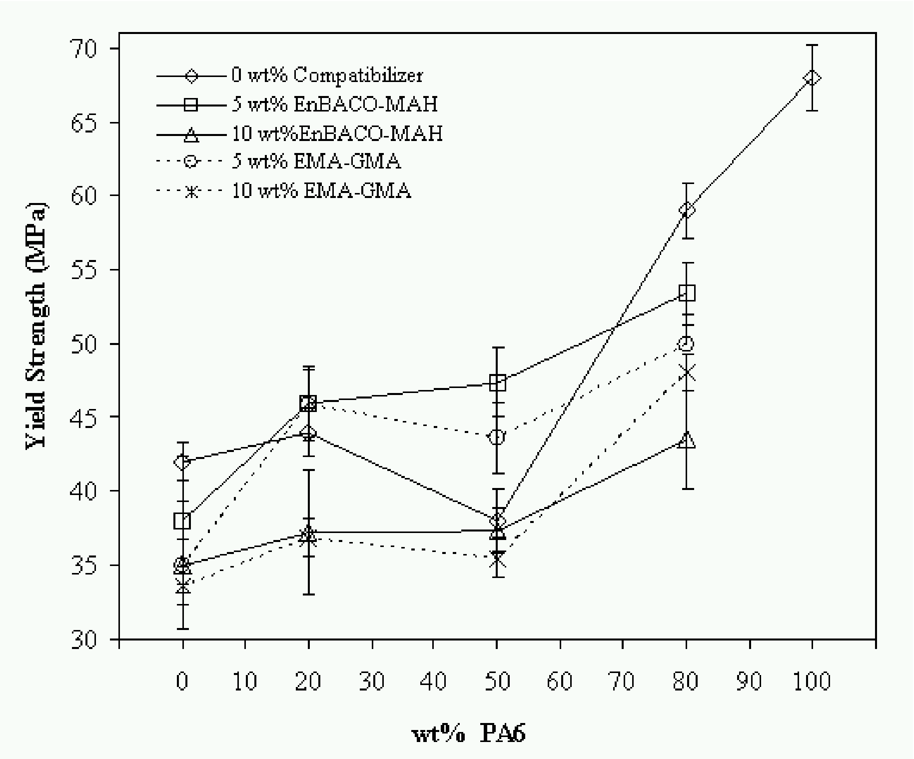

Figure 4.15 Variation of yield strength with respect to PA6 concentration and compatibilizer content

Variation of strain at break values with respect to PA6 concentration and compatibilizer content can be seen in Figure 4.16. It is observed that the strain at break values of blends increases with the increasing amount of PA6 after 50% of PA6 because of the continuity of PA6 phase. Incompatibilized blends showed the lowest strain at break values when compared with the compatibilized ones and exhibit more brittle behavior during tensile testing. When the strain at break values of blends compatibilized with EMA-GMA are considered, as EMA-GMA concentration decreases strain at break values increases after 50% PA6 concentration. With EnBACO-MAH both at 5% and 10% levels, the strain at break values are larger than 100% above 50% PA6 level.

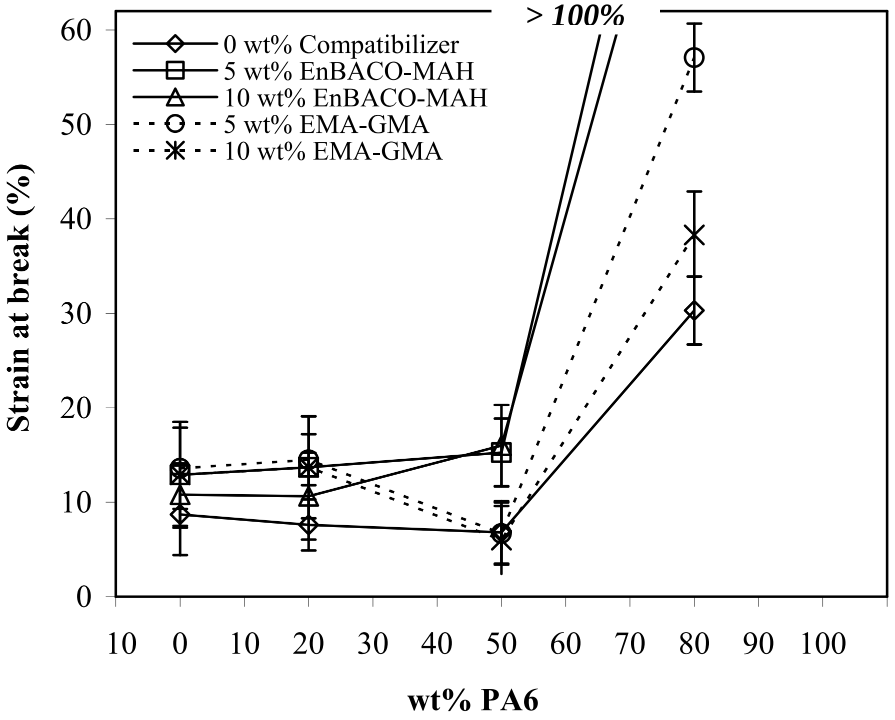

Figure 4.16 Variation of strain at break with respect to PA6 concentration and compatibilizer content

The failure behavior of the blends showed differences. The photograph of some selected tensile specimens after testing is shown in Figure 4.17. It is observed that in the absence of olefin based compatibilizers, blends with 20% and 50% PA6 failed in brittle manner without neck formation. Stress whitening, which is due to the light scattering from crazes in the matrix or cavities in the dispersed phase, can be observed. Even in the presence of compatibilizers, for the blends containing 20% PA6 exhibited brittle failure despite relatively higher elongation. The compatibilized blends containing 50% PA6 underwent necking and failed in ductile manner. When the continuous phase is PA6 (for blends containing 80%PA6), the specimens again deformed by neck formation, but this case after necking they underwent strain-hardening at the end of the tests which resulted in an increase in measured ultimate stresses.

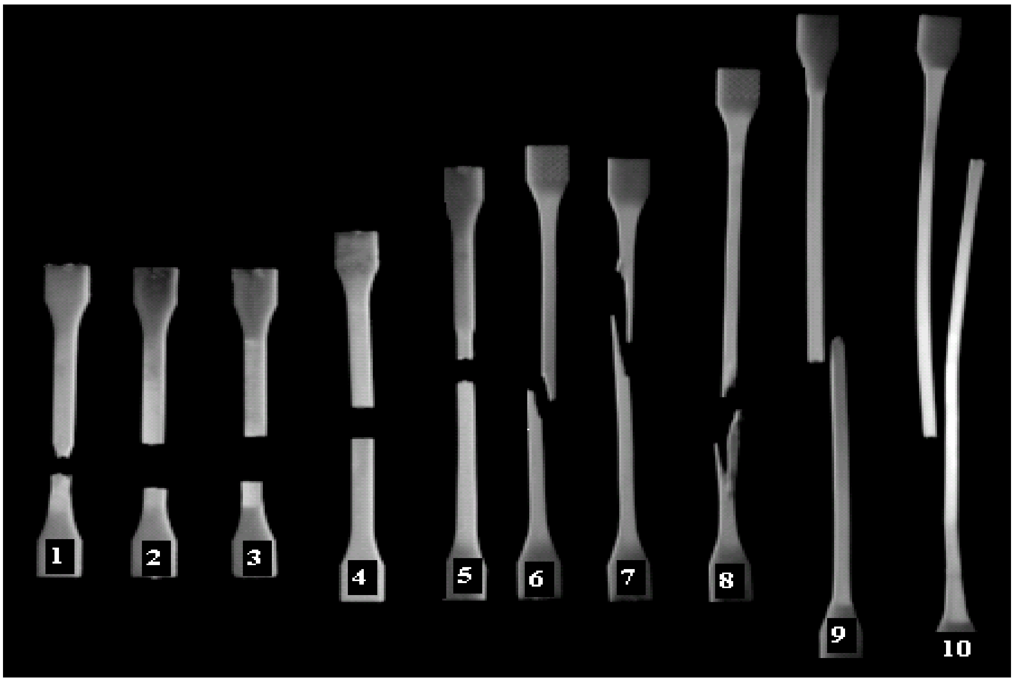

Figure 4.17 Selected tensile specimens after testing (numbers correspond to the numbers given in Table 4.1)

When the impact strength of blends are concerned, the incompatibilized blend exhibits decreasing trend in impact strength values, which can be observed in Figure 4.18 due to the coarse dispersed phase morphology seen in SEM micrographs. The incorporation of compatibilizers results in more than 4-fold of improvement. The impact strength of compatibilized blends increases as PA6 concentration increases up to 50% PA6. A maximum is obtained around 50% PA6 concentration regardless of the type and amount of compatibilizer possibility due to the co-continuous morphology of the blend. Such kind of impact modification was reported in the literature for the co-continuous polyoxymethylene/polyurethane blends. It was reported that an intermeshed network-like structure gave super-tough material; whereas distributed rubber particles resulted in more than 4-fold lower Izod impact strengths [195, 196].

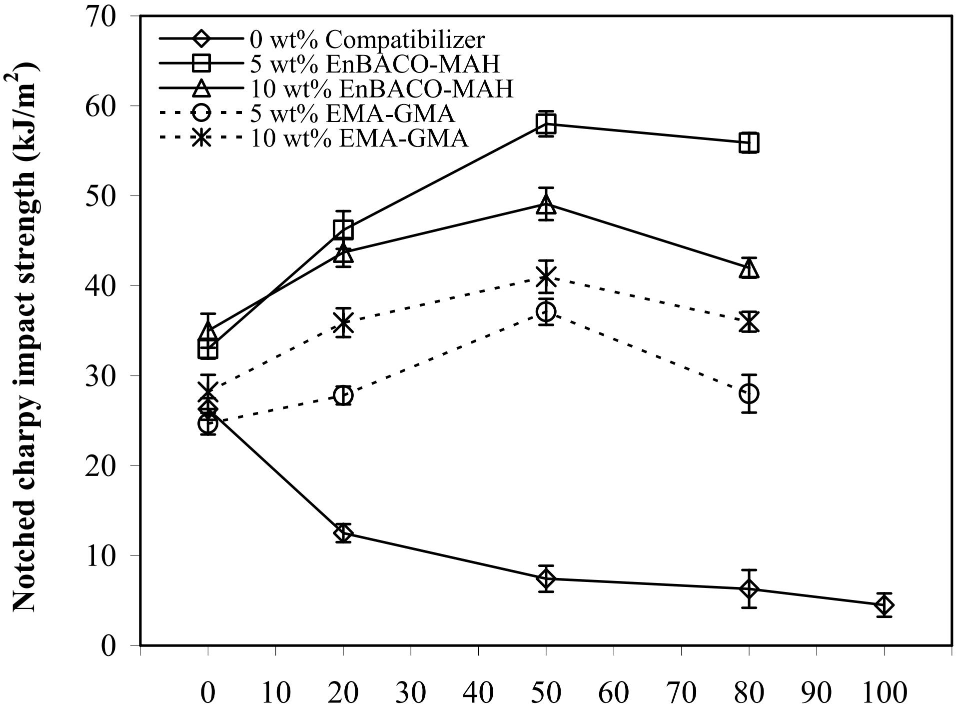

Figure 4.18 Variation of impact strength with respect to PA6 concentration and compatibilizer content

The impact strength of the polymer blends is highly dependent on the size and dispersion of the second phase. There are two reasons why the dispersed particles in the matrix give higher toughness: the cavitation and hence changing the stress state around the particles and to generate a local stress concentration, and the subsequent shear yielding of matrix [70, 197, 198]. However, the cavitated particle should not initiate the fracture process; therefore these particles have to be very small and not to grow to a size which can initiate a crack [195]. In literature, an optimum amount of compatibilizer which can provide fine and well-dispersed blend morphology was studied and the researchers found out that after saturation concentration of compatibilizer is exceeded, the impact properties either decreased or stayed constant [176, 199-201].

In the current study, the compatibilizers used can act as tougheners because of their elastomeric nature with low glass transition temperature. For a given PA6 content, the impact strength of the blends compatibilized with EnBACO-MAH gives higher toughness than EMA-GMA due to the finer morphologies obtained in the case of EnBACO-MAH at 5 and 10% loadings. For EnBACO-MAH, tougher blends are obtained at 5% loadings; however for EMA-GMA, tougher blends are obtained at 10% loading level for a given PA6 concentration.

4.1.2 Impact Essential Work of Fracture Toughness of Compatibilized ABS/PA6 Blends

In this part of the study, it was aimed to investigate the impact fracture behaviour of compatibilized ABS/PA6/Compatibilizer blends applying impact essential work of fracture methodology as a function of ABS to PA6 ratio and compatibilizer type.

The fracture energy data revealed from standard Izod and Charpy impact tests are the sum of the any kind of energy which can be absorbed during test. Despite their simplicity and convenience, they do not provide any general representation of the toughness of the samples. Since the notches are not sharp enough in standard tests, some ductile polymers do not completely break into two halves at the end of the test, which results in an incomplete fracture. In such cases, EWF concept can be utilized as an effective method for the determination of fracture toughness of ductile polymers having sharp cracks that deformed at high rates. During EWF testing, all the samples were broken into two halves except 20/80/5 blend system regardless of compatibilizer type. In these compositions, a thin film layer formed as skin-layer hindered specimens to completely part into two. Thus, the impact energy measured also included the toss energy (work done to throw the sample) of these samples. However, it was thought that the toss energy (~0.01 J) is very small compared to overall energy, therefore it was neglected.

To check if the yielding criterion was satisfied, the impact test was stopped just after the hammer stroke to the specimen. Visual inspection of the specimen indicated that crack propagated before the completion of the fully-yielding of the ligament. A representative photograph of one of the specimens is shown in Figure 4.19. This means that criterion was not satisfied. However, even in the presence of dissatisfaction in yielding criterion of EWF, Paul and co-workers demonstrated applicability of EWF methodology using a different notation given in Equation (2.28) [161].

The geometry of the stress-whitened zone formed during impact testing was investigated, since Mai and co-workers have noted that in order to achieve a linear relationship between the specific fracture energy and ligament length, the volume of the stress-whitened zone must scale with the square of the ligament length [141, 142]. The shape of the stress whitened zones was schematically represented in Figure 4.20. It is seen that the volume shown has an elliptical-base, whose volume is given as follows:

$$V = \frac{\pi}{2} s\ell t = \beta \ell^2 t \qquad (4.2)$$

where s and ℓ corresponds to radii of ellipse, $\beta = (\pi / 2)(s / \ell)$ is a constant [141]. This shows that the volume of the stress whitened zone was proportional to square of the ligament length.

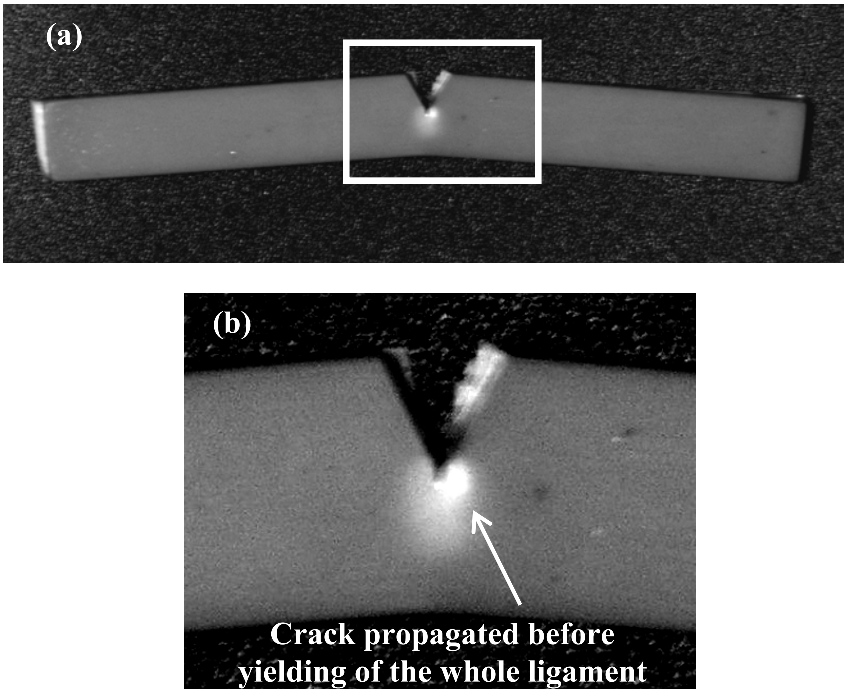

Figure 4.19 Representative image of deformation of the specimen

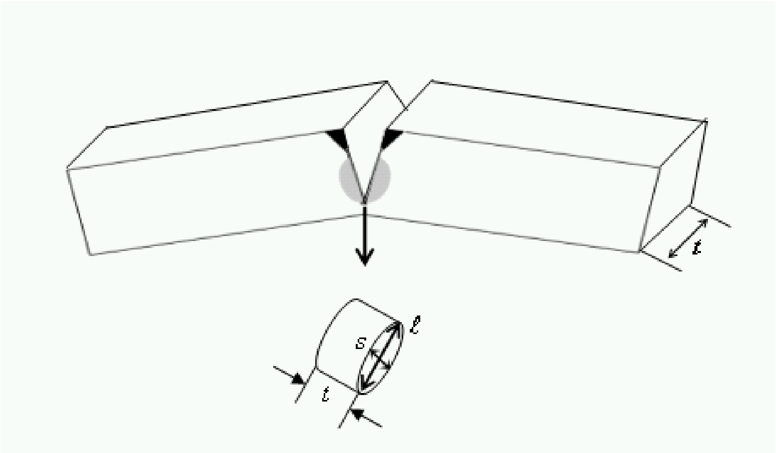

Figure 4.20 Illustration of geometry of stress whitening zone

Figure 4.21 shows representative impact load-displacement curves for 50/50/5-EnBACO-MAH, 50/50/5-EMA-GMA and incompatibilized 50/50/5 blend system. The maximum force values measured during EWF tests were nearly the same; however, for 50/50/5-EnBACO-MAH, the area under the curve prior to maximum force and after maximum force was much higher than that of 50/50/5-EMA-GMA indicating that crack propagation is slow with higher energy absorption associated with toughness. This kind of behaviour is typical for ductile materials [203]. In contrast, incompatibilized blends of 50/50 exhibited a load peak, and then the load dropped to zero (even below zero) very sharp indicating fast crack propagation without any energy absorption. This type of load versus displacement characteristic indicates brittle failure [203].

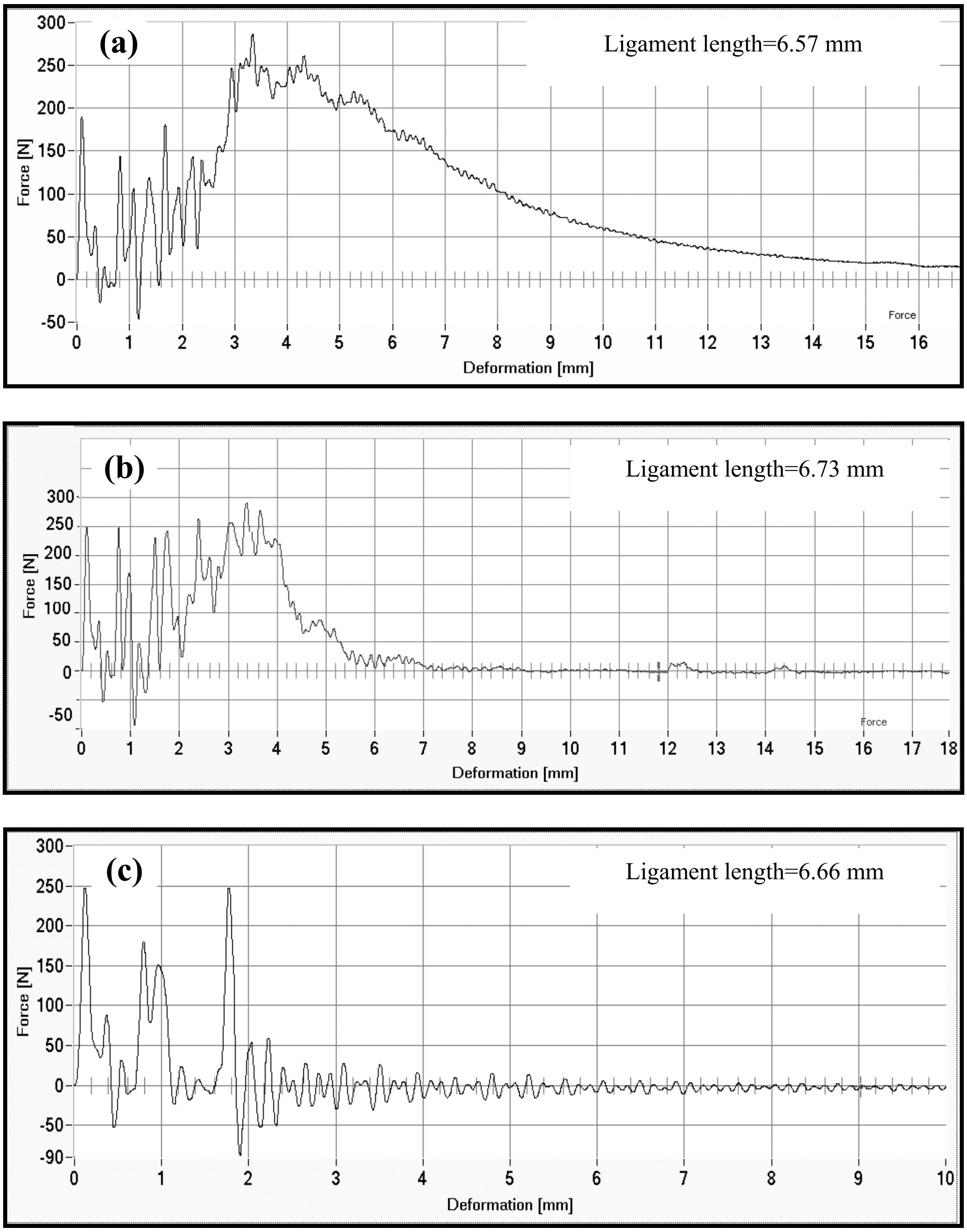

Figure 4.21 Force versus displacement for a.) 50/50/5-EnBACO-MAH b.) 50/50/5-EMA-GMA c.) incompatibilized 50/50

According to EWF methodology, the slopes of plots of total specific fracture energy versus ligament length are regarded as a measure of energy absorbing process that occur far away from the fracture surface, i.e. non-essential work in plastic zone. Figure 4.22 a, b and c shows the plots of specific total impact energy versus ligament length for ABS/PA6/Compatibilizer ternary blends. The incompatibilized blends of ABS/PA6 and neat-PA6 exhibited brittle behavior without showing any slope which is associated with non-essential energy term. As a result of that, no stress whitening was observed for PA6 (see Figure 4.23). On the other hand, ABS showed ductile fracture with a positive slope indicating energy absorption in the outer plastic zone due to the presence of rubbery phase [146, 204] with considerable stress whitening as seen from Figure 4.23. Regardless of compatibilizer type and blend composition, the ABS/PA6/Compatibilizer ternary blends fractured in a ductile manner with steep positive slope indicating non-essential work done in the outer plastic zone. The good linear regression lines seen in ABS, PA6 and incompatibilized blends was distorted, and the data were scattered considerably in the impact energy versus ligament length plots of compatibilized blends (see Figure 4.22 b and c). The photographs of specimens fractured in EWF testing showed evident stress whitening as can be observed from Figure 4.23.

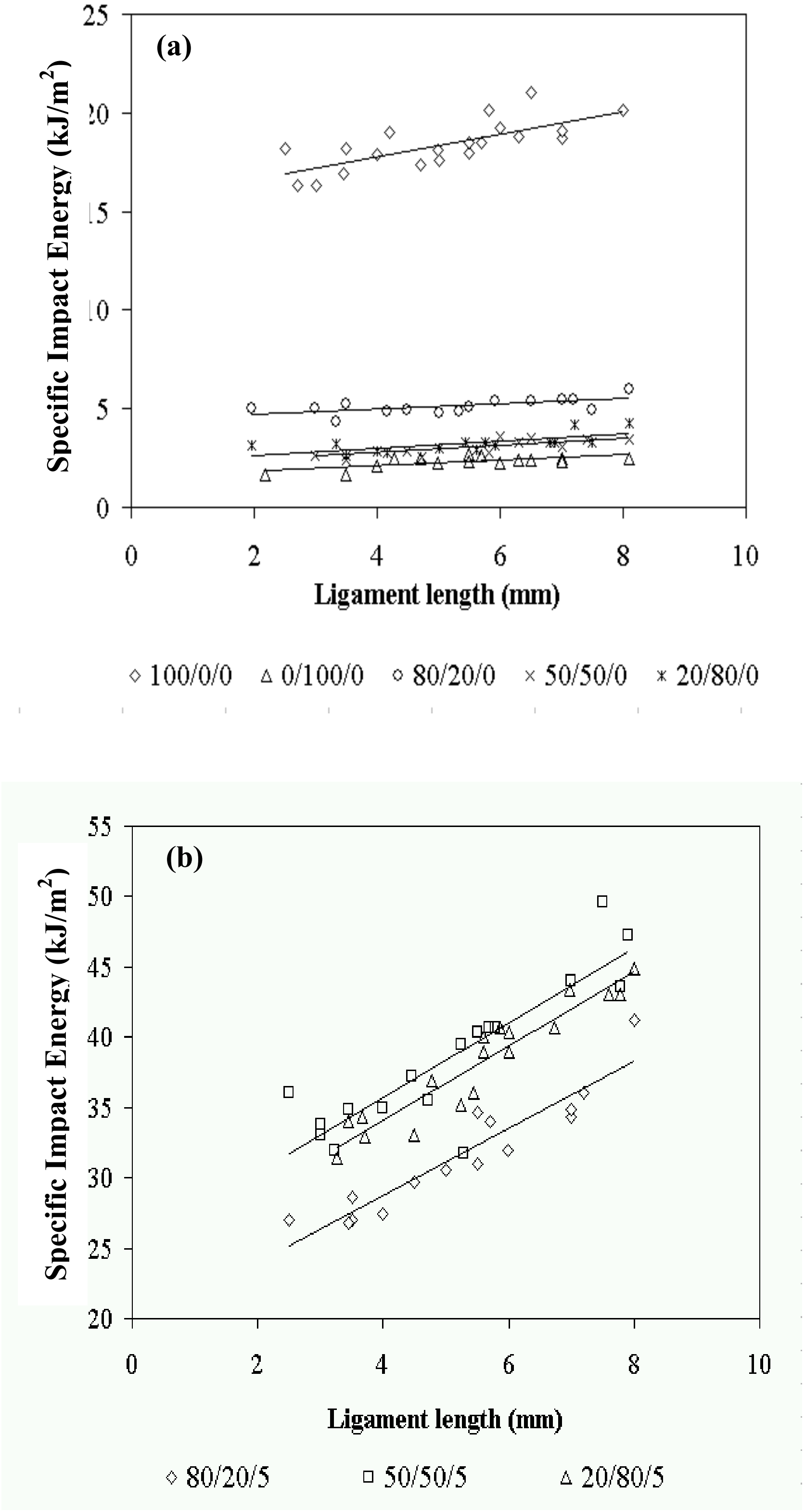

Figure 4.22 Impact energy versus ligament length for a.) Pure ABS, PA6 and uncompatibilized blends, b.) Blends compatibilized with EnBACO-MAH

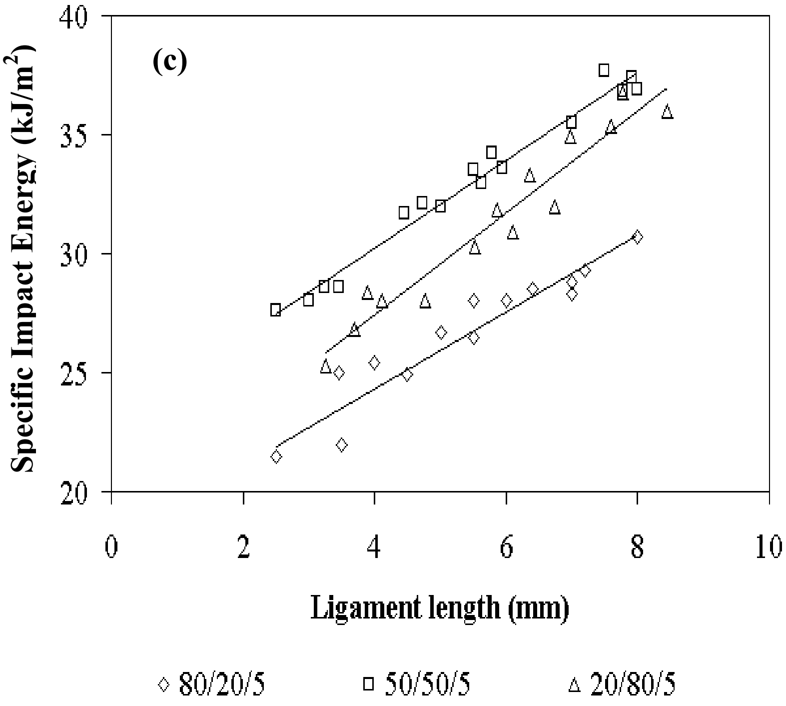

Figure 4.22 (Cont'd) Impact energy versus ligament length for c.) Blends compatibilized with EMA-GMA

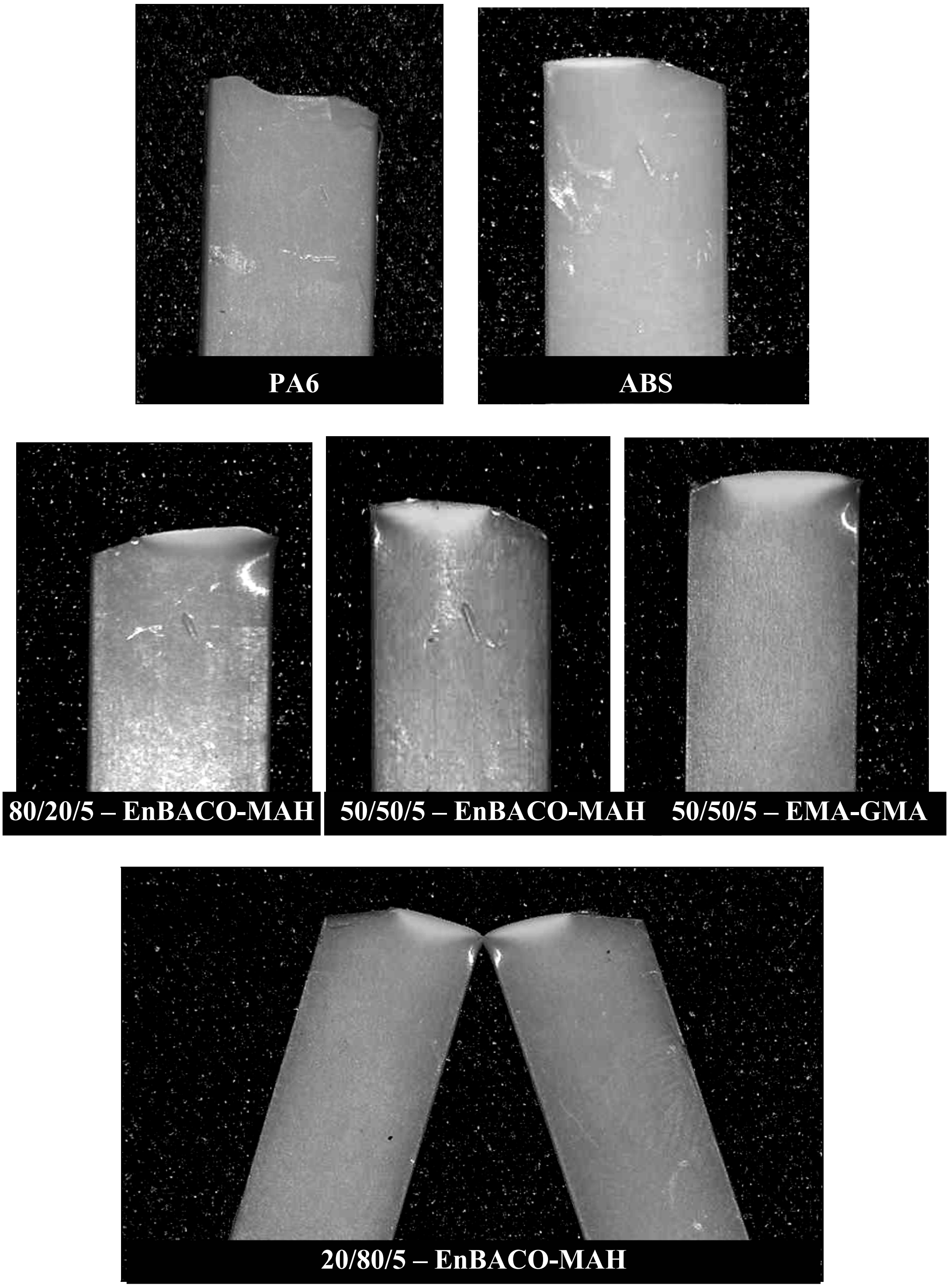

Figure 4.23 Representative broken samples of PA6, ABS compatibilized ABS/PA6 blends

The results of impact EWF testing are shown in Table 4.2 as a function of blend composition and compatibilizer type. The phase morphologies of the blends show variations with respect to composition. The incompatibilized blends exhibit dispersed-particle morphology regardless of composition. For 80/20 and 50/50 blends, ABS is continuous, on the other hand for 20/80, PA6 is continuous phase. Incorporation of compatibilizer alters the morphology of 50/50 blends from dispersed to co-continuous. The details about morphology can be found in previous part. Figure 4.24 shows the PA6 content versus w_e and βw_p for ABS/PA6/Compatibilizer blends. As can be seen, essential work increases with increasing PA6 content by giving a maximum at 50% PA6, then it decreases for both of the compatibilizers; on the other hand, non-essential term slightly increases at 50% PA6, regardless of compatibilizer type.

Table 4.2 Impact-specific EWF values, average dispersed phase particle size and standards Charpy impact strengths of materials

Material (ABS/PA6/Comptibilizer)	**Average dispersed phase particle size (μ)**	**Essential work of fracture, w_e (kJ/m^2)**	**Non-essential work of fracture, βw_p (MJ/m^3)**	**Notched Charpy impact strength ASTM D 256 (kJ/m^2)**
100/0/0	N/A	16.30	0.40	23.6
80/20/0	10.1	4.40	0.13	9.0
50/50/0	11.2	2.10	0.16	7.4
20/80/0	9.97	2.30	0.15	6.3
80/20/5- EnBACO-MAH	0.44	19.20	2.37	46.2
50/50/5- EnBACO-MAH	Co-continuous	25.10	2.64	58.0
20/80/5- EnBACO-MAH	0.86	21.10	2.22	55.9
80/20/5- EMA-GMA	1.04	17.90	1.64	25.9
50/50/5- EMA-GMA	Co-continuous	23.00	1.77	42.1
20/80/5- EMA-GMA	1.20	15.60	1.69	28.6
0/100/0	N/A	1.53	0.14	4.3

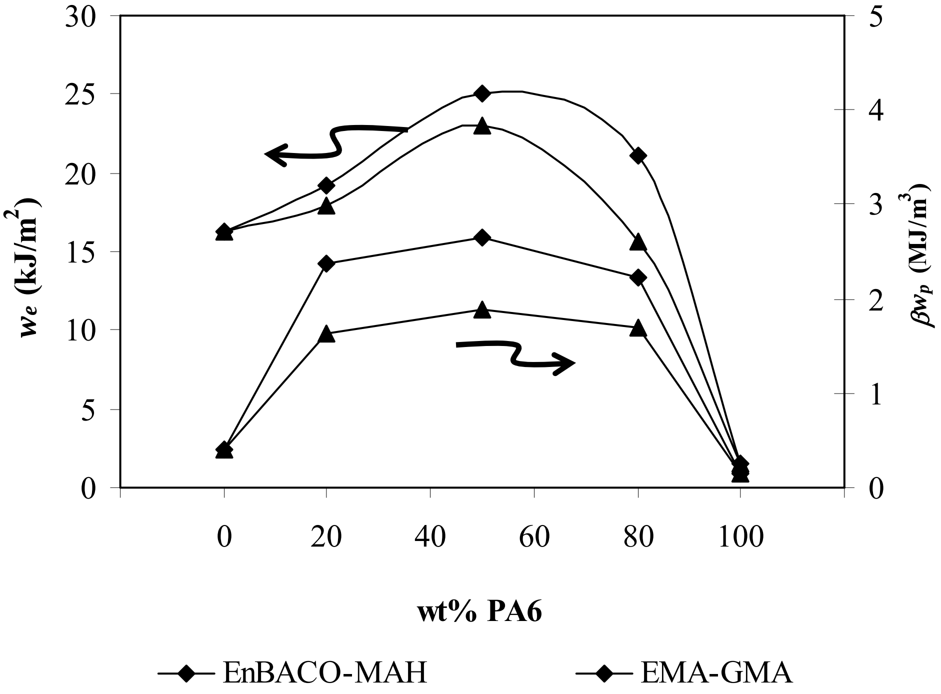

Figure 4.24 w_e and βw_p versus PA6 content

When two compatibilizers are compared, both essential and non-essential terms are higher in EnBACO-MAH than in EMA-GMA. It should be noted that the dispersed particle sizes are much smaller in EnBACO-MAH than those of EMA-GMA, as can be seen from Table 4.2. The study conducted by Huang and Paul showed that at a given rubber content, maxima were observed in both essential and non-essential terms (limiting and dissipative part, respectively). Beyond these maxima, further increase in rubber particle size reduced the essential and non-essential terms [205]. This phenomenon was also previously demonstrated elsewhere [206, 207].

The standard Charpy impact test results show similar trend in essential work of fracture depending on PA6 content (see Table 4.2). Strength of the materials increased with PA6 content up to 50/50/5 blend, beyond that it decreased. When the fracture energy values obtained in standard impact tests were compared with EWF test values, even in the highest ligament lengths, the values of EWF were lower than fracture energies obtained from standard impact test. This may account for the fact that the testing conditions in EWF are severe due to much sharper notches.

The difference in EWF parameters i.e. essential and non-essential terms as the function of blend composition stem from difference in deformation mechanisms for PA6, ABS, incompatibilized binary ABS/PA6 blends and compatibilized ternary ABS/PA6/Compatibilizer. Neat-PA6 exhibits ductile behaviour without a notch. Once a sharp notch is introduced, due to the preclusion of shear yielding by stress field ahead of the crack tip, PA6 fails in brittle manner [70]. On the other hand, the studies conducted on ABS have shown that the macroscopic specimens tend to fail by a combination of shear yielding and crazing of SAN matrix [208-213]. However, the microscopic combination of ABS and PA6, of course, was different than neat-materials.

For rubber-toughened semi-ductile polymers, cavitation of the rubber particles ahead of the crack may release the stresses; as a consequence shear yielding of matrix material resulting in a ductile-failure of the material [70]. Lazerri and Bucknall showed that fractured specimens of rubber toughened polyamides had lines of cavitated rubber particles separated by shear yielded polyamide ligaments and referred to these features as ‘dilational bands’ [123, 214]. Similar observation was also reported by Sue et al. for rubber toughened epoxy. They called these lines of cavitated rubber particles ‘croids’ [215-217]. Laura et. al. [203] and Huang et al. [205] has recently observed similar deformation in rubber toughened polyamides. The particle size also has a crucial importance in toughening mechanism. The crazes are initiated in rubber toughened materials by large particles at equatorial sites where stress concentration is maximum, sometimes subsequently rubber particle can cavitate [70]; therefore, larger rubber particles cavitate easier than smaller particles.

SEM micrograph of ABS, PA6 and incompatibilized 50/50 ABS/PA6 blend system are shown in Figure 4.25 a-c. The fracture surface of ABS is smooth but tortuous. The magnified picture shows black holes left by cavitated rubbery phase of ABS. PA6's fracture surface was smooth and includes large cracks indicating brittle fracture. The incompatibilized blends of ABS/PA6 fractured in brittle manner regardless of blend composition. This behavior can be attributed to the too large size of the dispersed phases for effective toughening.

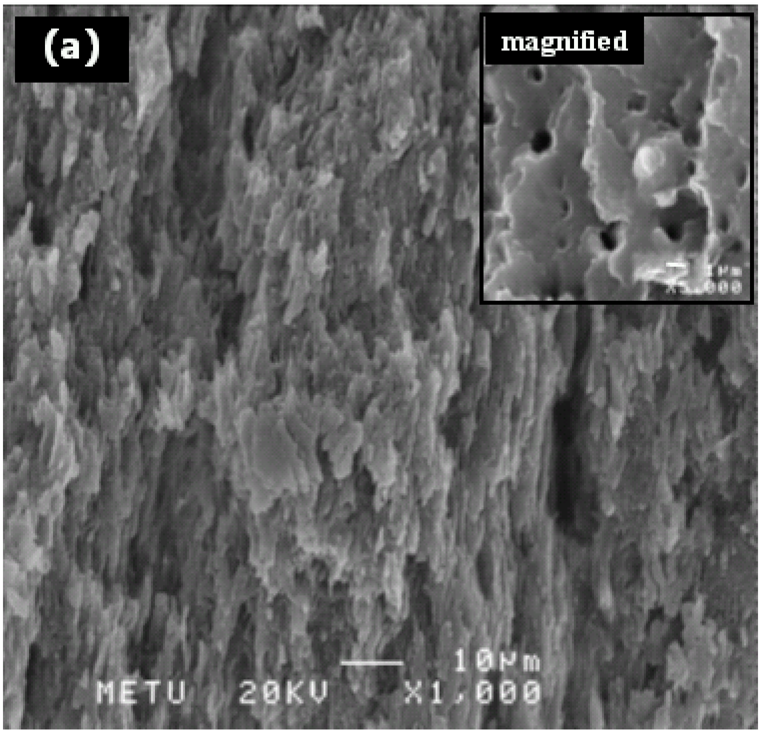

Figure 4.25 SEM micrographs of fracture surfaces of a.)ABS

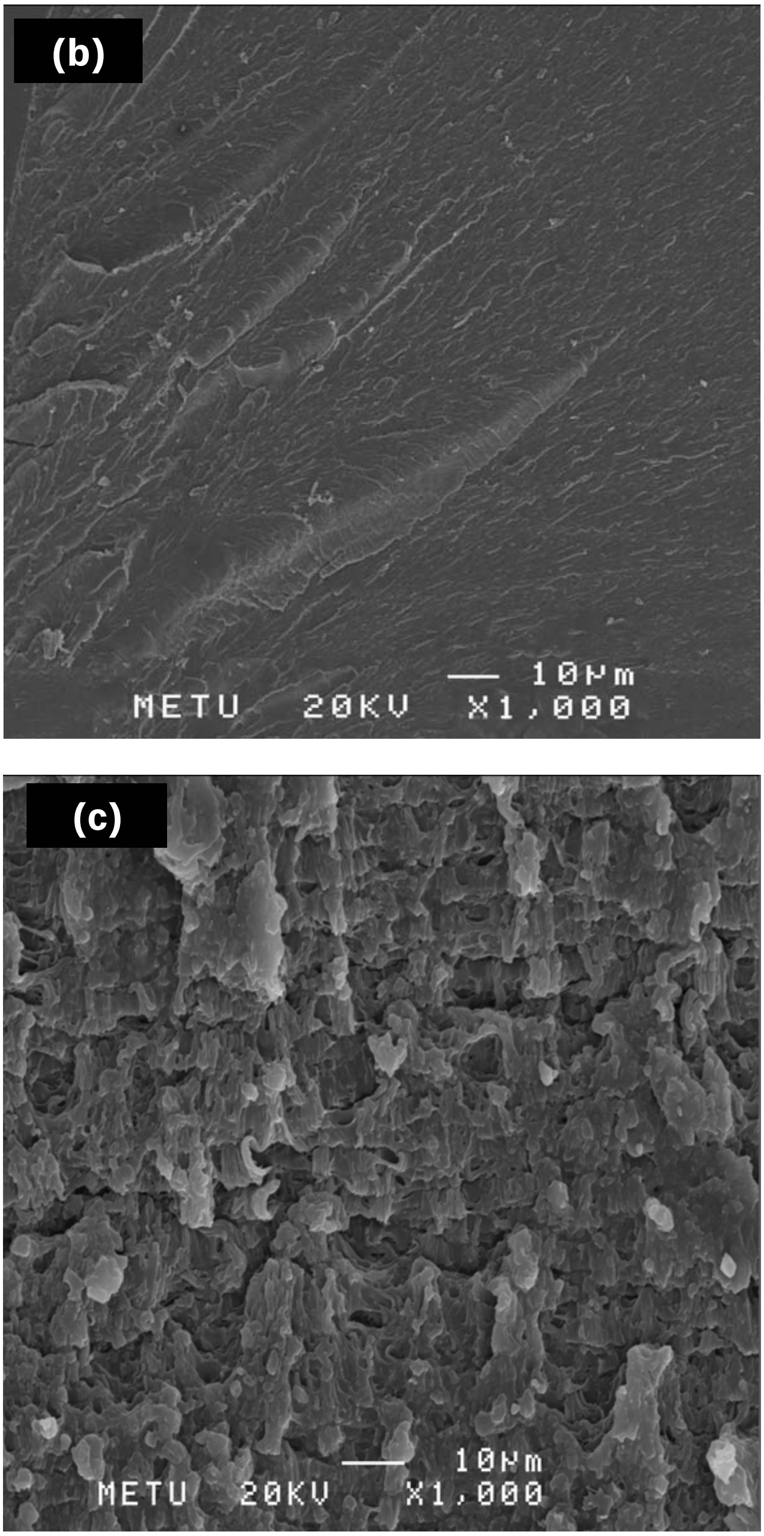

Figure 4.25 (Cont'd) SEM micrographs of fracture surfaces of b.)PA6 and, c.) 50/50/0

SEM micrographs of 80/20/5-EnBACO-MAH and 80/20/5-EMA-GMA blends are shown in Figure 4.26. In this blends, ABS is continuous whereas PA6 is dispersed phase. It is evident that the PA6 particles were pull-out from the ABS matrix. There is no deformation related to shear yielding that can be observed in the matrix phase, apparently due to the higher stiffness of PA6 particles. Besides, the rubbery charecterictic of compatibilizer can also increase the impact strength of material.

The morphology of fracture surface of 50/50/5 blends (see Figure 4.27) is different than that of observed in 80/20/5 blends. The failure is completely ductile. The fibrillar-morphology probably obtained due to the massive shear yielding which is the energy absorbing mechanism. In the case of EMA-GMA, some micro-voids are seen between interconnected ligaments resulting matrix tearing. However in EnBACO-MAH, extent of fibrillation is much higher and the micro-voids are much smaller.

Microstructure of the 20/80/5 blend system resembles traditional rubber-toughened polyamides (see Figure 4.28). The predominant deformation mechanism in these materials was previously reported as rubber particle cavitation and subsequent matrix shear yielding [218, 219]. In the blends considered here, the black holes seen are the locations of rubber particles pulled-out from the matrix, which are surrounded by yielded polyamide ligaments. The shear yielding and particle pull-out co-exists both in EnBACO-MAH and EMA-GMA compatibilizers. These pulled-out particle might be both ABS and compatibilizer domains.

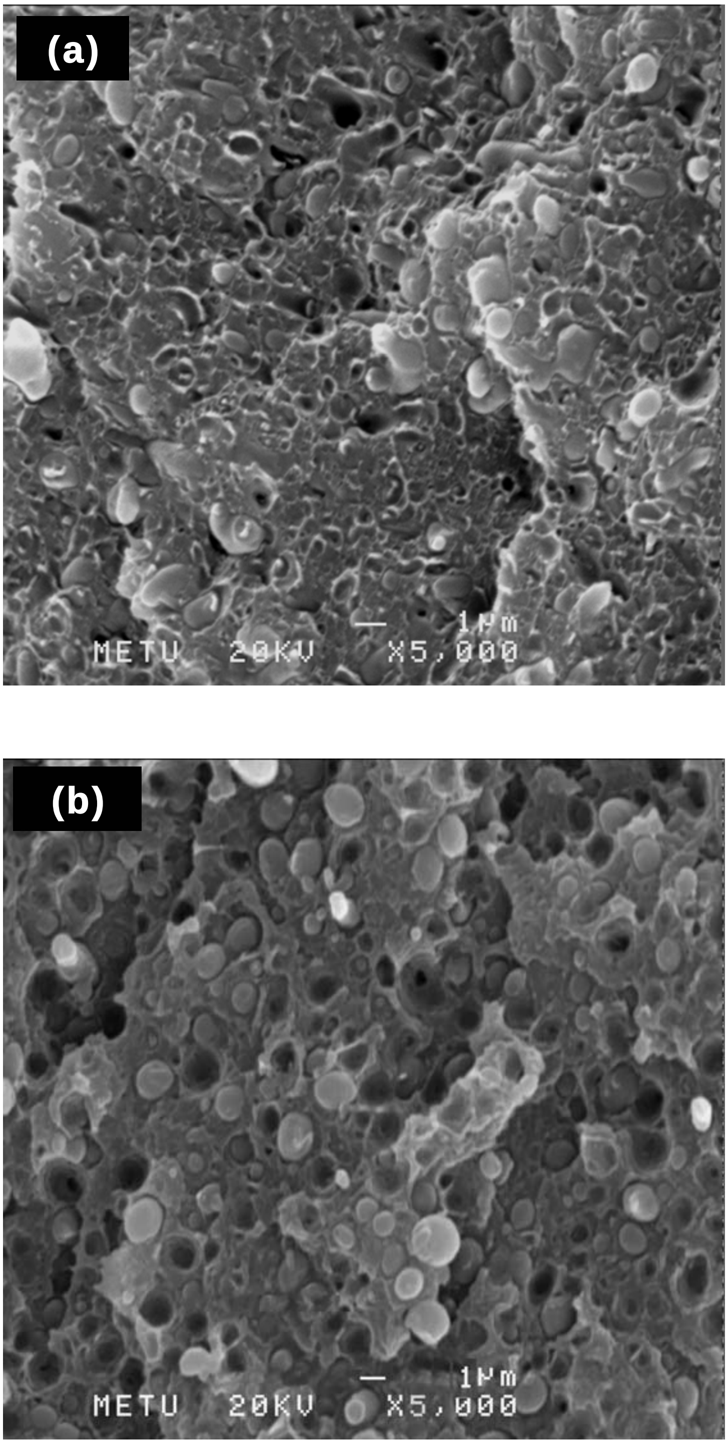

Figure 4.26 SEM micrographs of fracture surfaces of a.) 80/20/5-EnBACO-MAH, b.) 80/20/5-EMA-GMA

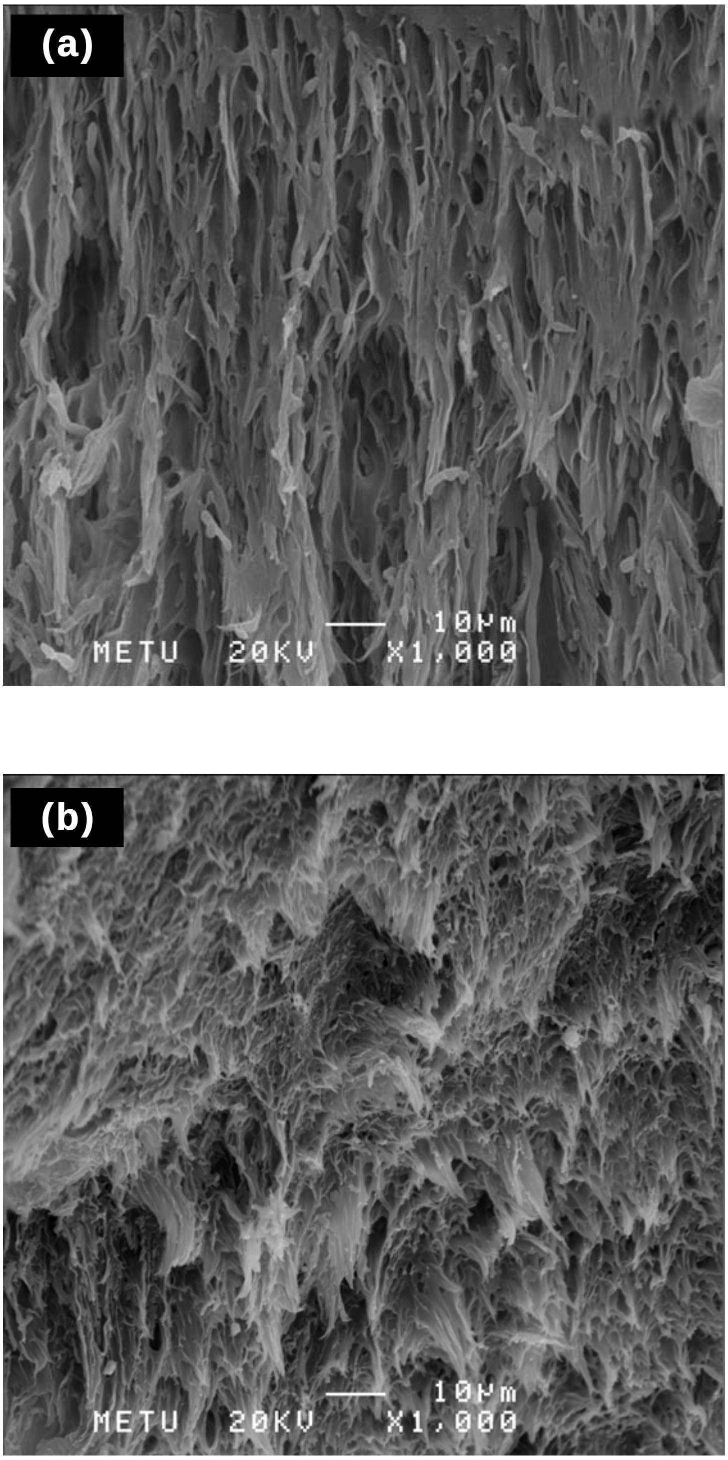

Figure 4.27 SEM micrographs of fracture surfaces of a.) 50/50/5-EMA-GMA, b.) 50/50/5-EnBACO-MAH

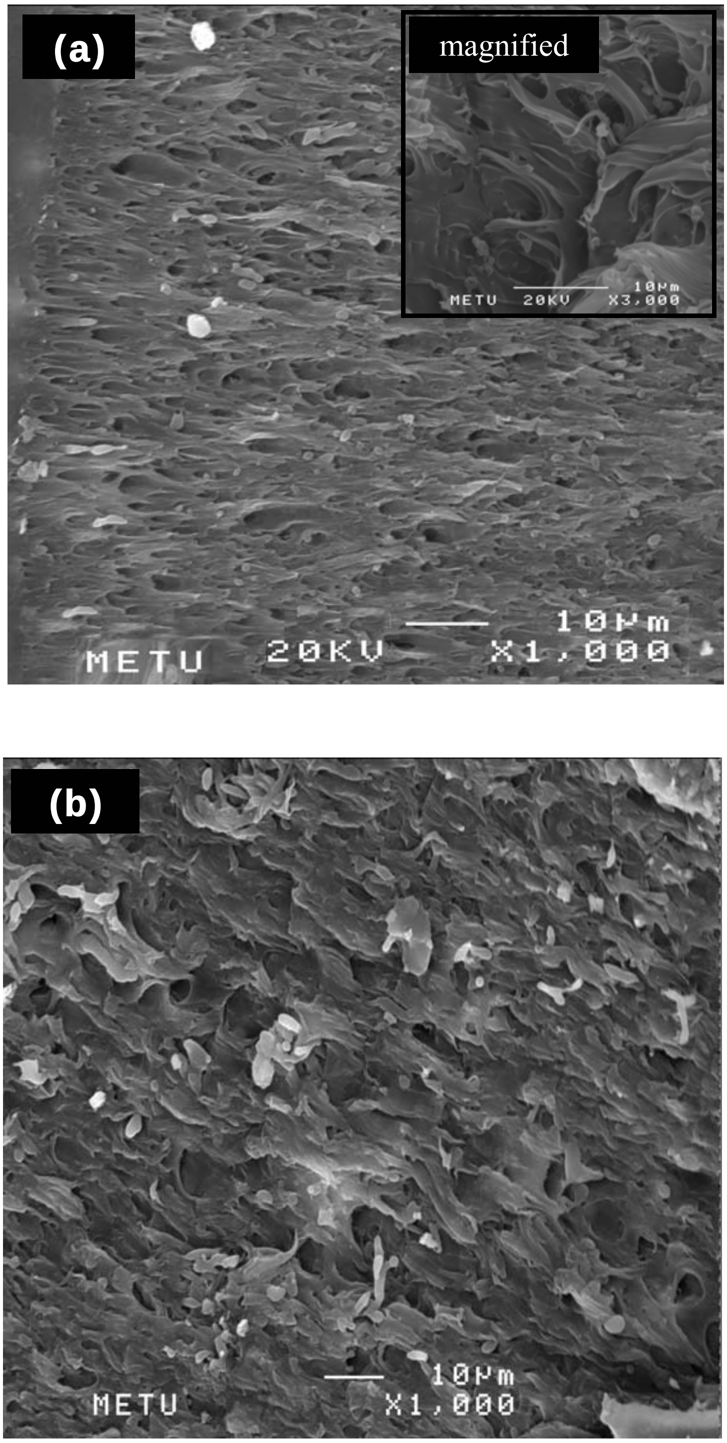

Figure 4.28 SEM micrographs of fracture surfaces of a.) 20/80/5-EnBACO-MAH, b.) 20/80/5-EMA-GMA

4.2 Short Glass Fiber (SGF) Reinforced ABS and ABS/PA6 Blends

4.2.1 Effects of SGF Surface Chemistry on the Morphology, Interfacial and Mechanical Properties of SGF/ABS and SGF/ABS/PA6 Composites

The properties of a composite not only depend on the properties of components but also the interface established between them. A strong interface can be formed if the components adhere to each other via chemical bonds or secondary interactions. Hence, the surface chemistry of the components has a crucial importance to achieve a strong interfacial adhesion. In this part of the study, the effects of the surface chemistry of the glass fibers on the morphology, interfacial adhesion and mechanical properties of SGF/ABS and SGF/PA6 composites were investigated. The glass fiber surfaces were treated with silane coupling agents. The most compatible silane for both ABS and ABS/PA6 blend was determined among the ones which were examined. The work of adhesion (Wa^{TOT}) is determined by the surface chemical affinity of the components in the composite, which can be a chemical bond or secondary attractions such as van der Waals or hydrogen bonding, or by the inter laminar shear strength (ILSS) due to mechanical adhesion. In this study, the W_a^{TOT} and ILSS values were calculated from experimentally determined interfacial tensions and short beam flexural tests, respectively.

The contact angles measured using the probe liquids and calculated surface tension components of the glass fibers with different surface treatments and polymers are shown in Table 4.3. DIM, EG and FA are corresponding to probe liquids diiodomethane, ethyleneglycol and formamide, respectively. γ^{LW}, γ^{+} and γ^{-} are standing for the dispersive, acidic and basic components of the surface tensions, respectively. Work of adhesion between contacting phases can be calculated from Equation (2.11) [220] by utilizing the contact angles and surface tension components. The thermodynamic work of adhesion, W_a^{TOT}, values including dispersive, W_a^{LW}, and acid/base, W_a^{AB}, components between matrix materials and various glass fiber surface coatings are given in Table 4.4, Figures 4.29 and 4.30.

Table 4.3 Contact angles (θ) in probe liquids and calculated surface tension components, (γ, mN/m)

Species	**Contact Angle, (°)**			**Surface tension components (mN/m)**		
	DIM	**EG**	**FA**	γ^{LW}	γ^{+}	γ^{-}
As Received	53.06	61.31	67.66	32.55	0.02	5.19
APS	49.46	56.63	63.90	34.58	0.03	7.31
MPS	50.58	65.16	69.51	33.95	0.09	0.38
Unsized glass fiber	52.41	45.57	50.21	32.90	4.38	0.82
ABS	59.34	59.34	65.79	28.96	0.42	4.96
PA6	44.76	40.97	40.97	37.14	4.11	1.07

Table 4.4 Thermodynamic work of adhesion between matrix materials and glass fibers with different surface treatment, (W_a, mJ/m^2)

	ABS			PA6		
	W_a^{LW}	W_a^{AB}	W_a^{TOT}	W_a^{LW}	W_a^{AB}	W_a^{TOT}
As Received	61.41	3.65	65.06	69.52	9.57	79.09
APS	63.29	4.21	67.50	71.67	11.29	82.96
MPS	62.71	2.10	64.81	71.02	3.11	74.13
Unsized	61.75	10.16	71.91	69.93	8.00	77.93

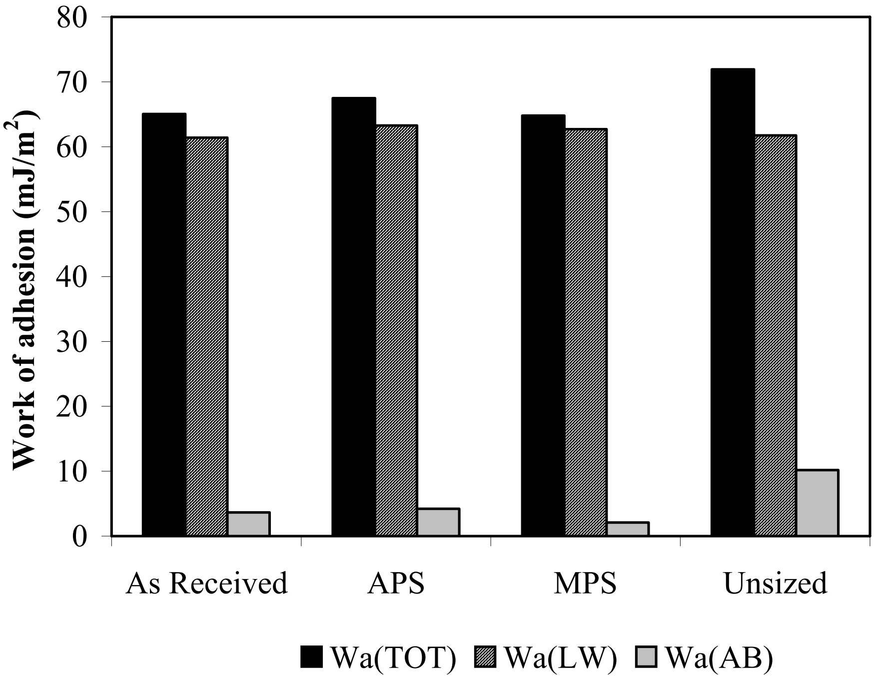

Figure 4.29 Work of adhesion between ABS and glass fibers with different surface treatments

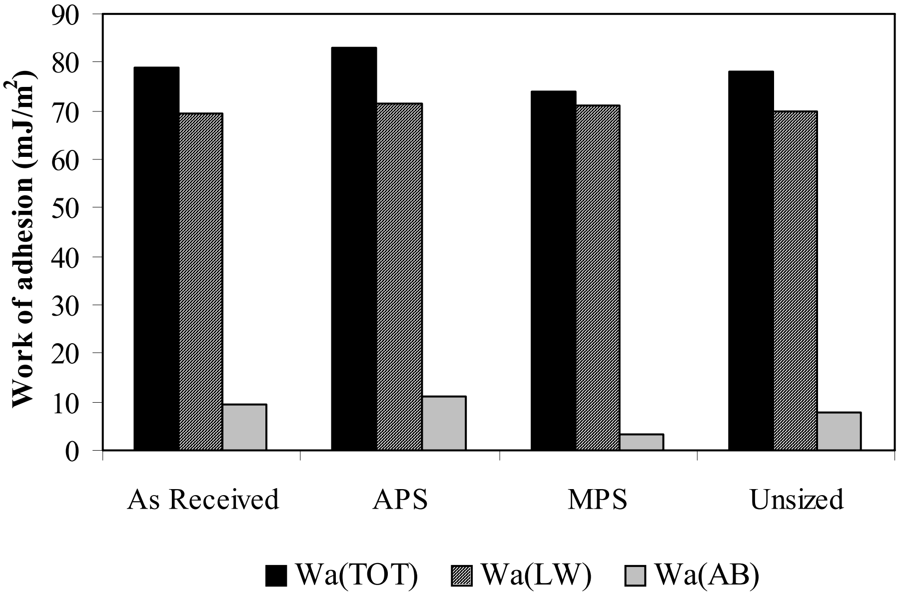

Figure 4.30 Work of adhesion between PA6 and glass fibers with different surface treatments

It is observed from Figure 4.29 that dispersive component (W_a^{LW}) of W_a^{TOT} remained almost constant for all of the species when ABS was concerned. As expected, APS, MPS and received silane treated fibers have basic surface characteristics due to electron rich groups in their structures. Thus, the acid/base interaction is not possible between electron donor groups, phenyl, nitrile and vinylidene, of ABS. As is seen from Figure 4.28, the W_a^{AB} between unsized fiber and ABS is higher than the others due to the presence of acidic -OH groups on the surface of the glass, which can interact with electron donor groups of ABS.

Figure 4.30 represents the thermodynamic adhesion between PA6 and glass fibers with different surface coatings. Similar dispersive components as in ABS are observed in PA6, therefore, it can be said that the variation of thermodynamic adhesion values arises from the difference in acid/base terms. Especially in APS, amines may react with both the amide groups on the backbone and carboxylic acid groups at the end of the PA6 chains [23]. Hence, it is reasonable to achieve high values for APS.

The representative Short Beam Flexural Test diagrams of ABS/GF and PA6/GF composites for different fiber surface treatment are seen in Figures 4.31 and 4.32. On the plots, y-axis corresponds to the force (N) required to bend the specimen and x-axis is the deformation (mm) of the specimen.

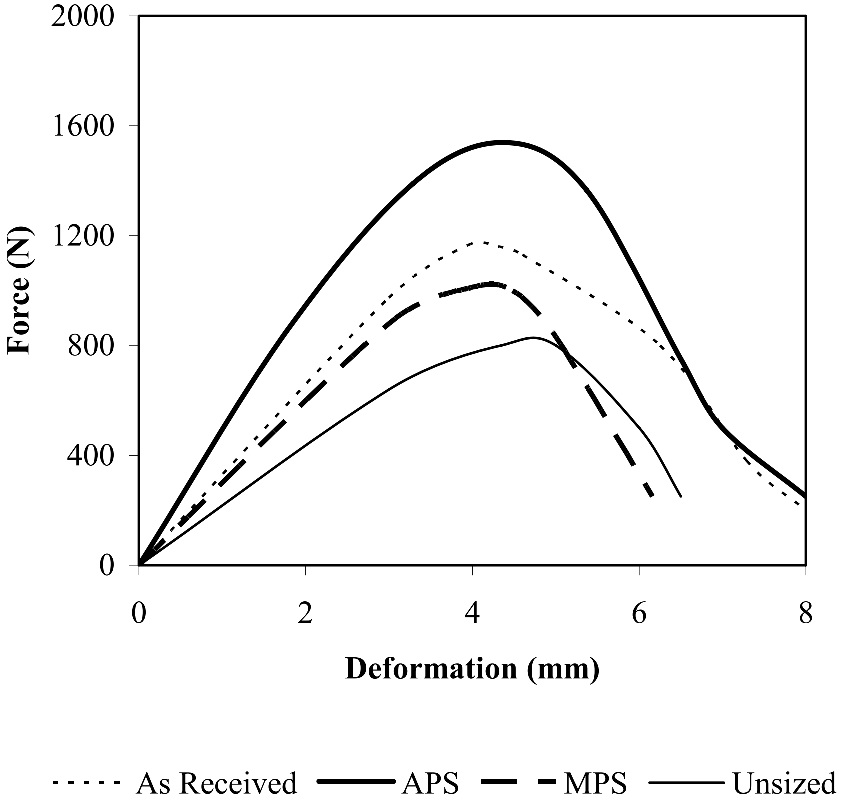

Figure 4.31 Short Beam Flexural Test diagrams for ABS/GF composites

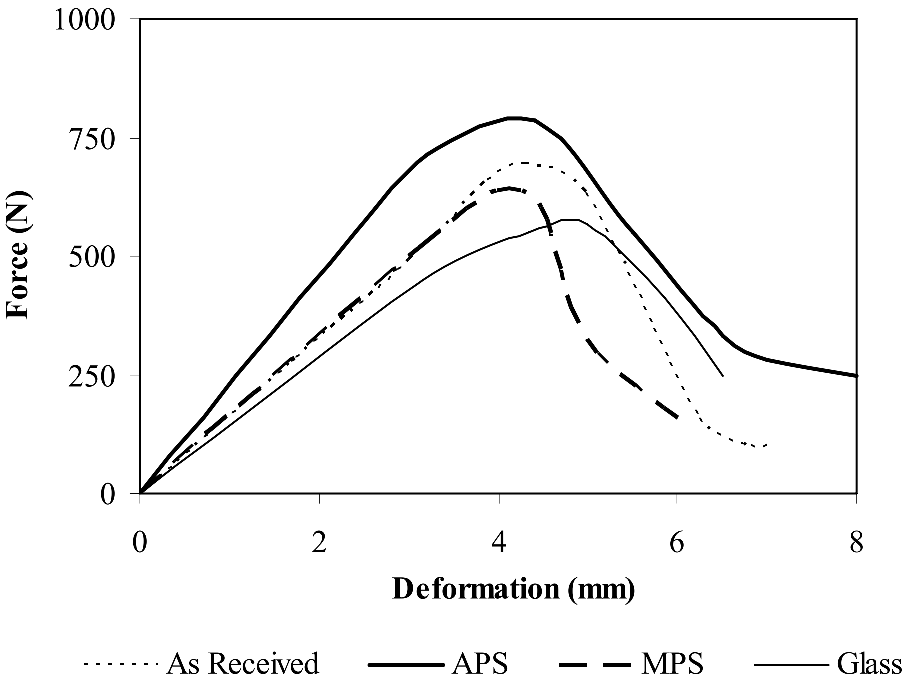

Figure 4.32 Short Beam Flexural Test diagrams for PA6/GF composites

The inter laminar shear strength (ILSS) values calculated from short beam flexural tests are given in Table 4.5, Figure 4.33 and Figure 4.34. In the case of ABS, unlike the highest W_a^{TOT} for unsized fiber, its ILSS is the lowest with respect to the others. A possible reason for this may be lack of mechanical interlocking between the fiber surface and molten ABS during specimen preparation. When the coupling agents are present on the surface, the variation of ILSS values may be attributed to the purely mechanical interlocking in the absence of acid/base interaction. The presence of the coupling agents on the surface may allow the chains to penetrate inside through the sizing layer. Hence, the highest ILSS was obtained with APS which is less bulky compared to MPS and REC; and may allow interchain diffusion to a larger extent.

Table 4.5 ILSS between matrix materials and glass fibers, (MPa)

	Inter Laminar Shear Strength (MPa)	
	ABS	**PA6**
As Received	5.25 ± 0.85	8.2 ± 1.25
APS	6.2 ± 0.52	15.01 ± 0.85
MPS	4.78 ± 0.80	7.94 ± 1.20
Unsized glass fiber	4.05 ± 1.98	6.26 ± 0.95

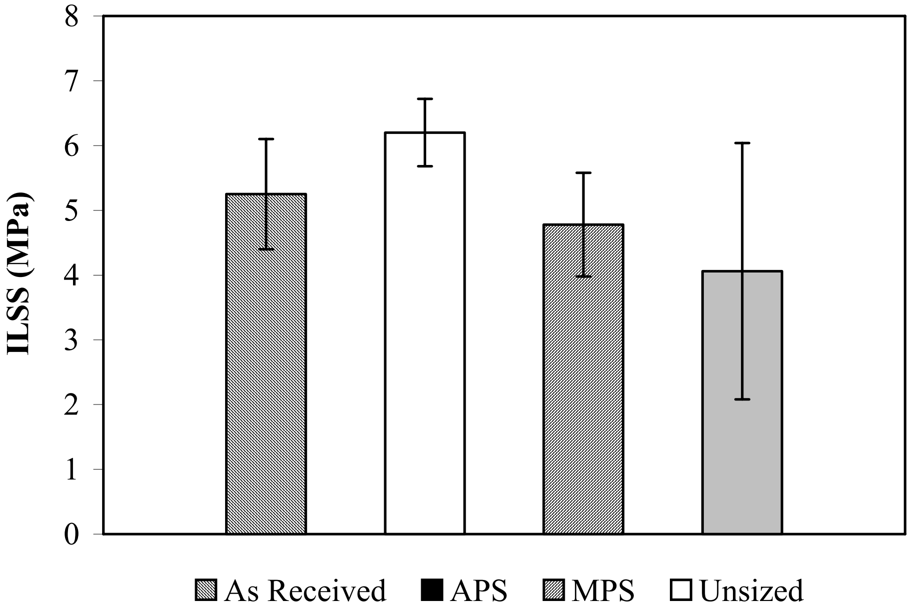

Figure 4.33 ILSS values between ABS and glass fibers with different surface treatments

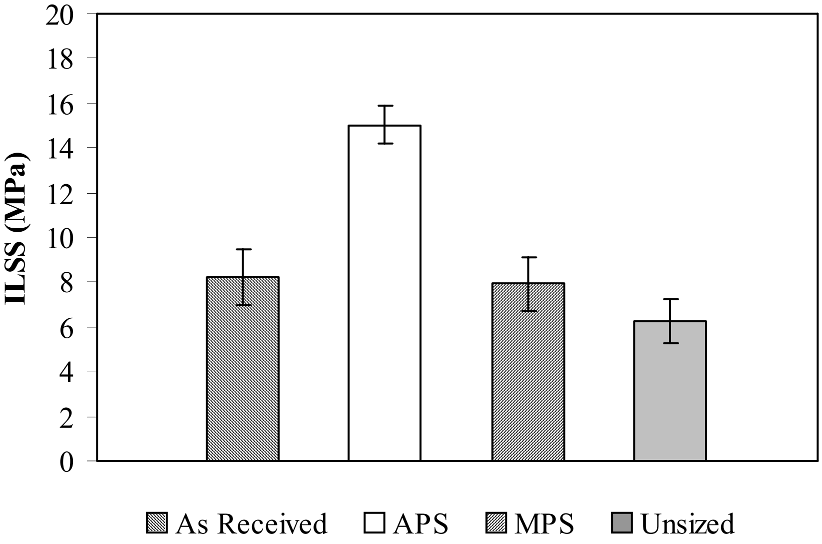

Figure 4.34 ILSS values between PA6 and glass fibers with different surface treatments

The ILSS values for the PA6 and fibers are harmonious with thermodynamic adhesion values because of the synergetic effect of both acid/base interactions and mechanical interlocking. The measured adhesion value for APS coated fibers is about two times higher than the others.

For the system involving poorly polar matrices or non-polar matrices such as PE, PVC, PU and surface treated glass fibers; it has been shown that a linear relationship can be established between ILSS and W_a^{TOT} [221]. Thus, it is possible to write the following relation:

$$ILSS = k(W_a^{TOT}) \qquad (4.3)$$

where k is the coefficient of proportionality. This equation indicates that physicochemical interactions between the fiber and the matrix determine, to a large extent, the mechanical behavior of the interphase from the very famous relation of Cox [222]. The constant "k" depends on the modulus of matrix and fiber, and the equilibrium center-to-center distance involved in physical interactions such as van der Waals and acid/base interactions [223]. The following Figures 4.35 and 4.36 show the dependence of W_a^{TOT} on ILSS measured between glass fibers with different surface coatings and polymer matrices (ABS and PA6).

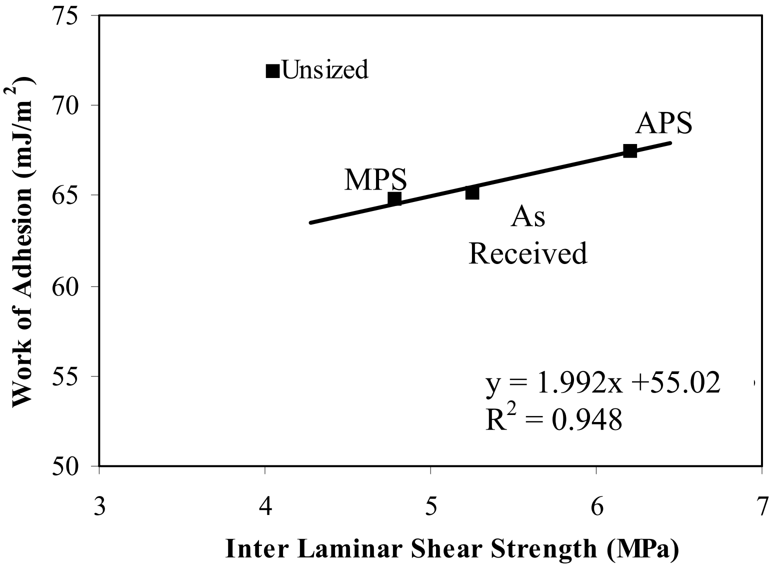

Figure 4.35 Dependence of W_a^{TOT} on ILSS for ABS and various sized glass fibers

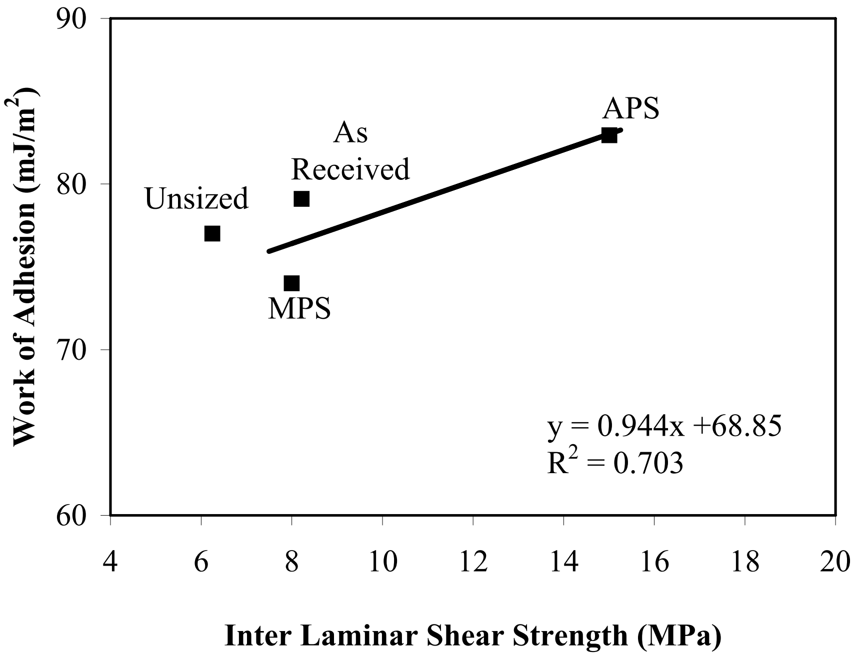

Figure 4.36 Dependence of W_a^{TOT} on ILSS for PA6 and various sized glass fibers

When trend lines were added to the plots of W_a^{TOT} versus ILSS in Figures 4.35 and 4.36, the unsized fibers were not included because of the lack of mechanical interactions. It is observed that there is a linear increasing dependence between W_a^{TOT} and ILSS for ABS/GF system when the fiber surfaces are treated with silane coupling agents. Similar results were obtained experimentally by Park and Jin [224] for the system including continuous glass fibers treated with different silane coupling agents and unsaturated polyester; and by Schultz and Lavielle [225] for carbon fiber reinforced different epoxy resins. This output indicates that good wettability of matrix, which is identified by high W_a^{TOT} between fiber and matrix, supports high interfacial strength, which is identified by ILSS.

The significant result extracted from Figures 4.35 and 4.36 is the divergence from the linear dependence between ILSS and W_a^{TOT} values (R^2=0.948 to R^2=0.703) when the polarity of the matrix increases, which gives rise to strong interactions between contacting phases, between PA6 and various sized glass fibers. This phenomenon was stated by Nardin and Schultz [221] that such linearity between W_a^{TOT} vs ILSS is no longer valid, since strong specific interactions are established at the interface. As a result of adhesion measurements, it was decided to use the APS treated SGF to reinforce the ABS and ABS/PA6 blends due to its highest acid-base interaction capacity with PA6 and its highest ILSS compared to other coupling agents studied.

The representative tensile stress-strain curves for 30wt% SGF reinforced ABS blended with various amounts of PA6 are shown in Figure 4.37. The variation of the response of the composites under tensile load gives useful information about the changes of the microstructure at the fiber/matrix interface. It was reported that a strong interfacial interaction enhances efficient load transfer from matrix to fibers in fiber reinforced systems [226-228]. The ultimate strength of composites is a direct indicator of the strength of the interfacial bonds since the applied stress is more efficiently transferred through the interface [229]. The results of tensile tests tabulated in Table 4.6 exhibit an increasing trend in ultimate strength of composites as the PA6 content in the matrix increases. This result can be attributed to the increasing extent of acid-base reaction between acidic end group of PA6 chains and aminopropyl functional group of coupling agent on the glass fiber surface as the amount of PA6 in the matrix increases. Moreover, these interactions might stiffen the polymer chains close to the fibers to resist against the applied tension leading to an improved Young's Modulus with increasing PA6 content (Table 4.6).

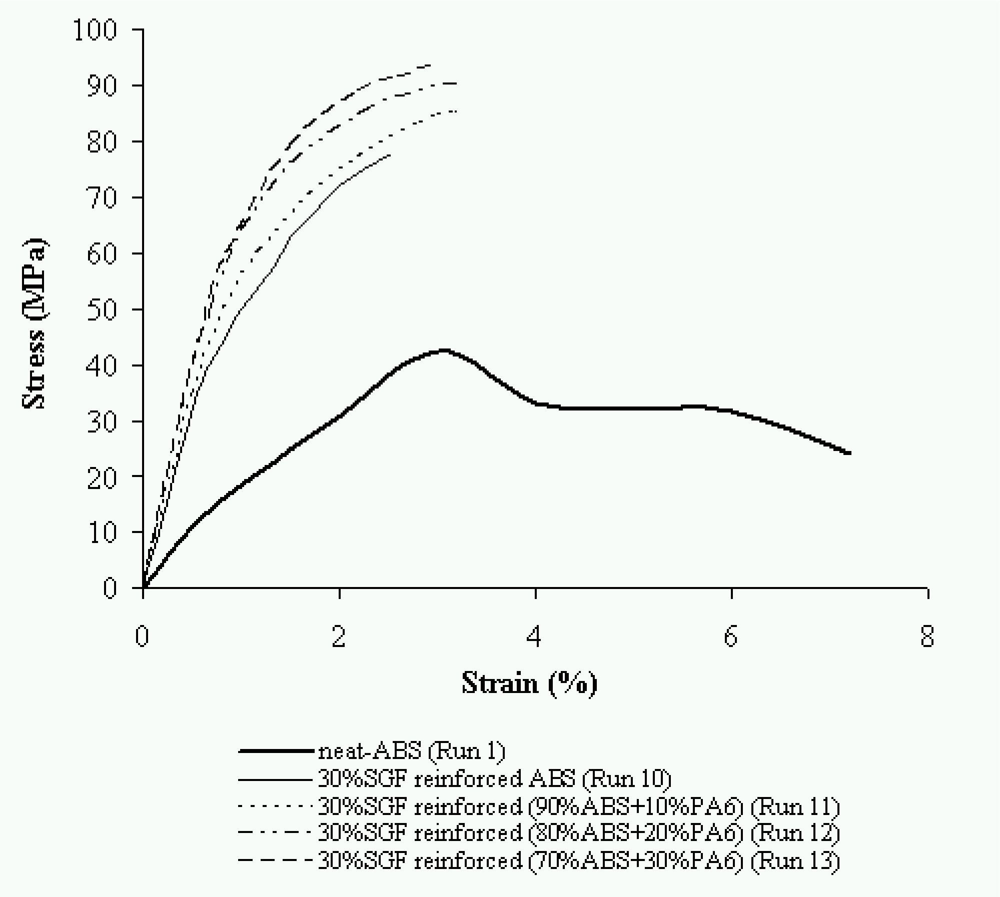

Figure 4.37 Representative stress-strain curves of materials produced

Table 4.6 Tensile test results of materials produced (Run numbers correspond to the conditions given in Table 3.5)

Material	**Tensile Strength (MPa)**	**Young's Modulus (MPa)**	**Strain at Break (%)**
Run 1	44.0 ± 6.0	2240 ± 183	7.5 ± 0.8
Run 10	78.0 ± 2.5	6500 ± 352	2.5 ± 1.3
Run 11	85.0 ± 3.0	6910 ± 205	3.2± 0.6
Run 12	91.0 ± 1.1	8045 ± 512	3.4 ± 0.9
Run 13	93.0 ± 1.8	8415 ± 333	3.2 ± 0.9

The fiber length distributions of composites after extrusion are illustrated in Figure 4.38. Because of the nature of the injection molding machine used for preparing specimens, it can be assumed that all of the fiber length reduction occurred during extrusion and the distribution curves are representative of the specimens tested. It is observed that the number of long fibers in the composites increases as the PA6 content increases in the matrix from 0% to 30%, although the corresponding average fiber length remains nearly the same (427, 447, 471, 482 microns). The melt viscosity of PA6 is lower than the viscosity of ABS, thus the shear forces are lower in the case of ABS/PA6 blends with high PA6 content which reduces fiber length degradation [230]. This can be followed from the MFI values given in Table 4.7 which shows that MFI values increase as the PA6 content increases. It is known that the load bearing capacity of fibers embedded into a matrix increases as their length gets longer; therefore improved tensile strength and Young's modulus must have resulted from increasing number of longer fibers together with the improved adhesion [21, 230, 231].

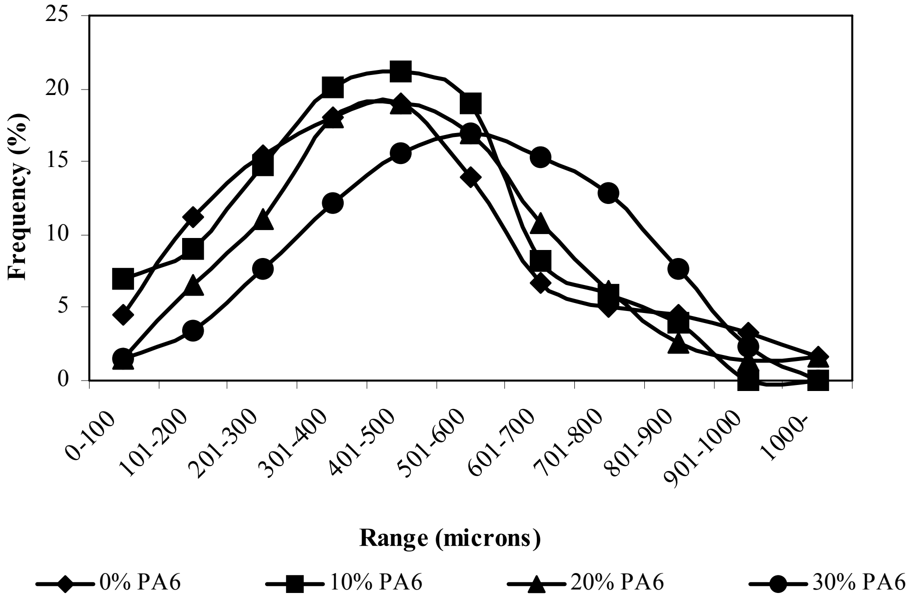

Figure 4.38 Fiber length distributions as a function of PA6 concentration in the matrix for 30wt% SGF reinforced ABS/PA6 composites

Table 4.7 Melt flow index values of materials produced with 5 kg load and 230°C (Run numbers correspond to the conditions given in Table 3.5)

Material	Melt Flow Index (g/10min)
Neat ABS	15.6
Run 10	3.2
Run 11	11.5
Run 12	12.2
Run 13	13.7
Neat PA6	36.4

Figure 4.39 illustrates the variation of unnotched charpy impact strength of materials produced. The neat ABS resin has the highest impact strength as expected. The incorporation of SGF to ABS results in a sharp reduction in impact strength because of the restricted deformation ability of matrix in the presence of fibers. When 10wt% of PA6 is incorporated to the matrix, a drastic improvement in the impact strength of composites is obtained. Further addition of PA6 decreases the impact strength value but it is still higher than the SGF/ABS system. This behavior may be attributed to the high chemical affinity between the amino functional coupling agent on the fiber surface and PA6 to decrease the total free energy of the system. The PA6 chains fed can concentrate near the surface of the glass fibers during melt processing and there might be a PA6 sheath formed on the fibers; therefore the ABS matrix will be free to deform similarly to the neat-ABS**.** This theory is supported by the SEM analysis that follows.

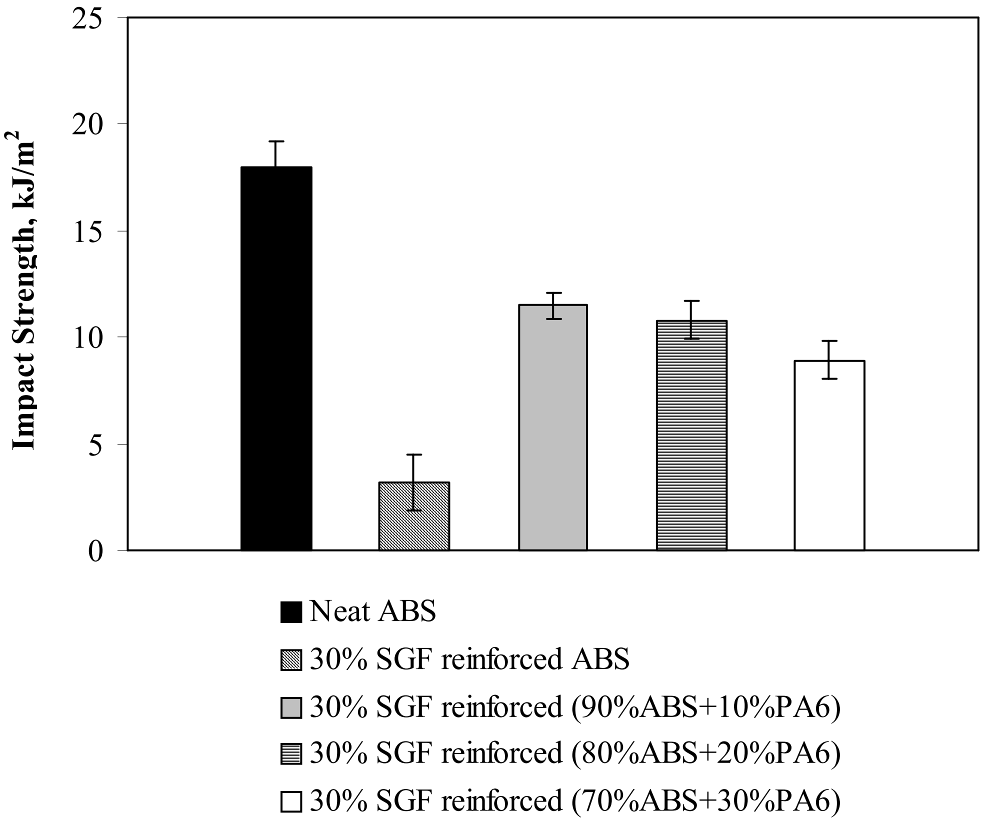

Figure 4.39 Unnotched impact strength of materials produced

In order to investigate the microstructure and extent of the adhesion between fibers and matrix, SEM study of tensile fracture surfaces of 30wt % SGF containing specimens is performed (see Figure 4.40). In the case of 30wt% SGF reinforced ABS, deformation of matrix is restricted and a brittle fracture is observed. Also it can be seen that the fibers are debonded, leaving a dark ring occurring at the interface, which also observed in the study of Fu and Lauke [231]. In that study, the authors interpreted the dark rings resulting from local deformation of the matrix around the fibers after fiber debonding. Most of the fibers were pulled-out from the matrix during deformation; however the matrix is still attached to the fibers. Failure occurs at the fiber matrix interface. In close-up view (see Figure 4.40-a), the fiber surface is clean and smooth, which supports the work of adhesion results indicating that there is lack of interaction between APS treated SGFs and ABS. Figures 4.40 b-d show the SEM micrographs of fracture surfaces of PA6 containing composites reinforced with 30wt% SGF. In the case of strong interphase, the physical properties (especially density) of matrix near the fiber surface are different than that of the bulk polymer; therefore the failure under tensile loading occurs at the matrix near the fibers. It is clear from these figures that the failure occurred at the matrix. The sheath of polymer observed on the surface of the fibers can be interpreted as an evidence of strong interactions.

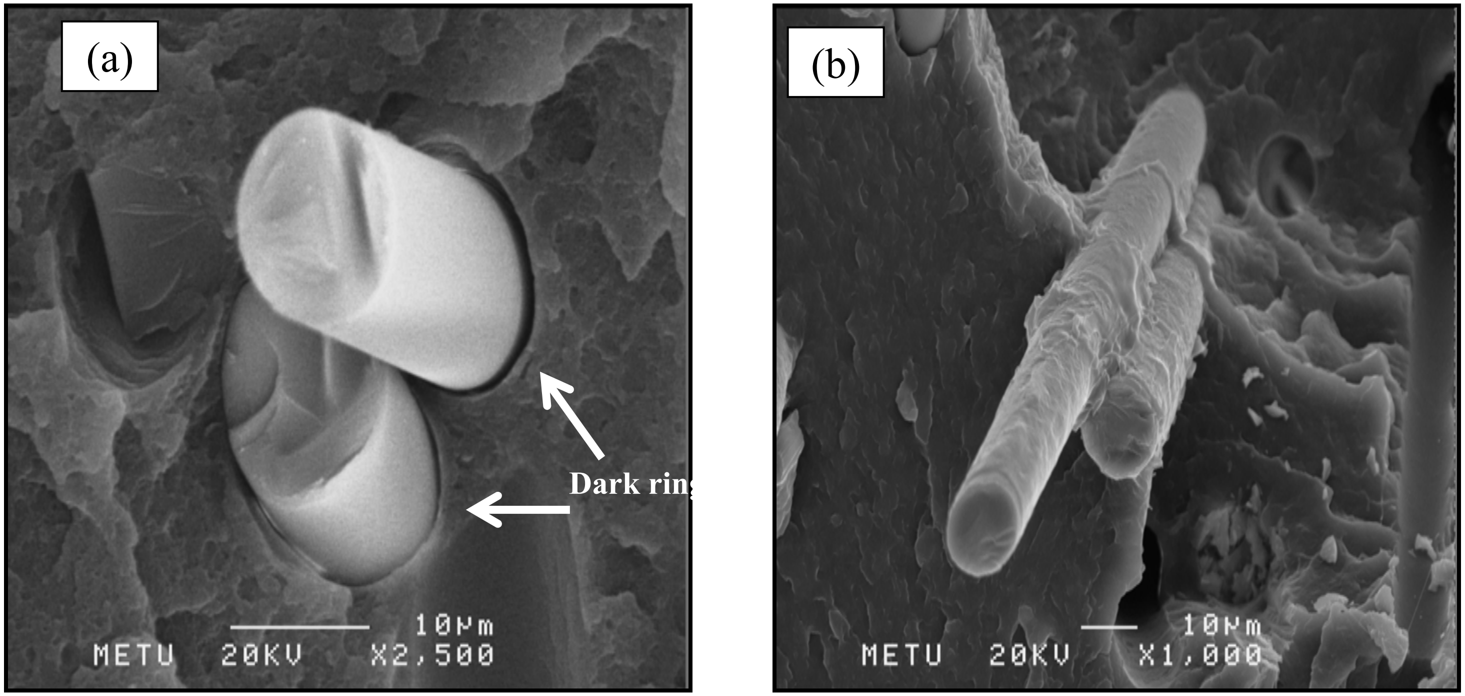

Figure 4.40 SEM micrographs (x1000) of tensile fractured surfaces of (a) 30wt% SGF reinforced ABS (b) 30wt% SGF reinforced (90%ABS+10%PA6)

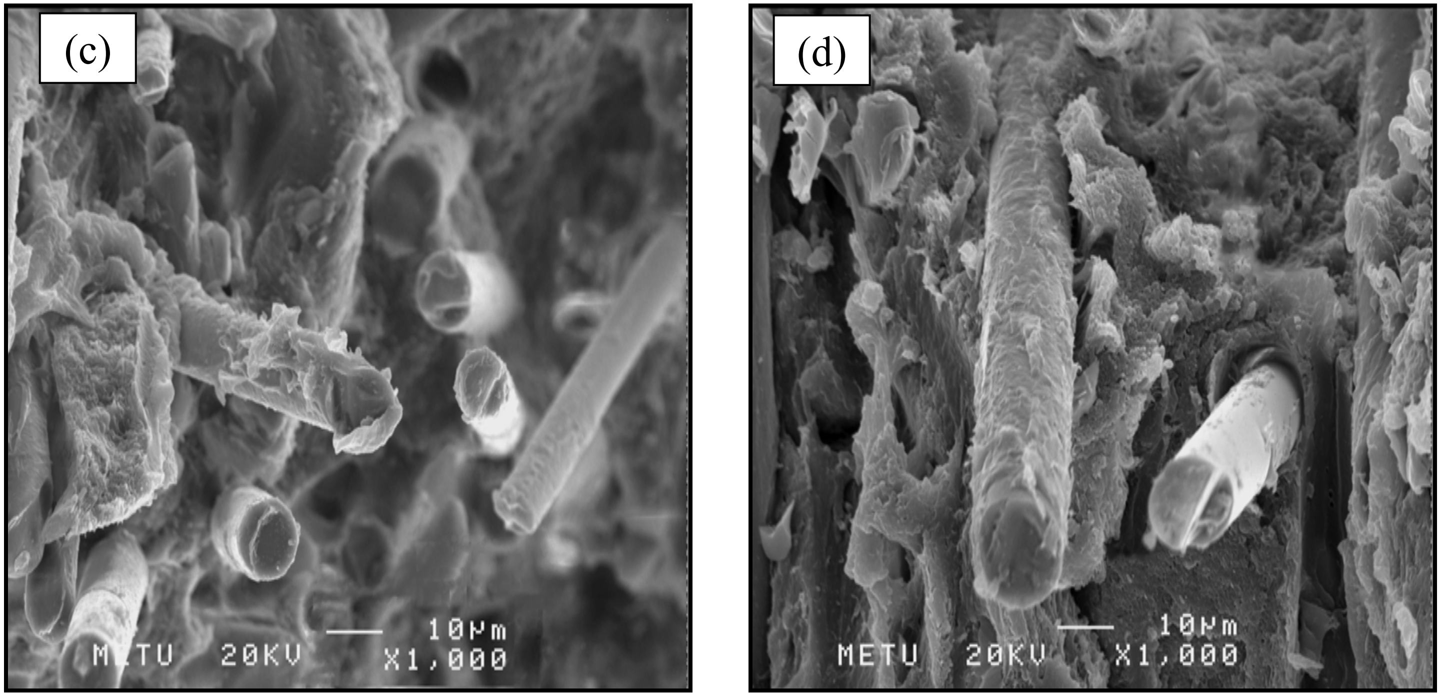

Figure 4.40 (Cont'd) SEM micrographs (x1000) of tensile fractured surfaces of (c) 30wt% SGF reinforced (80%ABS+20%PA6) (d) 30wt% SGF reinforced (70%ABS+30%PA6) composites

4.2.2 Effects of SGF Concentration on the Mechanical Properties and Morphologies of ABS/SGF Composites

In this part of the study, effects of SGF concentration on the mechanical properties and morphologies of ABS/SGF composites are evaluated. The fiber length distributions of ABS/SGF composites are given in Figure 4.41 and the effects of SGF concentration mechanical properties are presented in Table 4.8. (Runs 1, 2, 3 and 4). The average fiber length decreases with increasing SGF concentration (754µm, 653µm and 418 µm). The results indicate that as the fiber content increases the average fiber length decreases. The increased reduction in fiber length for a higher fiber concentration is mainly attributed to the increase in fiber/fiber interaction [21, 230-234]. Increasing SGF content increases the tensile strength and modulus of the composites, which is in accordance with the well-known equation of mixture of Kelly and Tyson [235] for short fiber reinforced composite materials:

for $L \geq L_c$,

$$\sigma_c = k\sigma_f V_f \left[1 - \left(\frac{L_c}{2L}\right)\right] + \sigma'_m V_m \tag{4.4}$$

and for $L < L_c$,

$$\sigma_c = \left(k\tau L V_f / d\right) + \sigma'_m V_m \tag{4.5}$$

where σ_c is the strength of composite, σ_f is the ultimate strength of fibers, L is the length of fibers, σ_m' is the tensile stress at break for matrix, k is the orientation factor, d is the diameter and τ is the adhesive bond strength, V_m and V_f are the volume fractions of matrix and fiber, respectively. L_c is the critical length of fibers. Fibers that are shorter than critical length will pull out the matrix under tensile load. For such a case, full load transfer is not realized. At the critical length, both the fiber and matrix will fracture along the same failure plane. An additional increase in fiber length will not increase the strength of the composite, since the failure will be the same as that experienced at the critical length [236].

Figure 4.41 Fiber length distributions of ABS/SGF composites for 10wt%, 20wt% and 30wt% SGF content

Table 4.8 Results of mechanical tests

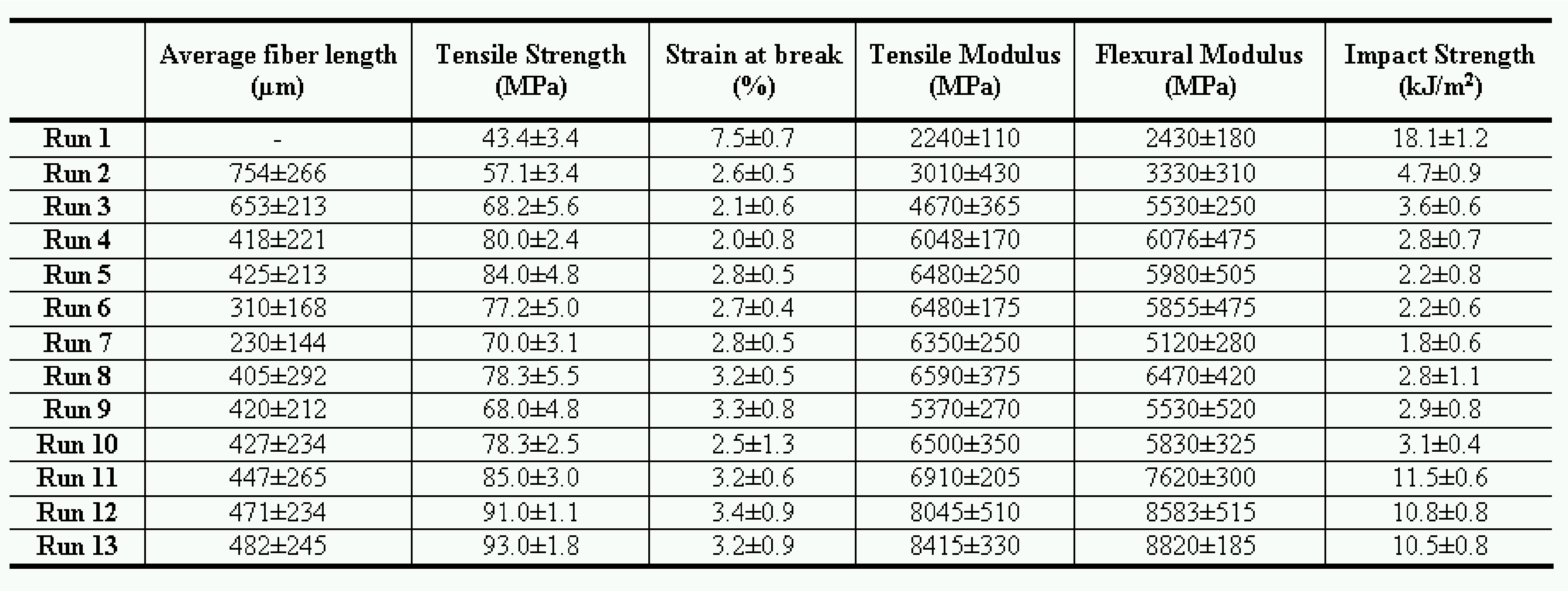

	Average fiber length (μm)	Tensile Strength (MPa)	Strain at break (%)	Tensile Modulus (MPa)	Flexural Modulus (MPa)	Impact Strength (kJ/m^2)
Run 1	-	43.4±3.4	7.5±0.7	2240±110	2430±180	18.1±1.2
Run 2	754±266	57.1±3.4	2.6±0.5	3010±430	3330±310	4.7±0.9
Run 3	653±213	68.2±5.6	2.1±0.6	4670±365	5530±250	3.6±0.6
Run 4	418±221	80.0±2.4	2.0±0.8	6048±170	6076±475	2.8±0.7
Run 5	425±213	84.0±4.8	2.8±0.5	6480±250	5980±505	2.2±0.8
Run 6	310±168	77.2±5.0	2.7±0.4	6480±175	5855±475	2.2±0.6
Run 7	230±144	70.0±3.1	2.8±0.5	6350±250	5120±280	1.8±0.6
Run 8	405±292	78.3±5.5	3.2±0.5	6590±375	6470±420	2.8±1.1
Run 9	420±212	68.0±4.8	3.3±0.8	5370±270	5530±520	2.9±0.8
Run 10	427±234	78.3±2.5	2.5±1.3	6500±350	5830±325	3.1±0.4
Run 11	447±265	85.0±3.0	3.2±0.6	6910±205	7620±300	11.5±0.6
Run 12	471±234	91.0±1.1	3.4±0.9	8045±510	8583±515	10.8±0.8
Run 13	482±245	93.0±1.8	3.2±0.9	8415±330	8820±185	10.5±0.8

*The corresponding experimental conditions to the Runs were given in Table 3.5.

According to the Kelly and Tyson model, tensile strength of the composite is linearly dependent to the volume fraction of fiber up to a certain loading level. The variation of tensile strength with respect to fiber volume fraction in our study is linear (see Figure 4.42), which proves the validity of the Kelly and Tyson equations for our system. On the other hand, another factor affecting the tensile strength of fiber-reinforced structure is the fiber length that competes with the effect of volume fraction of fibers. It is clear from the equation that higher the fiber length higher the strength is. Our results showed that the effect of fiber volume fraction is more dominant than the effect of fiber length.

The variation the tensile moduli as a function of fiber volume percent, which were calculated by means of densities of ABS (ρ=1.04 g/cm^3) and glass fiber (ρ=2.54 g/cm^3), is given in Figure 4.43. It can be seen that stiffness of the composites increases linearly with glass fiber content. This kind of dependence in composite materials is generally represented by the simple “rule of mixtures”:

$$E_c = \lambda_f E_f V_f + E_m (1 - V_f) \tag{4.6}$$

where E_f and E_m represent moduli of fiber and matrix, V_f represents volume fraction of short glass fibers and λ_f stands for fiber efficiency factor term including effects of fiber orientation and length. This implies that modulus of ABS/SGF composites are predominantly dependent on fiber loading level, not efficiency factor.

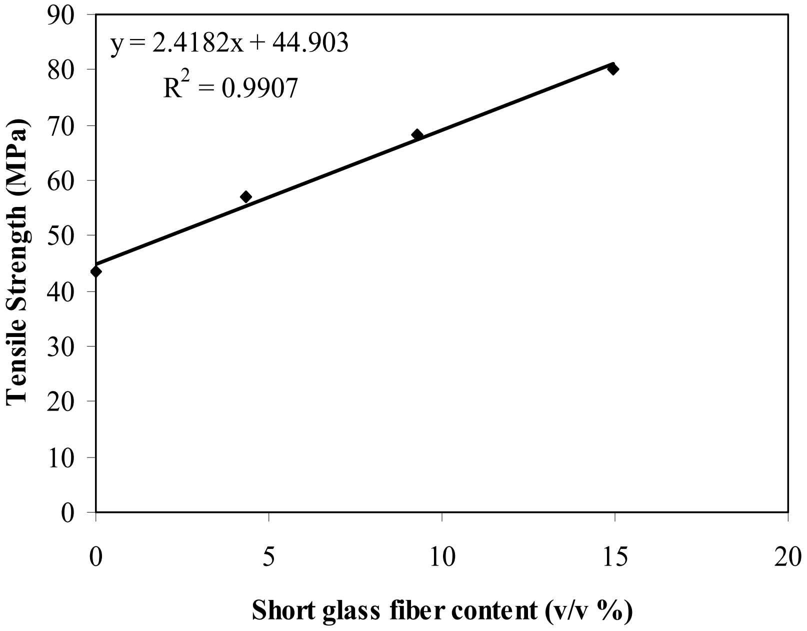

Figure 4.42 Composite tensile strength versus short glass fiber volume fraction

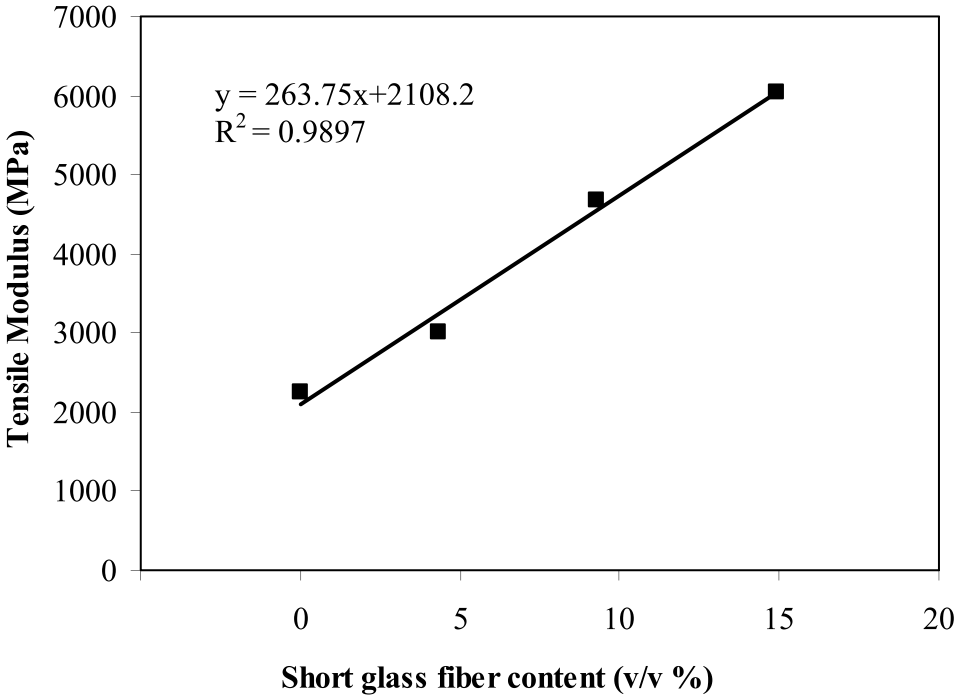

Figure 4.43 Composite tensile modulus versus short glass fiber volume fraction

The strain at break values of neat ABS and SGF reinforced ABS composites are shown in Table 4.8. As the fiber concentration increases, the strain at break values of the composites decrease. Because of stress-concentration at the ends of the fibers, matrix crack formation starts at these points. As the strain is increased, more cracks form. The cracking at the beginning of tensile test can be related to load transfer to fibers that connect the cracked regions. It is claimed in the literature that when the extent of cracking on the specimen reaches a critical level and the surrounding fibers and matrix can no longer support the increasing load, the failure of the specimen occurs in the weakest region [234, 237, 239]. This type of cracking and failure was observed during testing. The introduction of SGF to the ABS matrix changes the mode of failure from ductile nature to brittle nature also [19].

The trend in the flexural modulus of the composites as a function of SGF concentration is similar to the trend of tensile modulus of composites as SGF content increases.

The results of unnotched charpy impact tests are shown in Table 4.8. There is a sharp decrease in the impact strength with the addition of 10wt% SGF to the ABS, then the impact strength decreases slightly with further addition of SGF. When fiber reinforced thermoplastics are considered, the modeling of impact strength is even more complex than that of unfilled polymers. For a material to be very tough and to have high impact strength, in general there must be some mechanism for spreading and absorbing energy throughout a large volume of material [239]. ABS, a high impact resistant material, contains grafted polybutadiene (PB) rubbery domains on poly(styrene-co-acrylonitrile) (SAN) backbone similar to rubber toughened polymer blends [221]. The energy spreading mechanism responsible for rubber toughened structures are shear yielding of matrix and cavitations of rubber particles [233]. The previous literature [239] shows that SGF reinforcement can reduce or promote the impact strength of the thermoplastic materials. It was observed that the addition of

SGF to Nylon 6 matrix increased the impact fracture energy of the composite; whereas small amount of SGF introduced to ethylene-propylene rubber toughened Nylon 6 matrix decreased the energy of impact fracture dramatically [240]. Similar result obtained for SGF reinforced ABS composites may be attributed to the presence of small amount of glass fibers (10wt%), which may restrict the cavitation of the rubber particles [233]. Nevertheless, the addition of SGFs to a tough matrix brings new stress concentrated zones at the fiber ends and areas where fibers contact with each other; hence, this reduces the ductile deformation of the matrix [32].

Interfacial studies showed that only mechanical interlocking is present between APS sized glass fibers and ABS matrix, therefore, the desired interfacial bonding is not established [241]. The impact loading causes rapid crack propagation through the material. For ABS/SGF system, results of impact test indicated that the resistance to crack growth through a polymer/fiber interface was significantly less than that through a homogeneous polymer resin. Thus, the crack growth can easily take place by passing through the weak interfacial boundary that result in a sharp decrease in impact strength with the introduction of SGFs to ABS. The further slight decrease of impact strength of the ABS/SGF composites is due to the reduction of average fiber length; it increases the number of fiber ends and stress concentrated zones in composite bodies.

The fractured surfaces of ABS/SGF composites are presented in Figures 4.44 a and b. These figures show that deformation of ABS resin matrix is restricted seriously and a brittle fracture is observed. It can also be seen that the fibers are debonded, with a dark ring occurring at the interface. The dark ring results from local deformation of the matrix around the fibers after fiber debonding from the matrix. Most of the fibers were pulled-out from the matrix during deformation; however resin still holds fibers. The close-up views indicate that since the fiber surfaces are clean and smooth, there is not any significant adhesion between APS treated SGF and ABS matrix, as reported in elsewhere [241].

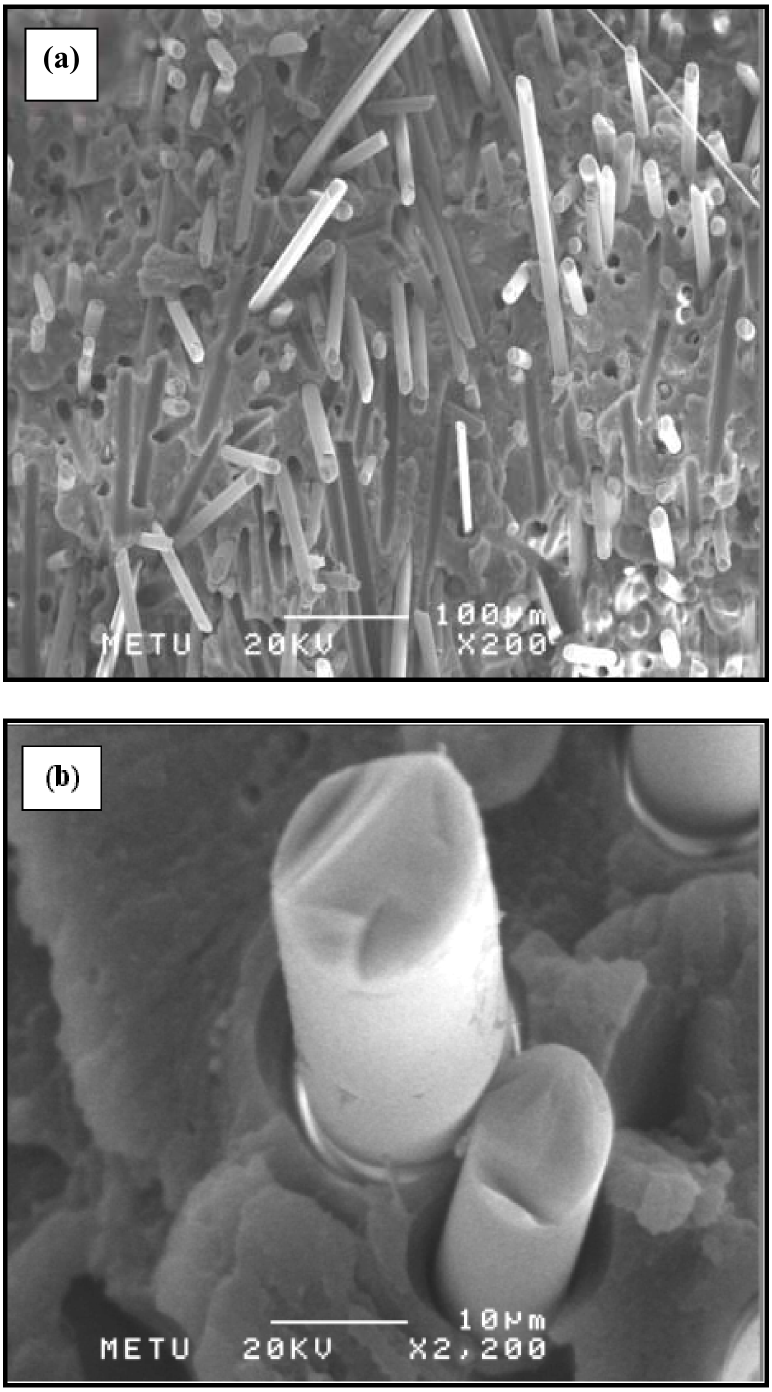

Figure 4.44 Scanning electron micrograph of the fractured surface of 30%wt SGF containing specimen (a) x 200 magnification (b) x 2200 magnification

4.2.3 Effects of Processing Conditions on the Mechanical Properties and Morphologies of ABS/SGF Composites

4.2.3.1 Screw Speed

In addition to the properties of the components and interphase between the components, processing conditions have influence on the properties of SGF reinforced polymer composites. In this part of the dissertation, the effects of processing conditions such as screw speed and barrel temperature on the morphologies and mechanica properties of ABS/PA6 composites were investigated.

Figure 4.45 shows the fiber length distributions with respect to the screw speeds (runs 4, 5, 6 and 7). The distribution curves shift to left and become narrower as the screw speed increases due to the fiber length reduction. The theoretical knowledge about the fiber degradation during twin screw extrusion is rather limited because of the complexity of the flow profile and the shear rate in the extruder.

Twin screw extrusion operate in starve feeding principle which means that the elements of screw are not fully filled through the whole screw, that is why shear rate differs in each region depending on the fill ratio of the screw elements. A basic empirical equation is given by Stade [242], which relates the number of shear cycles to processing conditions, extruder design and material properties:

$$k_2 = \frac{(L_2)(\rho)(f)(N)(A_f)}{F} \tag{4.7}$$

where k_2 is the key figure for the average glass fiber length in the composite; L_2 is the length of mixing section of extruder; ρ is the average density of material; f is the fill ratio; N is the screw speed; A_f is the free cross section of the extruder and F is the feed rate of the composite. Also it was determined that shear rate increases with increasing screw speed and decreasing feed rate [243]. Based on these studies, it can be said that the major factors affecting the extent of fiber degradation are proportional to N, f and 1/F for a given processing device. In this study, feed rate was constant while screw speed was increased; therefore the only parameter that was changed in Equation 4.7 was the screw speed.

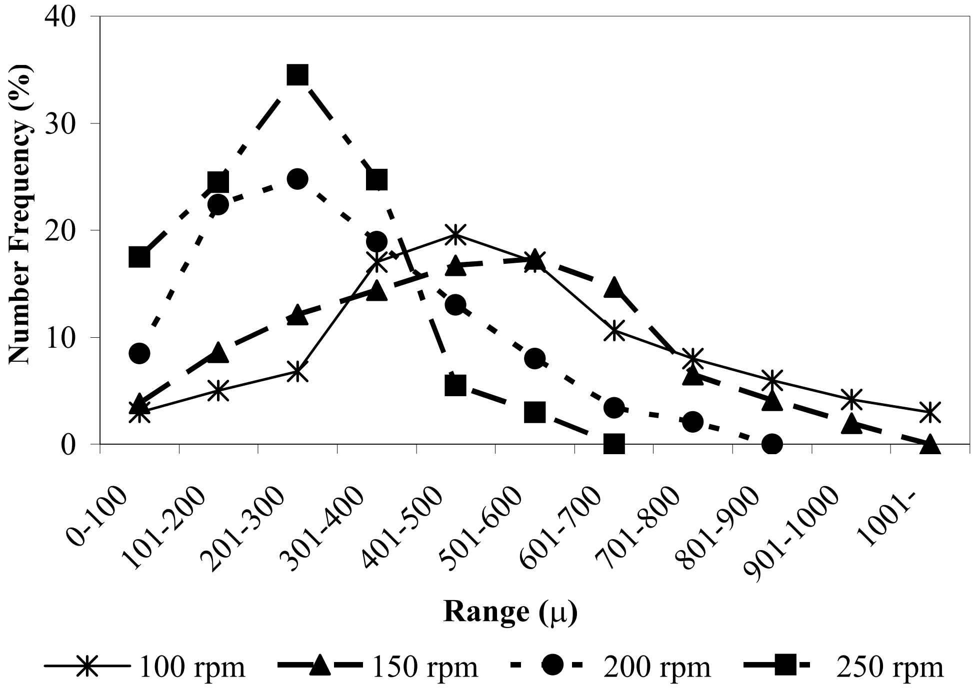

Figure 4.45 Fiber length distributions of SGF/ABS composites processed at screw speeds of 100, 150, 200 and 250 rpm

The change in mechanical properties with respect to screw speed and average fiber length is illustrated in Table 4.8, runs 4-7. According to the theory of Kelly and Tyson [235], tensile strength of a short fiber reinforced matrix improves as the fiber length increases. As seen in Table 4.8, when the screw speed increases, both the average fiber length and tensile strength decrease. The presence of higher portion of long fibers (see Figure 4.45) at 100 rpm is observed to affect the elongation at break negatively. In other words, the mobility of the matrix is restrained much more by the long fibers. The modulus of elasticity values indicate that modulus decreases as the screw speed increases from 150 to 250 rpm since the fiber length decreases with increasing screw speed. A decreasing trend was also observed in flexural modulus values as the screw speed increases, which is given in Table 4.8. Unnotched charpy impact strength values with respect to screw speed and average fiber length are also given in the same table. As the average fiber length decreases, impact strength also decreases. Fiber ends are points of stress concentrators that weaken the composite by acting as crack initiators. It is obvious that long fibers produce high impact composites compared to short ones because of lower number of fiber ends at the same SGF content.

SEM micrographs obtained from tensile fracture surfaces are shown in Figure 4.46. The brittle fracture of the matrix is seen in all four ABS/SGF composites, which were prepared at different screw speeds. It can easily be observed that fiber alignment was perturbed as the fiber length increases, which can be deduced from the tracks of fibers aligned perpendicular to fracture plane. It can be also seen from the SEM micrographs that most of the fibers were pulled out from the ABS matrix. When ABS/SGF system is considered, it is not surprising that many of the fibers were pulled-out of the matrix, because the adhesion measurements indicated that the interaction between ABS and APS sized fibers were very poor [241]; therefore under a tensile loading it is probable that fibers shorter than the critical length will be pulled-out of the matrix [236].

The critical length of the ABS/SGF system can be calculated by utilizing the following relationship [20]:

$$L_c = \frac{(r_f)(\sigma_{fu})}{\tau} \tag{4.8}$$

where L_c is the critical length, r_f is the radius of fibers, σ_{fu} is the ultimate strength of the fibers and τ is the interfacial strength of the composite. Employing ultimate strength and diameter of fiber as 3450 MPa and 13μm respectively, reported by the manufacturer, and the interfacial strength between APS sized glass fibers and ABS as 23.5 MPa reported by Pissanova and Mäder from the single fiber pull-out method [88], the critical length of 954 μm can be calculated from Equation (4.8). The calculated critical length of the fibers is much larger than the average fiber lengths; therefore the pull-out of most of the fibers is inevitable during the loading of composite.

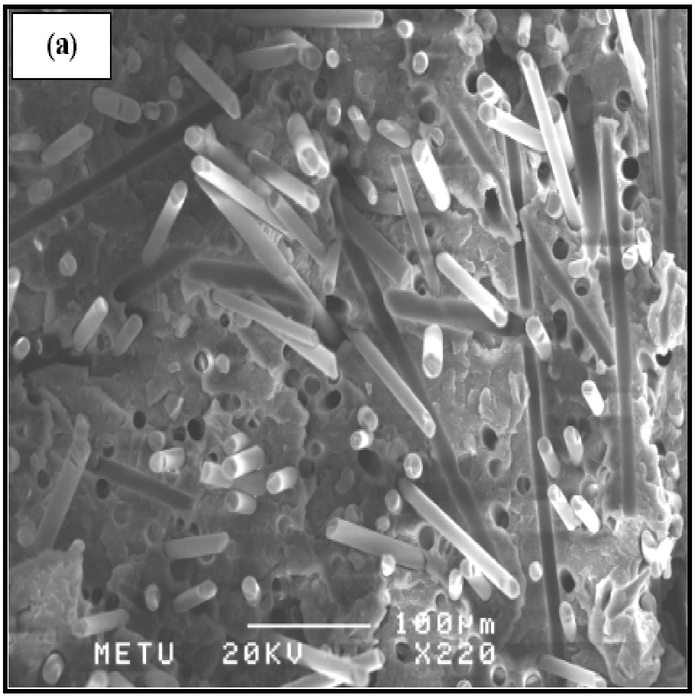

Figure 4.46 SEM micrographs of tensile fracture surfaces of ABS/30wt% SGF composites processed at a barrel temperature profile of 195-210-210-215-220 °C and screw speed of (a) 100 rpm

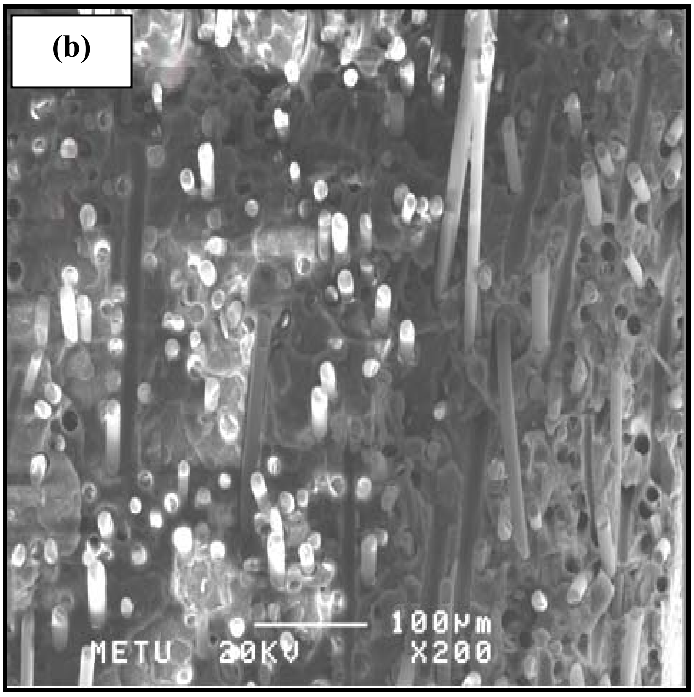

Figure 4.46 (Cont'd) SEM micrographs of tensile fracture surfaces of ABS/30wt% SGF composites processed at a barrel temperature profile of 195-210-210-215-220 °C and screw speed of (b) 250 rpm

4.2.3.2 Barrel Temperature Profile

The viscosity of the melt containing glass fibers depends on the viscosity of the polymer matrix as well as the process temperature. In order to avoid unfavorable shearing conditions, the melt temperatures should be kept as high as tolerable regarding thermal degradation. For the protection of fibers, a higher processing temperature and consequently low melt viscosity would be advantageous; since higher length enhances higher mechanical performance [244]. From this point of view, the fiber length distributions as a function of barrel temperatures are shown in Figure 4.47.

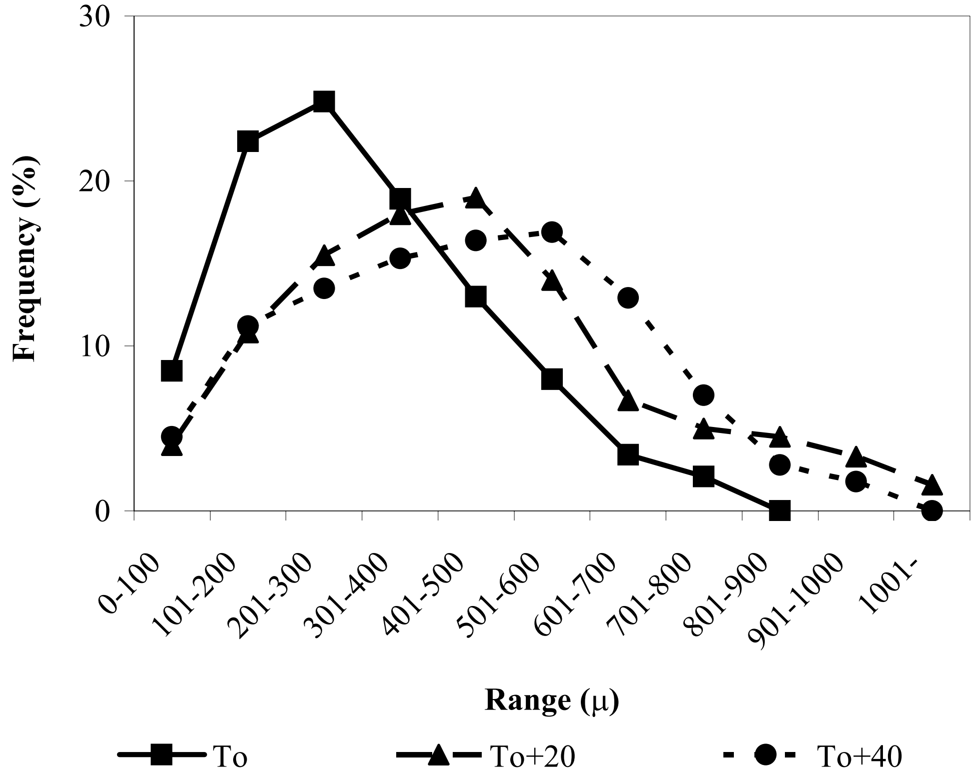

Figure 4.47 Fiber length distributions of SGF/ABS composites processed at barrel temperature profiles of 195-210-210-215-220°C (To), 195-230-230-235-240°C (To+20) and 195-250-250-255-260°C (To+40)

It can be observed that as the temperature increases, less fiber degradation occurs. As a result, the average fiber length value increases. The variation of mechanical properties with respect to the change in barrel temperature is given in Table 4.8 (runs 6, 8 and 9).

The increase in tensile strength and modulus as barrel temperature increases is due to the increase in fiber length that provides efficient load bearing capacity with 20°C of increase (Run 8). The sharp decrease in modulus at 40 °C of increment (Run 9) can be attributed to the thermal degradation of ABS matrix, which was observed as a darkening of colour during processing.

The strain values show a slight variation, but this variation is in the range of the experimental errors. It can be stated that no significant effect of temperature is observed on the strain at break values of composites produced at different processing temperatures.

Similar to the tensile modulus, values of flexural modulus are improved from Run 6 to Run 8 as the fiber length increases. The decrease in Run 9 can be again interpreted as thermal degradation of ABS. The degradation effect is somehow not observed in the case of impact strength.

4.2.4 Effects of Blend Composition, Compatibilizer Type and Content on the Morphologies and Mechanical Properties of ABS/PA6/SGF Composites

The properties of the glass fiber reinforced composites depend on the properties of matrix, fibrous glass and the interphase formed between them. Up to this part, the effects of interfacial adhesion and final fiber dimensions were investigated. The properties of the matrix have also great influence on the properties of ABS/PA6/SGF composites. The properties of the matrix were dominated by the compatibility of the phases and blend ratio. As shown in the previous part, EnBACO-MAH yielded much finer morphology, consequently, much improved mechanical properties rather than EMA-GMA. Therefore, EnBACO-MAH was also used as a compatibilizer in the SGF composites. In the matrix of the composites, the ABS/PA6 part was (100-x) % of the blend, where x is the compatibilizer weight percent in the blend which varied as 0, 5 and 10. The samples were named in the order of ABS/PA6/Compatibilizer by giving the corresponding compositions.

Figure 4.48 shows the tensile modulus of ABS/PA6/SGF composites as the function of PA6 and compatibilizer content. As it is seen from the graph that the dependence of tensile modulus on the PA6 content is almost linear regardless of compatibilizer content. The lowest modulus value measured in the absence of compatibilizer possibly due to the lower modulus of the matrix. As a matter of fact, there are two different competing mechanisms here in compatibilized blends based composites. One of them is improved interfacial adhesion between blend components with the addition of compatibilizer and the other is the softening of the matrix growing out of the elastomeric nature of the compatibilizer. The first case seems to be effective in the presence of 5% compatibilizer in which higher modulus values are obtained. On the other hand, as the compatibilizer content was doubled to 10%, the softening effect becomes dominant. However, one should note that in both two cases, the modulus of the composites were higher than that of incompatibilized blend based composites.

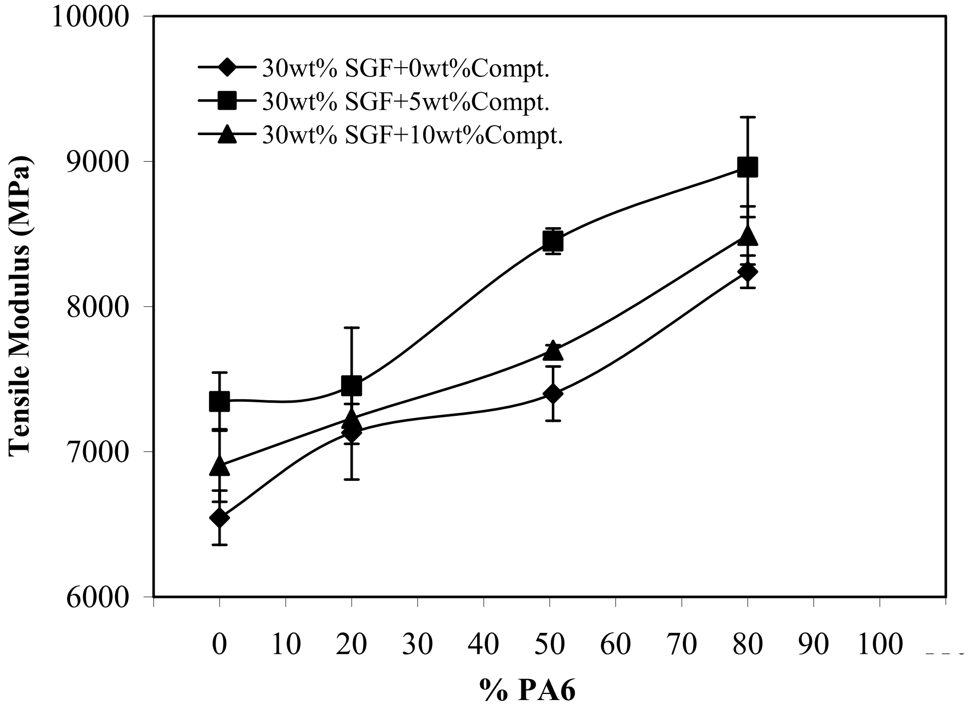

Figure 4.48 Tensile modulus of ABS/PA6/SGF composites as the function of PA6 and compatibilizer content

Yield strength of ABS/PA6/SGF composites as the function of PA6 and compatibilizer content are given in Figure 4.49. Yielding behavior of the composites are strongly designated by the interfacial adhesion [240, 241, 245-248]. The increasing PA6 content in the composite positively influenced the yield strengths of the composites. The possible reason can be the enhanced extend of interaction between aminosilan on the fiber surface and the PA6. When the effect of the compatibilizer content is considered, the lowest yield strength values were obtained in the absence of compatibilizer. On the other hand, addition of 5% compatibilizer resulted in higher yield strengths for each blend ratio. The difference between yield strength values was very small at 20% and 50% PA6; however at 80% PA6 the difference was very significant. The values measured for 10% compatibilizer existed between 0% and 5% compatibilizer.

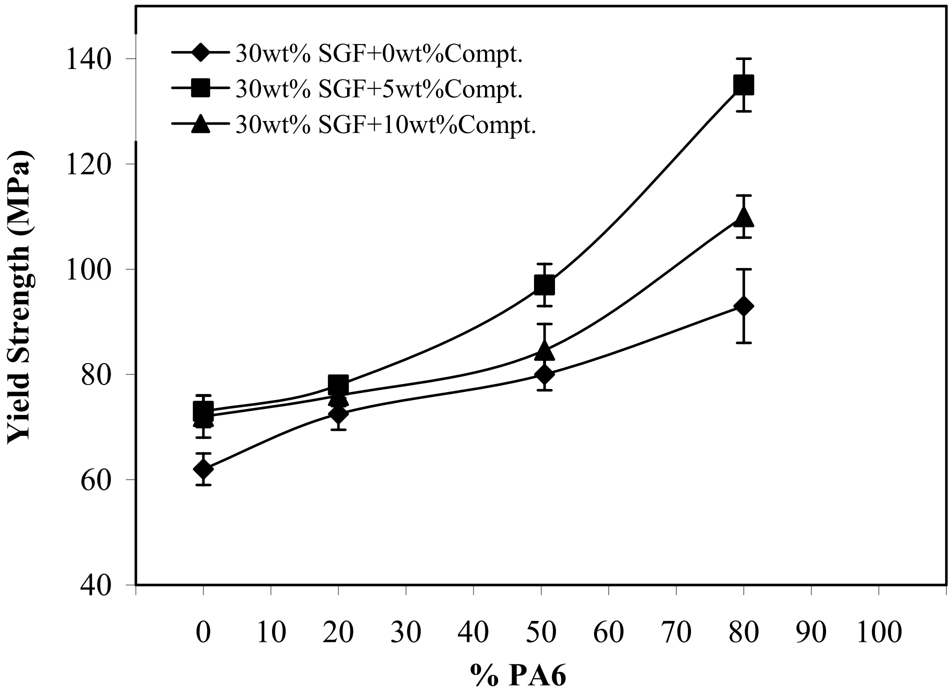

Figure 4.49 Yield strength of ABS/PA6/SGF composites as the function of PA6 and compatibilizer content

The critical fiber length of the compatibilized ABS/PA6/SGF composites could be calculated using Equation 4.8, if the adhesion strength between fibers and the matrix were known. In this case, by assuming well-established adhesion at fiber/matrix adhesion, consequentially failuring in matrix phase, Equation 4.8 was modified as [20, 233]:

$$\tau = \frac{1}{2}\sigma_m = \frac{\sigma_f d}{2l_c} \tag{4.9}$$

where τ is the interfacial adhesion which is equal to half of the matrix tensile strength σ_m (see Table 4.9) in the presence of well-established adhesion, σ_f is the tensile strength of the glass fiber used, which is 3500 MPa, d is the fiber diameter and l_c is the critical fiber length. The assumption made was proved by SEM analysis, which will be discussed in forthcoming paragraphs. Figure 4.50 shows the critical fiber length of ABS/PA6/SGF composites as the function of PA6 and compatibilizer content. The values vary between 600 and 1250 μ, however average fiber length of ABS/PA6/SGF measured experimentally were all below 500 μ (see Figure 4.51). It should also be noted that average fiber length values increased with increasing PA6 content in the blend. This can be attributed to the decreasing viscosity of the system with increasing PA6, which was shown with MFI measurements above.

Table 4.9. $\sigma_m/2$ of ABS/PA6/Compatibilizer matrix, (MPa)

		$\sigma_m/2$, (MPa)		
	ABS/PA6 Ratio	**EnBACO-MAH Content (%)**		
		0	**5**	**10**
$\sigma_m/2$ (MPa)	**100/0**	21	23	18
	80/20	22	23	19
	50/50	19	24	18
	20/80	29	26	22
	0/100	34	-	-

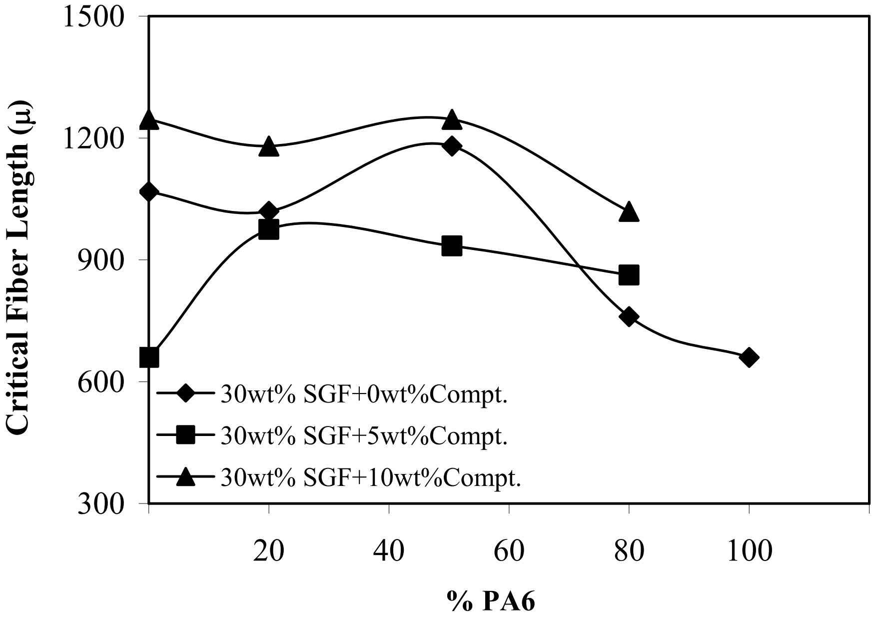

Figure 4.50 Critical fiber length of ABS/PA6/SGF composites as the function of PA6 and compatibilizer content

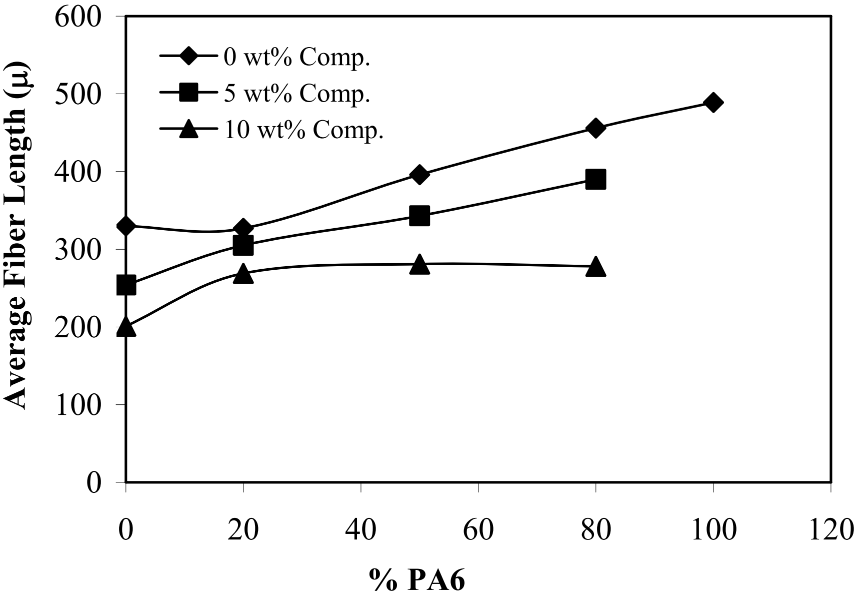

Figure 4.51 Average fiber length of ABS/PA6/SGF composites as the function of PA6 and compatibilizer content

Figure 4.52 shows strain at break values of ABS/PA6/SGF composites as the function of PA6 and compatibilizer content. It is seen that percent strain at break values increase with the increasing PA6 in the matrix. Moreover, increasing compatibilizer content also resulted in an increase in the percent strain at break values.

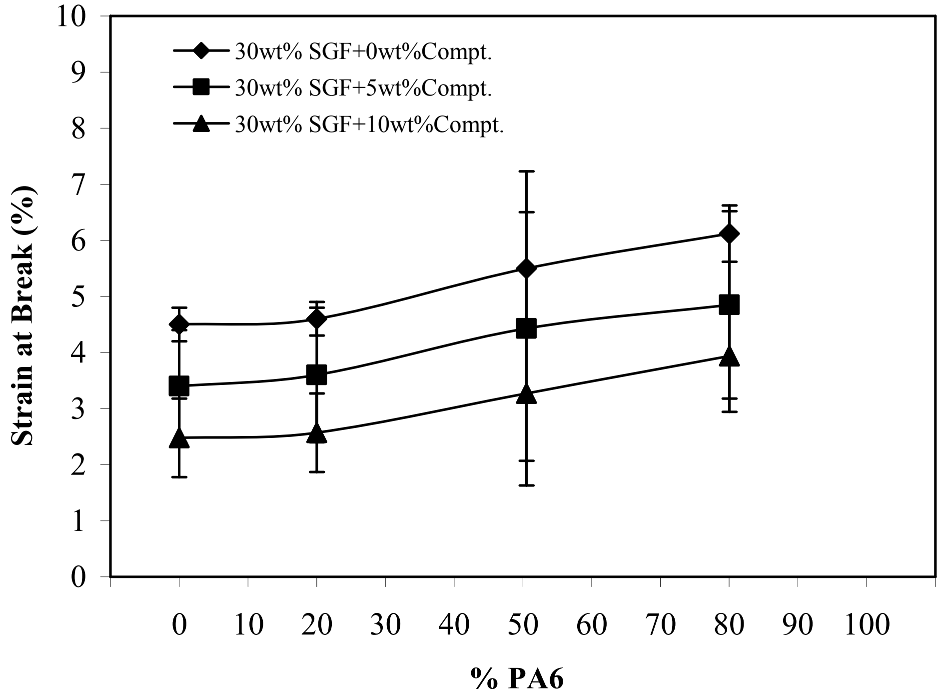

Figure 4.52 Strain at break values of ABS/PA6/SGF composites as the function of PA6 and compatibilizer content

Figure 4.53 shows the notched charpy impact strengths of ABS/PA6/SGF composites as the function of PA6 and compatibilizer content. The most striking effect of the compatibilizers was observed in impact strength of the composites. In the absence of compatibilizers, impact strength values were decreasing with PA6 concentration. When compatibilizers were added to the system, impact strength of composites was dramatically increased, and moreover at 50/50 blend ratio a maximum was obtained. 5% compatibilizer improved impact strength more than 10% for 100/0, 80/20 and 50/50 blends.

The SEM micrographs of tensile fracture surfaces of 30wt% SGF reinforced as a function of blend composition are given in Figure 4.54. It can be seen in SEM micrograph of SGF reinforced 80/20/5 blends that most of the fibers were pulled-out leaving dark holes in the matrix indicating poor interaction between fibers and matrix. Short fibers were aligned through flow direction however some longer fibers were misaligned. When the PA6 content is increased to 50%, the fibers became longer probably due to the reduced viscosity. The number of pull-out fibers is seemed to be lowered. Alignment of the fibers is less ordered due to the higher average fiber length. Similar to 50/50/5 blends, nearly any fiber was not pulled-out in the case of 20/80/5 blends. This can be attributed to the increased extent of interaction between silane coupling agent over the fiber surface and polymer matrix.

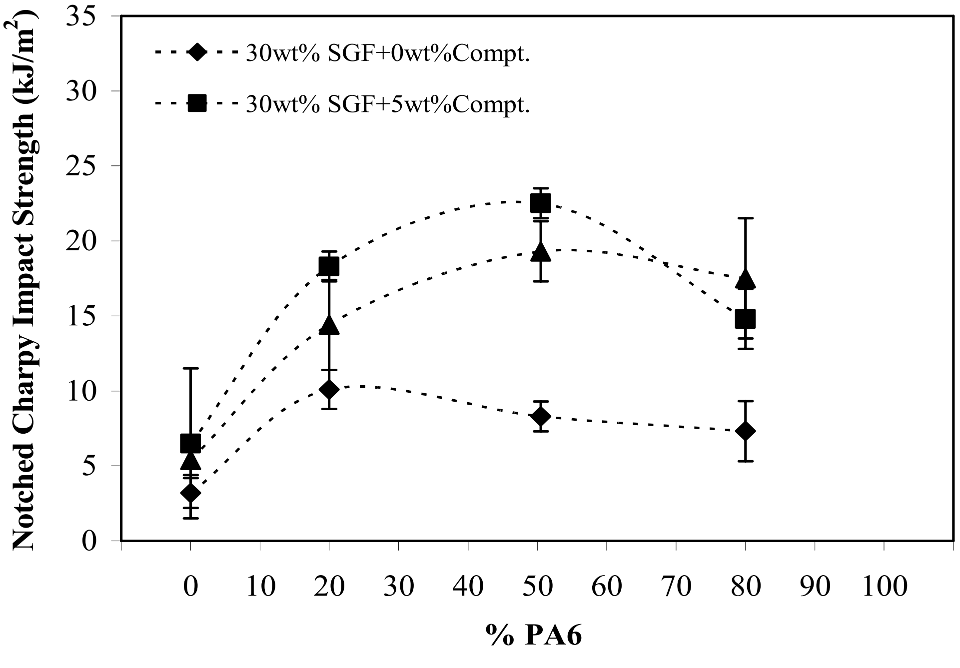

Figure 4.53 Notched charpy impact strengths of ABS/PA6/SGF composites as the function of PA6 and compatibilizer content

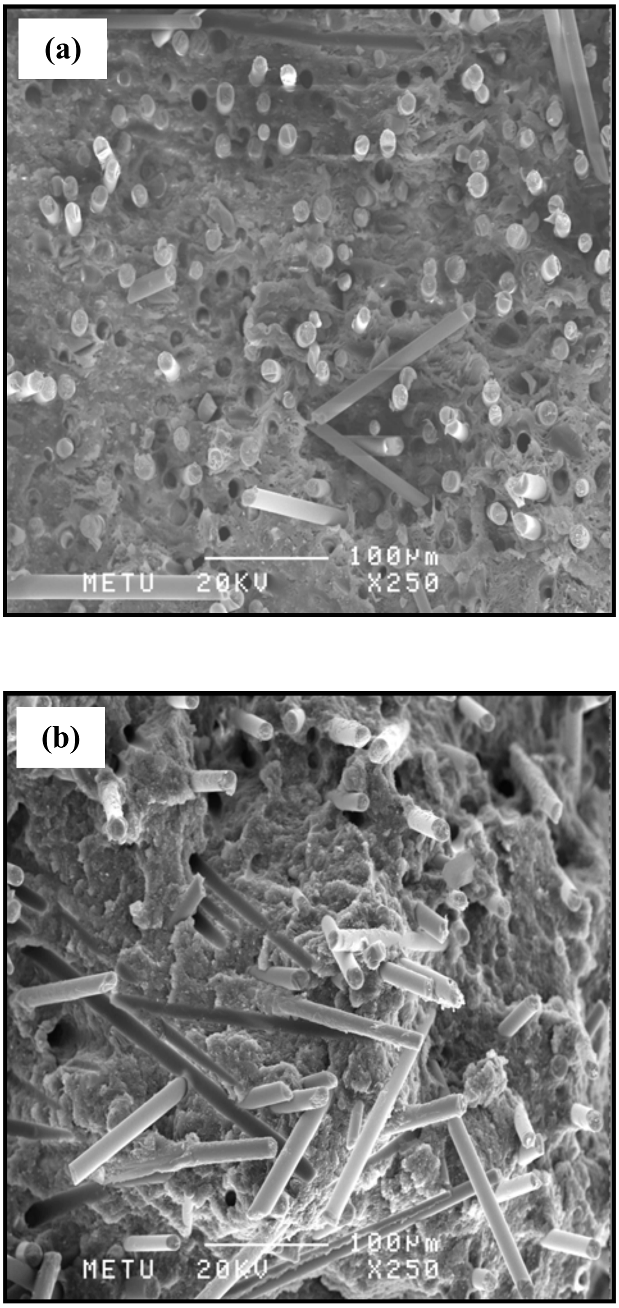

Figure 4.54 SEM micrographs of tensile fracture surfaces of 30wt% SGF reinforced (a) 80/20/5 (b) 50/50/5

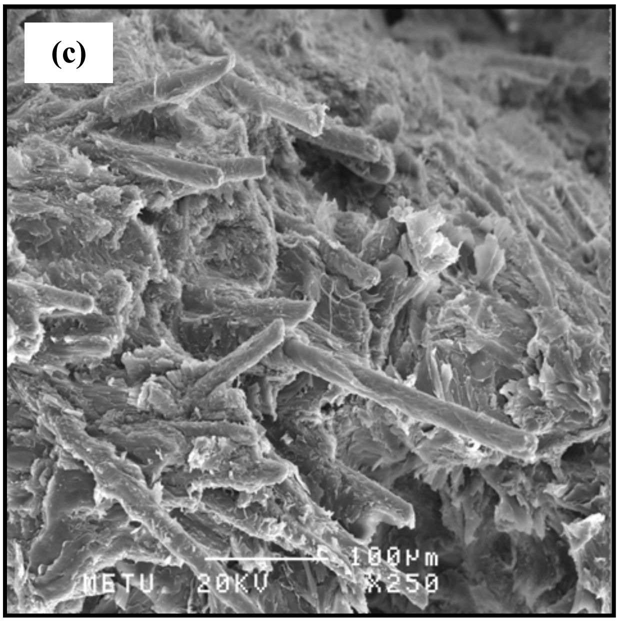

Figure 4.54 (Cont'd) SEM micrographs of tensile fracture surfaces of 30wt% SGF reinforced (c) 20/80/5 blends (x 250 magnification)

Figure 4.55 shows higher magnification SEM micrographs of fracture surfaces of SGF composites as the function of matrix composition. It is observed from Figure 4.55-a that some of the fibers were coated with a layer of polymer; however there still exists some uncovered fibers. As the matrix was zoomed in, the cavitated particles (possibly compatibilizers or PA6 particles) became visible. This cavitation of rubbers absorbs energy during fracture and forms new areas over which energy can be spread; therefore, increasing impact strength with the addition of PA6 and compatibilizer resulting from this energy absorbing mechanism. When the failure type was focused, it can be observed that the failure of the composite occurred in the matrix phase close to the fiber surface, which is typical for fiber reinforced systems with good interfacial interaction.

The morphology of 50/50/5 blend system resembles that of 20/80/5 blends (see Figure 4.55-b). Some of the fibers were coated a sheath of polymer matrix. The cavitation of the particles is still visible in the matrix phase.

As the matrix composition was changed to 20/80/5 blends (see Figure 4.55-c), it was observed that all the fibers were coated with a thick sheath of polymer. The zoomed picture taken from the surface of the fibers showed that the matrix was plastically deformed possibly due to the matrix-shear yielding. In this case, the cavitated dispersed particles were not obvious differing from the other compositions.

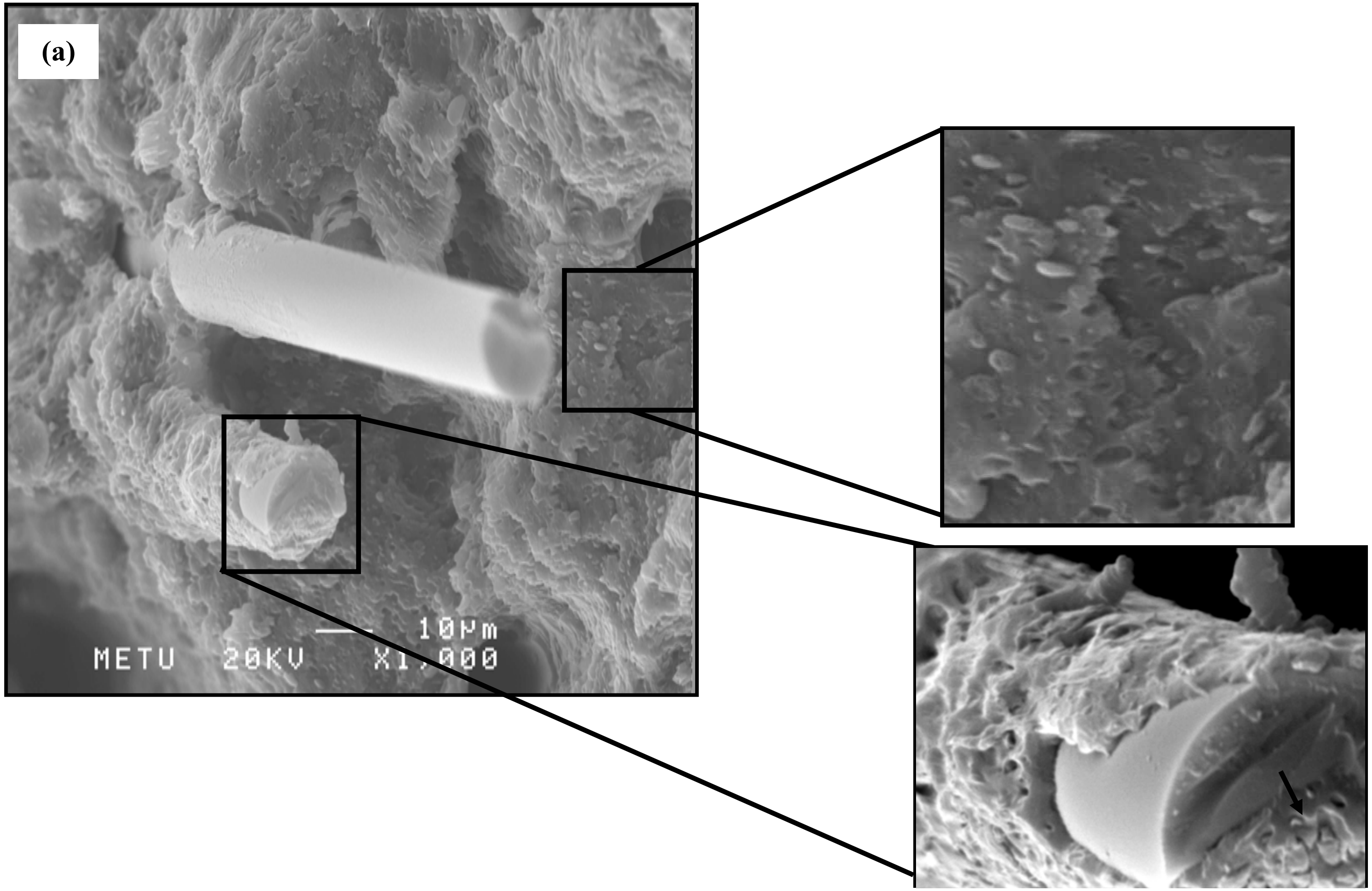

Figure 4.55 SEM micrographs of tensile fracture surfaces of 30wt% SGF reinforced (a) 80/20/5

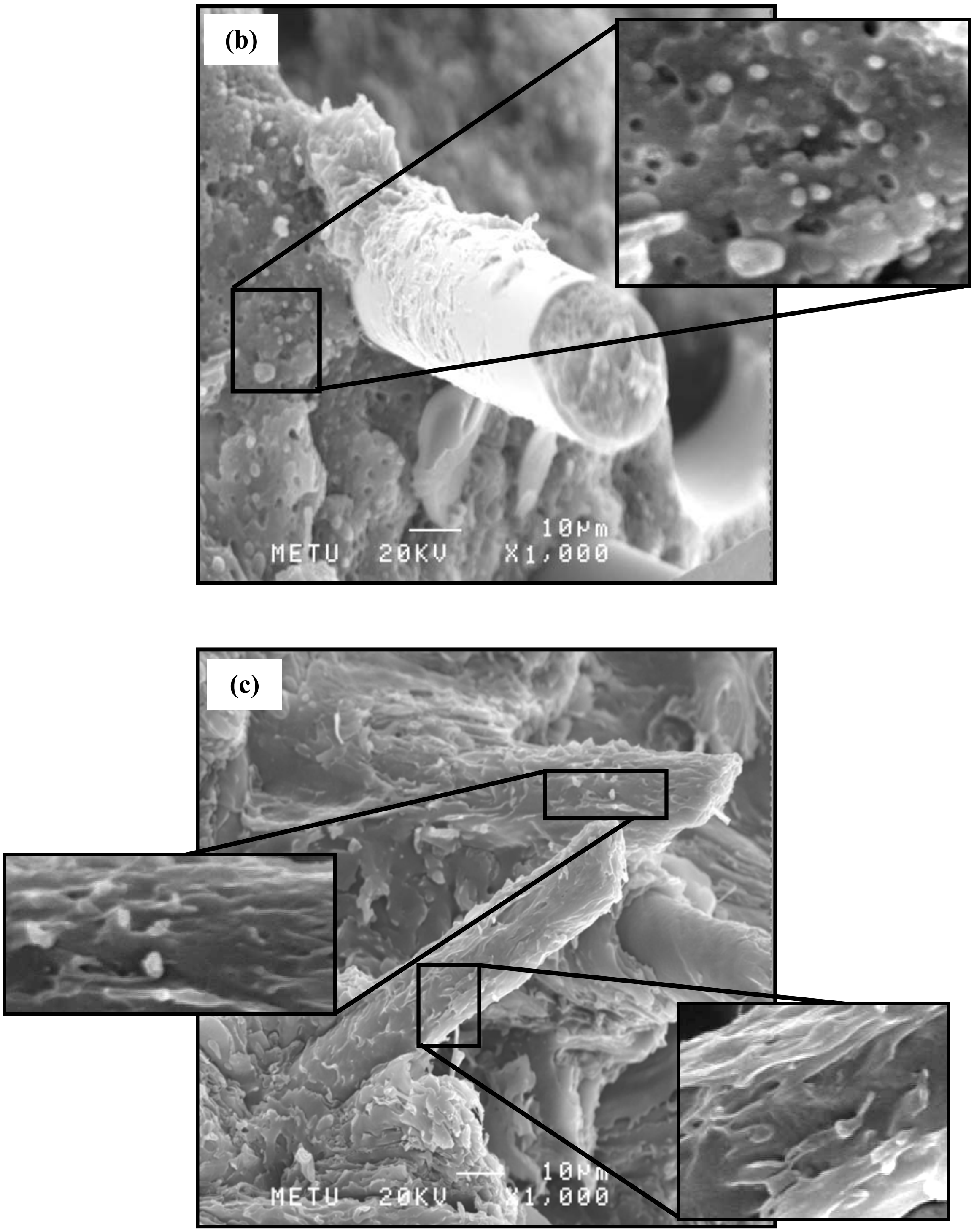

Figure 4.55 (Cont'd) SEM micrographs of tensile fracture surfaces of 30wt% SGF reinforced (b) 50/50/5 (c) 20/80/5 blends (x 1000 magnification)

4.3 Nanocomposites Based on ABS/PA6 Blends

4.3.1 Effects of Matrix Composition, Clay Loading Level and Screw speed on the Dispersability, Morphology and Mechanical Properties of Nanocomposites

In this part of the study, effects of matrix composition, clay loading level and screw speed of compounder on the dispersability, morphology and mechanical properties of organoclay based compatibilized ABS/PA6 nanocomposites were investigated. In the blends, the ABS/PA6 part was (100-x) % of the blend, where x is the compatibilizer weight percent in the blend which was 0 and 5 %. The samples were named in the order of ABS/PA6/Compatibilizer by giving the corresponding compositions.

Figure 4.56 compares the X-Ray diffraction patterns for the 5% organoclay and nanocomposites produced from compatibilized ABS/PA6 blends at different ratios. The X-Ray pattern for organoclay (see curve (a) in Figure 4.56) shows a broad intense peak at $2\Theta=5.0°$, corresponding to a basal spacing (d_{001}) of 18.0 Å. The nanocomposites based on 0/100/0 and 20/80/5 blends (see patterns (d) and (f) in Figure 4.56) do not show a characteristic basal reflection, which is an indication of completely exfoliated structure. The nanocomposites based on 100/0/0 blend (pattern (b) in Figure 4.56) has a peak at $2\Theta=2.44°$ corresponding to a basal spacing of 36.18 Å, which shows an intercalated structure. Stretz et al. studied the effect of organic modifier type on the exfoliation in ABS/OMLS nanocomposites [249]. They used different type of organoclays with different levels of polarities depending on the organic modifier type used. However, X-Ray studies showed that even in the case of the most polar clay, which was the same clay used in the current study, only intercalated structures are obtained. This result coincides with results of X-Ray investigation of ABS/OMLS nanocomposites given in the current study.

When the blend based nanocomposites are concerned, addition of PA6 to the system resulted in an increase in the exfoliation of the organoclays. The sharp peak appeared in the case of ABS based nanocomposites significantly broadened and got shallow for both 80/20/5 blend and 50/50/5 blend, which indicates that most of the clays were exfoliated but intercalated platelets still existed. However, when the ABS/PA6 ratio was moved to 20/80, the peak completely disappeared as in 0/100/0 based nanocomposites. The results of the X-Ray analysis imply that organoclays tend to exfoliate in the presence of the PA6, which is a result of chemical affinity between organoclays and PA6 chains.

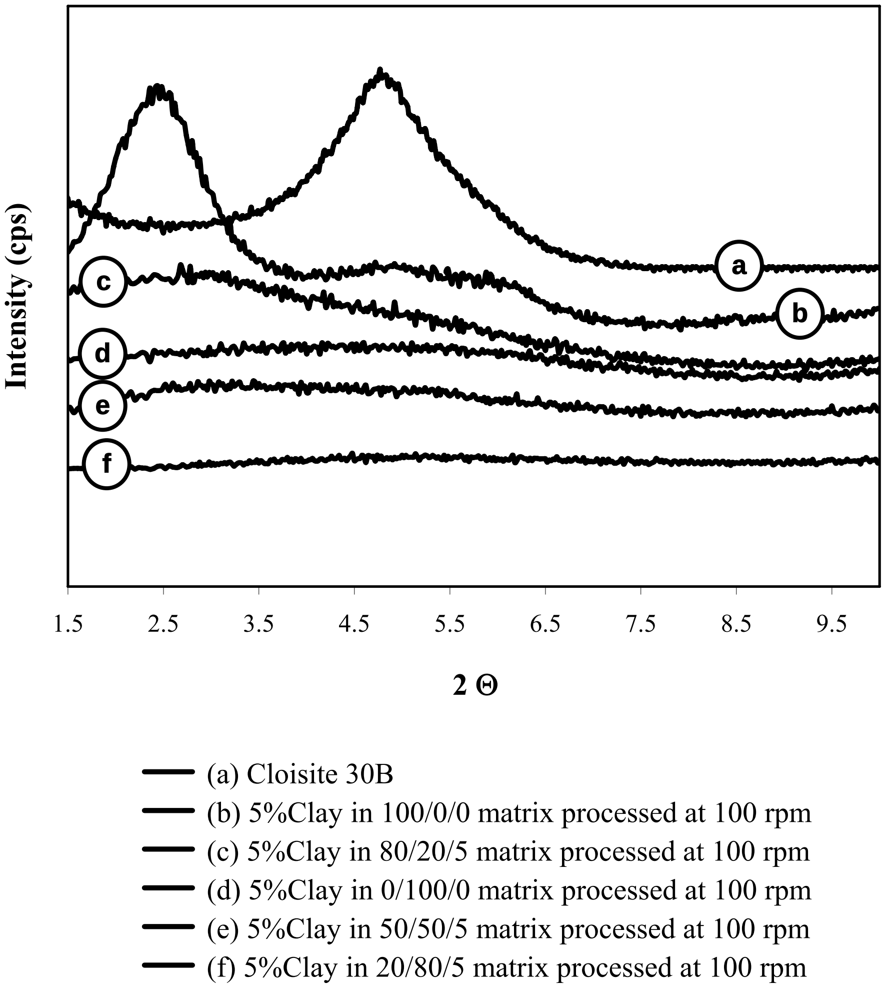

Figure 4.56 X-Ray patterns for organoclay and nanocomposites (The curves were vertically offset for clarity)

Scanning electron microscopy (SEM) was used to observe the effect of matrix composition and screw speed on the morphologies of ABS/PA6 blends and effect of matrix composition on the morphologies of ABS/PA6 blends based nanocomposites.

Because of the highly polar carboxylic acid and amine end groups of PA6, binary blends of ABS/PA6 are immiscible. Therefore, to obtain enhanced mechanical property, which is an outcome of fine morphology; these materials have to be compatibilized. Previous studies conducted showed that the olefin based copolymers, such as carbonmonoxide modified ethylene-n butyl acrylate-maleic anhydride (EnBACO-MAH) or ethylene-methyl acrylate-glycidyl methacrylate (EMA-GMA), yielded a fine morphology for the blends in which ABS or PA6 was dispersed with in each other [250, 251]. In the current study, ABS and PA6 were compatibilized by using EnBACO-MAH and the amount of the compatibilizer was kept constant (5 wt% of the matrix) throughout the experiments.

Figure 4.57-a shows the SEM micrograph of incompatibilized 80/20 blend system in which PA6 is dispersed in ABS matrix. It is obvious from the micrograph that the morphology is very coarse and the shape of the particles diverged from spherical form with average diameter of 17.4 microns. When the compatibilizer (EnBACO-MAH, at 5 wt%) was added to the system, the dispersed phase size of spherical particles became 1.72 microns, which is finer than the case of incompatibilized blend system (see Figure 4.58-a). Actually, the principle aim of the interfacial modification in immiscible polymer blends via addition of compatibilizers is to decrease the particle size and to narrow the particle size distribution [252, 253]. The reason of this reduction in particle size is a result of decreasing interfacial tension and coalescence [254]. In Figure 4.58-b, the SEM micrograph of 80/20/5 blend system processed at 200 rpm can be observed. According to Taylor model [255, 256], which assumes a single Newtonian drop deforming in shear flow:

$$D = \frac{4\sigma(\eta_r + 1)}{\dot{\gamma}\eta_m\left(\frac{19}{4}\eta_r + 4\right)} \quad \text{when} \quad \eta_r < 2.5 \tag{4.10}$$

where D is the dispersed particle diameter, σ is the interfacial tension, $\dot{\gamma}$ is the shear rate and the η_r is the ratio of the viscosity of the dispersed phase to the matrix phase (validity of $\eta_r < 2.5$ will be discussed in the forthcoming section). It is seen in the equation that the shear stress, $\tau = \dot{\gamma}\eta_m$ is inversely proportional to the dispersed phase size. This means that an increase in shear stress, which can be arranged by varying the screw speed for a given viscosity of the material to change the shear rate, can decrease the dispersed phase size. As a result of image analysis, the reduction in the average dispersed particle diameter is about 62% (1.72 μ to 1.06 μ), although the increase in screw speed is twofold.

SEM micrographs given in Figure 4.59-a and b show the phase morphologies of the ABS/PA6 blends at the equal amounts, 50/50 by weight. The dispersed phase morphology of incompatibilized 50/50 blends system seen in Figure 4.57-b became co-continuous, which means both ABS and PA6 phases are continuous. According to Paul and Barlow model [257], a co-continuous morphology can be observed when the ratio of volume fractions, Φ_1 and Φ_2 is equal to the ratio of viscosities, η_1 and η_2 of phases 1 and 2:

$$\frac{\Phi_1}{\Phi_2} = \frac{\eta_1}{\eta_2} \tag{4.11}$$

The volume ratios, $\Phi_{ABS}/\Phi_{PA6} = 0.965$ was calculated by using the melt densities of the ABS and PA6 system at 230°C, respectively, 0.97 g/cm^3 and 0.96 g/cm^3. According to equation (4.11), η_{ABS}/η_{PA6} is expected to be around 1 to obtain a co-continuous morphology. This can also confirm the validity of equation (4.10). The change in the morphology for the 50/50 blend system with the addition of compatibilizer can be attributed to the increasing viscosity of the PA6 phase because of the possible grafting reaction between amine end groups of PA6 chains and maleic anhydride group of compatibilizer [174]. Therefore, the viscosity ratio is able to converge to the ratio of volume fractions. Similar results were obtained for the blends prepared in conventional twin-screw extruder. When the screw-speed is increased to 200 rpm, the co-continuous morphology still exists but in this case, the phases are much smaller because of the increased shear rate (see Figures 4.59 a and b).

Figure 4.60-a and b show the SEM micrographs of 20/80/5 blend system prepared at 100 and 200 rpm. In this case PA6 is the matrix and ABS is the dispersed phase. The addition of compatibilizer reduces the dispersed particle size from 16.6 μ (see Figure 4.57-c) to 1.56 μ. When the screw speed increased to 200 rpm, the dispersed particle size decreased almost 50% (from 1.56 μ to 0.69μ), which is an influence of the increasing shear rate.

Figure 4.61-a shows the SEM micrographs of fracture surface of 5% clay reinforced 80/20/5 blend system processed at 100 rpm. Even though the addition of the clay in polymer blends has usually been seen to promote the compatibility between the blend components [54, 258-260], the addition of clay to the blend disturbed the morphology of the blend. The spherical particles became lamellar, fibril-like or distorted spheres (i.e. ellipsoids) in the presence of clays. The average dispersed particle size was increased by the addition of the clay to the 80/20/5 blend system. When the 50/50/5 blend based nanocomposite is considered, addition of clay did not make any significant change to the co-continuity of the matrix. Figure 4.61-c shows the SEM micrographs of the fracture surface of 5% clay reinforced 20/80/5 blend based nanocomposite. Addition of clay to the matrix slightly decreased the average dispersed particle diameter from 1.56 μ to 1.20 μ. One can draw a conclusion by considering the influences of addition of clay to the blends that incorporation of clays tend to increase the viscosity of PA6 phase; therefore, when

PA6 was the dispersed phase, morphology became coarser because of the difficulty in droplet break-up as the viscosity ratio increased, or when PA6 was matrix, the dispersed particle size decreased because of the ease of droplet break-up due to the reduced viscosity ratio.

TEM micrographs of 80/20/5, 50/50/5 and 20/80/5 blend based nanocomposites containing 5% clay is shown in Figure 4.62 a, b and c, respectively. The black regions seen in Figure 4.62-a are the PA6 phase dispersed in grey continuous matrix, which is ABS. Clay layers are selectively dispersed in PA6 phase rather than ABS because of the great affinity between highly polar tails of the organic modifier molecule and PA6. This observation is also valid for 50/50/5 and 20/80/5 blends based nanocomposites (Figure 4.62 b and c). When the magnification of the TEM micrographs are increased (Figure 4.63 a and b), it can be better seen that most of the organoclays are highly exfoliated into single layers which were selectively localized in PA6. Stacks of two or three layers can also be observed in PA6, but mainly in the interphase region of ABS/PA6 (encircled in Figure 4.63-b). These agglomerations of the clay layers at the interfacial region was also observed for PA6/polypropylene blends based nanocomposites and it was attributed to the surface tension [261].

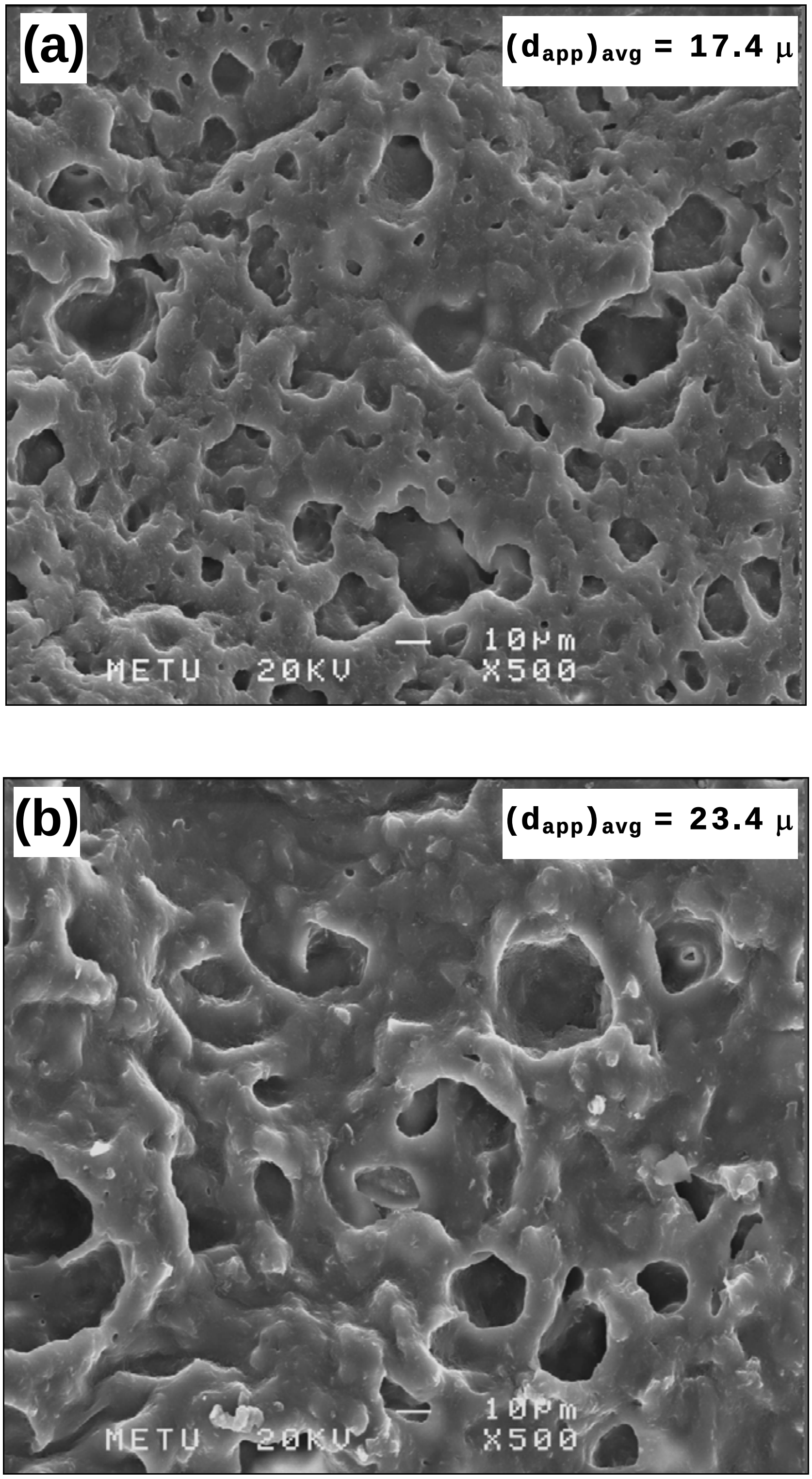

Figure 4.57 SEM micrograph of (x500) (a) incompatibilized 80/20 (b) incompatibilized 50/50

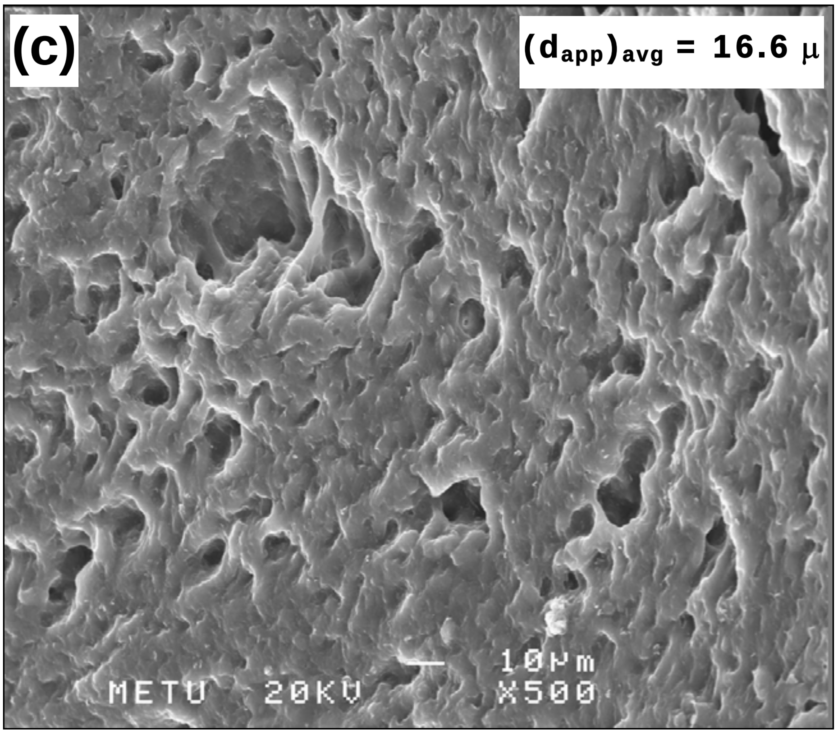

Figure 4.57 (Cont'd) SEM micrograph of (x500) (c) incompatibilized 20/80 blend system processed at 100 rpm (PA6 phase was etched-out by formic acid extraction)

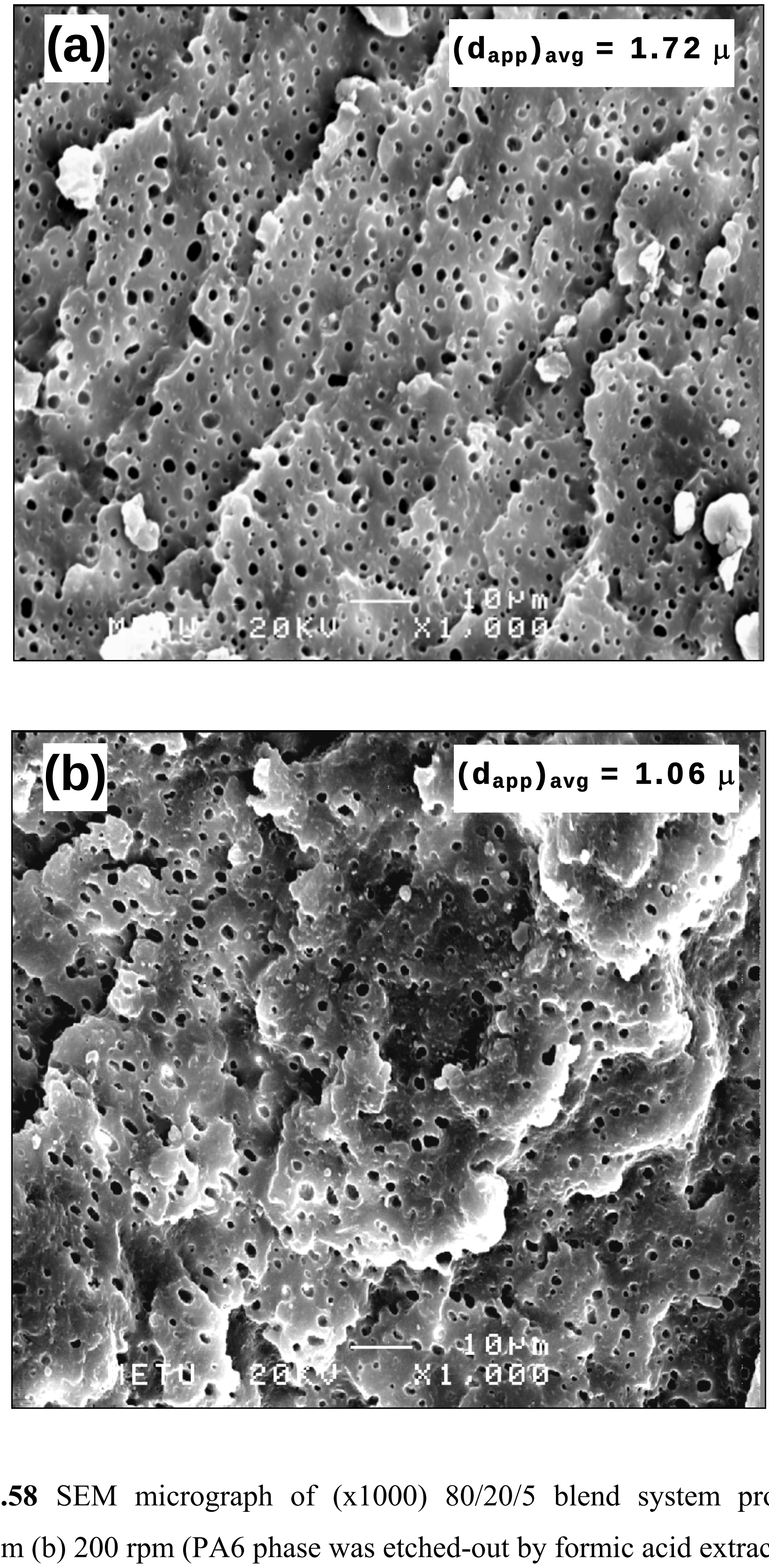

Figure 4.58 SEM micrograph of (x1000) 80/20/5 blend system processed at (a) 100 rpm (b) 200 rpm (PA6 phase was etched-out by formic acid extraction)

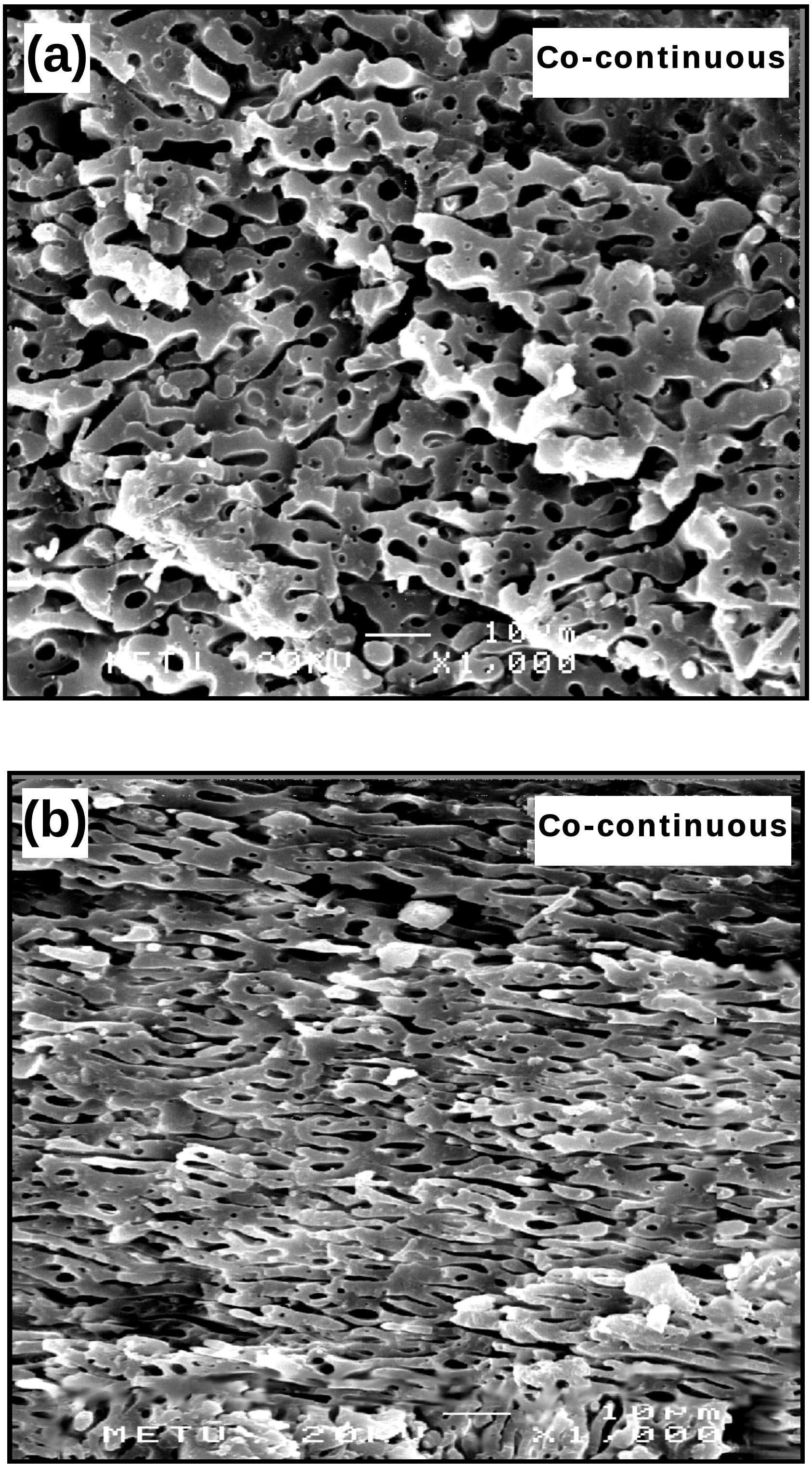

Figure 4.59 SEM micrograph (x1000) of 50/50/5 blend system processed at (a) 100 rpm (b) 200 rpm (PA6 phase was etched-out by formic acid extraction)

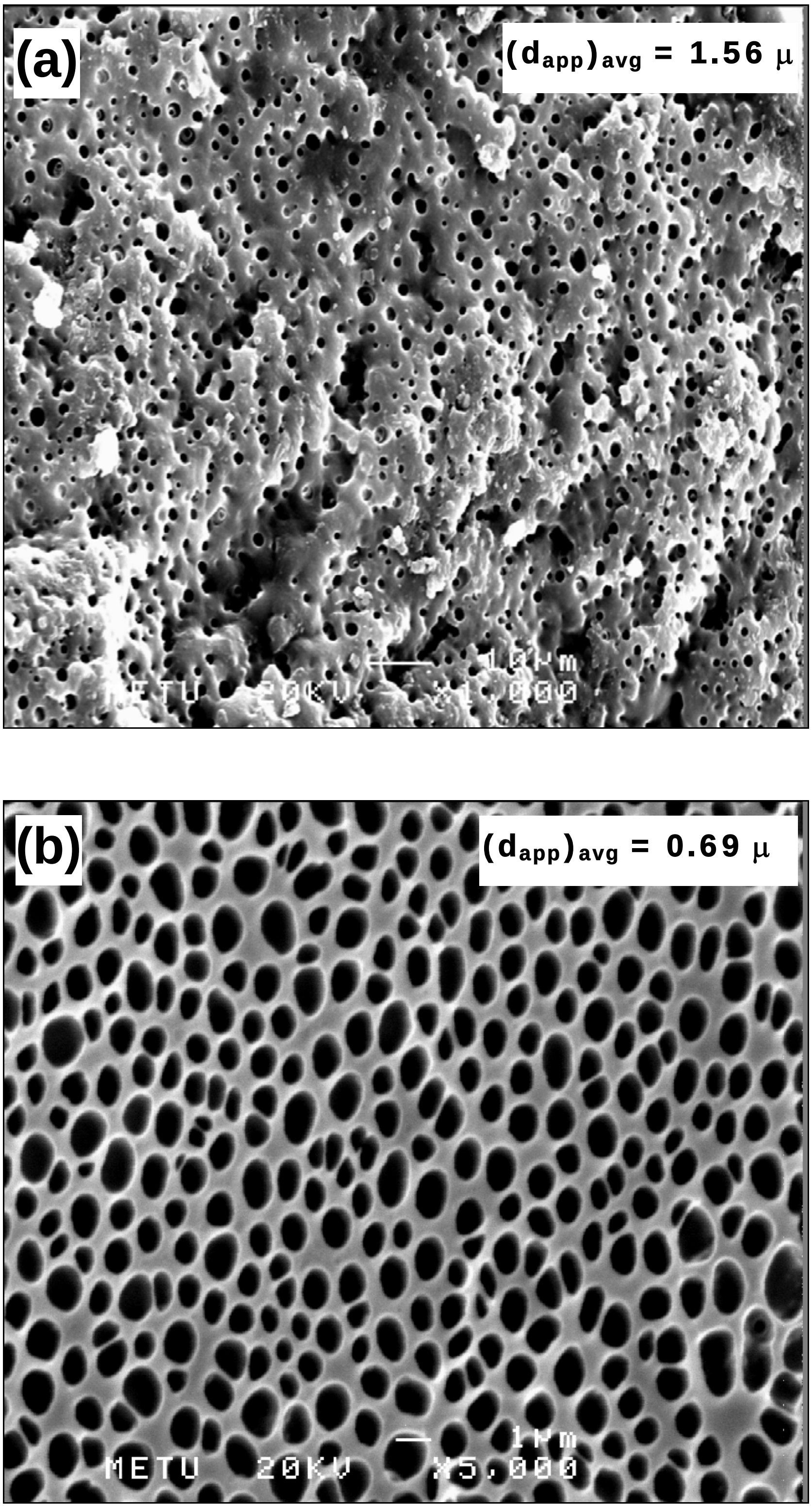

Figure 4.60 SEM micrograph of 20/80/5 blend system processed at (a) 100 rpm (x1000) (b) 200 rpm (x5000) (ABS phase was etched-out by THF extraction)

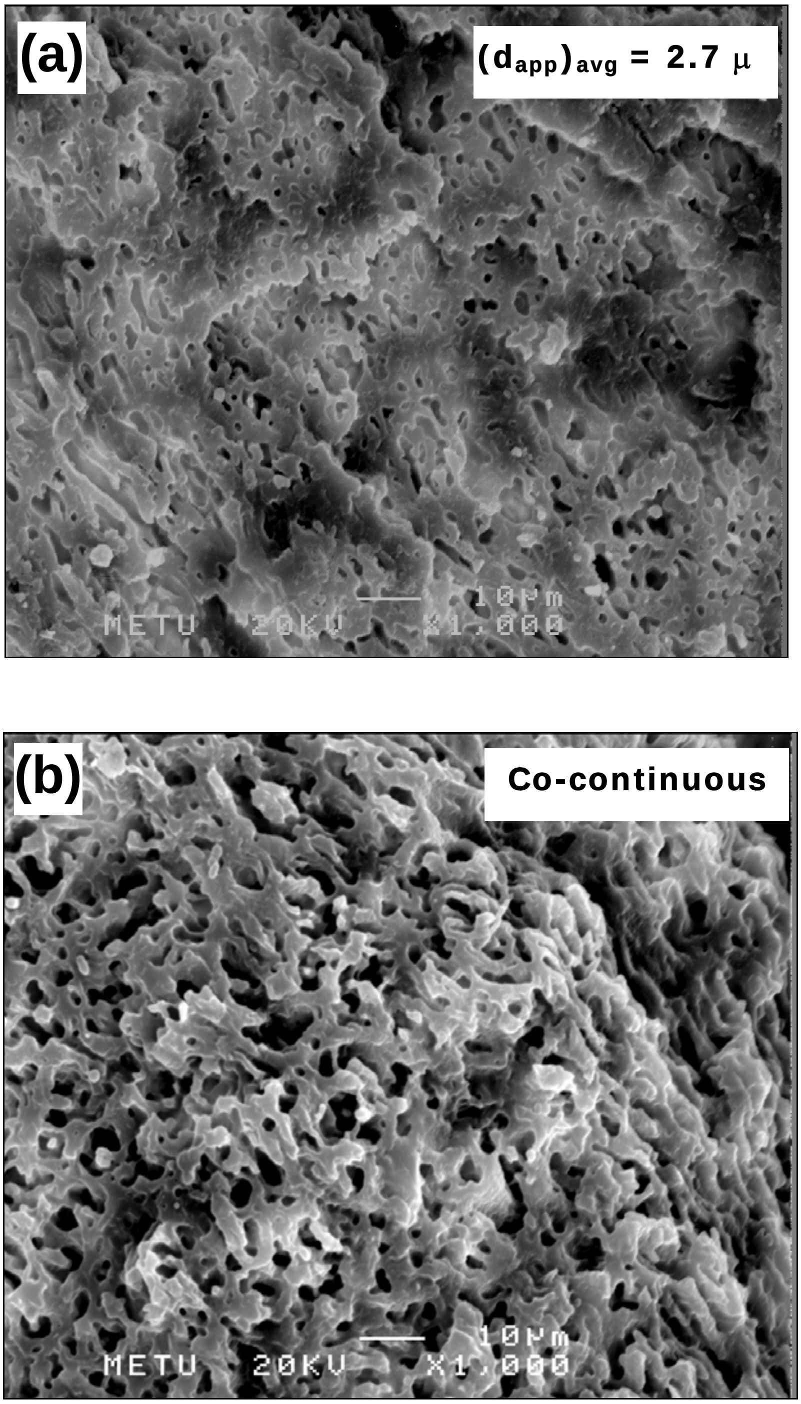

Figure 4.61 SEM micrograph (x1000) of nanocomposites at clay loading of 5% and processed at 100 rpm based on (a) 80/20/5 blend system (PA6 phase was etched-out by formic acid extraction), (b) 50/50/5 blend system (PA6 phase was etched-out by formic acid extraction),

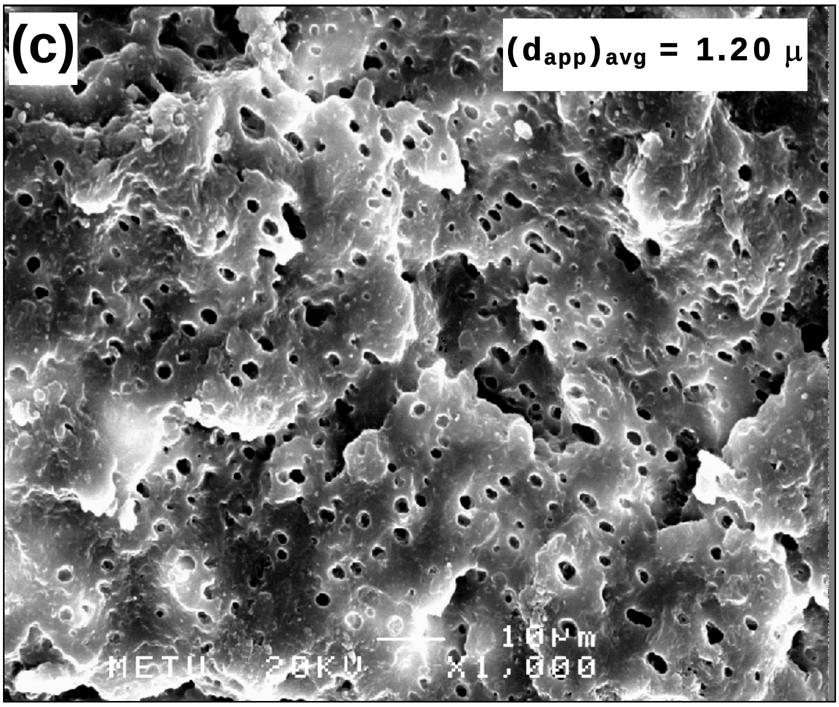

Figure 4.61 (Cont'd) SEM micrograph (x1000) of nanocomposites at clay loading of 5% and processed at 100 rpm based on (c) 20/80/5 blend system (ABS phase was etched-out by THF extraction)

The properties of organoclay based nanocomposites are highly dependent on the average aspect ratio (AR_{avg}) of the particle, which is the ratio of the average length (l_{avg}) to average particle thickness (t_{avg}) in the form of single platelets or stacks [262, 263]. In most cases, although the high levels of exfoliation are desired; mixture of exfoliated and intercalated structures can be obtained because of lack of thermodynamic favorability and insufficient shear. Because of the presence of these kinds of structures, the AR_{avg} of the particles can exhibit variations.

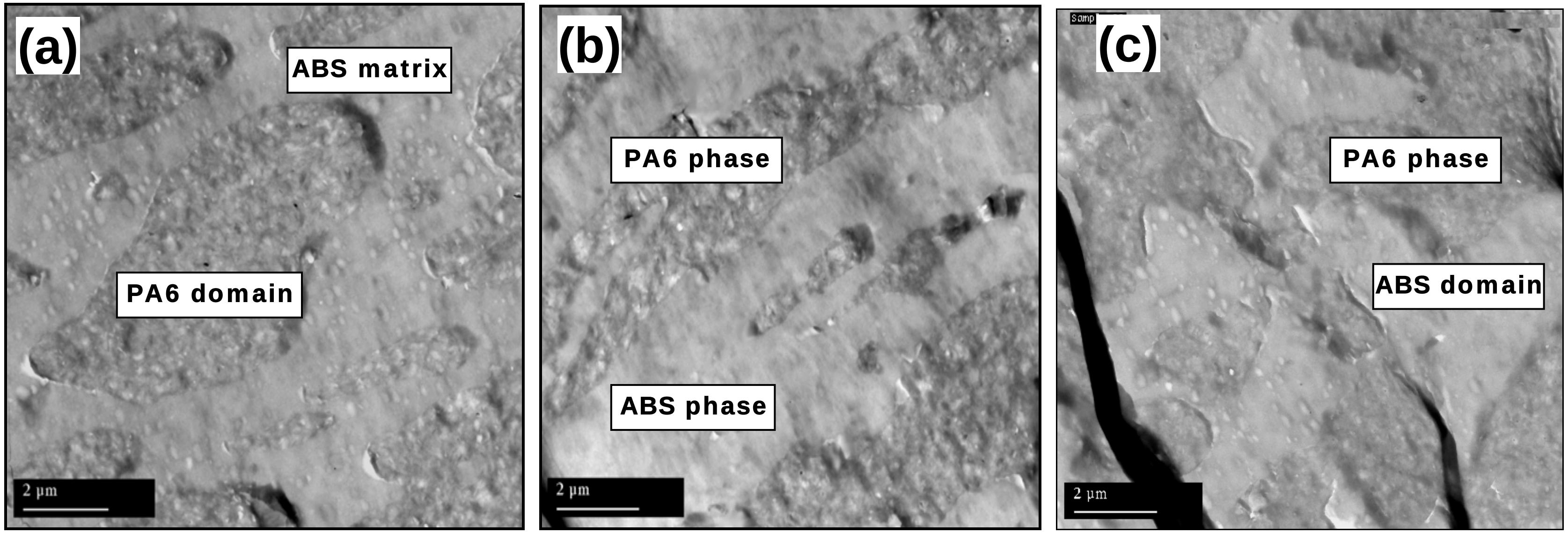

Figure 4.62 TEM micrographs of nanocomposites based on 5% clay reinforced blends (a) 80/20/5 (b) 50/50/5 (c) 20/80/5 processed at 100 rpm (scale bar corresponds to 2 μ)

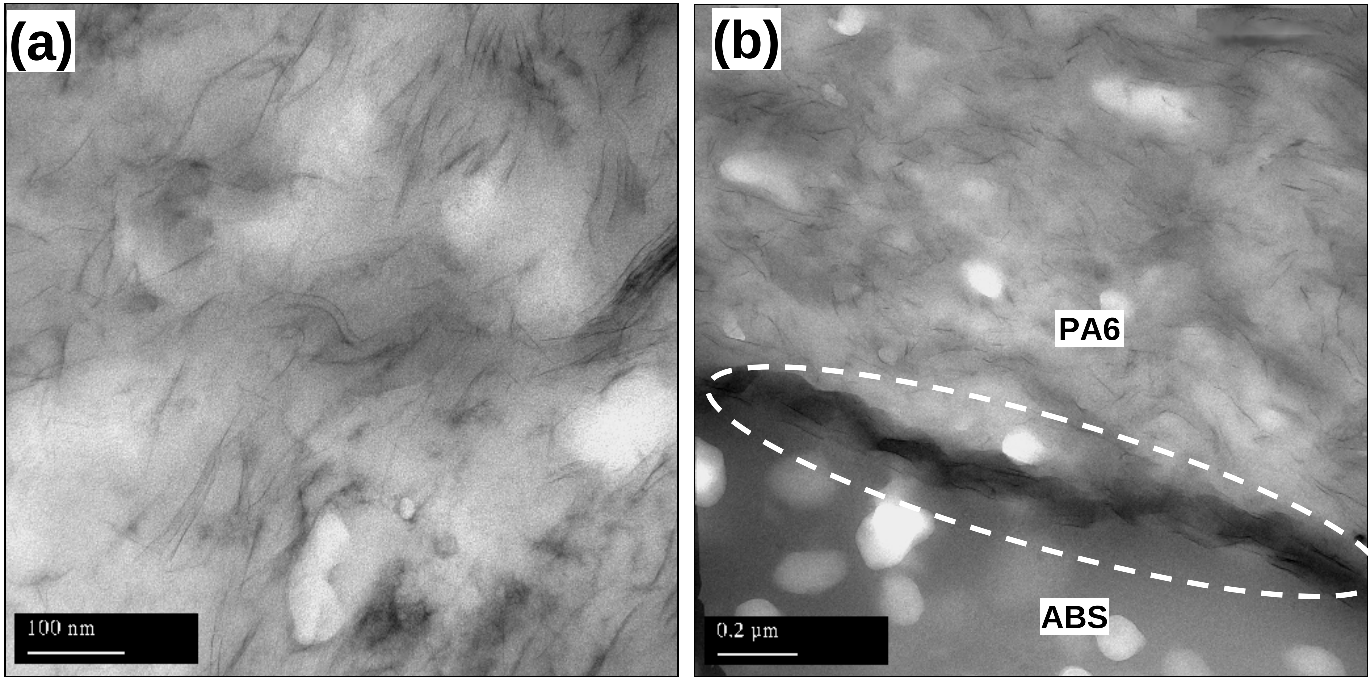

Figure 4.63 TEM micrographs of (a) PA6 phase (b) ABS/PA6 interphase in nanocomposites based on 5% clay reinforced 50/50/5 blend processed at 100 rpm

Different than glass fiber composites, the determination of filler aspect ratio for layered silicate nanocomposites is not an easy procedure. Good estimates require a thorough analysis of TEM photomicrographs at different magnifications. Figure 4.64 illustrates various complications of calculating an aspect ratio from TEM photomicrographs that arise from variations in both length, or diameter, and thickness. Clay platelets intrinsically have a distribution of lateral dimensions. The recovery, refinement, chemical treatment, and post-treatment of these clays may contribute to the variation in filler geometry [262].

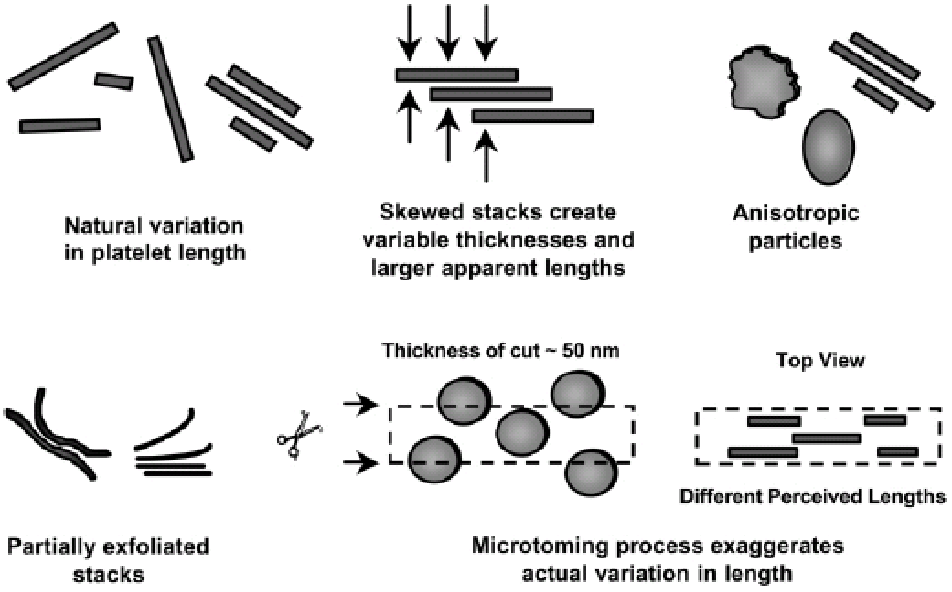

Figure 4.64 Examples of complications in the determination of the aspect ratio of layered silicate fillers within polymer nanocomposites [262]

Furthermore, extrusion of these clays with polymer and any additional melt processing steps that follow, i.e. injection molding, will increase the range of particle shapes and sizes, particularly when the organoclay is not completely exfoliated as illustrated in Figure 4.64 [262]. Moreover, microtoming of the nanocomposite sample into thin sections for TEM analysis will also result in an apparent distribution of observed particle sizes even if all disk-like platelets were the same size [262]. The experimental average length will thus be smaller than the true diameter; this effect is most severe when the thickness of the section is much less than the platelet diameter. As section thickness increases to levels well beyond the particle diameter, however, the experimental average becomes much closer to the true value [264]. In Figure 4.65, some examples of multilayered-clay structures obtained in TEM analysis were shown.

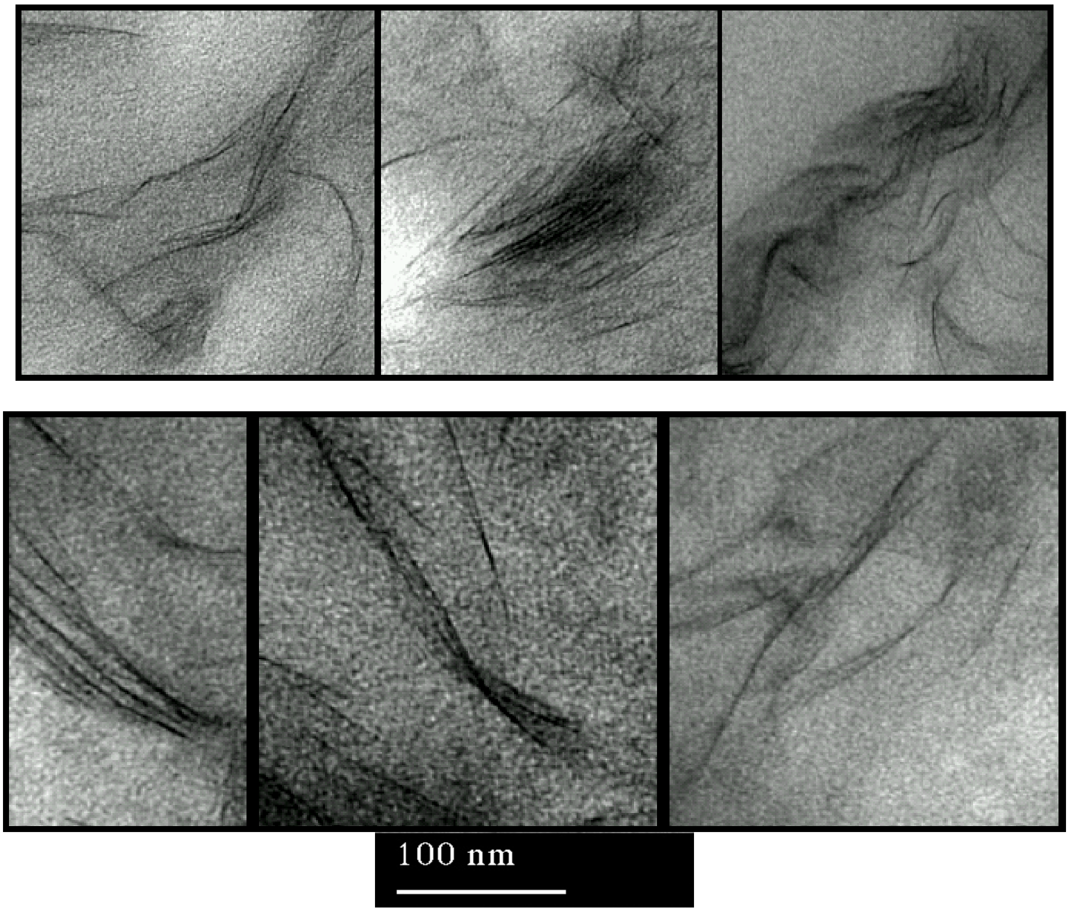

Figure 4.65 Some examples of multiple-layered particles seen in the TEM micrographs of the nanocomposites analyzed

In order to estimate the l_{avg} of the particles semi-automatic image analysis was conducted. As mentioned earlier, direct calculation of thickness of an incompletely exfoliated particle is not a straightforward method by image analysis. Stacks of platelets consist of residual original montmorillonite, non-expandable forms of clay, collapsed organoclay in which the organic surfactant has been completely degraded or has escaped, etc [262]. If the dispersed structure were pure montmorillonite or non-expandable clay, as depicted in Figure 4.66, the thickness of each particle may be calculated by [262]:

$$t_{particle} = d_{001}(n-1)+t_{platelet} \tag{4.18}$$

where $t_{particle}$ is the thickness of each particle, d_{001} is the repeat spacing for the intercalated clay or organoclays, n is the number of platelet per stack (obtained manually counting from the high resolution TEM images) and $t_{platelet}$ is the thickness of each individual clay platelet. d_{001} = 1.8 nm (obtained from X-Ray analysis of Cloisite 30B) and $t_{platelet}$= 0.94 nm (calculated theoretically) reported by Fornes and Paul [262] for the same clay, Cloisite 30B®, were used in the current study.

The results of image analysis and AR_{avg} calculation are summarized in Table 4.10 and corresponding distribution curves are given in Appendix C. It should be noted that the image analysis was only performed for the 5% clay containing blends as a function of blend composition and screw speed. Average number of platelet per particle is less than 2. This means that the number of exfoliated layers into single platelet is much higher than that of stacks formed by multiple platelets. As the PA6 content increased in the matrix, it can be seen that the l_{avg} increased, the average number of platelet per stack, therefore t_{avg} decreased, as a result AR_{avg} increased, both for 100 rpm and 200 rpm. One can attribute this increment in AR_{avg} to the affinity between organoclays and PA6, hence when the amount of PA6 increased in the blend it means that the possibility of diffusion of PA6 chains into the galleries of clays is much higher. On the other hand, as the PA6 concentration increases the clay concentration in the PA6 phases is diluted. Therefore, the possibility of contact of clay particles which can result in a reduction of the length of the filler in composites loose its effectiveness.

Basically, increasing shear rate in the melt processing is expected to promote the exfoliation through shearing apart of the clay platelets from the stacks. However, Dennis et al. [43] proved that when organoclays and polymer matrix are compatible, such as Cloisite 30B® and PA6, the exfoliation processes occurred regardless of the extruder type and shear intensity of the extruder; on the other hand, when the organoclay and polymer is marginally compatible, such as Cloiste 15A® (montmorillonite modified with dimethyldihydrogenated tallow quaerternary ammonium chloride) and PA6, for a given extruder type from medium to high shear intensity configuration, a degree of shear intensity was reached where exfoliation and dispersion did not increase, but it became worse. This means that for a given extruder type, the highest shear configuration or condition does not give the best exfoliation. In the present study, the combination of organoclays, Cloisite 30B®, and PA6 is an example of the compatible case.

As the screw speed doubled (from 100 rpm to 200 rpm), it is obtained that the average number of platelets per particle together with t_{avg} decreased, therefore the AR_{avg} increased. In our case, the system is much complicated than for a nanocomposite system which is formed only from PA6 and Cloisite 30B®. However, basically for the microcompounder, for a certain residence time, as the screw speed increased the number of recirculation of the melt in the closed-loop increased; therefore, the number of passes of the melt over the screws increased. Thus, higher degree of dispersion can be obtained as the screw speed doubled.

Mechanical properties of OMLS based nanocomposites for a given polymer and clay are strongly dependent on the state of dispersion of clay platelets (i.e. level of exfoliation), geometry of the filler (i.e. AR_{avg}), orientation of the clay platelets, interaction between platelets and polymer matrix (i.e. interfacial adhesion) and level of clay loading. Especially modulus of the nanocomposites is highly dependent on the state of dispersion of the clay platelets and can be determined at bulk sample sizes; therefore, it is easy and it can support the microscopic methods to evaluate the dispersion or morphology [265].

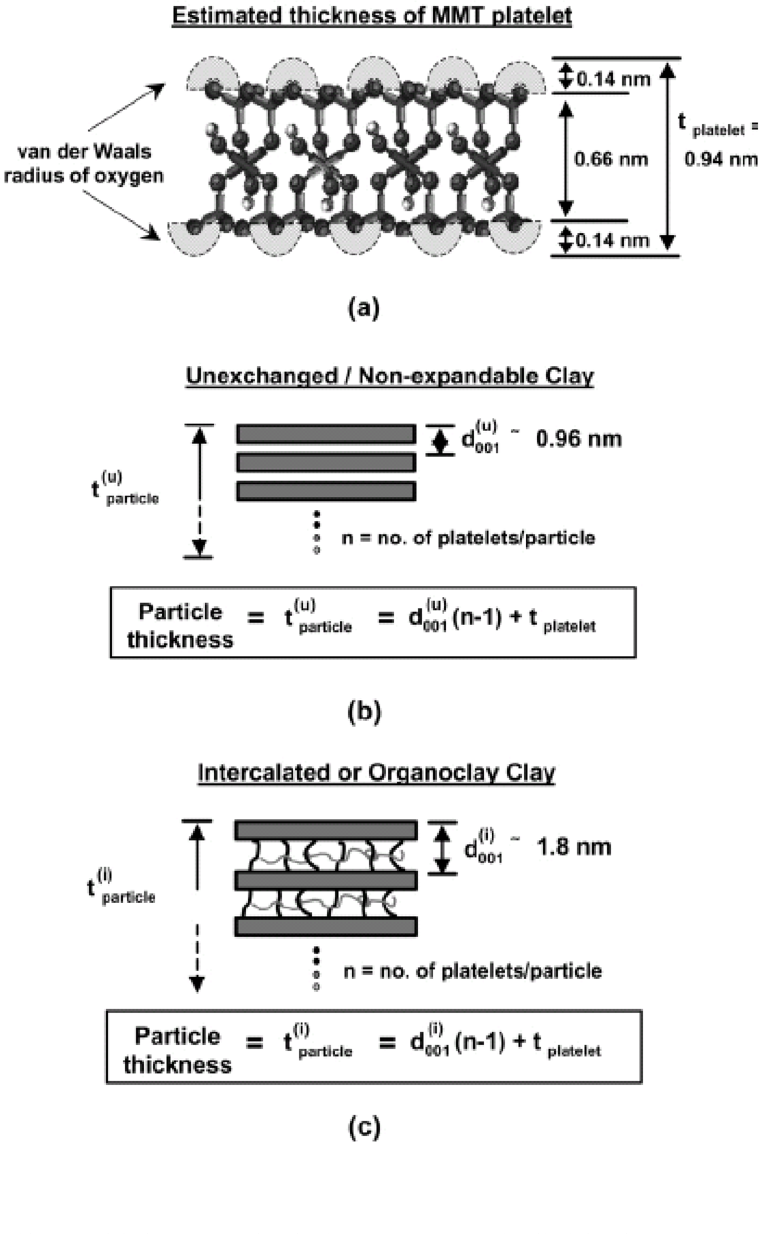

Figure 4.66 Details of thickness calculation of (a) an individual MMTplatelet, (b) an unexchanged or non-expandable clay stack, e.g. sodiumMMT or talc-like clay, (c) an organoclay stack intercalated with surfactant and polymer [262]

Table 4.10 Results of image analysis performed on TEM images for 5% clay reinforced blends based nanocomposites

Nanocomposite system (ABS/PA6/Compt.)	**Number of particles analyzed**	**Average particle length, l_{avg} (nm)**	**Average platelets/particle, n**	**Average particle thickness, t_{avg} (nm)**	**Average aspect ratio (l_{avg}/t_{avg})**
80/20/5 system processed @100 rpm	312	88.7	1.59	2.00	44.35
50/50/5 system processed @ 100 rpm	343	112.1	1.36	1.59	70.50
20/80/5 system processed @100 rpm	432	115.7	1.15	1.21	95.62
80/20/5 system processed @ 200 rpm	250	91.2	1.32	1.52	60.00
50/50/5 system processed @ 200 rpm	325	101.0	1.26	1.41	71.63
20/80/5 system processed @ 200 rpm	395	117.3	1.12	1.16	101.12

The complexity of present system arises from the selective dispersion of the clay between ABS and PA6 phases. The TEM study showed that clay layers are exfoliated in PA6 phase and agglomerated in the interfacial region between two phases. Therefore, prearranged experimental percentages of the clay loadings varied on the basis of PA6, which is the reinforced phase. Figure 4.67 shows the experimental clay loading level versus clay loading based on PA6 in the blend.This calculation was carried out by considering all the calys were located in PA6. When the clay loading level based on PA6 is considered, 80/20/5 blend system which contains experimentally 3 and 5 % clay, and both 50/50/5 and 20/80/5 blend systems which contain experimentally 5 % clay seem to be over-loaded. The others have around 5% or lower based on PA6, which is reasonable for thermoplastic based melt-intercalated nanocomposites.

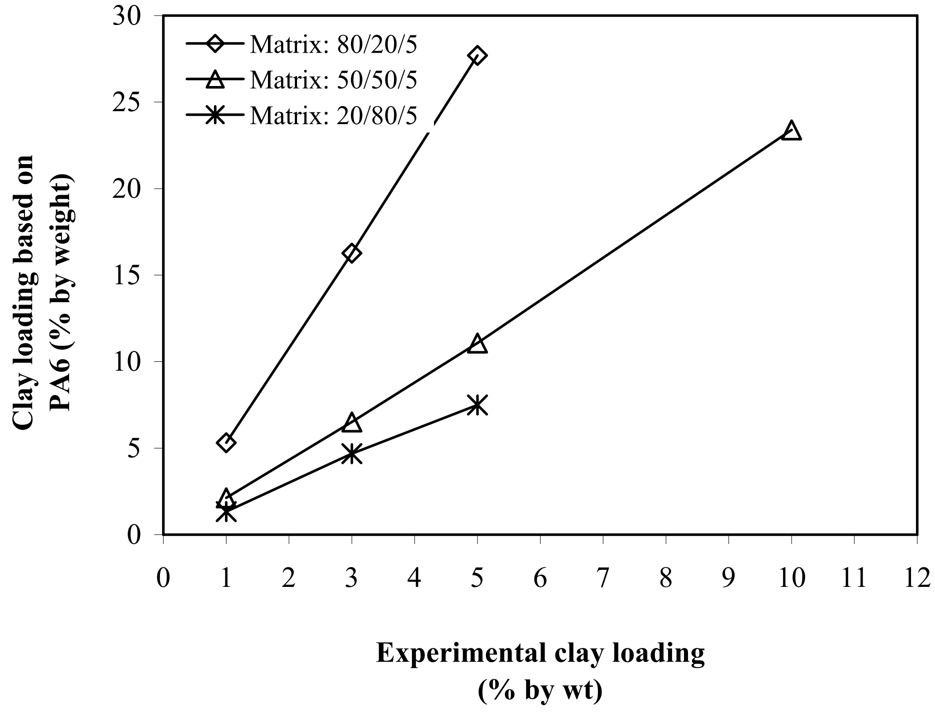

Figure 4.67 Experimental clay loading level vs clay loading based on PA6

Effect of blend composition and screw speed on Young's Moduli of blends and 5% clay reinforced blends based nanocomposite is given in Figure 4.68. When the moduli of the blends were compared as a function of blend composition, as the PA6 content increased, it was observed that the moduli increased monotonously for the compatibilized system. The effect of compatibilizer can also be observed from the moduli of 50/50 blend systems. In the presence of olefin based compatibilizer, the modulus of blend decreased with respect to blend without a compatibilizer due to the elastomeric, soft character of the compatibilizer.

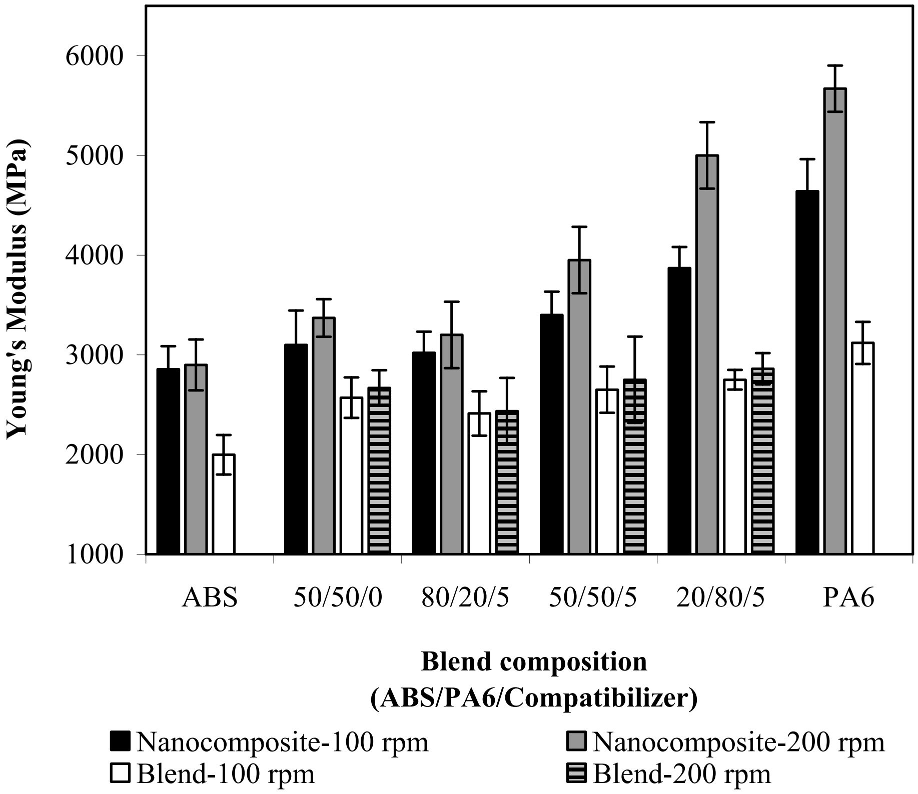

Figure 4.68 Effect of blend composition and screw speed on Young's Moduli of blends and 5% Clay reinforced blends based nanocomposite

Young's Moduli of nanocomposites are higher than that of blends, even for 80/20/5 system whose PA6 based clay content is almost 28 %. When the moduli of blends are considered, the values are higher than ABS's and lower than PA6's, and they gradually increase with increasing PA6 possibly due to the morphology change from dispersed PA6 to continuous PA6. As the PA6 content increased, as a general trend, the Young's Moduli increased also for nanocomposites. The improved AR_{avg} is believed to be the responsible for this behavior.

Increasing screw speed slightly increases the moduli of the blends. One can attribute this slight improvement to the reduction in the phase dimensions and the increased number of pass over the screws of the extruder, which can increase the extent of compatibilization reaction; therefore this can give rise to the interfacial adhesion. When the modulus ratio's of nanocomposites to that of its blends are compared, it can be seen that the ratio stays constant at 100 rpm regardless of PA6 content, on the other hand this ratio increases gradually with PA6 content for 200 rpm.

Figure 4.69 shows the effect of clay loading level on Young's Moduli of nanocomposites based on 50/50/5 blend system processed at 100 and 200 rpm. It is seen from the graph that regardless of screw speed, the moduli increased almost linearly with increasing clay content. As the screw speed doubled, a slight improvement was obtained, which can be attributed to the increase in the AR_{avg} and improved interfacial adhesion, as mentioned above. Beside the improvement in reinforcing efficiency of clays with increasing AR_{avg}, it maximizes the polymer clay contact area, so called interfacial area, which results in higher modulus due to resctriction in mobility of polymer chains.

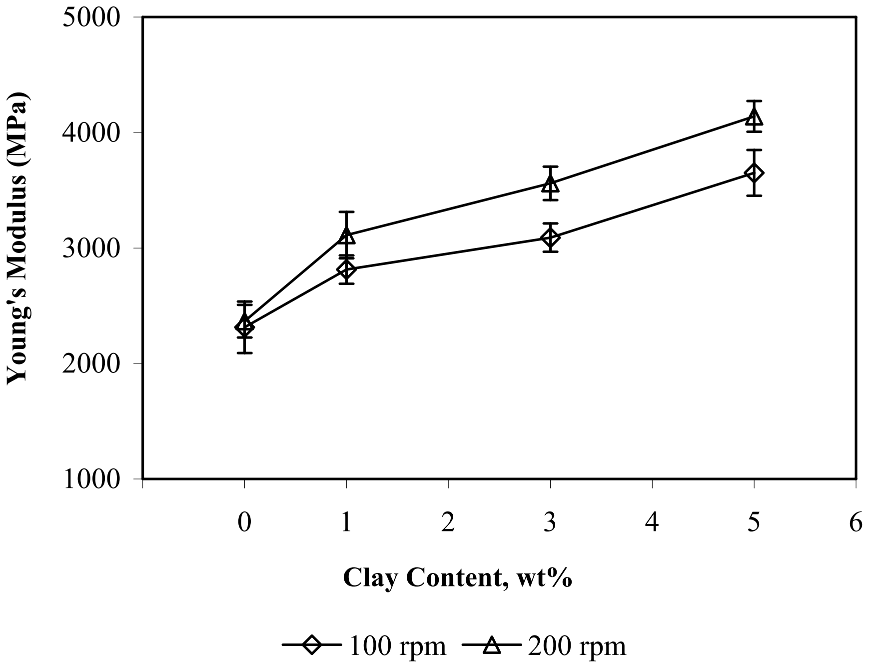

Figure 4.69 Effect of clay loading level on Young's Moduli of nanocomposites based on 50/50/5 blend system processed at 100 rpm and 200 rpm

The variation of yield strength and percent strain at break with respect to blend composition and screw speed at 5% clay loading, and clay loading level at 50/50/5 blend composition is exhibited in Table 4.11. For neat-ABS, neat-PA6 and the blends processed at 100 rpm, incorporation of 5% clay resulted in increase in yield strength value due to the restricted mobility of the polymer chains because of the their adsorption on the platelet surfaces. The level of improvement with the addition of 5% clay increased with increasing content of PA6 in the matrix. This can be attributed to the increment in AR_{avg} when the PA6 content increased. The effect of screw speed on yield strength is significant for 50/50/5 and 20/80/5 systems. For these systems the higher the screw speed the higher the yield strength, probably due to the improved dispersion of platelet which resulted in higher AR_{avg} values.

Table 4.11 Mechanical and flow properties of blends and blends based nanocomposites

Material (ABS/PA6/Comp.) and Process Condition		***Yield Strength (MPa)***	***Strain at break (%)***
ABS	Pure-100 rpm	44.2±1.8	28.2±3.2
	5% Clay-100 rpm	58.4±2.3	6.2±2.1
	5% Clay-200 rpm	60.1±1.9	5.6±1.3
80/20/5	Blend-100 rpm	48.1±2.1	13.1±3.2
	Blend-200 rpm	49.2±1.2	12.9±2.2
	5% Clay-100 rpm	58.6±2.3	6.9±3.4
	5% Clay-200 rpm	57.8±2.8	7.3±2.2
50/50/5	0% Clay -100 rpm	45.2±0.9	18.3±2.5
	0% Clay -200 rpm	52.3±1.7	19.4±4.3
	1% Clay-100 rpm	57.6±2.1	4.8±2.1
	1% Clay-200 rpm	60.1±3.0	5.1±1.1
	3% Clay-100 rpm	65.2±0.9	4.2±2.4
	3% Clay-200 rpm	69.4±2.1	4.4±2.5
	5% Clay-100 rpm	72.0±2.9	3.2±2.1
	5% Clay-200 rpm	77.5±4.3	3.3±2.0
	10% Clay-100 rpm	58.3±6.7	3.1±1.6
	10% Clay-200 rpm	56.4±3.7	3.6±0.9
20/80/5	0% Clay -100 rpm	56.4±3.2	56.2±3.2
	0% Clay -200 rpm	62.1±1.8	55.3±2.6
	5% Clay-100 rpm	78.3±2.7	7.6±4.3
	5% Clay-200 rpm	82.3±3.2	7.3±3.8
PA6	Pure-100 rpm	67.1±1.4	166.3±4.5
	5% Clay-100 rpm	87.2±2.1	9.1±4.2
	5% Clay-200 rpm	92.3±2.1	8.4±3.8

The effect of clay loading level on yield strength is also given for 50/50/5 blend. It can be observed that increasing the clay concentration up to 10% increased the yield strength values. For 10% clay loading the yield strength values decreased sharply. The factor that contributed to the lowering of the yield strength at high clay loadings is the filler-filler interaction of the platelets, resulting in agglomerates, which reduces the AR_{avg}. According to Akkapeddi [265], after a critical level of clay loading, the exfoliation-ability of the clays decreases. The explanation for the onset of a threshold organoclays concentration was stated by Chow et al. [266] that the matrix molecules are less than needed to intermingle with those of the intercalant (modifier); therefore clay layers stack together instead of delamination. This optimum loading level depends on the type of polymer/clay couple. For polyimide/montmorillonite nanocomposites, this limit is 6 wt% and for PA6 it is ≤5 wt% [266].

In the current study, PA6 based clay concentrations for 1, 3, 5 and 10 wt% reinforced 50/50/5 blend based nanocomposites are, respectively, around 2, 6.5, 12 and 24 wt% (see Figure 4.67). Especially, blends at 5 wt% clay concentrations seem to be very high when one considers the PA6 based concentrations. However, even for 5 wt% reinforced 80/20/5 blend, an improvement in mechanical properties was obtained with respect to pure matrix.

Possible clay dispersion mechanism was proposed to figure out the reinforcing mechanism in ABS/PA6 blends based nanocomposites in Figure 4.70, based on TEM observations. According to mechanism, at high clay loadings, the excess clays that can not be exfoliated by PA6 chains because of the inadequate number of matrix molecules to intermingle between the intercalants tend to accumulate at the ABS/PA6 interphase, because they can not be strongly bonded to matrix because of smaller surface area. In the core region (shown by white dashed lines) of PA6 phase, there exists fully exfoliated platelets; hence this region is reinforced by these exfoliated layers. Therefore even at high clay loading, presence of this reinforced core region can lead to increase the strength of the nanocomposite.

There should also be a maximum concentration of clay loading. Beyond this concentration, at which interfacial zone is saturated by stacks and platelet agglomerates, the excess exfoliated/unexfoliated clays can start to accumulate in the core region of the PA6. After this saturation concentration, one might expect a sharp decrease in the strength.

When the strain at break values are considered, it can be seen that incorporation of clay sharply reduced the strain values regardless of the screw speed because of the restricted mobility of the polymer chains in the presence of clay platelets. As the clay concentration increased, the strain values decreased gradually.

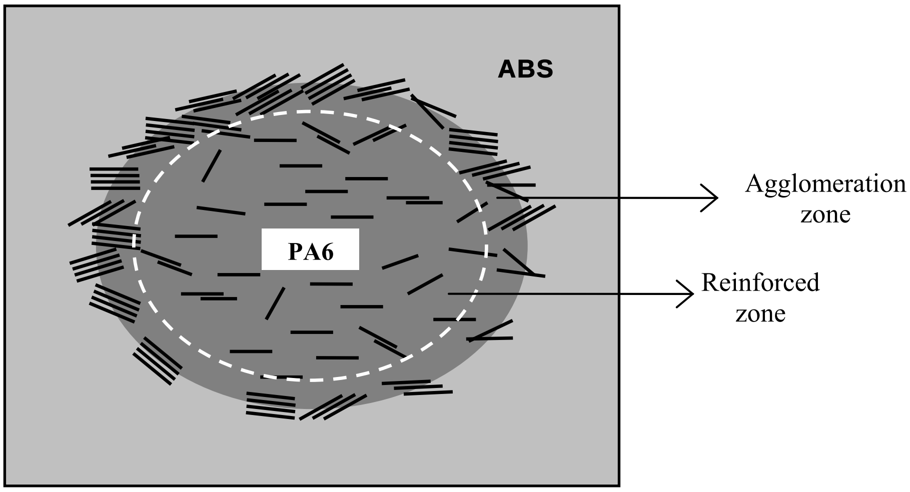

Figure 4.70 Illustration of proposed clay dispersion in ABS/PA6 blends based nanocomposites

4.3.2 Effects of Screw Rotation Mode, Mixing Time and Screw Modification on the Dispersability, Morphology and Mechanical Properties of Blends and Blends Based Nanocomposites

One of the important issues affecting the performance of the blends is the blend morphology. For multicomponent polymer systems, the morphology of the phases is controlled by droplet break-up process [255, 256]. The parameters that influence this process are given in the capillary number, *Ca*, which is the ratio of the deforming stress to the interfacial forces [237]:

$$Ca = \frac{\eta_m \dot{\gamma}}{\sigma / R} \tag{4.11}$$

where η_m is the matrix viscosity, $\dot{\gamma}$ is the shear rate in simple shear flow, σ is the interfacial tension and R is the droplet radius. If Ca is higher than a critical value, Ca_{crit} the particle becomes unstable and breaks-up. To have larger Ca, either a high $\dot{\gamma}$ or smaller σ should be required for a given polymer couple. In the current study, the matrix viscosity η_m and σ were fixed by fixing the composition of the ABS/PA6/Compatibilizer blends. Therefore, only parameter was the shear rate, $\dot{\gamma}$, imposed by the flow in the extrusion.

The SEM micrographs of 80/20/5 blend system processed at 100 rpm are shown in Figure 4.71 a and b as a function of screw rotation mode. The black holes seen in micrographs were left after removal of PA6 phase by etching. It is seen that, the particle size of PA6 in co-rotation is much finer than that of in counter-rotation (1.72 μ and 6.30 μ, respectively). This alternation in phase sizes can be attributed to the insufficient shear rate in counter rotation mode under same processing conditions [267]. Another factor is the flow patterns of the polymer melts. In tightly intermeshing counter-rotating extruders, the screw-speeds are in the intermeshing region are the same direction; therefore, material which enters the intermeshing section continues to flow through this region. However, when the clearance between the screws is very small, the amount of material which can flow through the intermeshing region will be quite small. As a consequence, a mass of material starts to accumulate at the entry of this region [268]. This accumulation can lead to coalescence of the dispersed phase which results in larger dispersed particles.

When the blend ratio was changed to 50/50/5 (see Figure 4.71 c and d, black holes seen in micrographs were left after removal of PA6 phase by etching), the dispersed phase morphology altered to co-continuous morphology [250, 251]. In co-rotation, this differentiation in morphology was much significant than in counter-rotation. In counter-rotation, a combination of co-continuous and very coarse, non-spherical dispersed phase morphology was seen.

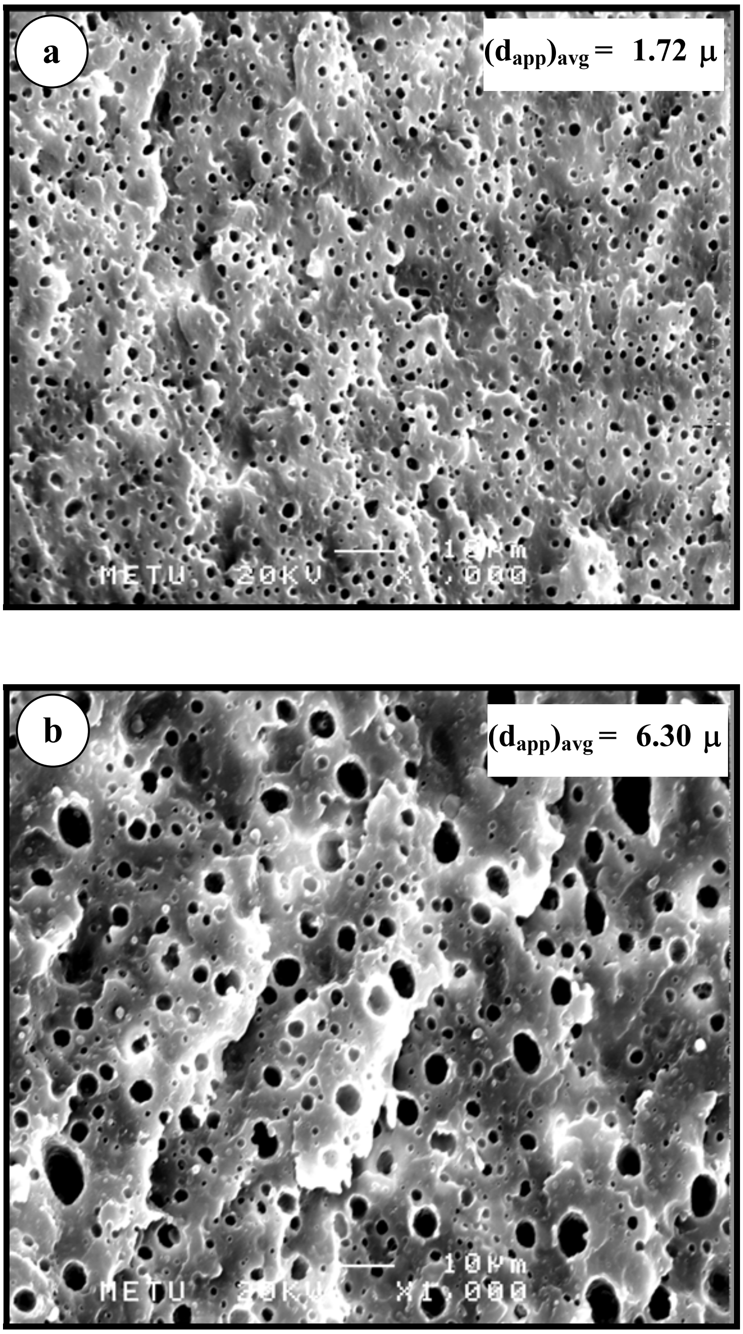

Figure 4.71 SEM micrographs of blends (a) 80/20/5 processed with co-rotating twin screws at 100 rpm (x1000), (b) 80/20/5 processed with counter-rotating twin screws at 100 rpm (x1000)

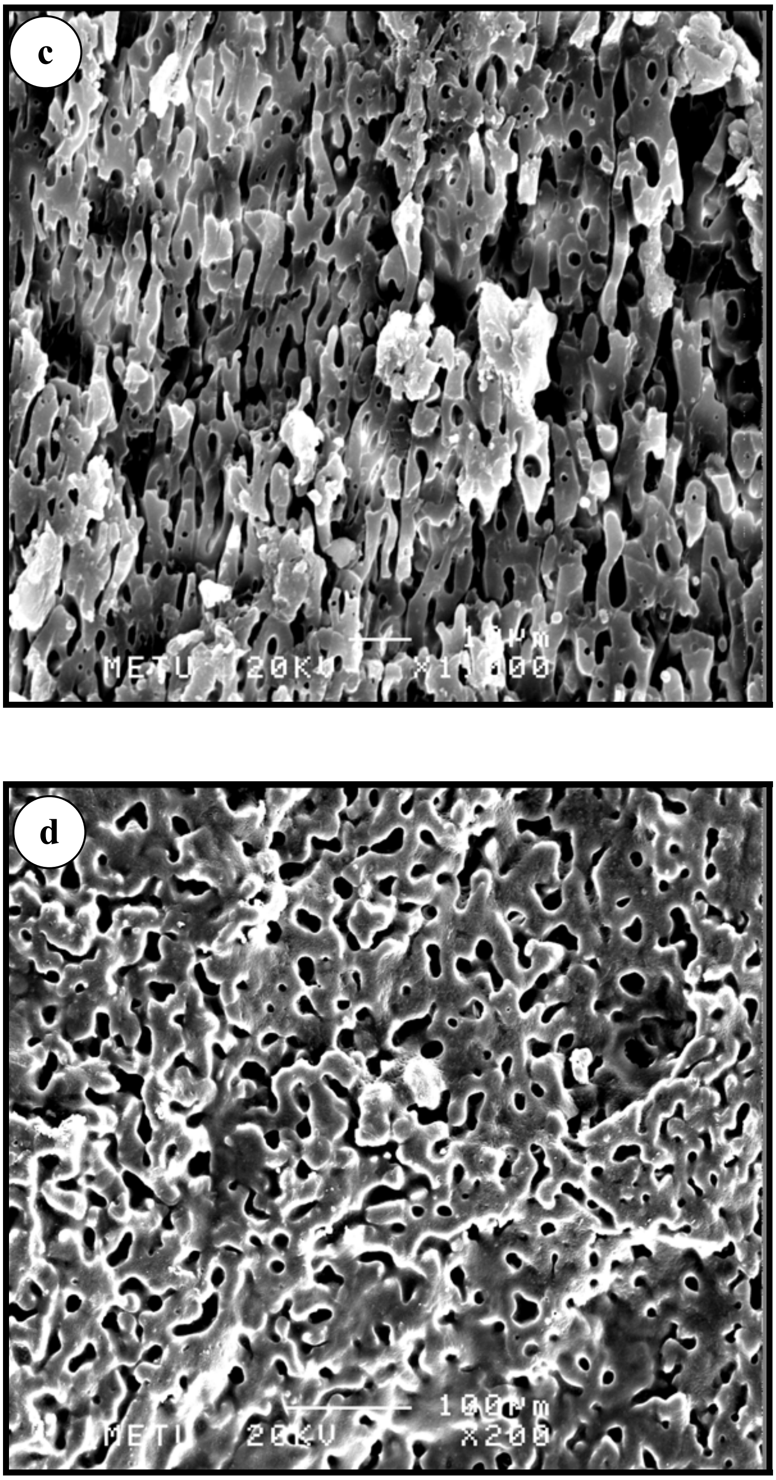

Figure 4.71 (Cont'd) SEM micrographs of blends (c) 50/50/5 processed with co-rotating twin screws at 100 rpm (x1000), (d) 50/50/5 processed with counter-rotating twin screws at 100 rpm (x200)

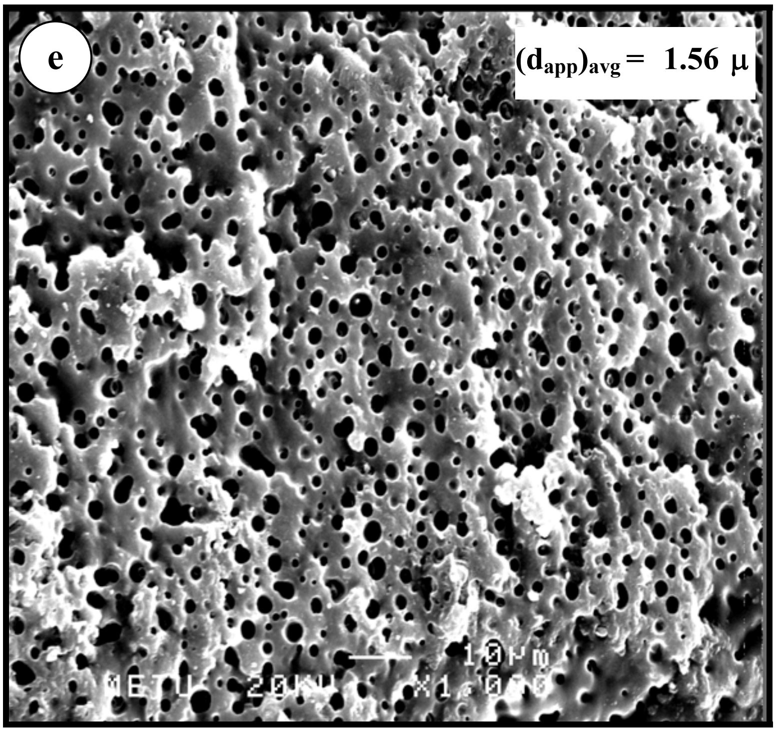

Figure 4.71 (Cont'd) SEM micrographs of blend (e) 20/80/5 processed with co-rotating twin screws at 100 rpm (x1000),

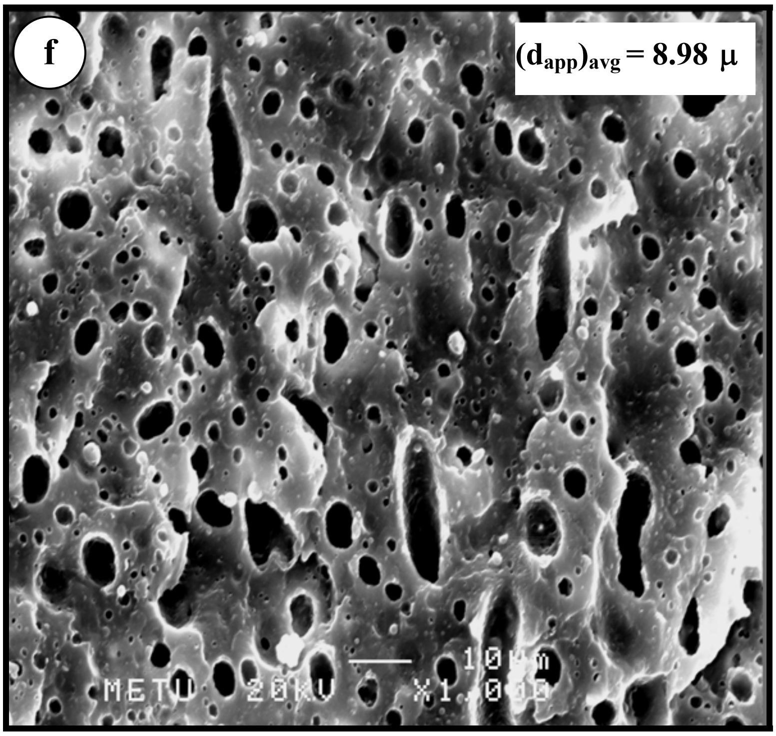

Figure 4.71 (Cont'd) SEM micrographs of blend (f) 20/80/5 processed with counter-rotating twin screws at 100 rpm (x1000)

Further increase in PA6 to ABS ratio resulted in a dispersed phase morphology, but in this case PA6 is continuous phase and ABS is dispersed (see Figure 4.71 e and f, black holes seen in micrographs were left after removal of ABS phase by etching.). Image analysis results indicated that in co-rotation the average dispersed phase size is smaller than that of counter-rotation.

The effect of the screw rotation-mode and modification on the morphology of 50/50/5 blend based 5% clay containing nanocomposite are shown in Figure 4.72 a, b and c. The black holes seen in micrographs were left after removal of ABS phase by etching. Regardless of processing history, all the three cases were co-continuous. However, the level of capillarity of the phases was different in all cases. In modified co-rotation, the phases were more intermingled than the ones in counter and co-rotation.

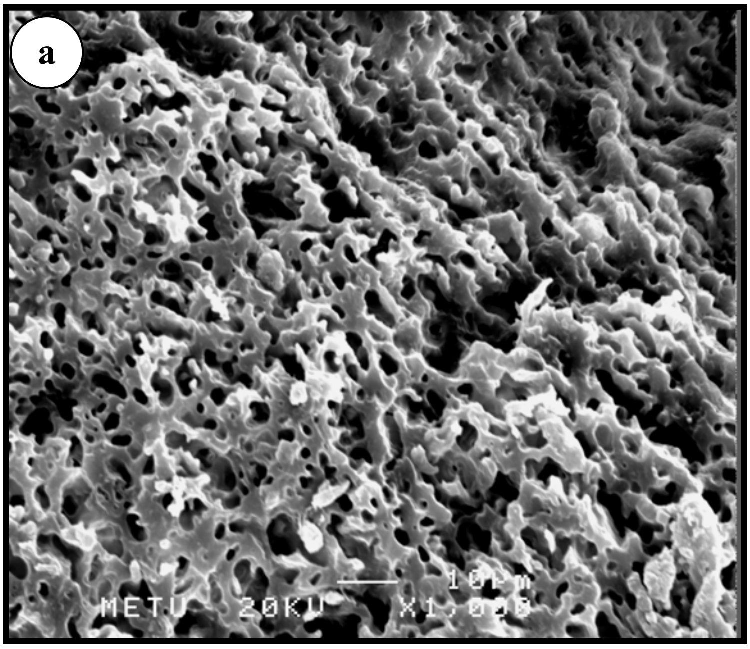

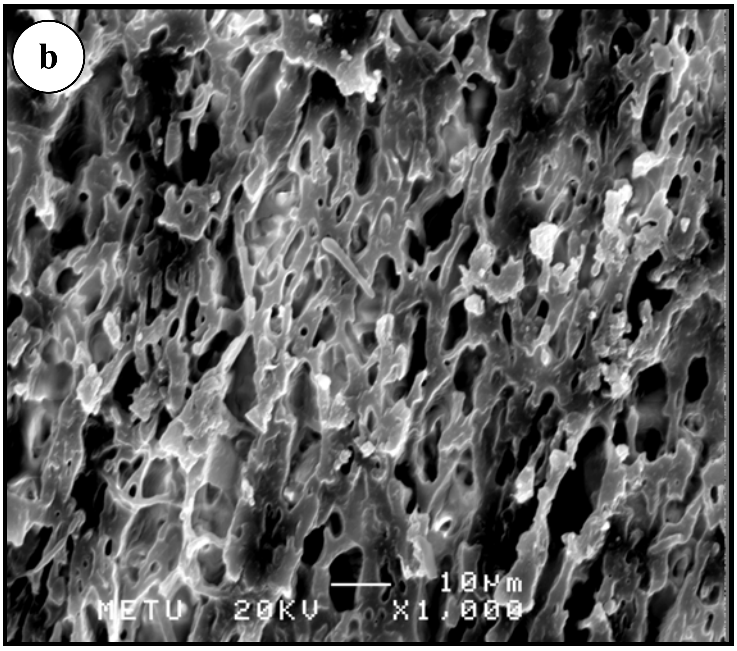

Figure 4.72 SEM micrographs of 5 %wt clay containing 50/50/5 blend based nanocomposites (a) processed with co-rotating twin screws at 100 rpm, (b) processed with counter-rotating twin screws at 100 rpm

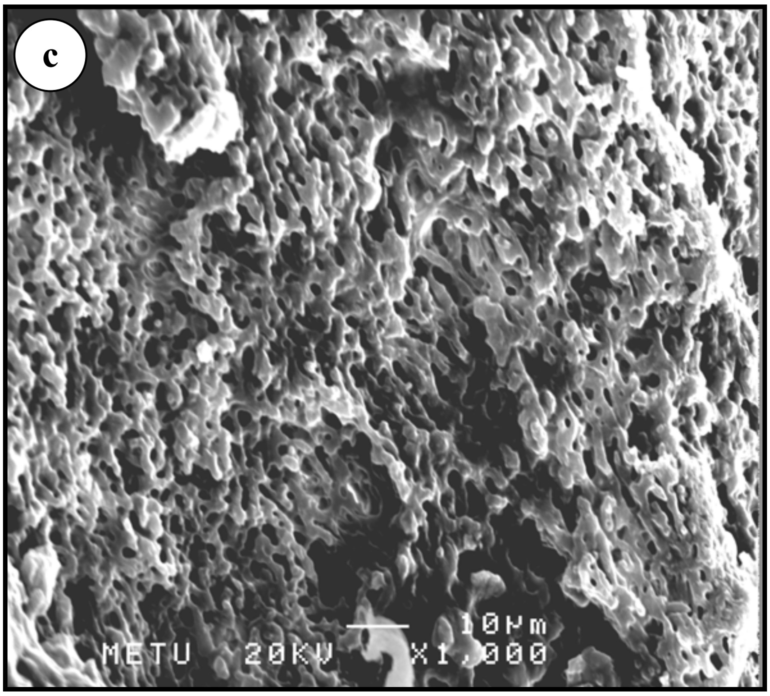

Figure 4.72 (Cont'd) SEM micrographs of 5 %wt clay containing 50/50/5 blend based nanocomposites (c) processed with modified co-rotating twin screws at 100 rpm

Figure 4.73 displays the XRD curves of 5wt% organoclay containing nanocomposites based on ABS, PA6 and their compatibilized blends as the function of processing conditions and blend composition. The curve (1) in Figure 4.73 a-d is the XRD pattern for Cloisite 30B showing an intense, broad peak at $2\Theta=5.0°$, corresponding to a basal spacing (d_{001}) of 18.0 Å. The nanocomposite based on only PA6 (0/100 in Figure 4.73-a) does not exhibit any peak relevant to clay layers. This can be considered as fully exfoliated structure. On the other hand, the nanocomposite based on ABS (100/0 in Figure 4.73-a) exhibits a sharp peak at $2\Theta=2.44°$ corresponding to a basal spacing of 36.18 Å and a broad peak around $2\Theta=5.0°$. This implies that most of the clays are intercalated but there still exists some unexfoliated stacks [269].

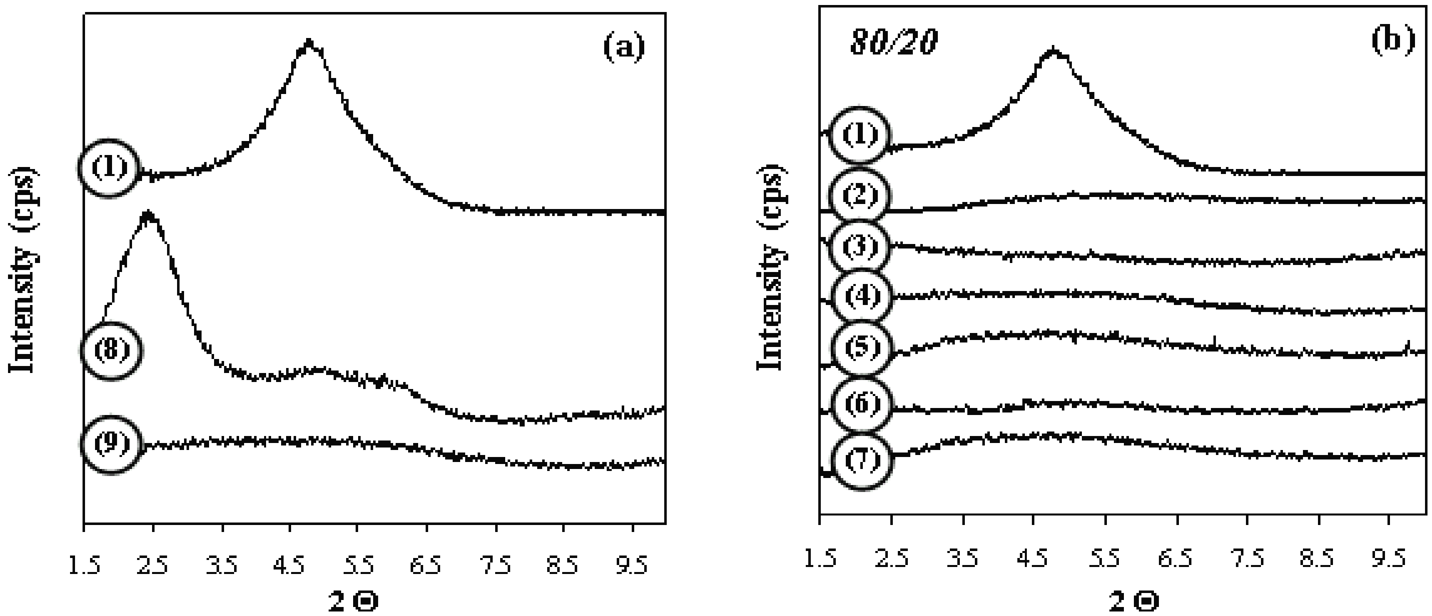

Figure 4.73 XRD patterns of nanocomposites containing 5wt% organoclay based on (a) pure matrices, (b) 80/20 blend, The numbers stand for (1) Cloisite® 30B, (2) 200 rpm modified co-rotation, (3) 100 rpm modified co-rotation, (4) 200 rpm counter-rotation, (5) 100 rpm counter-rotation, (6) 200 rpm co-rotation, (7) 100 rpm co-rotation, (8) ABS based nanocomposites, 100 rpm co-rotation, (9) PA6 based nanocomposites, 100 rpm co-rotation. (XRD patterns were vertically offset for clarity)

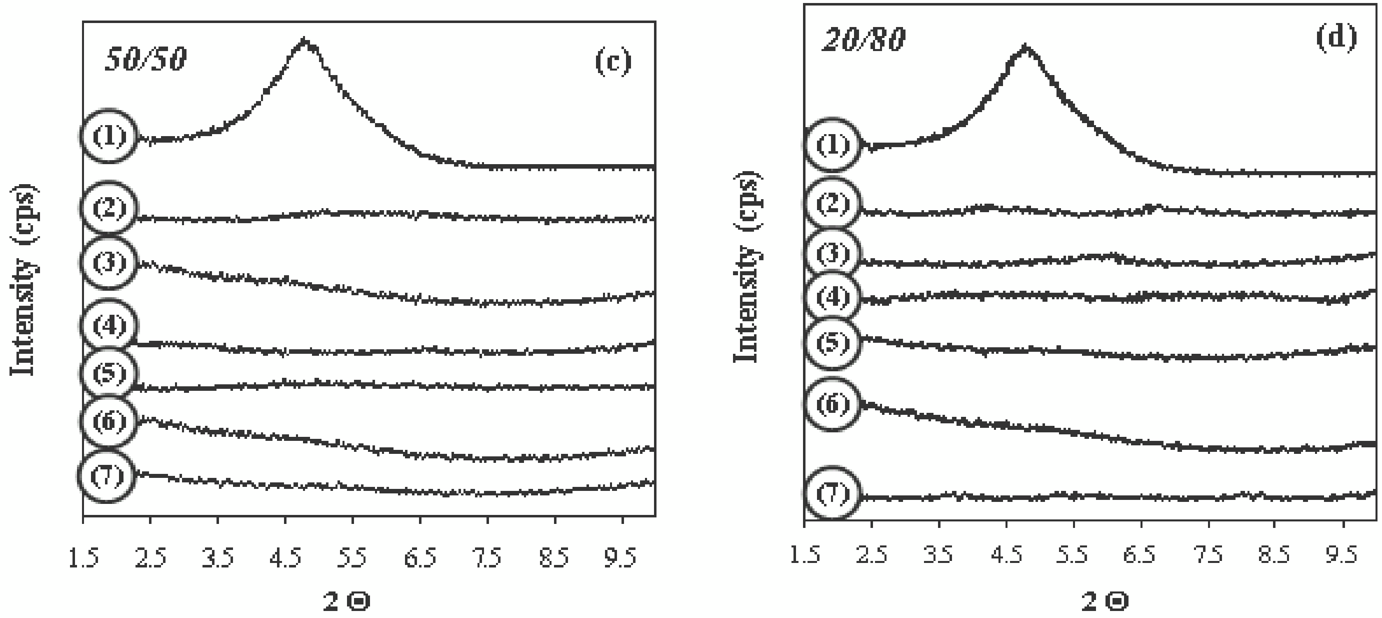

Figure 4.73 (Cont'd) XRD patterns of nanocomposites containing 5wt% organoclay based on (c) 50/50 blend, (d) 20/80 blend. The numbers stand for (1) Cloisite® 30B, (2) 200 rpm modified co-rotation, (3) 100 rpm modified co-rotation, (4) 200 rpm counter-rotation, (5) 100 rpm counter-rotation, (6) 200 rpm co-rotation, (7) 100 rpm co-rotation, (8) ABS based nanocomposites, 100 rpm co-rotation, (9) PA6 based nanocomposites, 100 rpm co-rotation. (XRD patterns were vertically offset for clarity)

XRD curves of 80/20 blends based nanocomposites prepared at different processing conditions are given in Figure 4.73-b. The addition of PA6 into the ABS together with a compatibilizer resulted in a very broad peak (see Figure 4.73-b (7)). This means that most of the clays were exfoliated; however there still exist unexfoliated or intercalated platelets, so called stacks. One should note that the organoclay, Cloisite 30B, used in the current study is confirmed to be compatible with PA6 in PA6/organoclay and PA6-polymer blends/organoclay nanocomposites [269-273]. Therefore, increase in level of exfoliation by the incorporation of PA6 can be attributed to improved compatibility between the organoclay and polymer matrix. Doubling the screw-speed to 200 rpm increased the level of exfoliation, therefore no peak was observed for curve (6). When counter-rotation is considered (curves 4 and 5), the broad peak at 100 rpm (curve 5) disappears as the screw speed increased to 200 rpm. XRD patterns of the nanocomposites prepared using modified screw (curves 2 and 3) did not exhibit any peak relevant to organoclay pointing a fully exfoliated dispersion of organoclay platelets.

In contrast, organoclay peaks are fully absent in all XRD curves of 50/50 and 20/80 blends based nanocomposites independent of processing history as the PA6 ratio is increased. Thus, it can be expected that morphology of nanocomposites based on 50/50 and 20/80 blends prepared at different processing conditions contains a substantial amount of individual platelets dispersed in matrix. XRD results suggest that the chemical affinity plays a significant role in exfoliation mechanism. If the chemical affinity is somehow prohibited (i.e. saturation of compatible phase), then processing conditions become significant as in the 80/20 blend system.

Some representative TEM micrographs of the nanocomposite systems are given in Figures 4.74-4.77. When the nanocomposite based on ABS is considered (see Figure 4.74), a combination of clay stacks seen as dark spots and delaminated platelets seen as individual particles located in the outer part of the stacks were observed. This also confirms the results of the XRD analysis which indicates an intercalated structure of ABS/organoclay nanocomposites. Figure 4.75-a and b display TEM micrographs of the representative 50/50 blend based composites processed at 100 rpm with co-rotating screws. The dark region is the PA6 and the grey surrounding region is the ABS phase. Clays were selectively dispersed in PA6 phase and there is no clay platelet seen in ABS phase possibly because of the higher chemical affinity to PA6 rather than ABS. Similar observation was also presented in elsewhere [270, 271, 274, 275] for PA6 blends based nanocomposites. The higher magnification in TEM image (see Figure 4.75-b) of PA6 phase shows that clay platelets were mostly exfoliated as individual layers indicating a nano-scaled dispersion; however some few double or triple layered skewed stacks [276, 277, 278] are also observed.

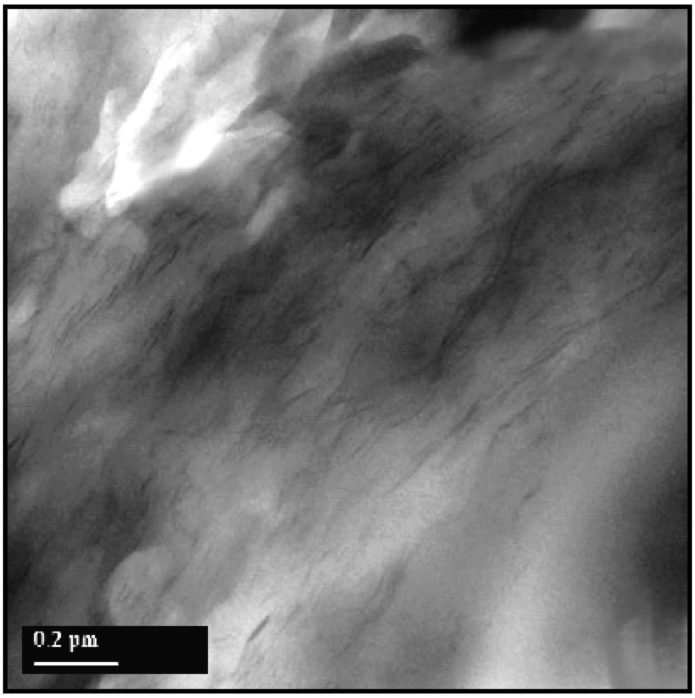

Figure 4.74 TEM micrograph of nanocomposite based on ABS (100/0) containing 5wt% organoclay processed at 100 rpm co-rotation mode

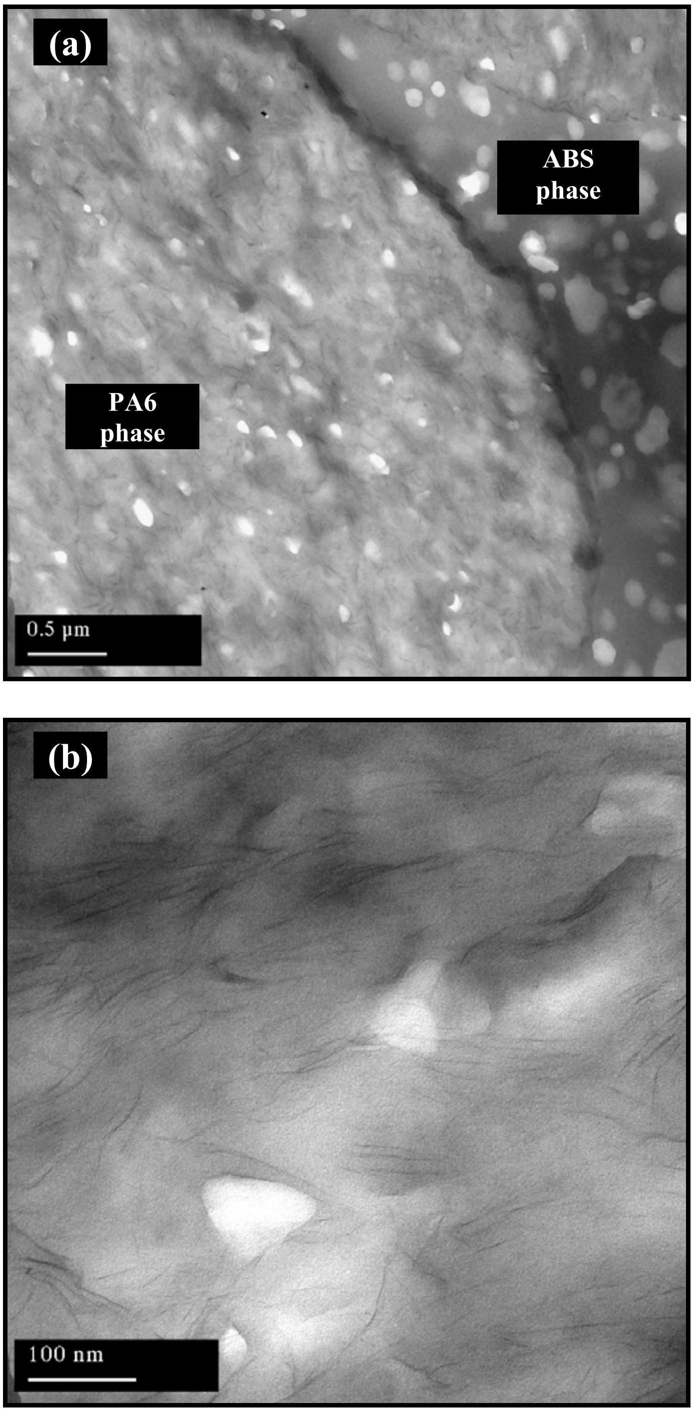

Figure 4.75 TEM micrographs of nanocomposite based on 50/50 blend system containing 5wt% organoclay processed at 100 rpm in co-rotation mode (a) Nanomorphology of blend showing both two phases, (b) Nanomorphology of PA6 phase only

The nanomorphology of the composites based on 50/50 blend processed at 100 rpm with counter-rotation or modified co-rotation is seen in Figures 4.76 and 4.77, respectively. Note that the selective dispersion of clay layers in PA6 was also valid for these materials. TEM micrographs show a well-exfoliated structure consisting largely of individual clay platelets dispersed within PA6 matrix.

The white spots seen in the TEM micrographs stand for the compatibilizer domains. It is seen that the phase sizes of the compatibilizer are smaller than 0.5 μ. The compatibilizer, EnBACO-MAH, dispersed in both ABS and PA6 phases; however, the domain sizes in ABS phase are much larger than those of PA6 phase (see Figure 4.75-a).

In order to better discern between the processing conditions, a semi-automated image analysis was conducted by aiming to obtain average aspect ratio (AR_{avg}) of nano-particles which can be considered as an indicator for the level of dispersion and defined as the length per thickness. The results of image analysis and AR_{avg} calculation are summarized in Table 4.12. It should be noted that the image analysis was only performed for the 5% clay containing 50/50 blends as a function of processing condition.

Average number of platelet per particle is less than 2 in each condition. This means that the number of exfoliated layers into single platelet is much higher than that of stacks formed by multiple platelets. Screw speed in co-rotation has no significant influence on the AR_{avg} (see I and II in Table 4.12). When average length of particles (l_{avg}) and platelet per particle (n) are taken into account, increasing screw speed slightly decreased both of them in the co-rotation. The modification of the screw to promote elongational flow resulted in an improvement in AR_{avg} with respect to unmodified co-rotating screws regardless of screw speed (III and IV in Table 4.12). The level of dispersion capability of counter-rotating screws was lower than that of modified or unmodified co-rotation when the AR_{avg} of the particles are taken into account at 100 rpm.

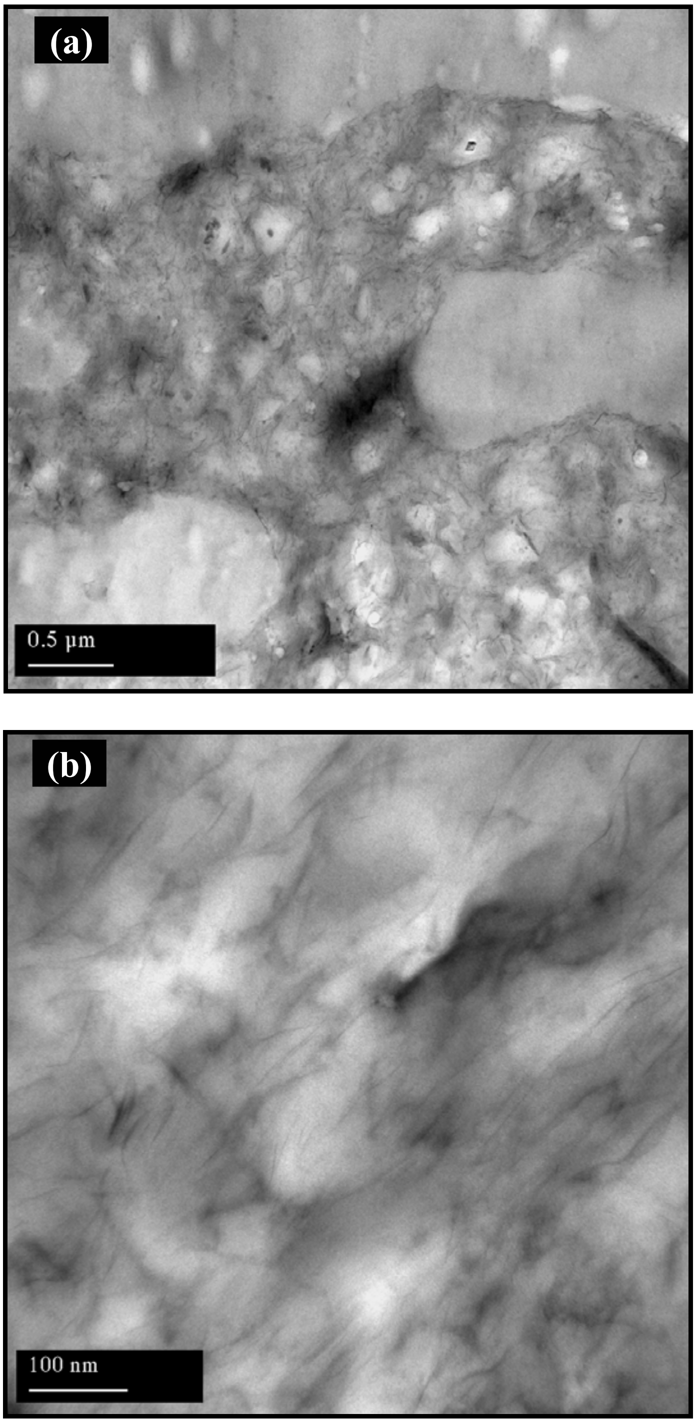

Figure 4.76 TEM micrographs of nanocomposite based on 50/50 blend system containing 5wt% organoclay processed at 100 rpm in counter-rotation mode a) Interfacial region, b) PA6 phase

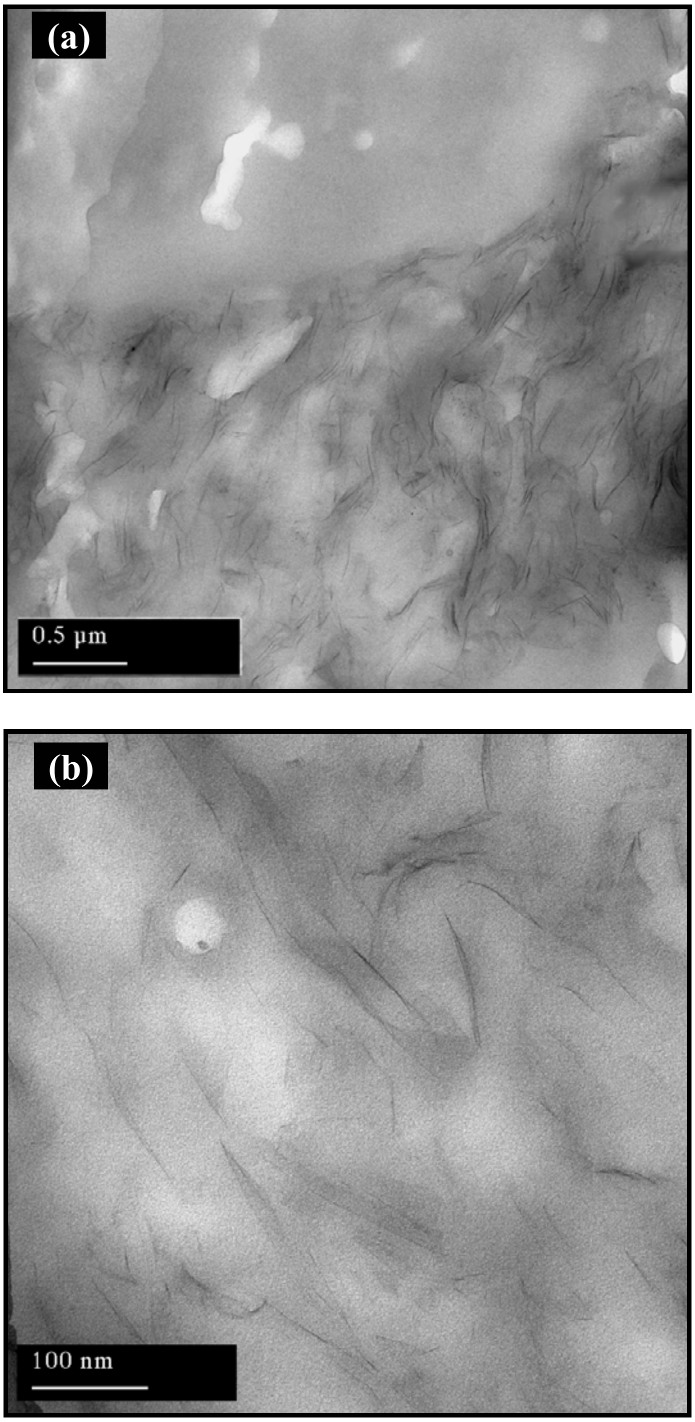

Figure 4.77 TEM micrographs of nanocomposite based on 50/50 blend system containing 5wt% organoclay processed at 100 rpm in modified co-rotation mode a) Interfacial region, b) PA6 phase

Table 4.12 Results of image analysis performed on TEM images for selected compositions

No	**Nanocomposite system (ABS/PA6/Comp.)**	**Number of particles analyzed**	**Average particle length, l_{avg} (nm)**	**Average platelets/particle, n**	**Average particle thickness, t_{avg} (nm)**	**Average aspect ratio (l_{avg}/t_{avg})**
I	50/50/5 processed @ 100 rpm co-rotation screws	343	112.1	1.36	1.59	70.50
II	50/50/5 processed @ 200 rpm co-rotation screws	325	101.0	1.26	1.41	71.63
III	50/50/5 processed @ 100 rpm with modified co-rotation screws	279	129.2	1.12	1.16	111.38
IV	50/50/5 processed @ 200 rpm modified co-rotation screws	322	128.2	1.13	1.17	109.57
V	50/50/5 processed @ 100 rpm counter-rotation	296	107.2	1.45	1.75	60.90

Figure 4.78 shows the schematic of axial force measurement set-up. The barrel of the micro-extruder is positioned on a lever, which swivels around a stationary axis and counter balanced by a load-cell at the other end. The load-cell is typically 10 kN in range and measures the axial force exerted by the barrel opposing the pushing forces imposed by the screws towards the bottom while the melt was pumped through the recirculation channel or die. Either screw speed or axial force can be controlled fixing one of them by means of a control unit. This also provides the opportunity of controlling throughput in some certain applications. In the current study, the axial force measurement is conducted to verify the screw modification and to obtain qualitative information about rheological properties of nanocomposites as a function of matrix composition. All the vertical force data obtained at the end of 2 minutes of mixing to ensure that there is no unmelt polymer remained in the extruder.

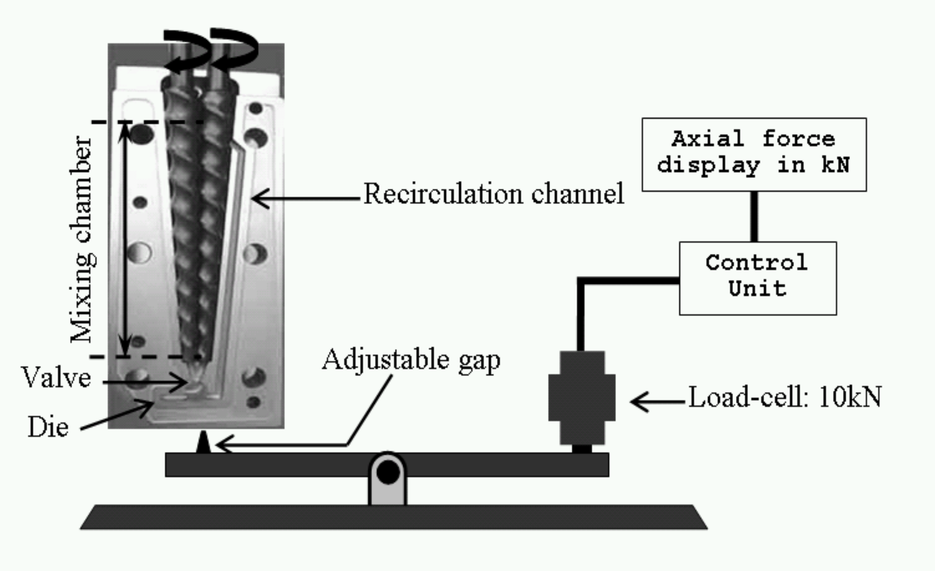

Figure 4.78 The schematic of axial force measurement set-up

Figure 4.79 represents the dependence of axial force on the screw geometry, speed and blend composition. Under same processing conditions (i.e. screw geometry, screw speed and barrel temperature), the axial force measured depends on the melt viscosity of the system. It can be observed from the Figure 4.79 that increasing PA6 in the nanocomposite decreased the axial force. This indicates that the melt viscosity of the nanocomposites is inversely proportional to the PA6 composition in the blend together with increasing level of exfoliation seen in XRD plots. Recently, Paul and co-workers have performed experiments using dynamic and steady shear capillary rheometers over a large range of frequencies and shear rate for pure polyamide-6 with different molecular weights and their nanocomposites [279]. The results of steady shear experiments showed that the nanocomposite melt viscosities of the low molecular weight polyamide, whose level of exfoliation was found to be lower than high molecular weight, is higher than its pure matrix; whereas, the nanocomposites of high molecular weight matrices exhibited lower melt viscosities than pure matrices. The decrease in melt viscosity with the exfoliation was associated to the clay platelet alignment and polymer matrix degradation [279, 280].

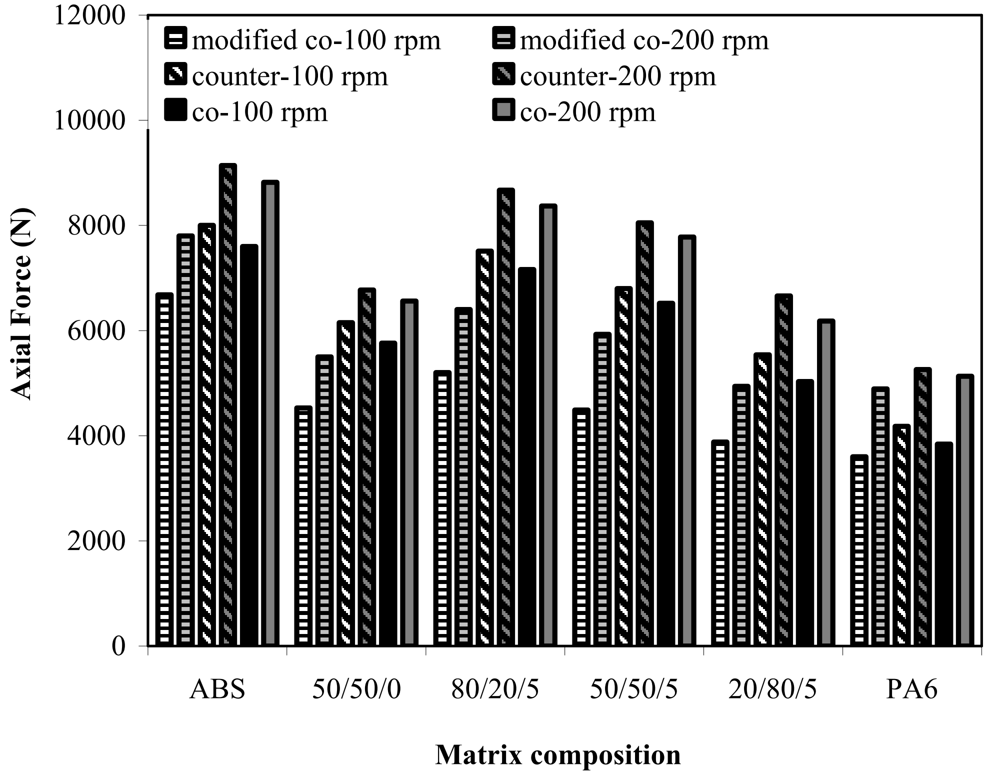

Figure 4.79 Dependence of axial force on screw geometry, speed and blend composition for nanocomposites containing 5% organoclay

The influence of addition of compatibilizer to the viscosity of the nanocomposite was only examined for 50/50 blend system. It is observed that the incorporation of compatibilizer to the blend resulted in a slight increase in the viscosity of the nanocomposite at 100 rpm and a significant increase at 200 rpm regardless of the screw geometry. Also, note that doubling the screw speed increased the axial force, as expected.

The most important result revealed from axial force measurements is the dependence of axial force on the screw geometry for a given blend system and screw speed. As the axial forces measured at the same processing conditions and for a given blend composition are considered, the screw modification in co-rotation resulted in a lower value in comparison with unmodified one. This result indicates that more material is flowing backward due to backpressure in presence of slots on the screw flights. As a result of backflow, the melt can be subjected to elongational flow due to jetting through the channels and broader residence time distribution can be achieved in the mixing chamber. Figure 4.80 shows the suggested flow pattern for modified co-rotating screws. The polymer was separated from the screws after cooling.

The axial force values measured in counter-rotation mode is higher than those measured in modified co-rotation mode for all screw-speeds and all blend compositions. In comparison with co-rotation, significantly higher values were also measured in the case of counter rotation, because of the mixing and transport characteristics of the counter rotation, which is discussed in morphology section.

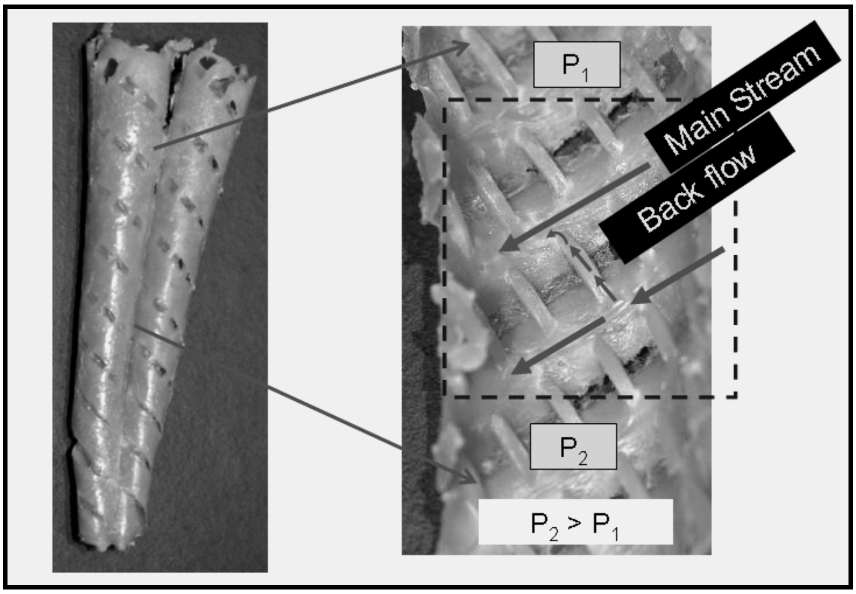

Figure 4.80 Schematic view of suggested flow pattern for modified co-rotating screws (P_1 and P_2 stands for pressure at the top and bottom, respectively)

It has been known that moduli of the composites are a function of filler volume fraction, filler aspect ratio, filler modulus, filler orientation and interfacial adhesion. Paul and Fornes conducted theoretical studies, which were benchmarked against experimental data, to model the modulus of the PA6/organoclay nanocomposites by utilizing Halpin-Tsai theory [262]. It was pointed out in their publications that modulus of a given nanocomposite system depends on the level of dispersion of the clay platelets as a result of processing history and surface chemistry. By using this approach, in the current study, the modulus of the nanocomposites were taken as an indication of level of dispersion of the platelets for a given matrix.

Figure 4.81 compares the responses of Young Modulus of 5 % clay containing nanocomposites as the function of screw speed, screw rotation mode and blend ratio. In the case of ABS, increasing screw speed and screw geometry from co-rotation to counter-rotation did not significantly influence the modulus of the resulting nanocomposite. The changes measured in ABS are between the error-limits. When the PA6 based nanocomposites were considered, the modulus of the nanocomposites is higher in co-rotation than that of in counter-rotation regardless of the screw speed. In either co-rotation or counter rotation, doubling the screw speed resulted in an increase in modulus of the PA6 based nanocomposites. The tensile modulus of the ABS/PA6 blends based nanocomposites also shows variations with processing conditions. For the 80/20 blend system, the modulus in co-rotation was higher than that in counter-rotation (see Figure 4.81). Improved clay dispersion in PA6 phase together with much smaller diameter of the reinforced spherical PA6 phase seen in SEM micrographs are the possible reason of obtaining higher modulus in co-rotation. The nanocomposites formed from 80/20/5 blend can be handled as particulate filled ABS in which clay reinforced PA6 and ABS can be considered as reinforcing fillers and polymer matrix, respectively. For such systems, it was shown experimentally that the filler size is inversely proportional to the strength and stiffness of the composites [28, 281-282]. Increasing screw speed caused an improvement in modulus of nanocomposites in co-rotation, however no effect was observed in counter-rotation with the doubling of the screw speed.

The dependence of tensile moduli on screw rotation mode was more pronounced in nanocomposites based on 50/50/5 and 20/80/5 blends. The moduli measured in co-rotation deteriorated in counter rotation at both 100 and 200 rpm. When the screw speed was doubled, a slight increase in moduli was obtained. When the moduli of the blend based nanocomposites are considered, an improvement with PA6 content was observed. Possible reason for this increase can be the dilution of the intercalated clays by the increasing PA6 concentration, which can prevent the formation of the clusters of the intercalated and/or exfoliated platelets.

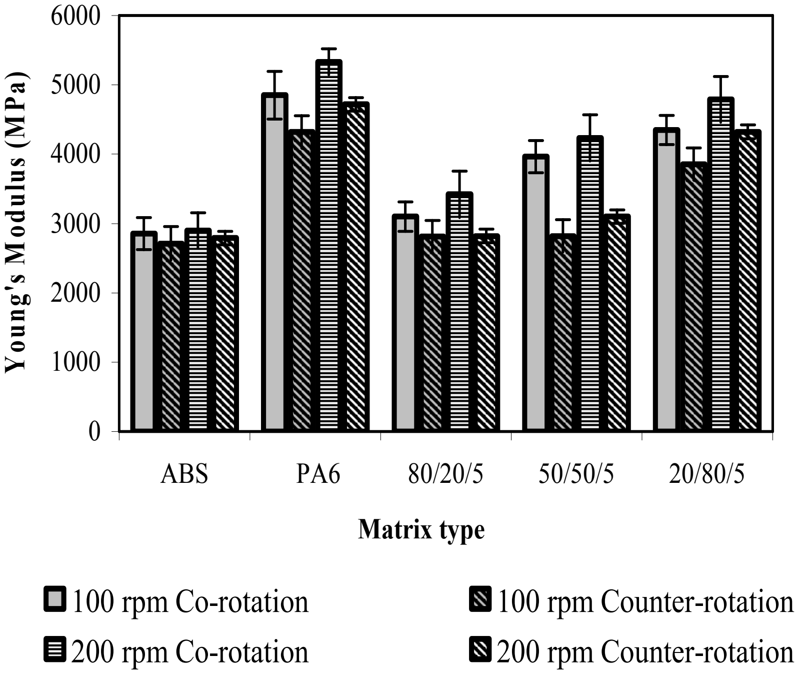

Figure 4.81 Young Modulus of nanocomposites containing 5% clay as the function of screw speed, screw geometry and blend ratio

Figure 4.82 shows the Young Modulus of 50/50/5 blend based nanocomposites as the function of screw speed, screw modification and clay loading level. As can be seen, incorporation of organoclay improved the modulus of the blends substantially. Similar trends in modulus were reported by the researchers in the literature for different polymer/clay systems [249, 262, 277, 283]. This increasing stiffness of the final structure can be a consequence of the interaction of the polyamide and organic surfactant. This interactions lead to restriction of the mobility of the polyamide molecules. As a result, one of the components of the blend system becomes stiffer, which increase the overall modulus of the blend. Increasing clay concentration resulted in an increase in modulus regardless of the screw speed and screw modification.

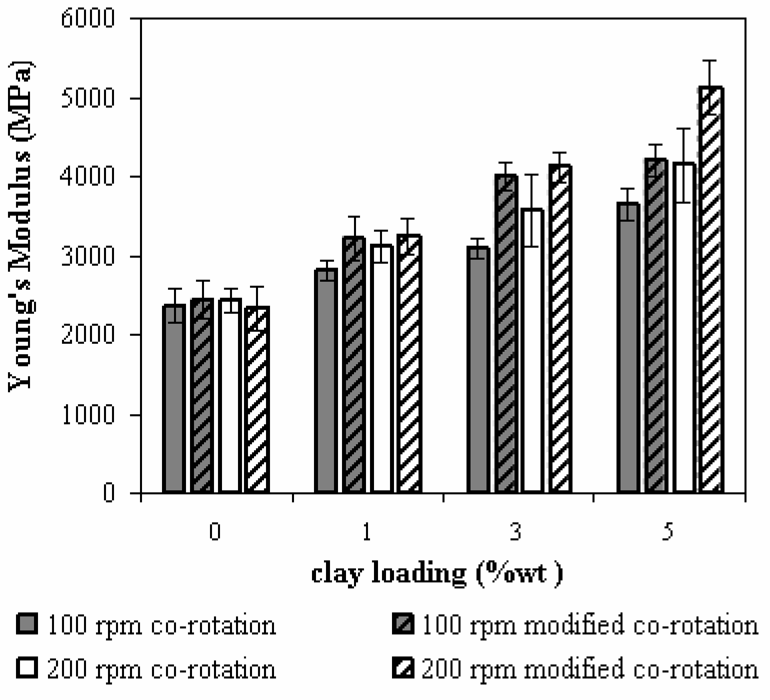

Figure 4.82 Young Modulus of 50/50/5 blend based nanocomposites as the function of screw speed, screw rotation mode and clay loading

Table 4.13 Stress-strain data for 5% clay reinforced blends, ABS and PA6 as the function of screw rotation mode and screw speed

Material	**Process conditions**		**Yield Strength (MPa)**	**Strain at break (%)**
ABS	*Co-rotation*	*100 rpm*	58.4±2.3	6.2±2.1
		200 rpm	60.1±1.9	5.6±1.3
	Counter-rotation	*100 rpm*	53.6±3.2	4.2±2.3
		200 rpm	55.7±.9	3.6±1.4
	Modified co-rotation	*100 rpm*	58.7±1.6	7.2±3.1
		200 rpm	62.5±2.4	7.4±1.0
80/20/20	*Co-rotation*	*100 rpm*	58.6±2.3	6.9±3.4
		200 rpm	57.8±2.8	7.3±2.2
	Counter-rotation	*100 rpm*	52.6±3.3	4.9±3.8
		200 rpm	53.8±1.5	6.2±2.9
	Modified co-rotation	*100 rpm*	58.9±4.2	6.3±1.7
		200 rpm	61.8±1.3	5.3±4.5
50/50/5	*Co-rotation*	*100 rpm*	72.0±2.9	3.2±2.1
		200 rpm	77.5±4.3	3.3±2.0
	Counter-rotation	*100 rpm*	62.4±4.3	4.3±2.5
		200 rpm	64.7±3.9	3.1±0.9
	Modified co-rotation	*100 rpm*	75.6±1.9	4.1±1.0
		200 rpm	76.3±2.3	5.5±2.9
20/80/5	*Co-rotation*	*100 rpm*	78.3±2.7	7.6±4.3
		200 rpm	82.3±3.2	7.3±3.8
	Counter-rotation	*100 rpm*	72.6±2.2	6.6±3.3
		200 rpm	73.3±5.4	7.2±1.7
	Modified co-rotation	*100 rpm*	82.3±2.1	7.4±2.7
		200 rpm	84.3±1.2	9.3±2.7
PA6	*Co-rotation*	*100 rpm*	87.2±2.1	9.1±4.2
		200 rpm	92.3±2.1	8.4±3.8
	Counter-rotation	*100 rpm*	82.6±1.5	7.1±4.9
		200 rpm	83.9±2.9	7.5±3.3
	Modified co-rotation	*100 rpm*	92.7±3.4	9.1±4.7
		200 rpm	95.3±2.6	9.4±3.3

It has been already shown that modification of the screw by inserting flight slots resulted in more backflow which is known as more effective in obtaining dispersive mixing [268, 284, 285]. In the current study, the effects of screw modification and screw speed on the modulus of 50/50/5 blend based nanocomposites were not significant at 1 % clay loading level (see Figure 4.82). Modification of the screws resulted in an increase in modulus of 3 and 5 % clay containing nanocomposites at given screw speeds. Increasing screw speed also improved the modulus of the nanocomposite at 3 and 5 % clay loading level. This improvement was so significant at 5% clay loading for modified screws.

Table 4.13 shows the stress-strain data for 5% clay reinforced blends, ABS and PA6 as the function of screw rotation mode and screw speed. As can be observed from the table, the yield strengths of the materials increased with PA6 content in the blend. Unlike the modulus of elasticity, yield strength of the composites are preferentially affected by the interfacial adhesion rather than filler geometry (i.e. aspect ratio). From this point of view, the increasing strength with increasing PA6 content can be attributed to the increasing extent of interaction between matrix and clays, resulting delayed formation of micro-voids/crazes that brings material to failure when they combine and form a crack. Also it should be noted that increasing PA6 improved the matrix's strength.

As a general trend, yield strength of the nanocomposites processed in counter-rotation was lower than that of processed in co-rotation (see Table 4.13). The effect of screw modification on yield strength did not follow a trend; besides, for some compositions it improved the yield strength. Doubling screw speed resulted in an improvement in yield strength of nanocomposites which were processed in modified or unmodified co-rotation. There is no significant effect of screw speed observed on yield strength when the nanocomposites processed in counter-rotation were taken into consideration. Strain at break values of nanocomposites increased in modified co-rotation with respect to unmodified co- and counter rotation. However differences between average data are not so significant.

For laboratory mixing systems, which resembles the one used here, the residence times were much longer (i.e. >10 min) in the literature than that of in the current study [167, 168]; however, in commercial systems, the average residence times are shorter. To examine the effect of residence time (1, 3, 5 and 7 minutes) on the modulus data as the function of screw speed, screw geometry of 50/50 blend based nanocomposites for the current mixing system were judged (see Figure 4.83). It was observed that increasing residence time from 1 to 3 minute yielded an increase in modulus for given screw speed and screw rotation mode. Despite the further increase in residence time, there was not any significant influence on the modulus. It should be also noted that the colour of nanocomposite was more brownish than the others at 7 minutes of residence time, possibly because of the thermal degradation of organic modifier [280] or ABS.

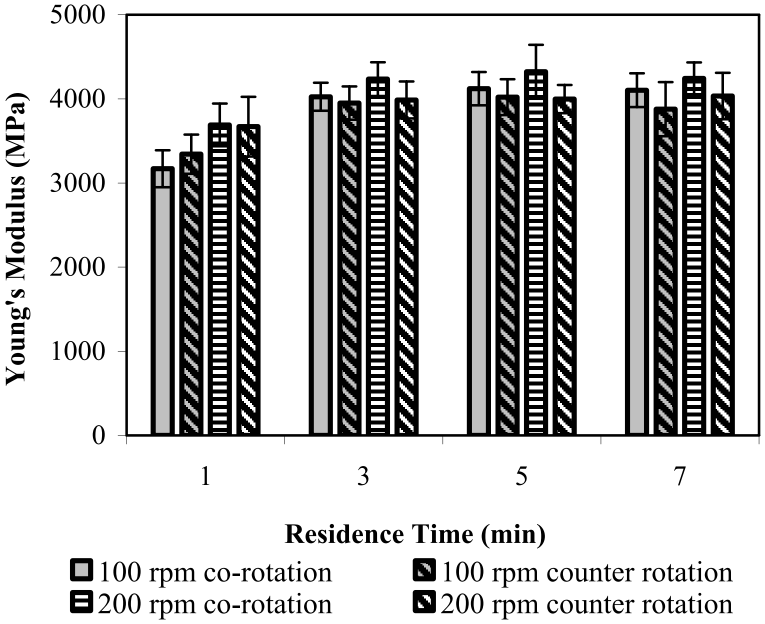

Figure 4.83 Young Modulus of nanocomposites as the function of screw speed, screw geometry and residence time for 5% clay reinforced 50/50/5 blend

CHAPTER 5

CONCLUSIONS

5.1 Compatibilization of ABS/PA6 Blends

Blends of ABS and PA6 compatibilized with/without EnBACO-MAH and EMA-GMA at various amounts were explored as a function of blend composition. The conclusions drawn out are given below:

i. Morphological studies indicated that incorporation of the maleated and epoxydized olefin based polymers compatibilize the ABS/PA6 polymers.
ii. When the compatibilization efficiencies were compared in terms of blend morphologies, it was observed that EnBACO-MAH resulted in finer dispersion of second phase than that of EMA-GMA.
iii. Tensile behavior of the blends was complex but in general the yield strength of blends increased with the increasing amount of PA6 in the blend.
iv. Incompatibilized blend showed decreasing trend in impact strength values. Incorporation of the compatibilizers improved the toughness of the blends significantly.
v. Despite the inconvenience in yielding criterion, essential work of fracture (EWF) methodology was successfully demonstrated in ABS/PA6/Compatibilizer ternary blends at different composition.

5.2 SGF Reinforced ABS and ABS/PA6 Blends

The effects of SGF surface chemistry, ABS/PA6 ratio, processing conditions and compatibilization in ABS/PA6 blends on the morphologies and mechanical properties of SGF/ABS/PA6 composites were examined. The conclusions drawn out are given below:

i. Comparison of thermodynamic adhesion values with the experimental ILSS values indicates the importance of inter-chain diffusion and mechanical interlocking of polymer chains at the interfacial region between the fiber and the matrix.

ii. Among the silane coupling agents, aminopropyltriethoxysilane functions the best which is manifested by high ILSS and thermodynamic adhesion values with PA6 and ABS.

iii. Incorporation of PA6 to the ABS improves the stiffness and strength of SGF composites.

iv. Incorporation of SGF to the ABS resulted in brittle fracture. The PA6 containing ABS/SGF composites tend to have higher impact strength than the one which does not contain PA6.

v. SGF concentration, barrel temperature in extrusion and screw speed have influence on the mechanical properties on SGF/ABS composites.

vi. Incorporation of EnBACO-MAH as the compatibilizer improved the mechanical properties of the SGF/ABS/PA6 composites.

vii. The most important result is the improvement of notched impact strengths. Addition of the compatibilizer drastically increased the impact strength of the 30% SGF reinforced ABS/PA6 blends.

5.3 ABS/PA6 Blends Based Nanocomposites

Organoclay based nanocomposites were prepared using compatibilized ABS/PA6 blends as the matrix applying melt intercalation method in a microcompounder. The effects of blend composition, clay loading level and screw speed were examined in terms of dispersability of the clay platelets, phase morphology and mechanical properties. The conclusions drawn out are given below:

i. Clay addition and microprocessing conditions influenced the blend morphology.

ii. Nanocomposite composed of ABS and OMLS were intercalated only however the nanocomposites composed of PA6 and OMLS were exfoliated.

iii. The level of exfoliation and dispersion in the blends highly depends on the amount of PA6 in the matrix.

iv. The clays were selectively exfoliated in PA6 phase and formed stacks at the interfacial region between ABS and PA6.

v. Increasing screw speed and mixing in co-rotation and modified co-rotation mode promoted the dispersibility of the clays and the stiffness of the nanocomposites.

vi. The melt viscosity of the nanocomposites revealed from axial force measurements was inversely proportional to the PA6 composition in the blend. The reduction in axial force in modified co-rotation with respect to unmodified co-rotation was an indication of enhanced backflow at a given nanocomposite system and processing condition.

CHAPTER 6

RECOMMENDATIONS

ABS/PA6 blends combine good properties of the individual components by resulting synergistic property profile. It provides an interesting combination of important product properties such as excellent impact strength, high surface quality, easy processing, chemical resistance and heat resistance. The key issue is the "compatibilization". The results of this study showed that due to low T_g of acrylic grafted olefin based maleated or epoxydized copolymers are good candidates of compatibilizers especially high toughness is desired. In this study, two types of olefinic copolymers containing certain amount of maleic anhydride or glycidiyl methacrylate were utilized to examine compatibilization efficiency. In addition to that, for simplicity only 5 and 10 % compatibilizer containing blends were processed. It is uncertain, though; at what percent of functional group does these compatibilizers function or what the optimum loading level of these compatibilizer is. On the other hand, only certain grades of ABS and PA6 were utilized in the current study. The results would differ, if different grades of matrix materials were used. For instance, the butadiene content of ABS or the molecular weight of PA6 would have influence on the final properties of blends prepared. All of these issues related to the materials open the door of unlimited number of studies.

The toughness of the materials are generally characterized by standard impact tests such as notched/unnotched Izod or Charpy testing according to relevant standard methods. These tests are practical, industry-friendly, the results obtained from these tests are comparable to each other and they do not require any complicated experimental systems. However, the fracture energies obtained by these tests are not a material property and depend on various parameters such as material dimensions, crack geometry and rate of deformation. In the current study, the Impact Essential Work of Fracture Toughness Methodology was applied to characterize the toughness and deformation mechanism under impact conditions of ABS/PA6 blends. Despite the insatisfaction of the criteria of the method, the results of the study emphasize the applicability of the method to the current blends. However, more works need to be conducted to find acceptance from science society about the applicability of this method for blends, composites and nanocomposites.

From the mechanical property point of view, short glass fiber reinforced ABS/PA6 blends resulted in improved stiffness to toughness. However, incorporation of the short glass fibers annihilates the good surface texture which is the one of the reasons of preference of ABS/PA6 blend. Therefore, from industrial point of view, a surface finish is definitely needed for short glass fiber reinforced ABS/PA6 blends. On the other hand, nanocomposites based on ABS/PA6 blends may be a good substitute for SGF reinforced ABS/PA6 blends.

The results of this study emphasized that the processing conditions has a great influence on the properties of blends and nanocomposites. Besides, screw design which defines the flow type during processing determines the morphology of the final structure. However, the processing equipment used in this part of the study is a micro-compounder and generally used as a screening device for R&D purposes. Therefore, potentially one could expect that the properties of the system might change when it is processed with conventional processing devices.

One of the interesting results arising from the nanocomposite part of the study was the selective localization of the clay platelets in PA6 phase and accumulation at the ABS/PA6 interface. Regarding to this type of dispersion, this material serves as a potential case to investigate the effects of surface properties on the selective localization of fillers in the blends. Moreover, it is obvious that the type of organic modifier of the clay, grades of ABS and PA6, and method of compatibilization will have influence on the properties of the nanocomposites.

REFERENCES

1. Utracki, L.A., Commercial Polymer Blends, Chapman and Hall, London, 1998.

2. Majumdar B., Keskkula, H., Paul, D.R., Polymer, 35, 5468 (1994).

3. Majumdar B., Keskkula, H., Paul, D.R., Polymer, 35, 3164 (1994).

4. Kudva, R.A., Keskkula, H., Paul, D.R., Polymer, 41, 225 (2000).

5. Kudva, R.A., Keskkula, H., Paul, D.R., Polymer, 41, 239 (2000).

6. Kitayama, N., Keskkula, H., Paul, D.R., Polymer, 42, 3751 (2001).

7. Chiu, H.T., Hsiao, Y.K., Polym Eng Sci, 44, 2340 (2004).

8. Lee, C.W., Ryu, S.H., Kim, H.S., Journal of Applied Polymer Science, 64, 1595 (1997).

9. Lai, S.M., Liao, Y.-C., Chen, T.-W., Polymer Engineering and Science, 45, 1461 (2005).

10. Araujo, E.M., Hage, E., Carvalho, A.J.F., Journal of Materials Science, 39, 1173 (2004).

11. Kim, B.K., Lee, Y.M., Polymer, 34, 2075 (1993).

12. Cho J.W., Paul D.R., Journal of Applied Polymer Science, 80, 484 (2001).

13. Gan, P.P., Paul, D.R., Parwa, A.R., Polymer, 35, 3513 (1994).

14. Nishimoto, M., Keskkula, H., Paul, D.R., Polymer, 30, 1279 (1989).

15. Chu, J.P., Paul, D.R., Polymer, 40, 2687 (1999).

16. Kudva, R.A., Keskkula, H., Paul, D.R., Polymer, 39, 2447 (1998).

17. Araujo, E.M., Hage, E., Carvalho, A.J.F., Journal of Applied Polymer Science, 37, 842 (2003).

18. Araujo, E.M., Hage, E., Carvalho, A.J.F., Journal of Applied Polymer Science, 90, 2643 (2003).

19. Yılmazer, U., Composite Science and Technology, 44, 119 (1992).

20. Fu, Y.S., Lauke, B., Mader, E., Yue, C.Y., Hu, X., Composites Part A, 31, 1117 (2000).

21. Thomason, J. L., Vlug, M.A., Composites Part A, 27, 477 (1996).

22. Tjong, S.C., Xu, S.A., Li, R.K.Y., Mai, Y.W., Composite Science and Technology, 62, 2017 (2002).

23. Laura, D.M., Keskkula, H., Barlow, J.W., Paul, D.R., Polymer, 43, 4673 (2002).

24. Frenzel, H., Bunzel, U., Hassler, R., Pompe, G., Journal of Adhesion Science and Technology, 14, 651 (2000).

25. Gonzalez, V.A., Uc, J.M.C., Olayo, R., Franco, P.J.H., Composites Part B, 30, 309 (1999).

26. Bikiaris, D., Matzinos, P., Prinos, J., Flaris, V., Larena, A., Panayiotou, C., Journal of Applied Polymer Science, 80, 2877 (2001).

27. Akbay, A.R., Bayramlı, E., Journal of Adhesion Science and Technology, 50, 155 (1995).

28. Sharpe, L.H., Interfacial Interactions in Polymeric Composites, Akovalı G. (Ed.), Nato ASI Series, Kluiwer Academic Publisher, Netherlands, 1992.

29. Plueddeman, E.P., Silane Coupling Agents, Plennum Pres, New York, 1991.

30. Pak, H.S., Caze, C., Journal of Applied Polymer Science, 65, 143 (1997).

31. Xanthos, M., (Ed.), Reactive Extrusion Principles and Practice, Carl Hanser Verlag, New York, 1992.

32. Fu, Y.S., Lauke, B., Composites Part A 29, 631 (1995).

33. Fu, Y.S., Lauke, B., Composites Part A, 29, 575 (1998).

34. Usuki, A., Kojima, Y., Kawasumi, M., Okada, A., Fukushima, Y., Kurauchi, T., Kamigatio, O., Journal of Materials Research, 8, 1179 (1993).

35. Usuki, A., Koiwai, A., Kojima, Y., Kawasumi, M., Okada, A., Kurauchi, T., Kamigatio, O., Journal of Applied Polymer Science, 55, 119 (1995).

36. Okada, A., Usuki, A., Materials Science and Engineering, 3, 109 (1995).

37. Okada, A., Fukushima, Y., Kawasumi, M., Inagaki, S., Usuki, A., Sugiyama, S., Kurauchi, T., Kamigatio, O., U.S. Patent No. 4739007, 1998.

38. Dennis, H.R., Hunter, D.L., Chang, D., Kim, S., White, J.L., Cho, J.W., Paul, D.R., SPE ANTEC Technical Paper, 40, 428 (2000).

39. Nahin, P.G., Backlund, P.S., U.S. Patent No. 3084117, 1963.

40. Liu, L., Qi, Z., Zhu, X. J., Journal of Applied Polymer Science, 71, 1113 (1999).

41. Ajayan, P.M., Schadler, L.S., Braun, P.V., Nanocomposite Science and Technology, Wiley-VCH Verlag GmbH&Co., Weinheim, 2003.

42. Alexandre, M., Dubois, P., Materials Science and Engineering, 28, 1 (2000).

43. Dennis, H.R., Hunter, D.L., Chang, D., Kim, S., White, J.L., Cho, J.W., Paul, D.R., Polymer, 42, 9513 (2001).

44. Cho, J.W., Paul, D.R., Polymer, 42, 1083, (2001).

45. Modesti, M., Lorenzetti, A., Bon, D., Besco, S., Polymer, 46, 10237 (2005).

46. Artzi, N., Narkis, M., Siegman, A., Journal of Polymer Science: Polymer Physics, 43, 1931 (2005).

47. Khatua, B.B., Lee, D.J., Kim, H.Y., Kim, J.K., Macromolecules, 37, 2454 (2004).

48. Baldi, F., Bignotti, F., Tieghi, G., Ricco, T., Journal of Applied Polymer Science, 99, 3406 (2006).

49. Gonzalez, I., Eguiazabal, J.I., Nazabal, J., European Polymer Journal, 42, 2905 (2006).

50. Isik, I., Yilmazer, U., Bayram, G., SPE ANTEC Technical Paper, (2006).

51. Chow, W.S., Abu Bakar, A., Ishak, Z.A.M., Karger-Kocsis, J., Ishiaku, U.S., Apostolov, A.A., European Polymer Journal, 41, 687 (2005).

52. Pötschke, P., Kretzschmar, B., Janke, A., Composite Science and Technology, Article in press, doi: 10.1016/j.compscitech.2006.02.034 (2006).

53. Li, J.Y., Shimizu, H., Polymer, 45, 7381 (2004).

54. Gelfer, M.Y., Song, H.H., Liu, L.Z., Hsiao, B.S., Chu, B., Rafailovich, M., J Polymer Science: Polymer Physics, 41, 44 (2003).

55. Keskkula, H., Paul, D.R., Polymer Blends in Kirk Othmer Encyclopedia of Chemical Technology, John Willey & Sons Inc., 1996.

56. Ting, S.P., Pearce, E.M., Kwei, T.K., J. Polymer Science Polymer Letter Editor, 18, 201 (1980).

57. Joseph, E.A., Lorenz, M.D., Barlow, J.W., Paul, D.R., Polymer, 23, 112 (1982).

58. Yee, A.F., Polymer Engineering Science, 17, 213 (1977).

59. Stein, R.S., Paul, D.R., (Ed.), Newman, S., (Ed.), Polymer Blends, Academic Press Inc., New York, 1978.

60. Maeda, Y., Paul, D.R., Polymer, 26, 2055 (1985).

61. Kambour, R.P., Smith, S.A., Journal of Polymer Science Polymer Physics, 20, 2069 (1982).

62. Murff, S.R., Barlow, J.W., Paul, D.R., Advances in Chemistry, 211, 313 (1986).

63. Callaghan, T.A., Takakuwa, K., Paul, D.R., Padwa, A.R., Polymer 34, 3796 (1993).

64. Barlow, J.W., Paul, D.R., Polymer Engineering and Science, 24, 525 (1984).

65. http://www.specialchem4polymers.com/tc/Adhesion-Promoters/, 2007.

66. Majumdar, B., Keskkula, H., and Paul, D.R., Polymer 35, 1386 (1994).

67. Mamat, A., Khanh, V.T., Cigana, P., Favis, B.D., Journal of Polymer Science: Part B, 35, 2583-2592 (1997).

68. Pressly, T.G., Keskkula, H., Paul, D.R., Polymer, 42, 3043-3055 (2000).

69. Modern Plastic Encyclopedia, McGraw Hill, New York, USA, 1986.

70. Bucknall, C.B., Toughened Plastics, Applied Science Publishers, London, 1997.

71. Echte, A., Rubber-Toughened Plastics, Advances in Chemistry, American Chemical Society, 222, Washington, 1989.

72. http://www.the-innovation-group.com/ChemProfiles/ABS%20Resin.htm, 2007.

73. Kim, K.B., Lee, M.Y., Polymer, 34, 2075 (1993).

74. Majumdar, B., Kekkula, H., Paul, D.R., Polymer, 35, 6468 (1994).

75. Liu, X., La Mantia, F., Scaffaro, R., Journal of Applied Polymer Science, 86, 449 (2002).

76. Datta, S., Lohse D., Polymeric Compatibilizers, First Edition, Hanser Publisher, New York (1996).

77. Akovalı, G., Handbook of Composite Fabrication, Rapra Technology Lmt., UK, 2001.

78. Ramsteiner, F., Theysohn, R., Composite, 35, 111 (1979).

79. Kelly, A., Tyson, W.R., Journal of Mechanics and Physics of Solids, 13, 329 (1965).

80. Fu, Y.S., Lauke, B., Mader, E., Yue, Y.C., Hu, X., Composites Part A, 31, 1117 (2000).

81. Cansever, M., Effect of twin screw compounding conditions on the mechanical properties of nylon 6/glass fiber composites, M.Sc. Thesis, Middle East Technical University, 1999.

82. Hull, D., An introduction to Composite Materials, Cambridge University Press, U.K., 1987.

83. Eberhardt, C., Clarke, A., Wincent, M., Giroud, T., Flouret, S., Composite Science and Technology, 61, 1961 (2001).

84. Nielsen, L.E., Landel, F.R., Mechanical properties of polymers and composites, Marcel Dekker, New York, 1994.

85. Bigg, D.M., Polymer Composites, 6, 20 (1985).

86. Turkovich, R., Erwin, L., Polymer Engineering and Science, 23, 743, (1993).

87. Park, S.J., Jin, J.S., Journal Polymer Science Part: B, 41, 55 (2003).

88. Pisanova, E., Mader, E., Journal Adhesion Scicience and Technology, 14, 415 (2000).

89. Nardin, M., Schultz, J., Interfacial Interactions in Polymeric Composites, Nato ASI Series, Kluiwer Academic Publisher, The Netherlands, 1992.

90. Sharpe, L.H., Interfacial Interactions in Polymeric Composites, Nato ASI Series, Kluiwer Academic Publisher, The Netherlands, 1992.

91. Oss, J.C., Good, J.R., Chaudhury, M.K., Langmuir, 4, 884, (1988).

92. Akovalı, G., Torun, T.T., Bayramlı, E., Erinç, N.K., Polymer, 39, 1363, (1998).

93. Annual Book of ASTM Standards, ASTM D 2344: Standard Test Method for Inter Laminar Shear Strength by Short Beam Flexural Test, 08.01, Philadelphia, 1993.

94. Le Baron, P.C., Wang, Z., and Pinnavaia, T.J., Applied Clay Science, 15, 11, (1999).

95. Ajayan, P.M., Schadler, L.S. and Braun, P.V., Nanocomposite Science and Technology, Wiley-VCH Verlag H&Co., Weinheim, 2003.

96. Schmidt, D., Shah, D., Giannelis, E.P., Current Opinion in Solid State and Materials Science, 6, 205 (2002).

97. http://zeus.plmsc.psu.edu/nano.html, 2007.

98. Dennis, H.R., Hunter, D.L., Chang, D., Kim, S., White, J.L., Cho, J.W., Paul, D.R., Polymer, 42, 9513 (2001).

99. Seymour, R.B., Reinforced Plastics: Properties and Applications, ASM International, Katleen Mills Editorial, USA, 1993.

100. http://www.nanocompositech.com/review-nanocomposite.htm, 2007.

101. Hussain, F., Hojjati, M., Okamoto, M., Gorga, R.E., Joutnal of Composite Materials, 40, 1511 (2006).

102. Kornmann, X., Synthesis and Characterisation of Thermoset-Clay Nanocomposites, Licenciate Thesis, Luleå University of Technology, Sweden 2000.

103. Schmidt, D., Shah, D., Giannelis, E.P., Current Opinion in Solid State and Materials Science, 6, 205, (2002).

104. Beyer, G., Plastics Additives & Compounding, October, 22 (2002).

105. Krishnamoorti, R., Yurekli, K., Current Opinion in Colloid & Interface Science, 6, 464 (2001).

106. Fried, JR., Polymer Science and Technology, Prentice Hall PTR, USA, 2003.

107. Kılınç, M., Processing and Characterization of Poly(ethylene terephthalate) Based Composites, M.S., Middle East Technical University, Ankara, 2004.

108. Annual Book of ASTM Standards, ASTM D 638 M-91a: Standard Test Method for Tensile Properties of Plastics, 08.01, Philadelphia, 1993.

109. Annual Book of ASTM Standard, ASTM D 790 M-92: Standard Test Methods for Flexural Properties of Unreinforced and Reinforced Plastics and Electrical Insulating Materials, 08.01, Philadelphia, 1993.

110. Callister, W.D., Materials Science and Engineering: An Introduction, John Wiley and Sons Inc., New York, 1997.

111. http://www.testlopedia.com/, 2007.

112. Seymour, R.B., Carraher, C.E., Structure-Property Relationships in Polymers, Plenum Press, New York, 1984.

113. Annual Book of ASTM Standards, ASTM D 256-92: Standard Test Methods for Impact Resistance of Plastics and Electrical Insulating Materials, 08.01, Philadelphia, 1993.

114. Concise Encyclopedia of Polymer Science and Engineering, John Wiley and Sons, Inc., New York, 1990.

115. http://en.wikipedia.org/wiki/Transmission_electron_microscope, 2007.

116. Annual Book of ASTM Standard, ASTM D 1238 M-92: Standard Test Methods for Melt Flow Index of Plastics, 08.01, Philadelphia, 1993.

117. Watson, E.S., O'Neill, M.J., Justin, J., Brenner, N., A Differential Scanning Calorimeter for Quantitative Differential Thermal Analysis, Analytical Chemistry, 36, 1233, (1964).

118. Lobo, H., Bonilla, J.V., Handbook of Plastics Analysis, Marcel Dekker Inc., New York, 2003.

119. Encyclopedia of Polymer Science and Technology: Plastics, Resins, Rubbers, and Fibers, John Wiley and Sons Inc., New York, 1970.

120. Rosen, S.L., Fundamental Principles of Polymeric Materials, John Wiley and Sons Inc., New York, 1993.

121. Menard, K., Dynamic mechanical analysis: A practical introduction, CRC press, New York, 1999.

122. Sinha, S., Ray, K., Okamoto, M., Macromolecules, 36, 2355 (2003).

123. Kayano, Y., Keskkula, H., Paul, D.R., Polymer, 39, 2835 (1998).

124. Crouch, B. A., Huang, D.D., Journal of Materials Science, 29, 861 (1994).

125. Duffy, J., Shih, C.F., Proceedings of the Seventh International Conference on Fracture, Permagon, Oxford, 1989.

126. Hashemi, S., Williams, J.G., Journal of Materials Science, 26, 621 (1991).

127. Huang, D.D., Williams, J.G., Journal of Materials Science, 22, 2503 (1987).

128. Huang, D.D., Proceedings of the Seventh International Conference on Fracture, Permagon, Oxford, 1989.

129. Huang, D.D., Joyce J.A., (Ed.), The application of the multispecimen *J*-integral technique to toughened polymers. Inc. Elastic-plastic test methods: the user’s experience, Philadelphia, ASTM, 1991.

130. Seidler, S., Grellmann, W., Journal of Materials Science, 28, 4078 (1993).

131. Zhou, Z., Landes, J.D., Huang, D.D., Polymer Engineering and Science, 34, 128 (1994).

132. Annual Book of ASTM Standards, ASTM E 399: Standard test method for plane-strain fracture toughness of metallic materials, 03.01, Philadelphia, 1990.

133. Williams, J.G., Fracture Mechanics of Polymers, Ellis Horwood Series in Engineering, Chicher, 1984.

134. Annual Book of ASTM Standards, ASTM E-813: Standard test method for J_{Ic}, a measure of fracture toughness, 03.01, Philadelphia, 1990.

135. Mai, Y.W., Powell, P., Journal of Polymer Science: Polymer Physics, 29, 785 (1991).

136. Wu, J., Mai, Y.W., Polymer Engineering and Science, 36, 2275 (1996).

137. Wu, J., Mai, Y.W., Cotterell, B., Journal of Materials Science, 28, 3373 (1993).

138. Mai, Y.W., Cotterell, B., Engineering Fracture Mechanics, 21, 123 (1985).

139. Mai, Y.W., Cotterell, B., International Journal of Fracture, 32, 105 (1986).

140. Mai, Y.W., Cotterell, B., Horlyck, R., Vigna, G., Polymer Engineering and Science, 27, 804 (1987).

141. Test Protocol for Essential Work of Fracture (Version 5), European Structural Integrity Society, 1997.

142. Paul, D.R., Bucknall, C.B., Polymer Blends: Formulation and Performance, Wiley, New York, 1999.

143. Chan, W.Y.F., Williams, J.G., Polymer, 35, 1666 (1994).

144. Paton, C.A., Hashemi, S., Journal of Materials Science 1992, 27, 2279 (1992).

145. Hashemi, S., Journal of Materials Science, 28, 6178 (1993).

146. Fasce, L., Bernal, C., Frontini, P., Mai, Y.W., Polymer Engineering Science, 41, 1 (2001).

147. Vu-Khanh, T., Polymer, 29, 1979 (1998).

148. Vu-Khanh, T., de Charentenay, F.X., Polymer Engineering and Science, 25, 841 (1985).

149. http://www.aoe.vt.edu/~devenpor/aoe3054/manual/expt5/text.html, (2006).

150. Vu-Khanh, T., Theoretical and Applied Fracture Mechanics, 21, 83 (1994).

151. Hourston, D.J., Lane, S., Zhang, H.X., Polymer, 36, 3051 (1995).

152. Kayano, Y., Keskkula, H., Paul, D.R., Polymer, 38, 1885 (1997).

153. Kayano, Y., Keskkula, H., Paul, D.R., Polymer, 39, 821 (1998).

154. Hashemi, S., Journal of Materials Science, 32, 1563 (1997).

155. Levita, G., Parisi, L., Marchetti, A., Journal Materials Science, 29, 4545 (1994).

156. Levita, G., Parisi, L., Marchetti, A., Journal of Materials Science, 31, 1996 (1996).

157. Karger-Kocsis, J., Czigany, T., Polymer, 37, 2433 (1996).

158. Karger-Kocsis, J., Czigany, T., Moskala, E., Polymer, 38, 4587 (1997).

159. Karger-Kocsis, J., Czigany, T., Moskala, E., Polymer, 39, 3939 (1998).

160. Kudva, R.A., Keskkula, H., Paul, D.R., Polymer, 41, 335 (2000).

161. Rauwendaal, C., Polymer Extrusion, Hanser Publisher, Munic, 2001.

162. Tiesnitsch, J., www.xplore-together.com/data/xplore_internet_paper.pdf, 2007.

163. www.xplore-together.com/home.htm, 2007.

164. Tiesnitsch, J., SPE ANTEC Papers, 2005.

165. Walia, P., Barger, M., Mc Kelvy, M., SPE ANTEC Papers, 2005.

166. Potyrailo, R., Wroczynki, R., Rubinsztajn, M., SPE ANTEC Papers, 2003.

167. Stretz, H.A., Paul, D.R., Polymer, in press, (2006).

168. Pötschke, P., Kretzschmar, B., Janke, A., Composite Science and Technology, in press, doi:10.1016/j.compscitech.2006.02.034 (2006).

169. Maric, M., Macosko, C.W., Polymer Engineering and Science, 41, 118 (2001).

170. Breuer, O., Sundararaj, U., Toogood, R.W., Polymer Engineering and Science, 44, 868 (2004).

171. Yamaoka, I., Polymer, 39, 1765 (1998).

172. Rauwendaal, C., Polymer Mixing, Hanser Publisher, Munic, 2001.

173. Sclavons, M., Carlier, V., De Roover, B., Franquinet, P., Devaux, J., Legras, R., Journal of Applied Polymer Science, 62, 1205 (1996).

174. Ozkoc, G., Bayram, G., Bayramli, E., SPE ANTEC, (2003).

175. Fornes, T.D., Paul, D.R., Polymer, 44, 4993 (2003).

176. Thomas, S., Groeninckx, G., Polymer, 40, 5799 (1999).

177. Tedesco, A., Krey, P.F., Barbosa, R.V., Mauler, R.S., Polymer International 51, 105 (2001).

178. Creton, C., Kramer, E.J., Hui, C.Y., Brown, H.R., Macromolecules, 25, 3075 (1999).

179. Jin, K.K., Hwayong, L., Polymer, 37, 305 (1996).

180. Jeon, H.K., Jin, K.K., Polymer, 39, 6227 (1998).

181. Paul D.R., Barlow, J.W., Journal of Macromolecular Science, C18, 109 (1980).

182. Majumdar, B., Keskkula, H., Paul, D.R., Polymer, 35, 1399 (1994).

183. Oshinski, A.J., Keskkula, H., Paul, D.R., Polymer, 33, 284 (1992).

184. Majumdar, B., Paul, D.R., Oshinski, A., Polymer, 38, 1787 (1997).

185. Hage, E., Ferreira, L.A.S., Manrich, S., Pessan, L.A., Journal of Applied Polymer Science, 71, 423 (1999).

186. Gao, Ge., Wang, J., Jinghua, Y., Yu, X., Ma, R., Tang, X., Yin, Z., Zhang, X., Journal of Applied Polymer Science, 72, 683 (1999).

187. Ju, M. Y., Chang, F.C., Polymer, 41, 1719 (2000).

188. Kim, B.O., Woo, S.I., Polymer Bulletin, 41, 707 (1998).

189. Tol, R.T., Mathot, V.B.F., Reynaers, H., Goderis, B., Groeninckx, G., Polymer, 46, 2966 (2005).

190. Ramesh, C., Bhoje, G.E., Macromolecules, 34, 3308 (2001).

191. Hou, L., Yang, G., Macromolecular Chemistry and Physics, 206, 1887 (2005).

192. Sun, S. L., Xu, X.Y., Yang, H.D., Zhang, H.X., Polymer, 46, 7632 (2005).

193. Sudhin, D, David, J.L., Polymer Compatibilizers, Hanser Publishers, Munich, 1996.

194. Evstatiev, M., Schultz, J.M., Petrovich, S., Georgiev, G., Fakirov, S., Friedrich, K., Journal of Applied Polymer Science, 67, 723 (1998).

195. Tang, T., Huang, B., Polymer, 35, 281 (1994).

196. Paul, D.R., Bucknall, C.B., Polymer Blends, Wiley, New York (2000).

197. Wadhwa, L.H., Dolce, T.L., La Nieve, H.L., SPE RTEC, 1985.

198. Huang, J.J., Paul, D.R., Polymer, 41, 3505 (2000).

199. Dijkstra, K., van der Wal A., Gaymans, R.J., Journal of Material Science 29, 3489 (1994).

200. Chiu, H.T., Hsiao, Y.K., Polymer Engineering Science, 44, 2340 (2004).

201. Liu, X., La Mantia, F., Scaffaro, R., Journal of Applied Polymer Science, 86, 449 (2002).

202. Lee, C.W., Ryu, S.H., Kim, H.S., Journal of Applied Polymer Science, 64, 1595 (1997).

203. Laura, D.M., Keskkula, H., Barlow, J.W., Paul, D.R., Polymer, 44, 3347 (2003).

204. Sivaraman, P., Chandrasekhar, L., Mishra, V.S., Chakraborty, B.C., Varghese, T.O., Polymer Testing, 25, 562 (2006).

205. Huang, J.J., Paul, D.R., Polymer, 47, 3505 (2006).

206. Borggreve, R.J.M., Gaymans, R.J., Schuijer, J., Housz, J.F.I., Polymer, 28, 1489 (1987).

207. Margolina, A., Wu, S., Polymer, 29, 2170 (1998).

208. Ben Jar, P.Y., Wu, R.Y., Kuboki, T., Takahashi, K., Shinmura, T., Journal of Materials Science, 18, 1489 (1997).

209. Castellani, L., Frassine, R., Pavan, A., Rink, M., Polymer, 37, 1329 (1996).

210. Donald, A.M., Kramer, E.J., Journal Materials Science, 17, 1765 (1987).

211. Hagerman, E., Journal Applied Polymer Science, 17, 2203 (1973).

212. Ni, B.Y., Li, J.C.M., Berry, V.K., Polymer, 32, 2766 (1991).

213. Bernal, C.R., Frontini, P.F., Sforza, M., Bibbo, M.A., Journal Applied Polymer Science, 58, 1 (1995).

214. Lazerri, A., Bucknall, C.B., Polymer, 36, 2895 (1995).

215. Sue, H.J., Journal Materials Science, 27, 3098 (1992).

216. Sue, H.J., Bertram, J.L., Garcia-Meitin, E.I., Puckett P.M., Journal Polymer Science Part B: Polymer Physics, 33, 2003 (1995).

217. Sue, H.J., Garcia-Meitin, E.I., Orchard, N.A., Journal of Polymer Science Part B: Polymer Physics, 31, 595 (1993).

218. Sue, H.J., Yee, A.F., Journal of Materials Science, 26, 3449 (1991).

219. Wong, S.C., Mai, Y.W., Polymer, 41, 5471 (2000).

220. Oss, J.C., Good, J.R., Chaudhury, M.K., Langmuir, 4, 884 (1998).

221. Schultz, J., and Nardin, M., Handbook of Adhesive Technology, Marcel and Dekker, New York, 1994.

222. Cox, H.L., British Journal of Applied Physics, 3, 72 (1952).

223. Israelachvili, J.N., Intermolecular and Surface Forces, Academic Press, London, 1985.

224. Park, S.J., Jin, J.S., Journal of Polymer Science Part B, 41, 55 (2003).

225. Schultz, J., Lavielle, L., Science and New Applications of Carbon Fibers, Proceedings International Symposium in University of Toyohashi, Japan, 1987.

226. Hamada, H., Ikuta, N., Nishida, N., Maekawa, Z., Composites, 25, 512 (1994).

227. Dilsiz, N., Erinç, N.K., Bayramlı, E., Akovalı, G., Carbon, 33, 853 (1995).

228. Zafeiropoulos, N.E., Baillie, C.A., Hodgkjnson, J.M., Composites Part A, 33, 1185 (2002).

229. Yue, C.Y., Cheung, W.L., Journal of Materials Science, 27, 3943 (1992).

230. Turkovich, R., Erwin, L., Polymer Engineering and Science, 23, 743 (1983).

231. Fu, Y.S., Lauke, B., Composite Science and Technology, 56, 1179 (1996).

232. Thomason, J.L., Composite Science and Technology, 59, 2315 (1999).

233. Tjong, S.C., Xu, S.A., Mai, Y.W., Materials Science and Engineering A, 347, 338 (2003).

234. Fu, Y.S., Lauke, B., Mader, E., Yue, Y.C., Hu, X., Composites Part A, 31, 1117 (2000).

235. Kelly, W.R., Tyson, Journal of Mechanics and Physics of Solids, 13, 329 (1965).

236. Bigg, D.M., Polymer Composites, 6, 20 (1985).

237. Sato, N., Kurauchi, T., Sato, S., Kamigaito, O., Journal of Materials Science 19, 1145 (1984).

238. Takahashi, K., Choi, N.S., Journal of Materials Science, 26, 4648 (1991).

239. Nielsen, L.E., Landel, F.R., Mechanical Properties of Polymers and Composites, Marcel Dekker, New York, 1994.

240. Laura, D.M., Keskkula, H., Barlow, J., Paul, D.R., Polymer, 41, 7165 (2000).

241. Ozkoc, G., Bayram, G., Bayramli, E., Polymer, 45, 8957 (2004).

242. Stade, K., Polymer Engineering and Science, 17, 50 (1977).

243. Goffart, D., Van Der Wal, D.J., Klomp, E.M., Hoogstraten, H.W., Janssen, L. P.B.M., Breyssee, L., Trozley, Y., Polymer Engineering and Science, 36, 901 (1998).

244. Yilmazer, U., Cansever, M., Polymer Composites, 23, 61 (2002).

245. Fu, SY., Lauke, B., Li, R.K.Y., Mai, Y.W., Composites Part B: Engineering, 37, 183 (2006).

246. Thomason, J.L., Composites Part A: Applied Science and Manufacturing, 36, 995 (2004).

247. Sui, G.X., Wong, S.C., Yang, R., Yue, C.Y., Composite Science and Technology, 65, 221 (2005).

248. Thomason, J.L., Composites Part A: Applied Science and Manufacturing, 33, 1283 (2002).

249. Stretz., H.A., Paul, D.R., Cassidy, P.E., Polymer, 46, 3818 (2005).

250. Ozkoc, G., Bayram, G., Bayramli, E,. Journal of Applied Polymer Science, Article in Press (2006).

251. Ozkoc, G., Bayram, G., Bayramli, E., SPE ANTEC Papers (2006).

252. Willis, J.M., Favis, B.D., Polymer Engineering and Science, 28, 1416 (1988).

253. Serpe, G., Jarrin J., Dawans, F., Polymer Engineering and Science, 30, 553 (1990).

254. Cigana, P., Favis, B.D., Jerome, R., Journal of Polymer Science: Polymer Physics, 34, 1691 (1996).

255. Taylor, G., International Proceedings of Royal Soceity, London, A138, 41 (1932).

256. Taylor, G. International Proceedings of Royal Soceity, London, A146, 501 (1934).

257. Paul, D.R., Barlow, J.W., Journal of Macromolecular Science, Revievs Macromolecular Chemistry, C18, 109 (1980).

258. Wang, Y., Zhang, Q., Fu, Q, Macromolecular Rapid Communications, 24, 231 (2003).

259. Ray, S.S., Pouliot, S., Bousmina, M., Utracki, L.A., Polymer, 45, 8403 (2004).

260. Zhang, B.Q., Ding, Y.F., Chen, P., Liu, C.Y., Zhang, J., He, J.S. et. al. Polymer, 46, 5385 (2005).

261. Wang, S., Hu, Y., Song, L., Liu, J., Chen, Z., Fan, W., Journal of Applied Polymer Science, 91, 1457 (2004).

262. Fornes, T.D., Paul, D.R., Polymer, 44, 4993 (2003).

263. Stretz., H.A., Paul, D.R., Cassidy, P.E., Polymer, 46, 3818 (2005).

264. Chavarria, F., Paul, D.R., Polymer, 45, 8501 (2004).

265. Akkapeddi, M.A., Polymer Composites, 21, 576 (2000).

266. Chow, W.S., Ishak, A.M., Ishiaku, U.S., Karger-Kocsis, J., Apostolov, A.A., Journal of Applied Polymer Science, 91, 175 (2004).

267. Chow, W.S., Ishak, A.M., Ishiaku, U.S., Karger-Kocsis, J., Apostolov, A.A., Journal of Applied Polymer Science, 91, 175 (2004).

268. Rauwendaal, C., Polymer Mixing, Hanser Publisher, Munic, 2001.

269. Homminga, D., Goderis, B., Hoffman, S., Reynaers, H., Groeninckx, G., Polymer, 46, 9941 (2005).

270. Ahn, C.Y., Paul, D.R., Polymer, 47, 2830 (2006).

271. Li, Y., Shimizu, H., Macromolecular Rapid Communications, 26, 710 (2005).

272. Chiu, F.C., Lai, S.M., Chen, Y.L., Lee, T.H., Polymer, 46, 11600 (2005).

273. Li, L., Bellan, L.M., Craighead, H.G., Frey, M.W., Polymer, 47, 6208 (2006).

274. Gonzalez, J., Eguiazabal, I., Nazabal, J., European Polymer Journal, 42, 2905 (2006).

275. Gonzalez, J., Eguiazabal, I., Nazabal, J., Composite Science and Technology 66, 1833 (2006).

276. Oshinski, A. J., Keskkula, H., Paul, D.R., Polymer, 37, 4891 (1996).

277. Chavarria, F., Paul, D.R., Polymer, 47, 7760 (2006).

278. Lee, H.S., Fasulo, P.D., Rodgers, W.R., Paul, D.R., 46, 11673 (2005).

279. Incarnato, L., Scarfato, P., Scatteia, L., Acierno, D., Polymer, 45, 3487 (2004).

280. Fornes, T.D., Yoon, P.J., Keskkula, H., Paul, D.R., Polymer, 44, 7545 (2003).

281. Gatos, K.G., Martínez Alcázar, J.G., Psarras, G.C., Thomann R., Karger-Kocsis, J., Composites Science and Technology, in press, doi:10.1016/j.compscitec.2006.07.025 (2006).

282. Lewis T.B., Nielsen L.E., Journal of Applied Polymer Science, 14, 1449 (1970).

283. Cho J.W., Paul D.R., Polymer, 42, 1083 (2001).

284. Manaz-Zloczower, I., Tadmor, Z., Mixing and compounding of polymers, Hanser Publisher, Munic, 1994.

285. Utracki L.A., Two phase polymer systems, Hanser Publisher, Munic, 1991.

APPENDIX A

REPRESENTATION OF FTIR SPECTRA

Table A.1 FTIR absorptions of ABS

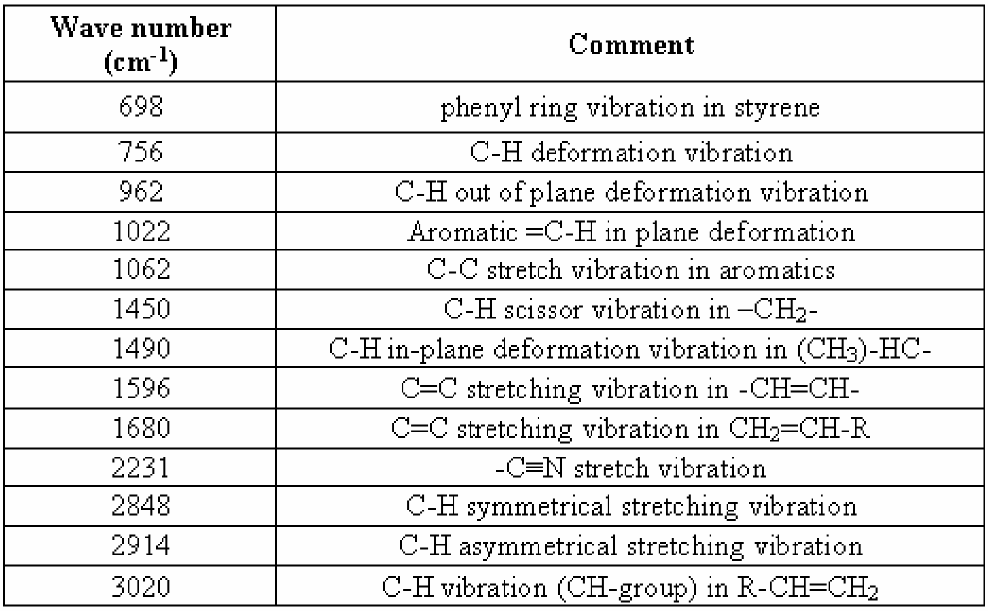

Wave number (cm^{-1})	Comment
698	phenyl ring vibration in styrene
756	C-H deformation vibration
962	C-H out of plane deformation vibration
1022	Aromatic =C-H in plane deformation
1062	C-C stretch vibration in aromatics
1450	C-H scissor vibration in $-CH_2-$
1490	C-H in-plane deformation vibration in (CH_3)-HC-
1596	C=C stretching vibration in -CH=CH-
1680	C=C stretching vibration in CH_2=CH-R
2231	-C≡N stretch vibration
2848	C-H symmetrical stretching vibration
2914	C-H asymmetrical stretching vibration
3020	C-H vibration (CH-group) in R-CH=CH_2

Table A.2 FTIR absorptions of PA6

Wave number (cm^{-1})	**Comment**
676	C-H wagging vibration
964	C-H out of plane deformation vibration
1064	C-N stretching vibrations in $-CH_2-NH-$
1112	C-N stretching vibrations in -CH-NH-
1166	C-N stretching vibrations in -R-NH-CO-
1255	Coupled C-N and C-O stretching vibration
1363	C-H deformation vibration in $-N-CH_2-$
1465	C-H scissor vibration in $-CH_2-$
1537	Amide II
1625	C=O stretching vibration
2850	C-H symmetrical stretching vibration
2916	C-H asymmetrical stretching vibration
3068	N-H stretch vibration
3284	O-H stretching vibration in -COOH

Table A.3 FTIR absorptions of EMA-GMA

Wave number (cm^{-1})	**Comment**
718	C-C skeleton vibration (rocking) in $-(CH_2)_n-$
792	CH_2 rocking vibration
910	Oxiarine ring vibration
1101	C-O stretching vibration
1370	C-H symmetrical deformation vibration in $R-CH_3$
1460	C-H asymmetrical deformation vibration in $R-CH_3$
1731	C=O stretching vibrations
2848	C-H stretching vibration in $-CH_2-$
2916	C-H asymmetrical stretching vibration
3363	O-H stretching vibration in -COOH

Table A.4 FTIR absorptions of EnBACO-MAH

Wave number (cm^{-1})	Comment
719	C-C skeleton vibration (rocking) in $-(CH_2)_n-$
940	C-H deformation vibration
1056	C-O-C symmetric stretching vibration in R_1-O-(C=O)-R
1157	C-O-C symmetric stretching vibration R_1- (C=O)- O-R
1232	CH_2 deformation vibration in $-CH_2-(C=O)-$
1242	C-H symmetrical deformation vibration
1375	C-H symmetrical deformation vibration in $R-CH_3$
1407	C-H deformation vibration in –(C=O)-CH-
1461	CH_2 symmetrical deformation vibration in esters
1639	C=C stretching vibration in acrylates
1706	C=O stretching vibrations in -(C=O)-(C=O)-C-
1778	C=O sym. stretching vibration in anhydrides
2852	C-H stretching vibration in $-CH_2-$
2921	C-H asymmetrical stretching vibration
2987	CH_3 asym. stretching vibration in CH_3-O-
3298	O-H stretching vibration in -COOH

APPENDIX B

DSC THERMOGRAMS OF ABS/PA6 BLENDS

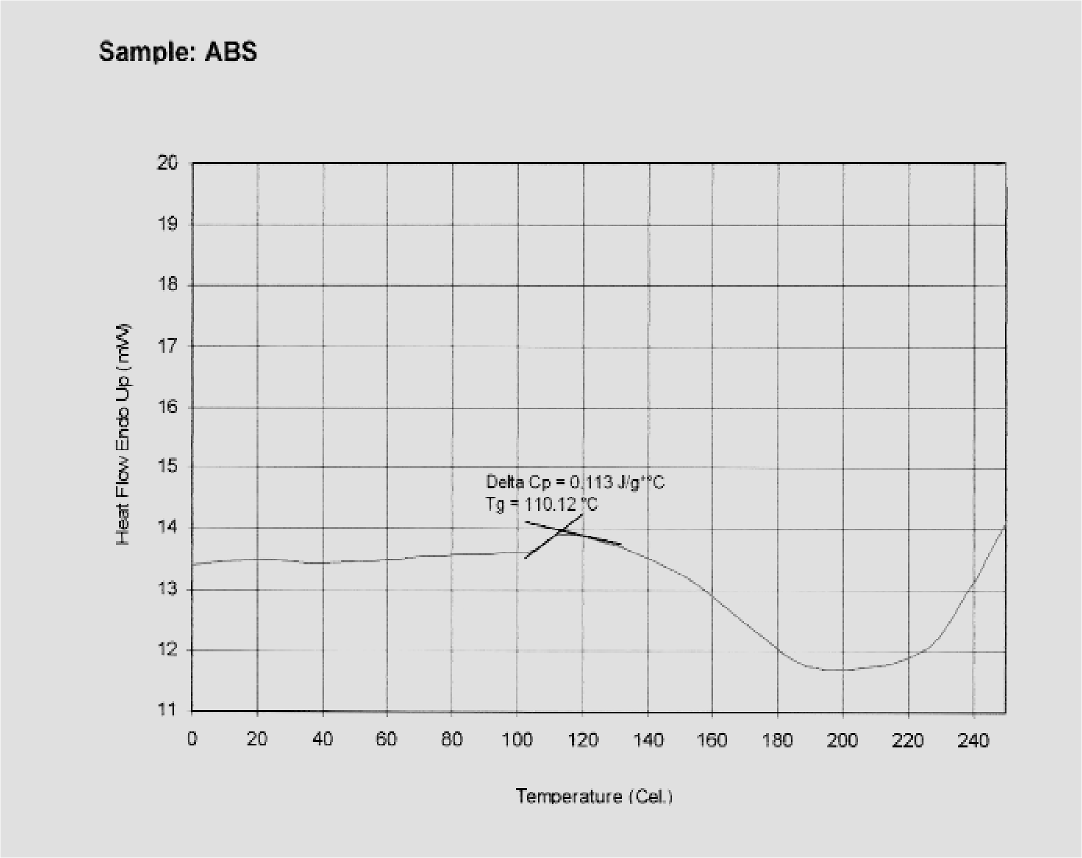

Figure B.1 DSC thermogram of ABS (second heating)

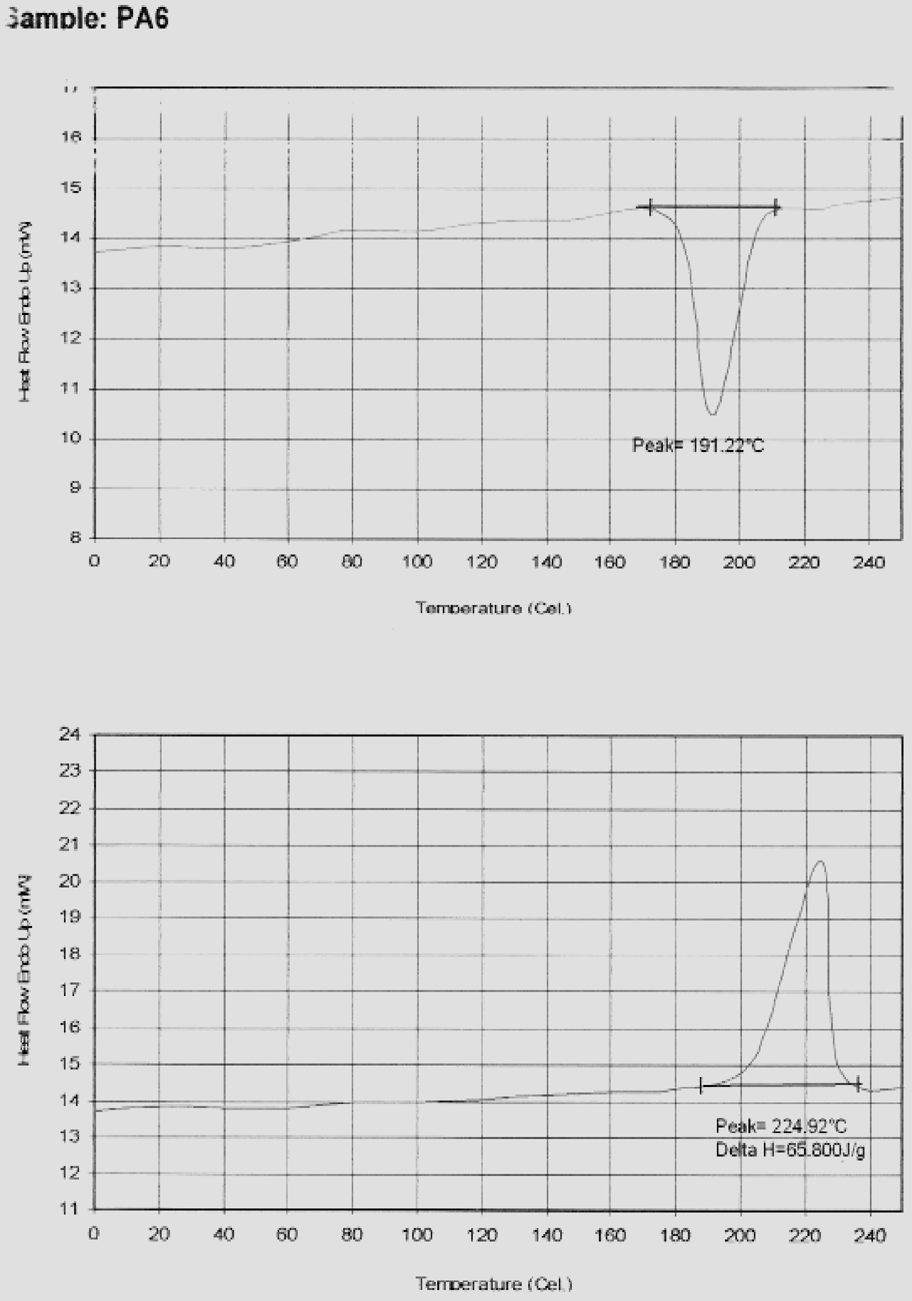

Figure B.2 DSC thermogram of PA6 (cooling and second heating)

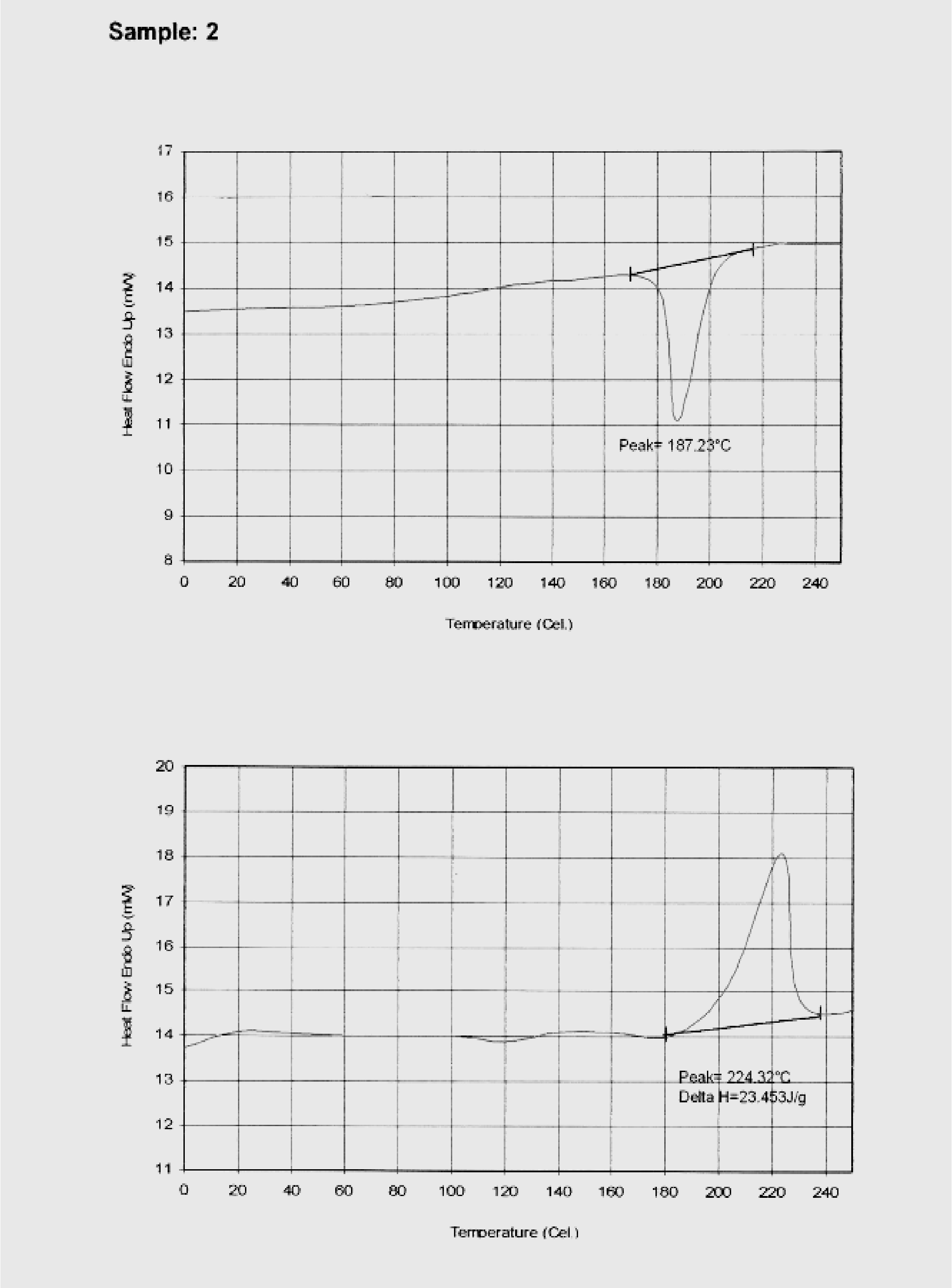

Figure B.3 DSC thermogram of 50/50/0 (cooling and second heating)

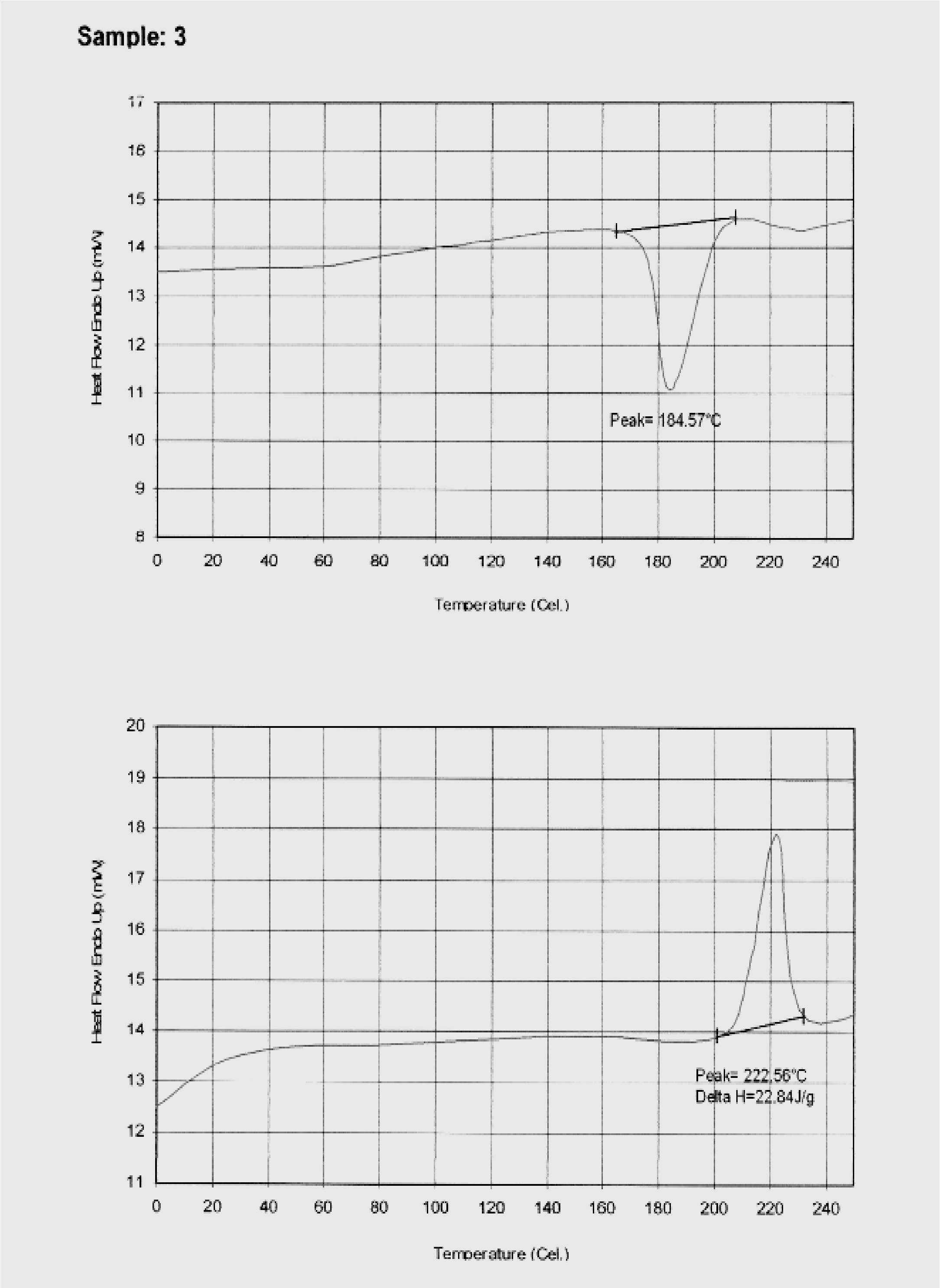

Figure B.4 DSC thermogram of (50/50)/5 E-MA-GMA (cooling and second heating)

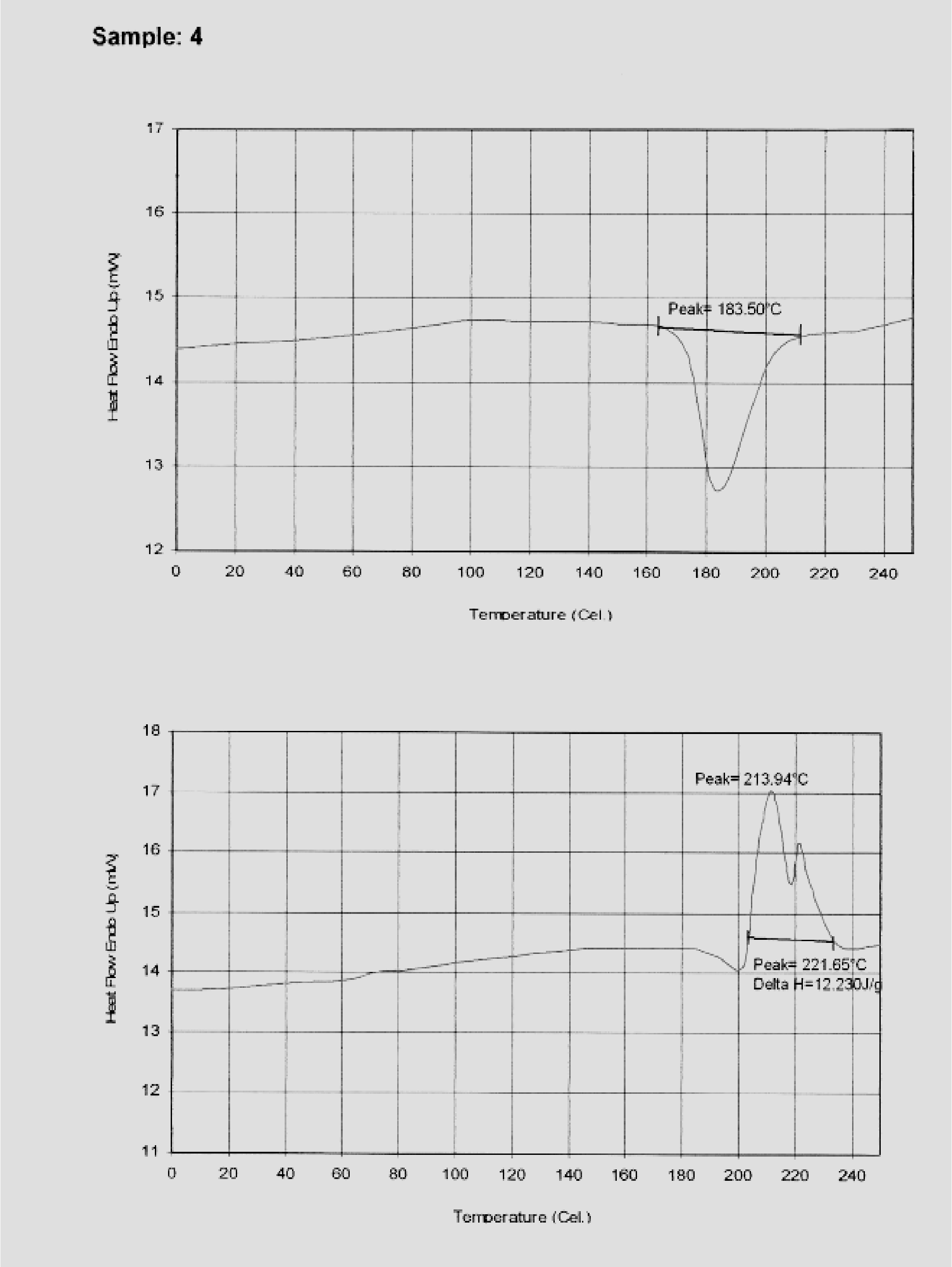

Figure B.5 DSC thermogram of (50/50)/10 E-MA-GMA (cooling and second heating)

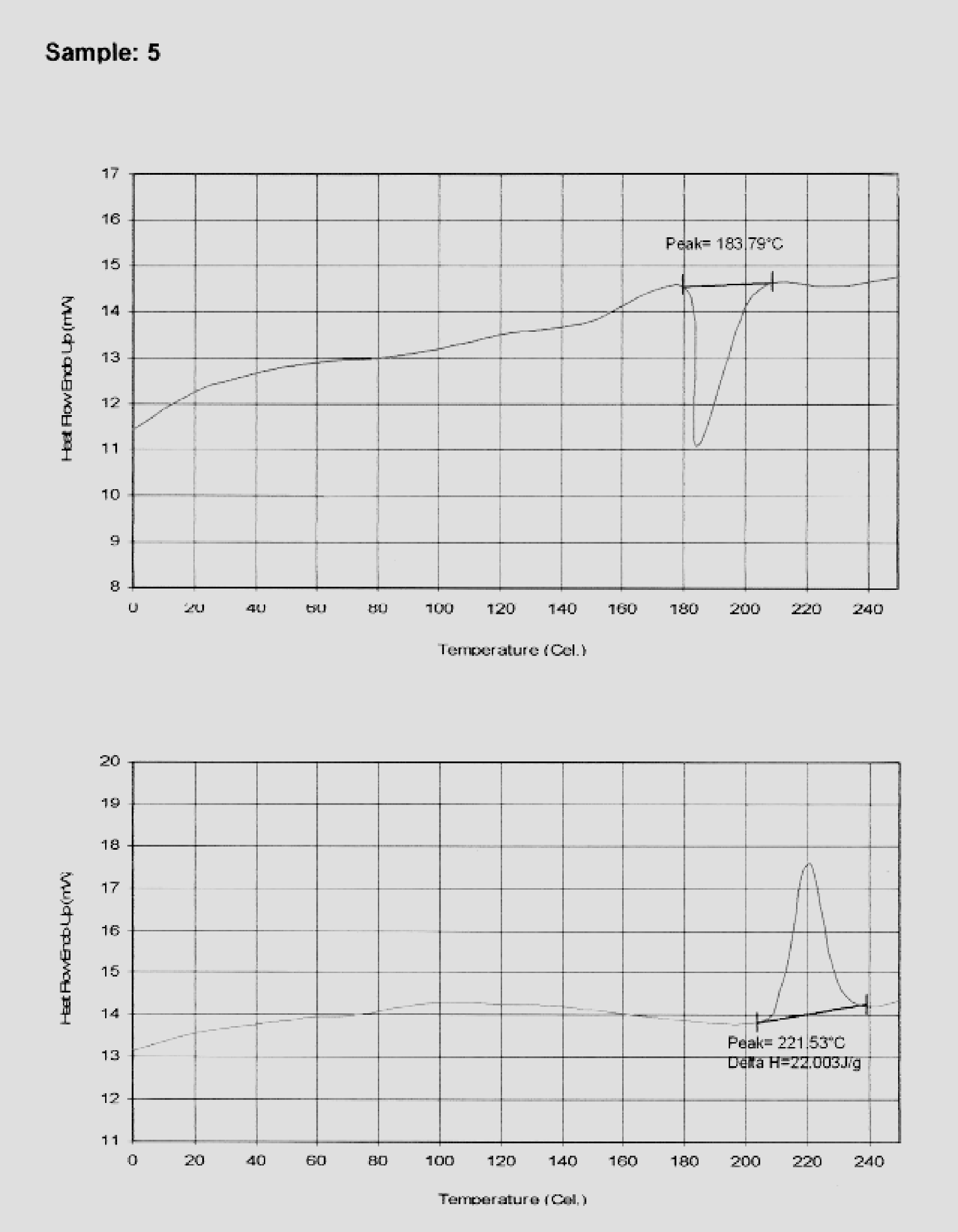

Figure B.6 DSC thermogram of (50/50)/5 EnBACO-MAH (cooling and second heating)

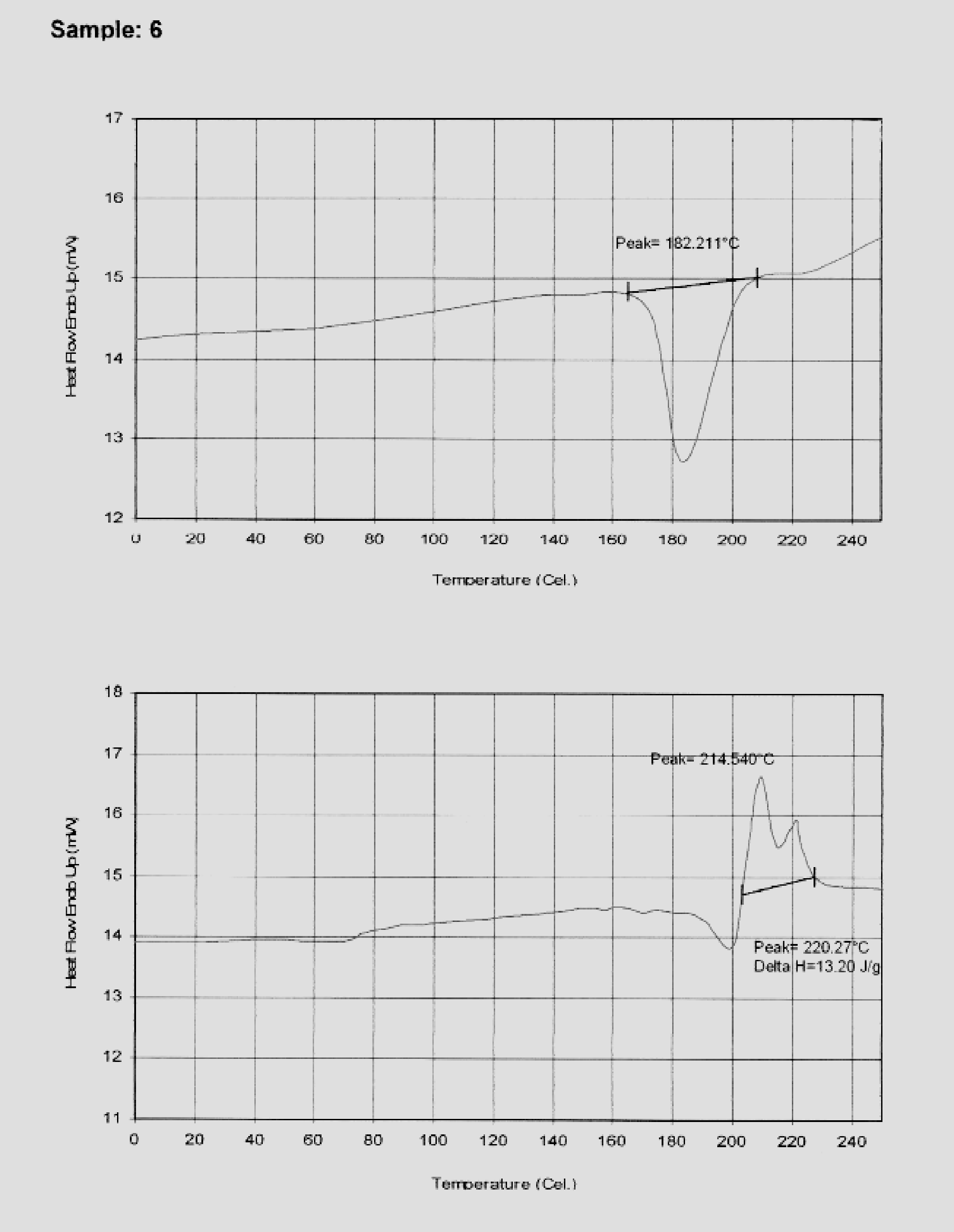

Figure B.7 DSC thermogram of (50/50)/10 EnBACO-MAH (cooling and second heating)

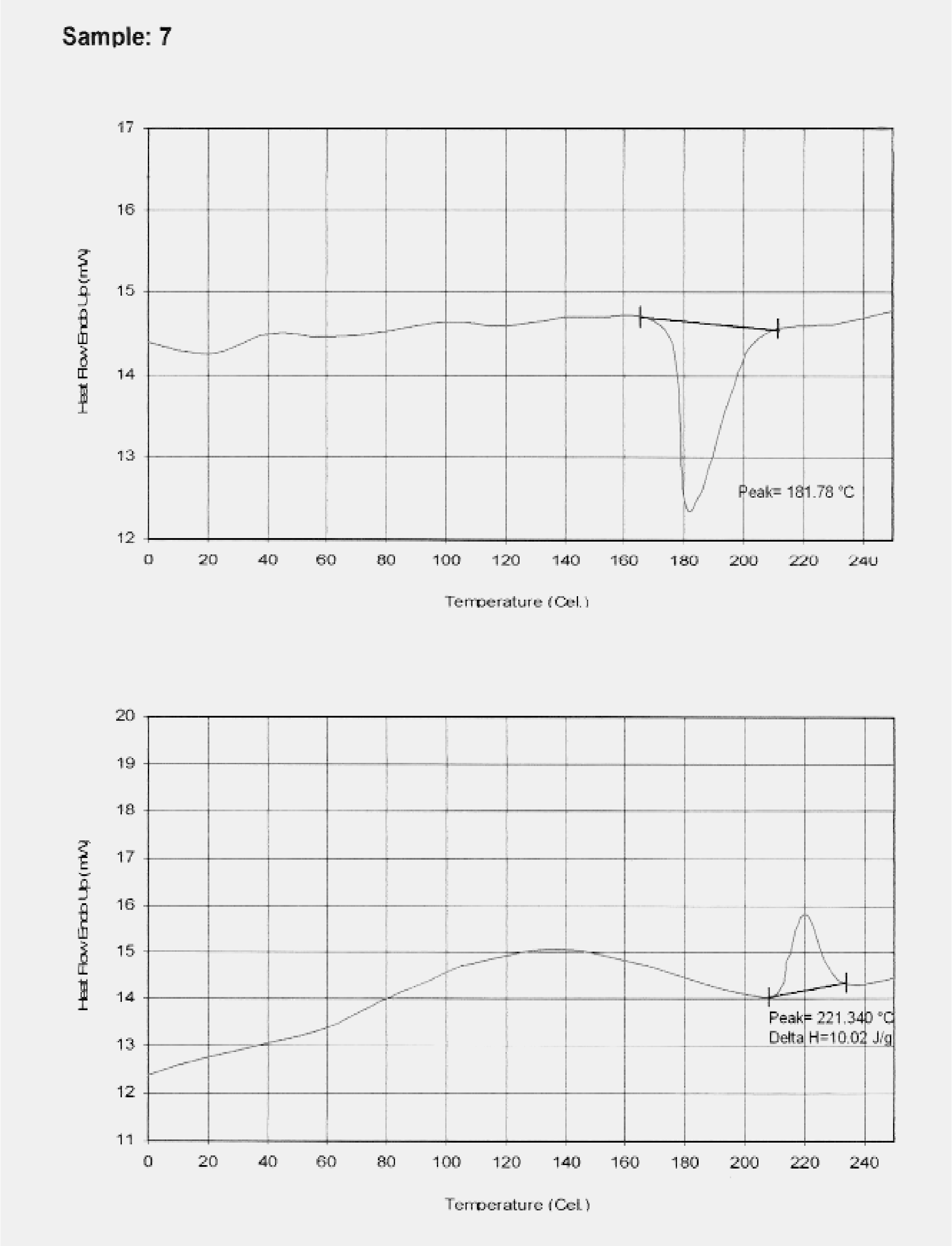

Figure B.8 DSC thermogram of (80/20)/5 EnBACO-MAH (cooling and second heating)

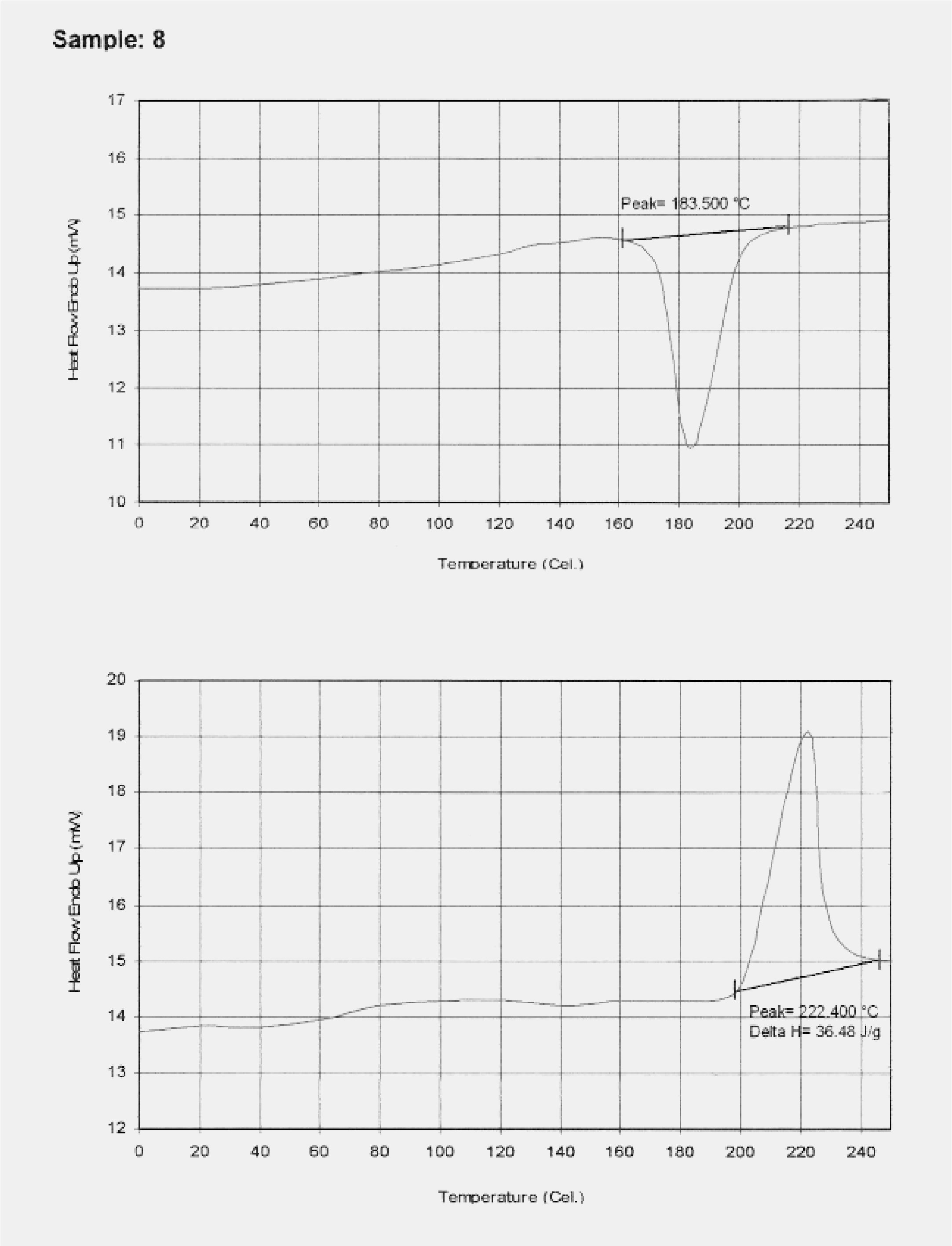

Figure B.9 DSC thermogram of (80/20)/5 EMA-GMA (cooling and second heating)

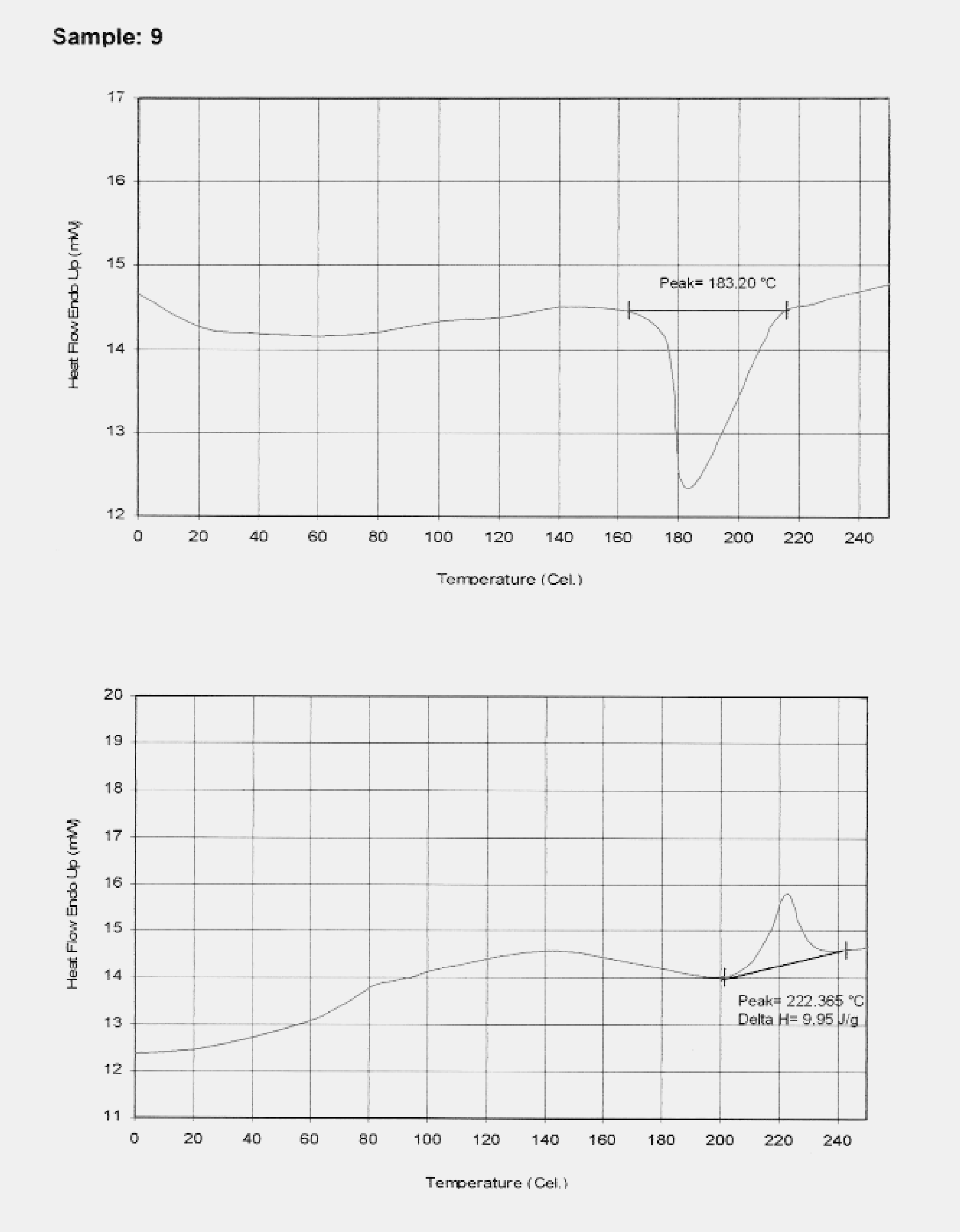

Figure B.10 DSC thermogram of (20/80)/5 EMA-GMA (cooling and second heating)

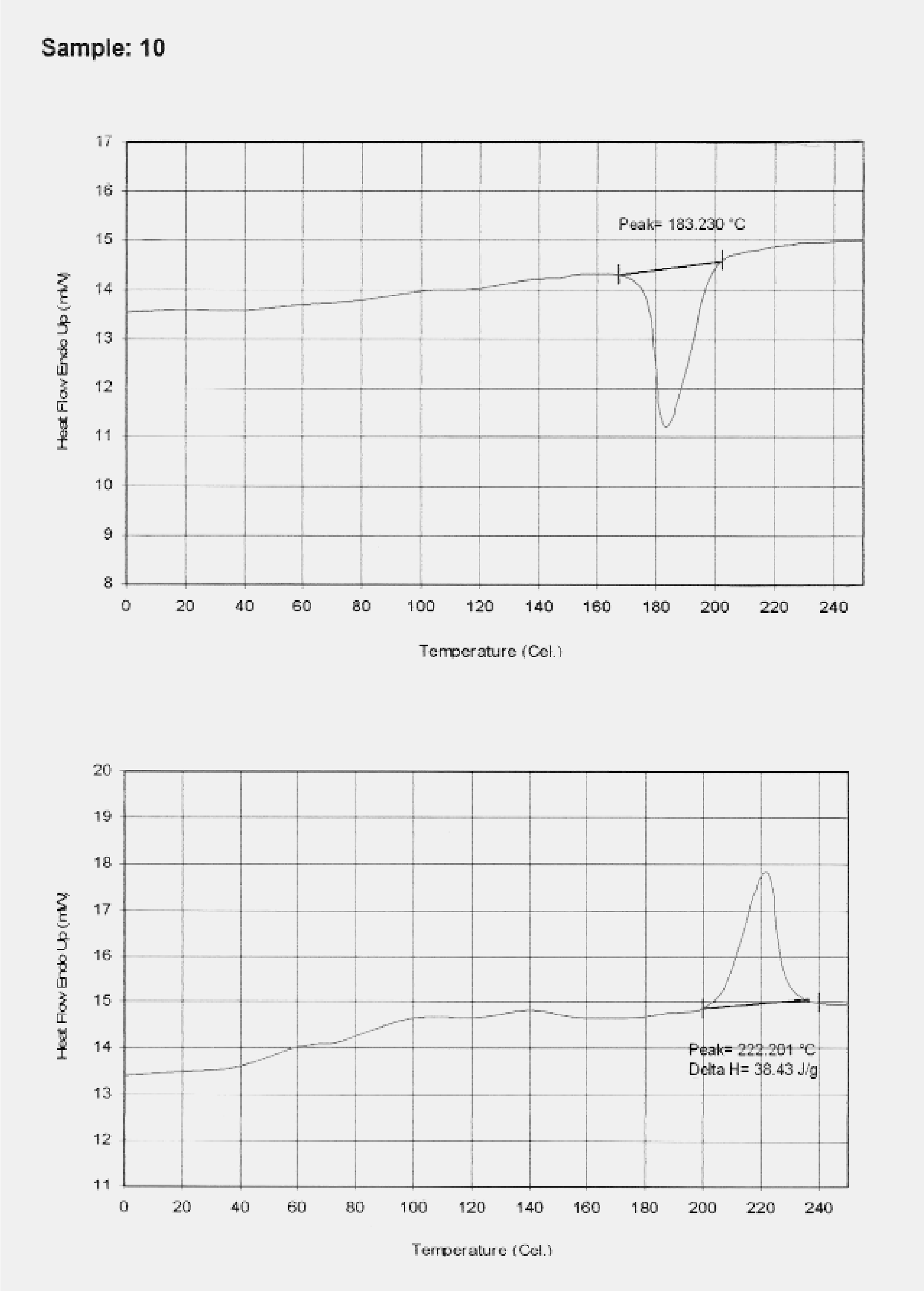

Figure B.11 DSC thermogram of (20/80)/5 EMA-GMA (cooling and second heating)

APPENDIX C

DISTRIBUTION CURVES USED TO CALCULATE “l_{avg}” and “n”

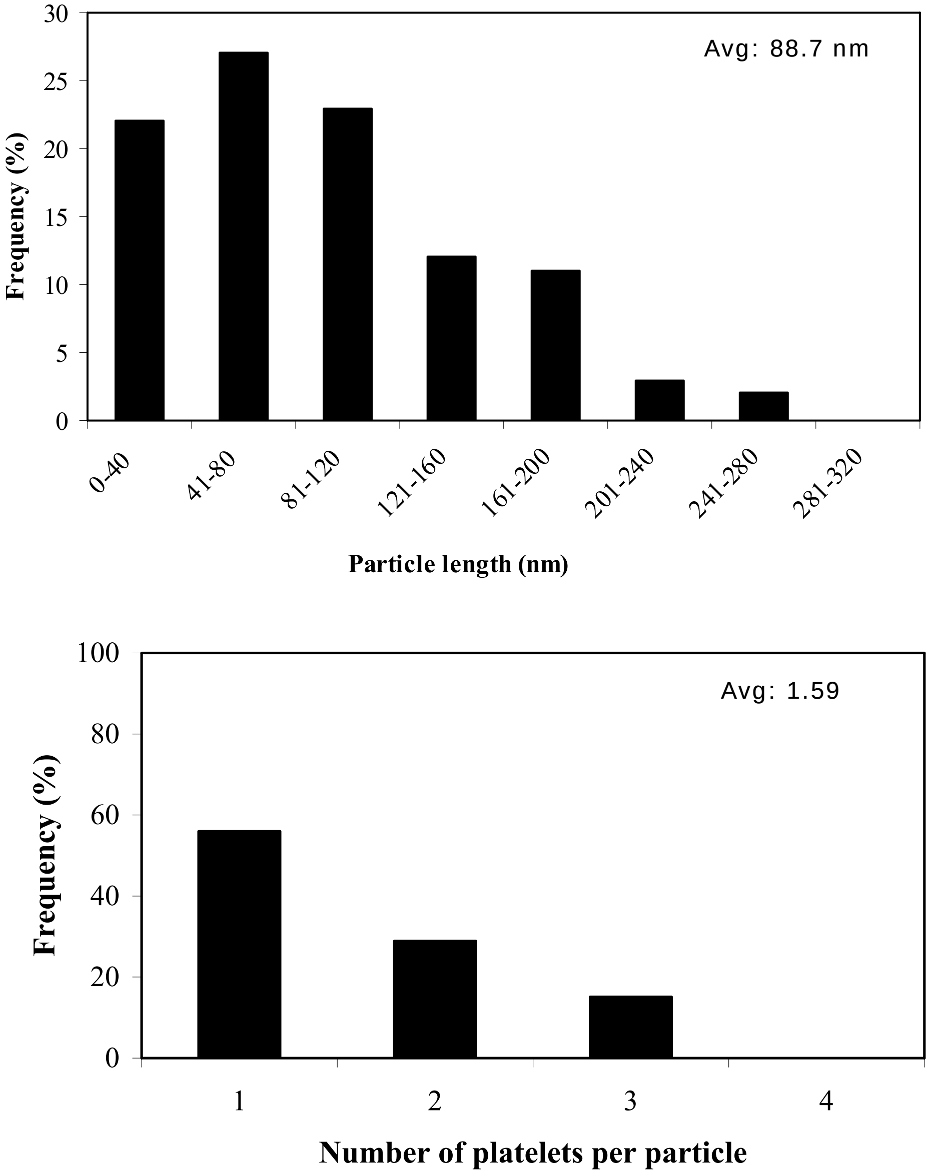

Figure C.1 (a) Particle length distribution (b) number of platelets per particles obtained from 80/20/5 blend system based nanocomposites at a clay loading level of 5% and processed at 100 rpm with co-rotating screws.

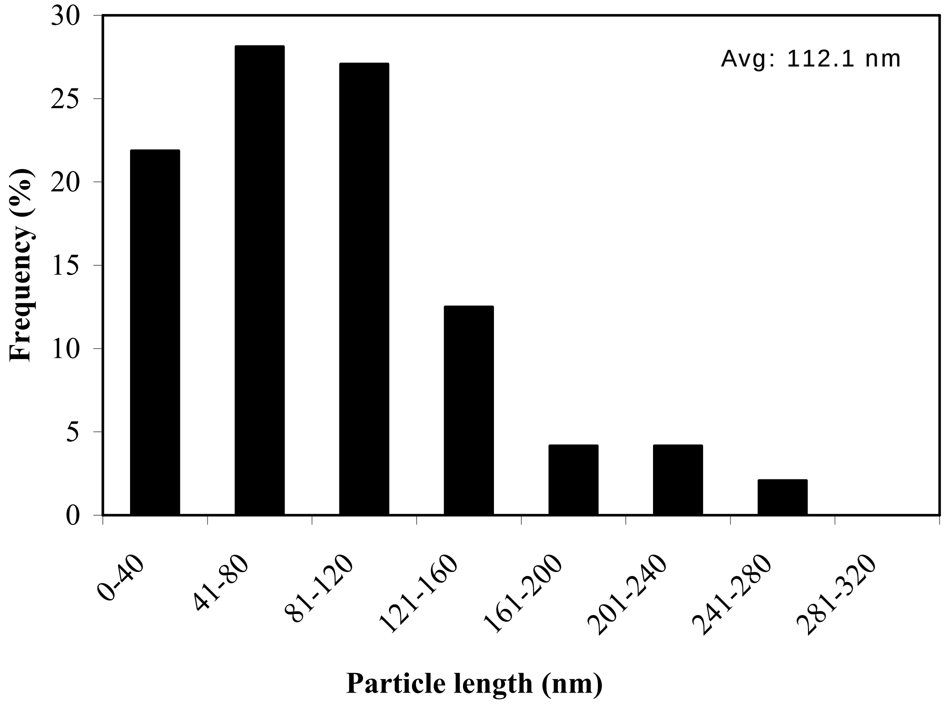

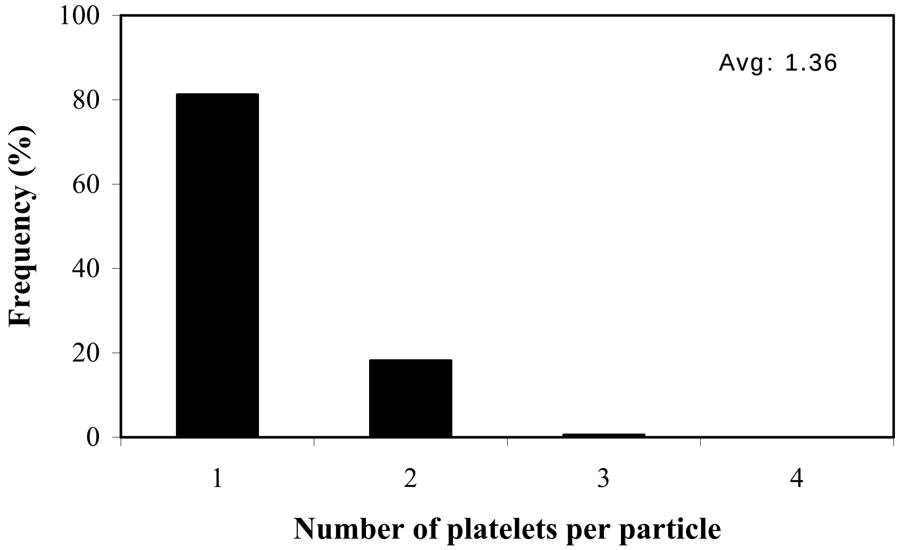

Figure C.2 (a) Particle length distribution (b) number of platelets per particles obtained from 50/50/5 blend system based nanocomposites at a clay loading level of 5% and processed at 100 rpm with co-rotating screws.

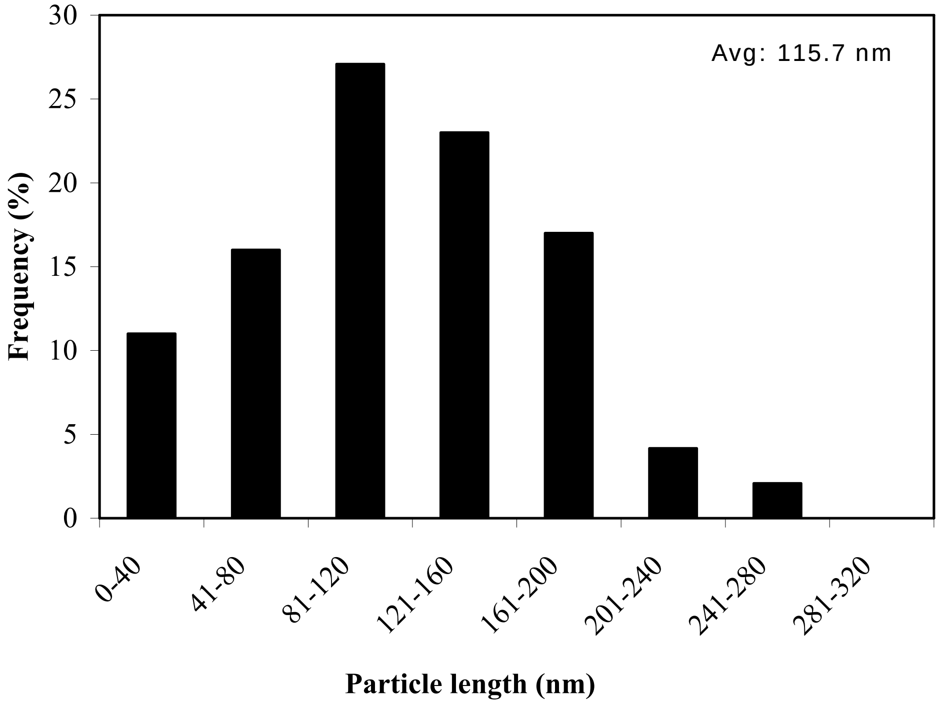

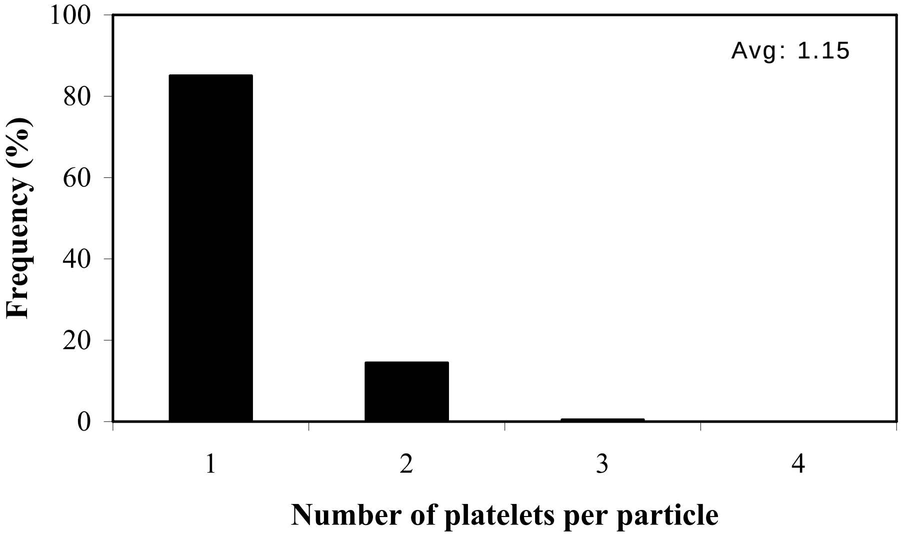

Figure C.3 (a) Particle length distribution (b) number of platelets per particles obtained from 20/80/5 blend system based nanocomposites at a clay loading level of 5% and processed at 100 rpm with co-rotating screws.

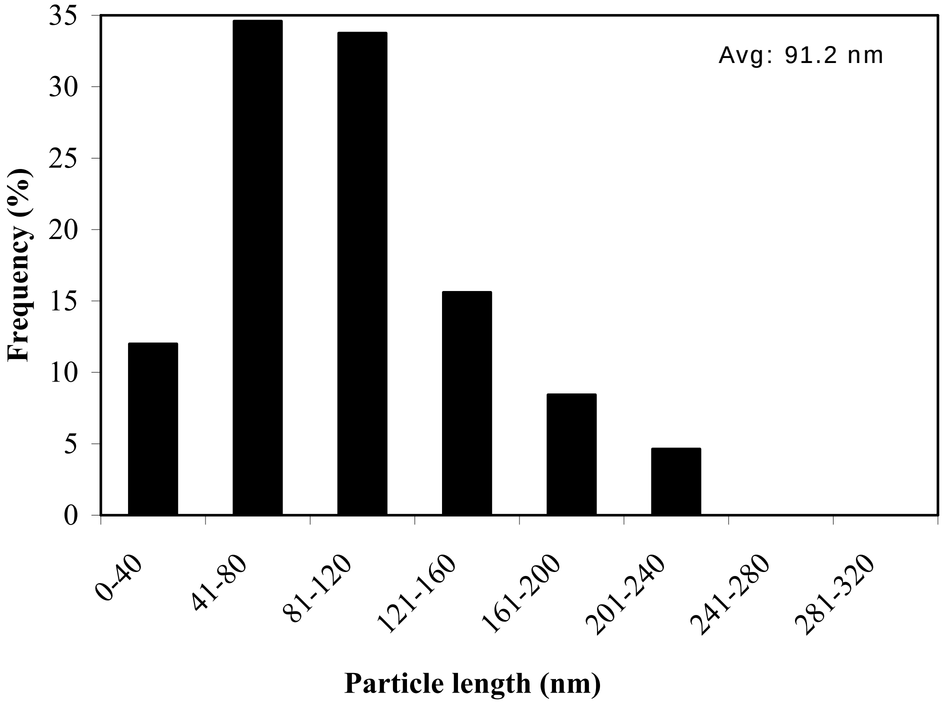

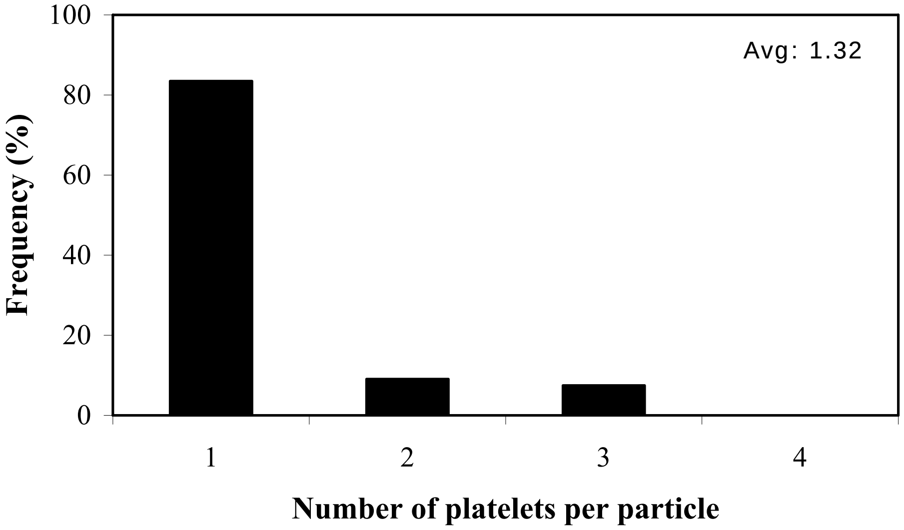

Figure C.4 (a) Particle length distribution (b) number of platelets per particles obtained from 80/20/5 blend system based nanocomposites at a clay loading level of 5% and processed at 200 rpm with co-rotating screws.

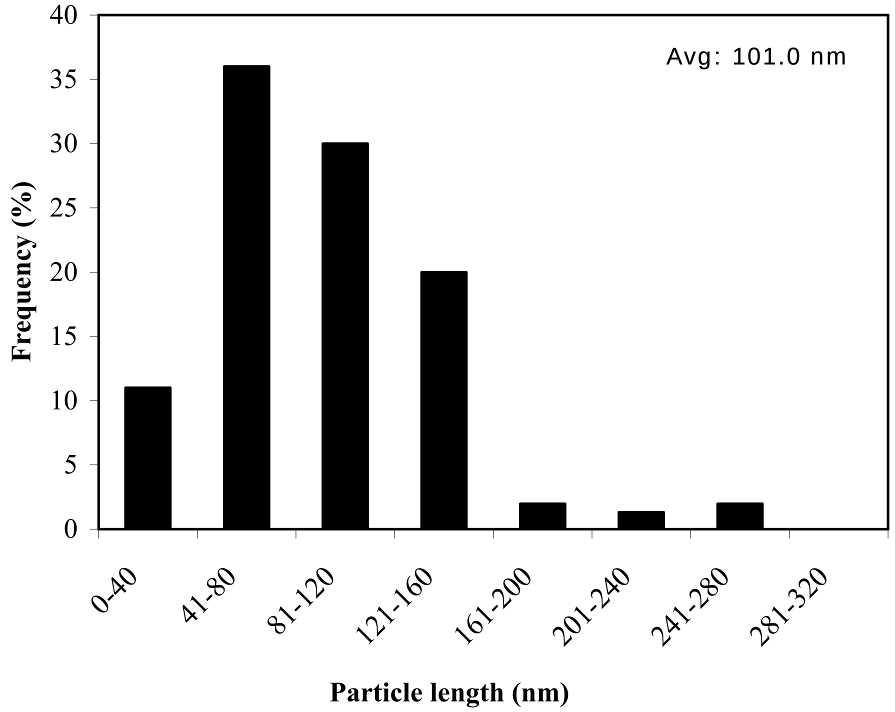

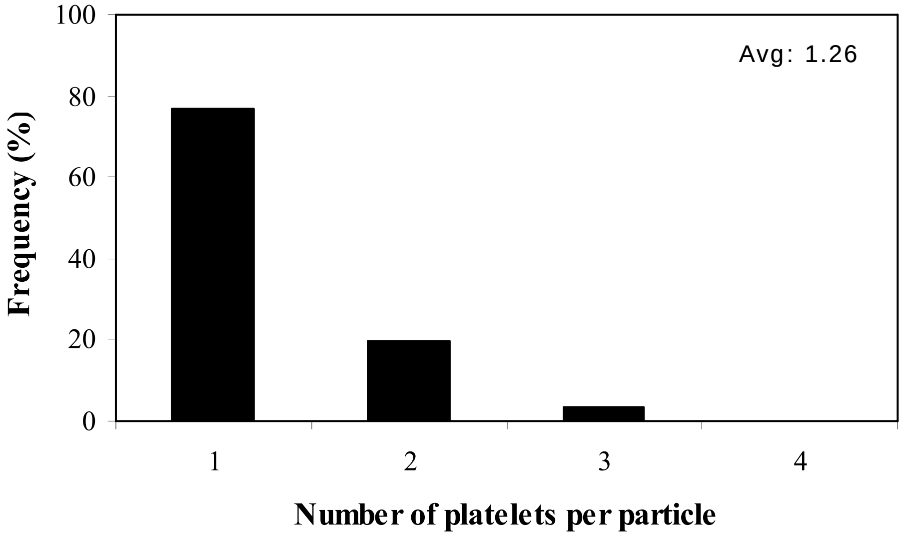

Figure C.5 (a) Particle length distribution (b) number of platelets per particles obtained from 50/50/5 blend system based nanocomposites at a clay loading level of 5% and processed at 200 rpm with co-rotating screws.

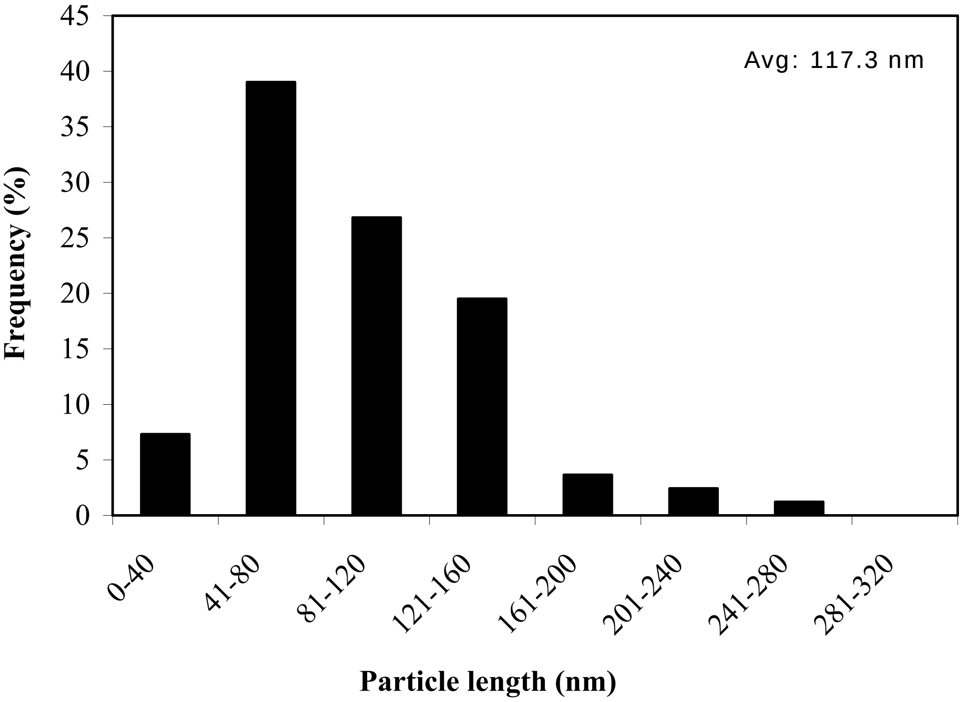

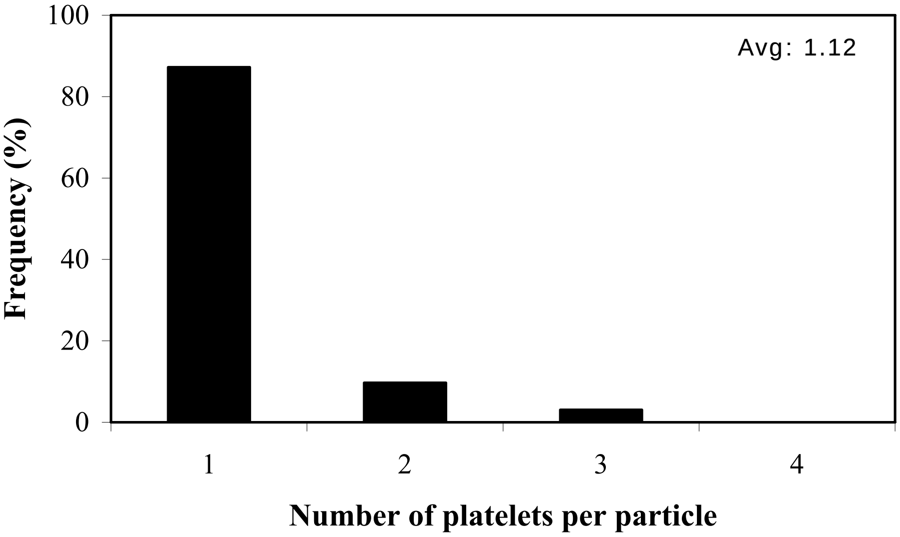

Figure C.6 (a) Particle length distribution (b) number of platelets per particles obtained from 20/80/5 blend system based nanocomposites at a clay loading level of 5% and processed at 200 rpm with co-rotating screws.

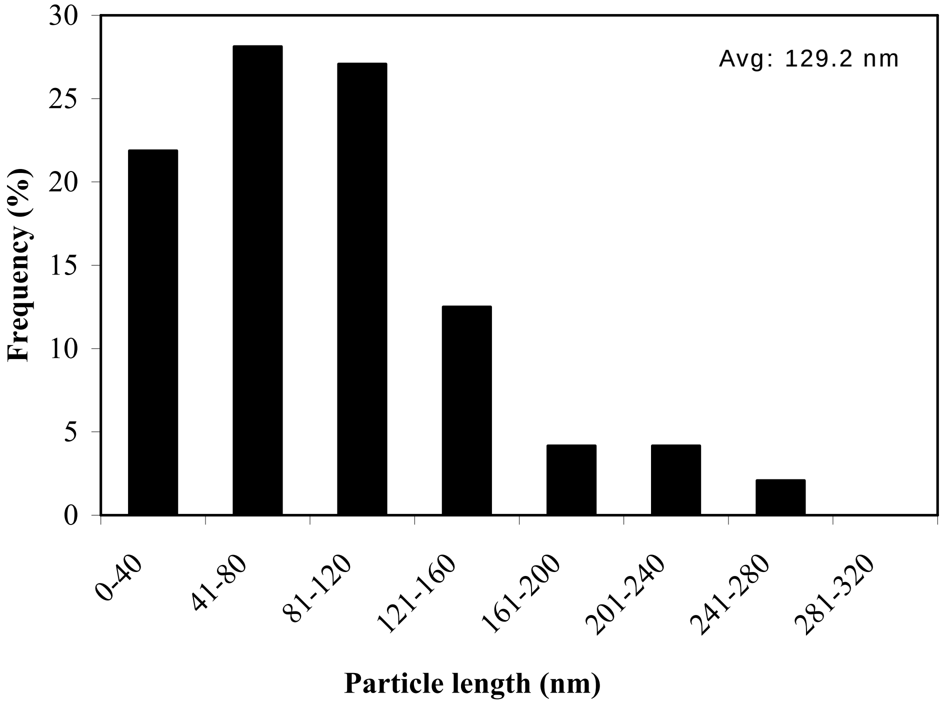

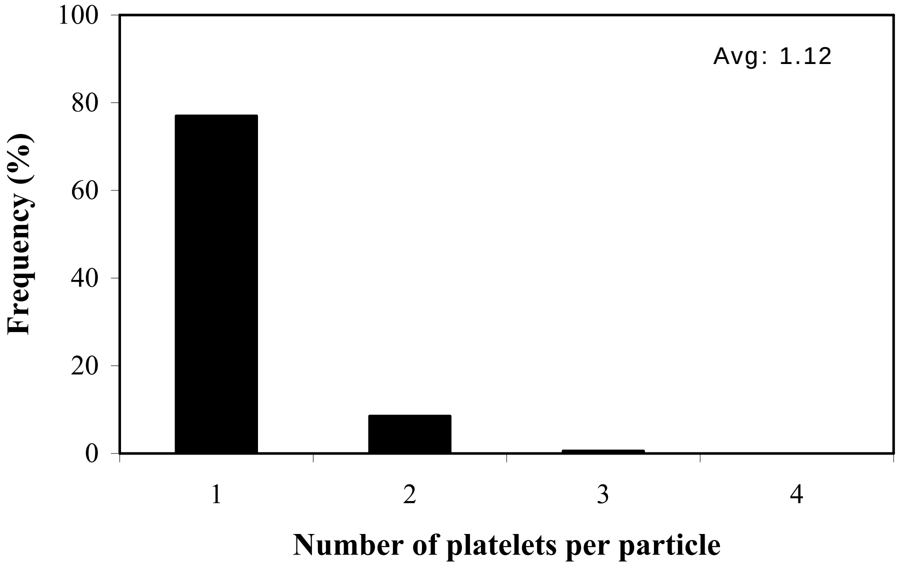

Figure C.7 (a) Particle length distribution (b) number of platelets per particles obtained from 50/50/5 blend system based nanocomposites at a clay loading level of 5% and processed at 100 rpm with modified co-rotating screws.

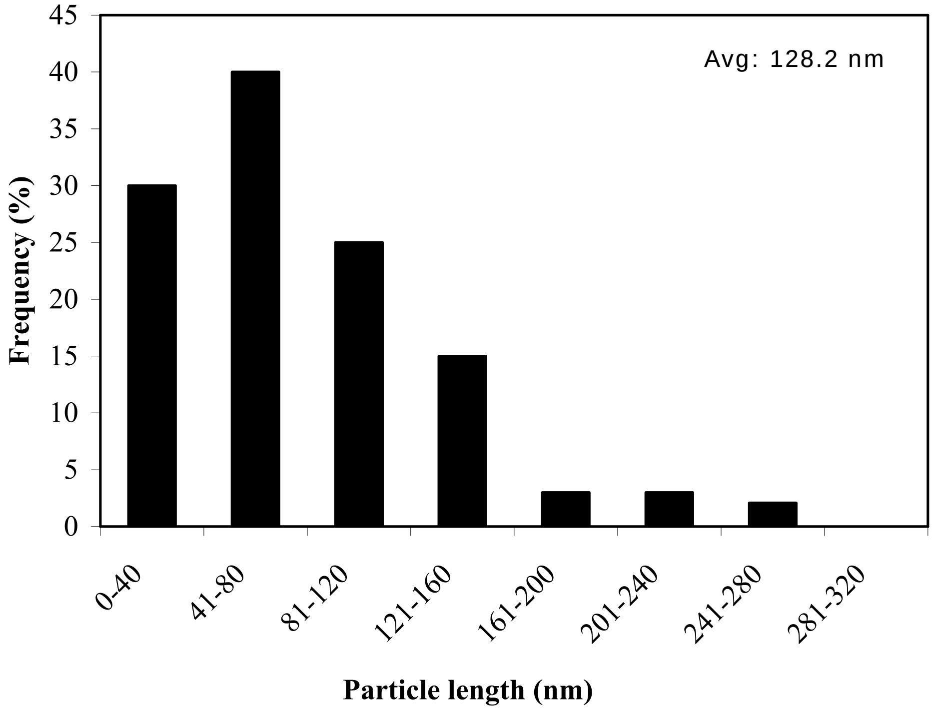

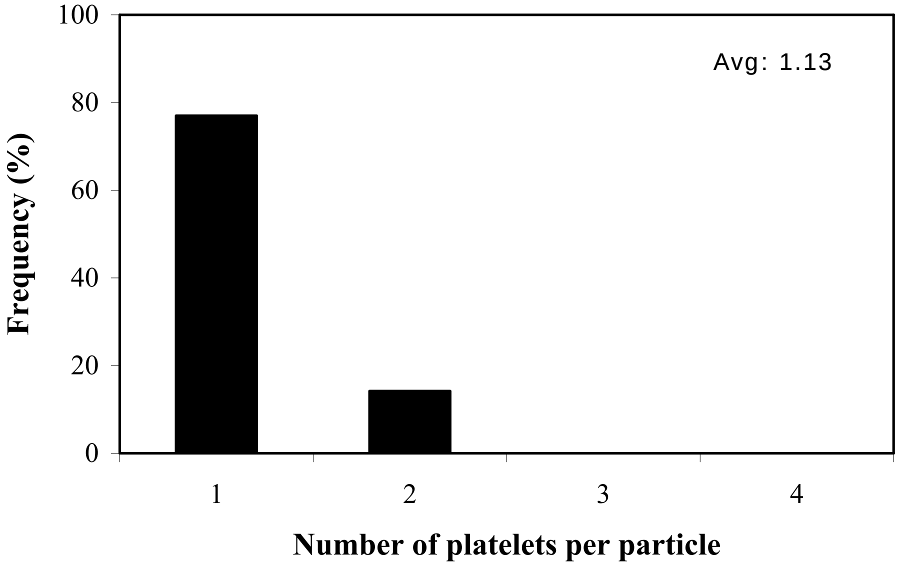

Figure C.8 (a) Particle length distribution (b) number of platelets per particles obtained from 50/50/5 blend system based nanocomposites at a clay loading level of 5% and processed at 200 rpm with modified co-rotating screws.

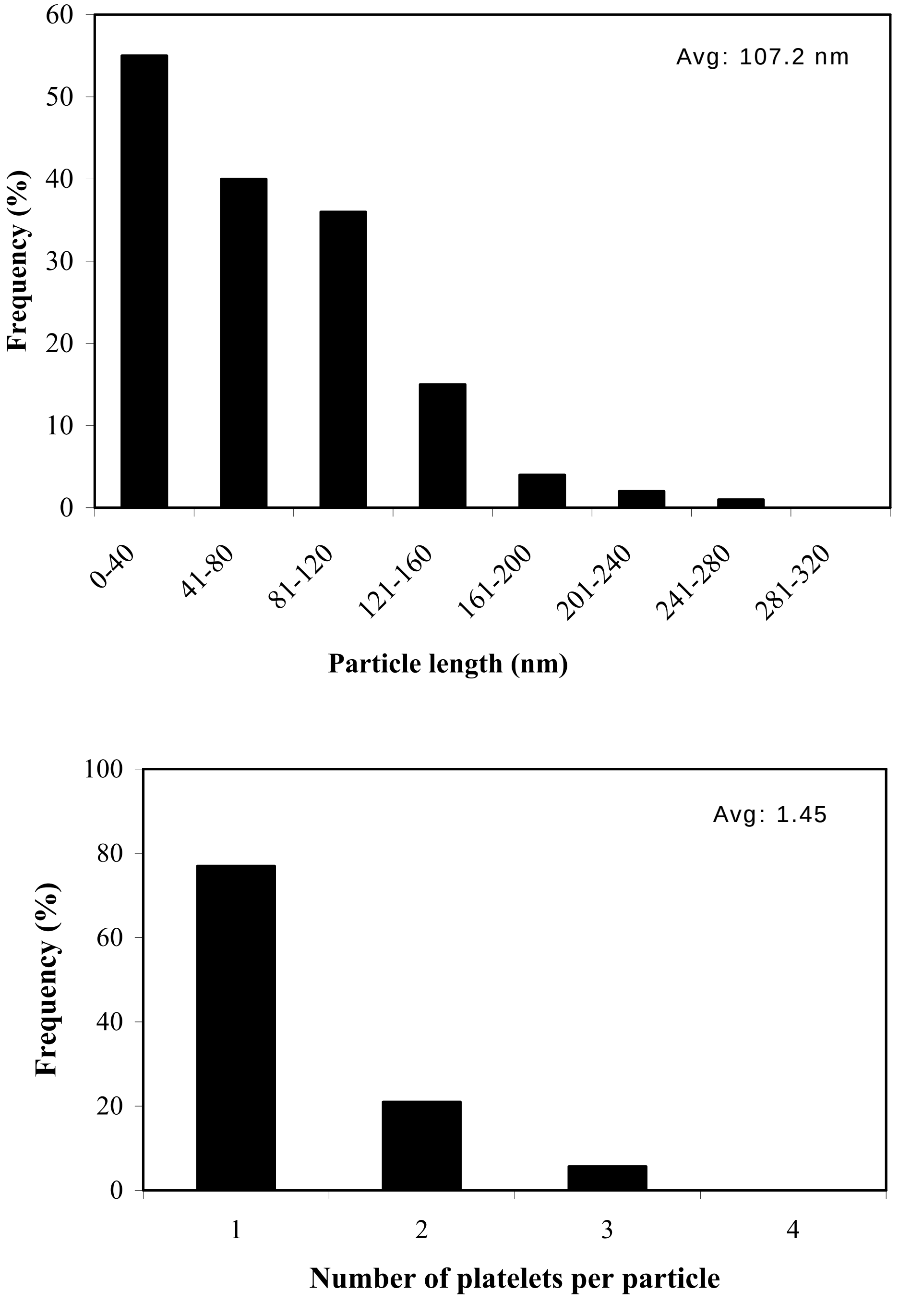

Figure C.9 (a) Particle length distribution (b) number of platelets per particles obtained from 50/50/5 blend system based nanocomposites at a clay loading level of 5% and processed at 100 rpm with counter-rotating screws.

APPENDIX D

MECHANICAL PROPERTIES

Table D.1 Variation of yield strength with respect to PA6 concentration and compatibilizer content

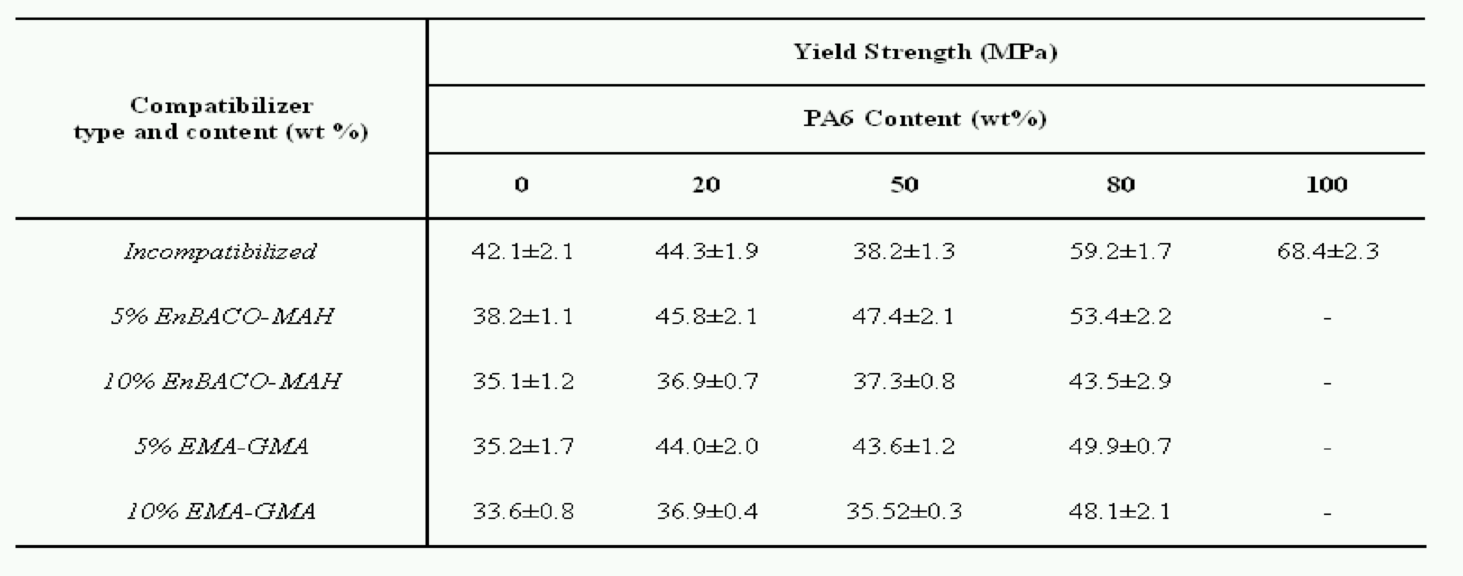

Compatibilizer type and content (wt %)	**Yield Strength (MPa)**				
	PA6 Content (wt%)				
	0	**20**	**50**	**80**	**100**
Incompatibilized	42.1±2.1	44.3±1.9	38.2±1.3	59.2±1.7	68.4±2.3
5% EnBACO-MAH	38.2±1.1	45.8±2.1	47.4±2.1	53.4±2.2	-
10% EnBACO-MAH	35.1±1.2	36.9±0.7	37.3±0.8	43.5±2.9	-
5% EMA-GMA	35.2±1.7	44.0±2.0	43.6±1.2	49.9±0.7	-
10% EMA-GMA	33.6±0.8	36.9±0.4	35.52±0.3	48.1±2.1	-

Table D.2 Variation of strain at break with respect to PA6 concentration and compatibilizer content

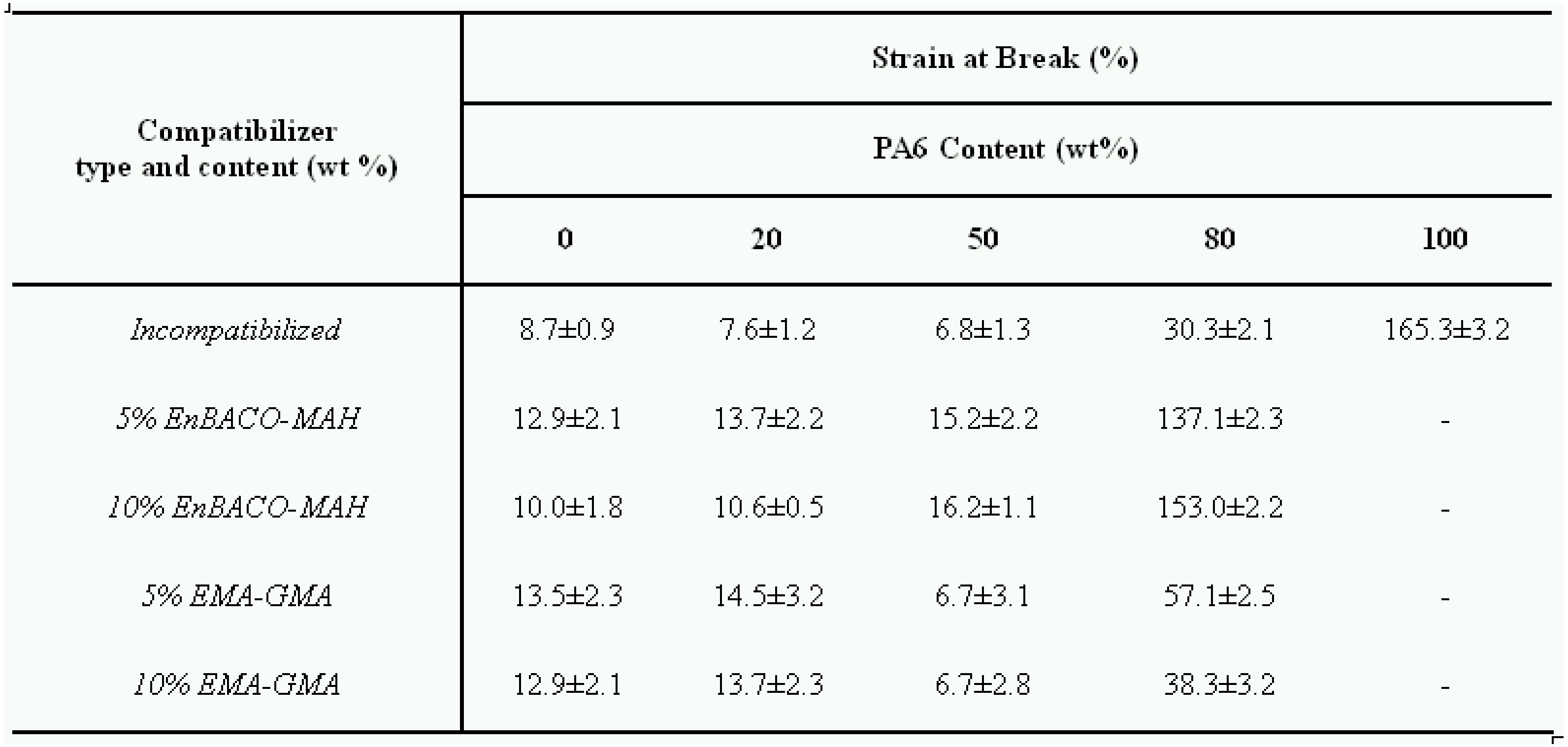

Compatibilizer type and content (wt %)	Strain at Break (%)				
	PA6 Content (wt%)				
	0	20	50	80	100
Incompatibilized	8.7±0.9	7.6±1.2	6.8±1.3	30.3±2.1	165.3±3.2
5% EnBACO-MAH	12.9±2.1	13.7±2.2	15.2±2.2	137.1±2.3	-
10% EnBACO-MAH	10.0±1.8	10.6±0.5	16.2±1.1	153.0±2.2	-
5% EMA-GMA	13.5±2.3	14.5±3.2	6.7±3.1	57.1±2.5	-
10% EMA-GMA	12.9±2.1	13.7±2.3	6.7±2.8	38.3±3.2	-

Table D.3 Variation of impact strength with respect to PA6 concentration and compatibilizer content

Compatibilizer type and content (wt %)	**Notched Charpy Impact Strength (kJ/m^2)**				
	PA6 Content (wt%)				
	0	**20**	**50**	**80**	**100**
Incompatibilized	24.7±3.1	12.5±0.8	7.4±1.1	6.3±1.7	4.5±0.8
5% EnBACO-MAH	33.1±1.9	46.2±2.1	58.4±1.6	55.9±1.6	-
10% EnBACO-MAH	35.2±2.3	43.7±0.6	49.1±2.0	42.3±1.1	-
5% EMA-GMA	24.7±1.6	27.8±0.6	37.±1.4	28.3±2.2	-
10% EMA-GMA	28.2±1.7	35.9±2.2	41.5±1.5	36.8±1.3	-

Table D.4 Tensile modulus of ABS/PA6/SGF composites as the function of PA6 and compatibilizer (EnBACO-MAH) content

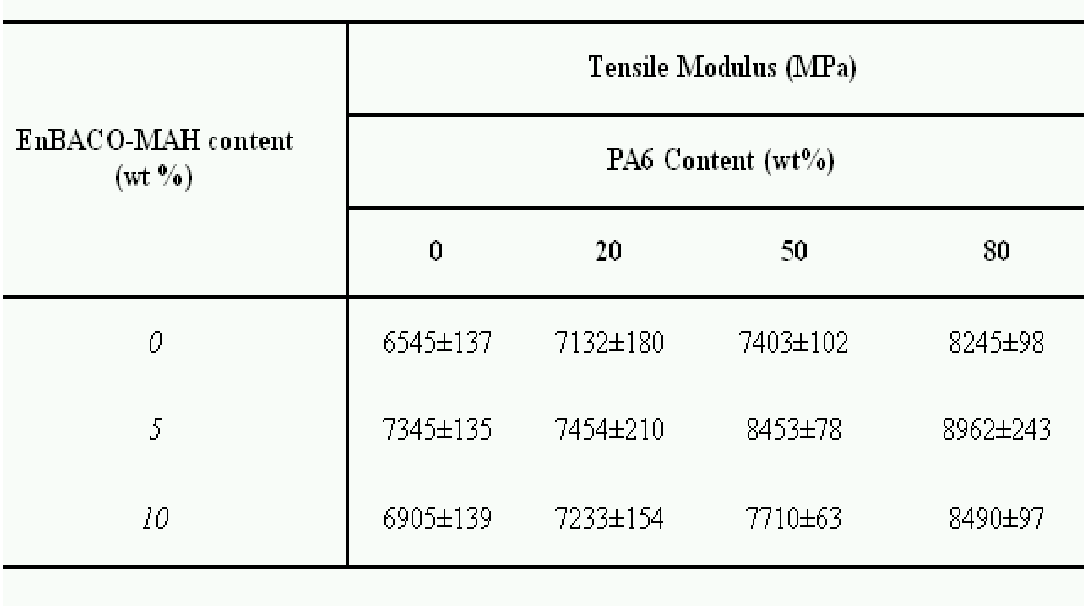

EnBACO-MAH content (wt %)	Tensile Modulus (MPa)			
	PA6 Content (wt%)			
	0	20	50	80
0	6545±137	7132±180	7403±102	8245±98
5	7345±135	7454±210	8453±78	8962±243
10	6905±139	7233±154	7710±63	8490±97

Table D.5 Yield strength of ABS/PA6/SGF composites as the function of PA6 and compatibilizer (EnBACO-MAH) content

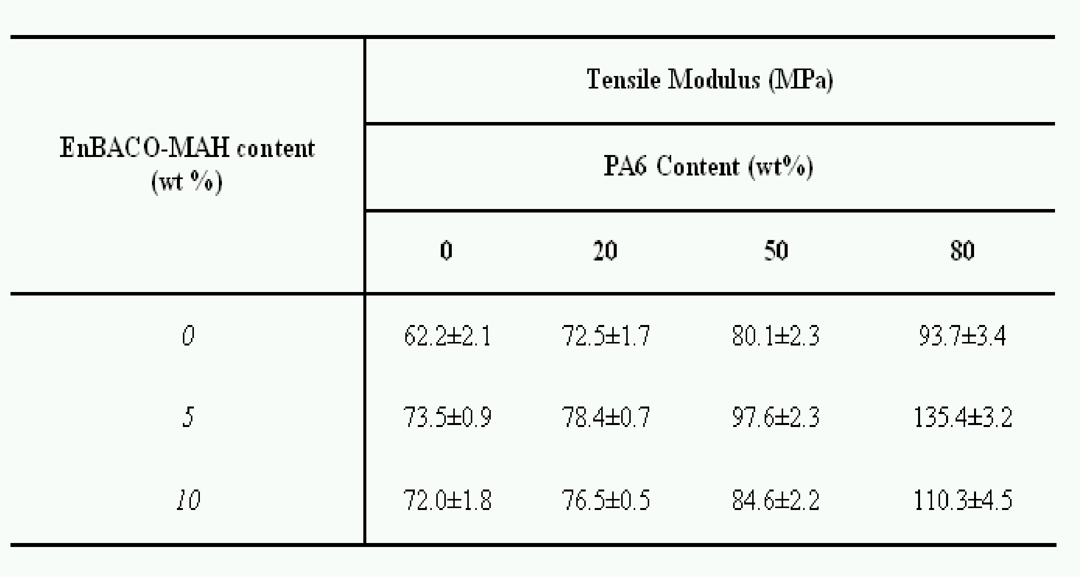

EnBACO-MAH content (wt %)	Tensile Modulus (MPa)			
	PA6 Content (wt%)			
	0	20	50	80
0	62.2±2.1	72.5±1.7	80.1±2.3	93.7±3.4
5	73.5±0.9	78.4±0.7	97.6±2.3	135.4±3.2
10	72.0±1.8	76.5±0.5	84.6±2.2	110.3±4.5

Table D.6 Strain at break (%) of ABS/PA6/SGF composites as the function of PA6 and compatibilizer (EnBACO-MAH) content

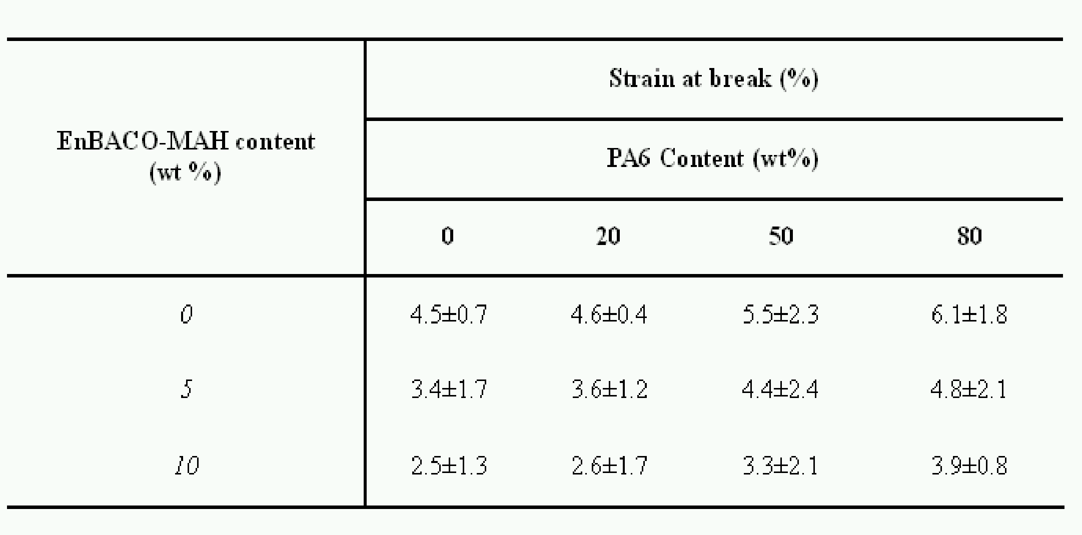

EnBACO-MAH content (wt %)	Strain at break (%)			
	PA6 Content (wt%)			
	0	20	50	80
0	4.5±0.7	4.6±0.4	5.5±2.3	6.1±1.8
5	3.4±1.7	3.6±1.2	4.4±2.4	4.8±2.1
10	2.5±1.3	2.6±1.7	3.3±2.1	3.9±0.8

Table D.7 Impact strength of ABS/PA6/SGF composites as the function of PA6 and compatibilizer (EnBACO-MAH) content

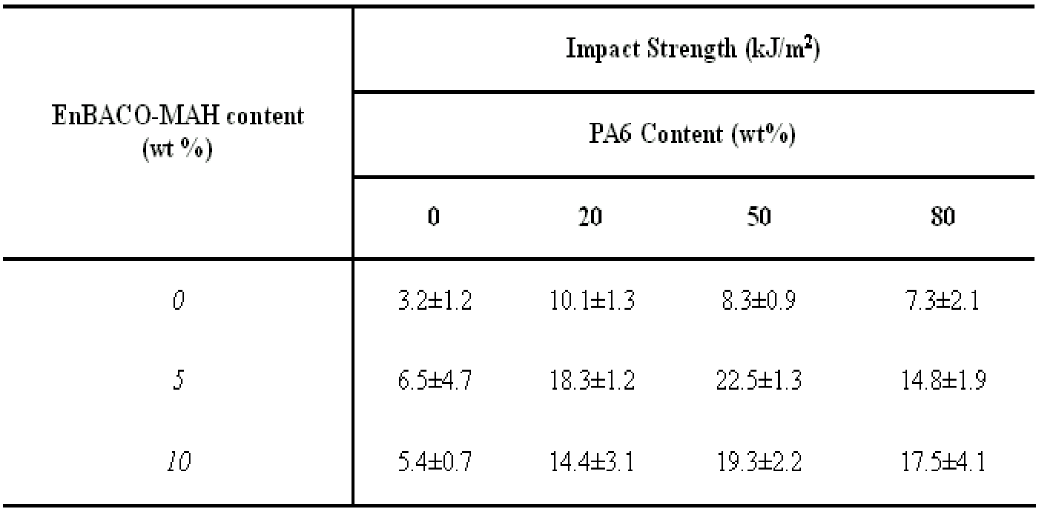

EnBACO-MAH content (wt %)	Impact Strength (kJ/m^2)			
	PA6 Content (wt%)			
	0	20	50	80
0	3.2±1.2	10.1±1.3	8.3±0.9	7.3±2.1
5	6.5±4.7	18.3±1.2	22.5±1.3	14.8±1.9
10	5.4±0.7	14.4±3.1	19.3±2.2	17.5±4.1

Table D.8 Effect of blend composition and screw speed on Young's Moduli of blends and 5% Clay reinforced blends based nanocomposite

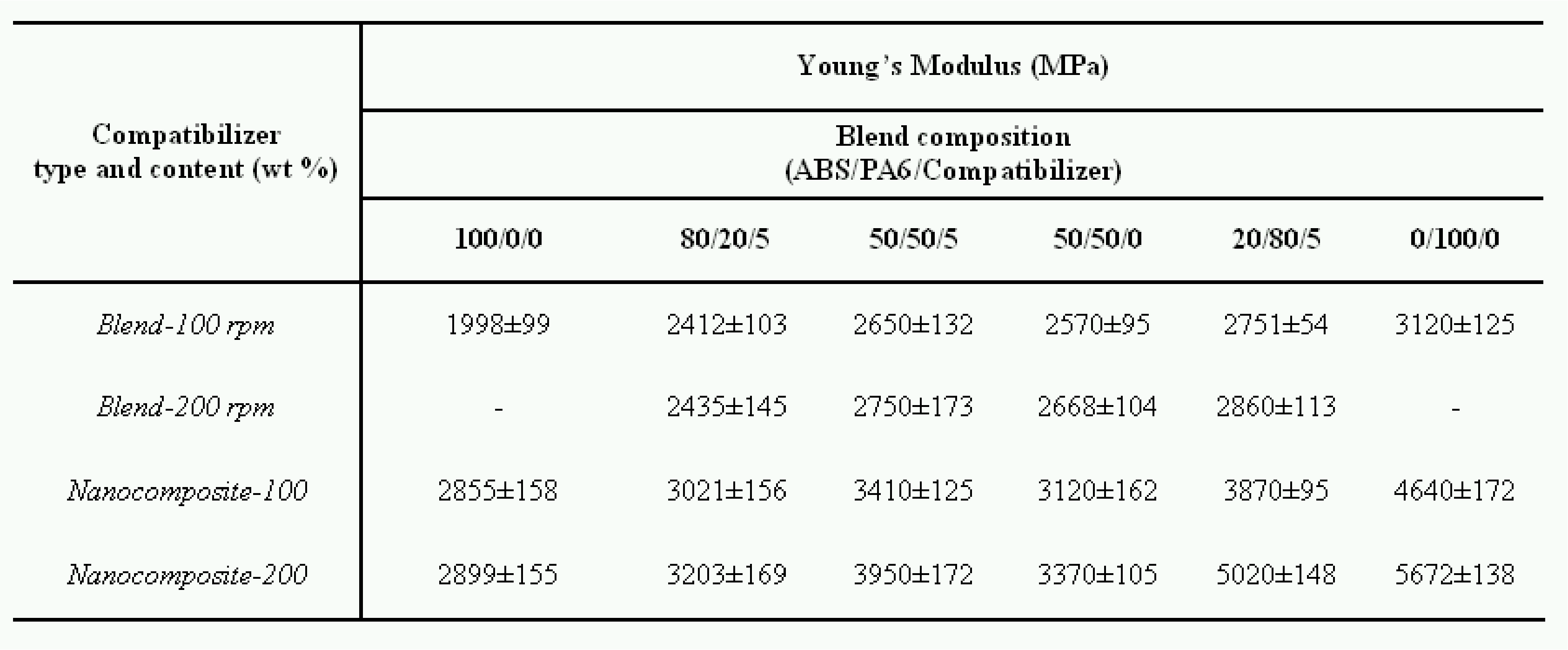

Compatibilizer type and content (wt %)	Young's Modulus (MPa)					
	Blend composition (ABS/PA6/Compatibilizer)					
	100/0/0	**80/20/5**	**50/50/5**	**50/50/0**	**20/80/5**	**0/100/0**
Blend-100 rpm	1998±99	2412±103	2650±132	2570±95	2751±54	3120±125
Blend-200 rpm	-	2435±145	2750±173	2668±104	2860±113	-
Nanocomposite-100	2855±158	3021±156	3410±125	3120±162	3870±95	4640±172
Nanocomposite-200	2899±155	3203±169	3950±172	3370±105	5020±148	5672±138

Table D.9 Effect of clay loading level on Young's Moduli of nanocomposites based on 50/50/5 blend system processed at 100 rpm and 200 rpm

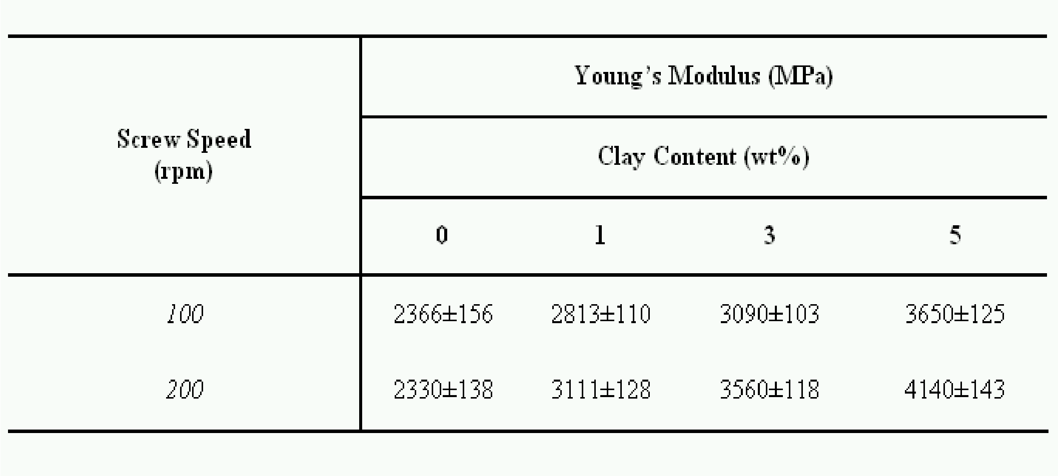

Screw Speed (rpm)	Young's Modulus (MPa)			
	Clay Content (wt%)			
	0	1	3	5
100	2366±156	2813±110	3090±103	3650±125
200	2330±138	3111±128	3560±118	4140±143

Table D.10 Young Modulus of nanocomposites containing 5% clay as the function of screw speed, screw geometry and blend ratio

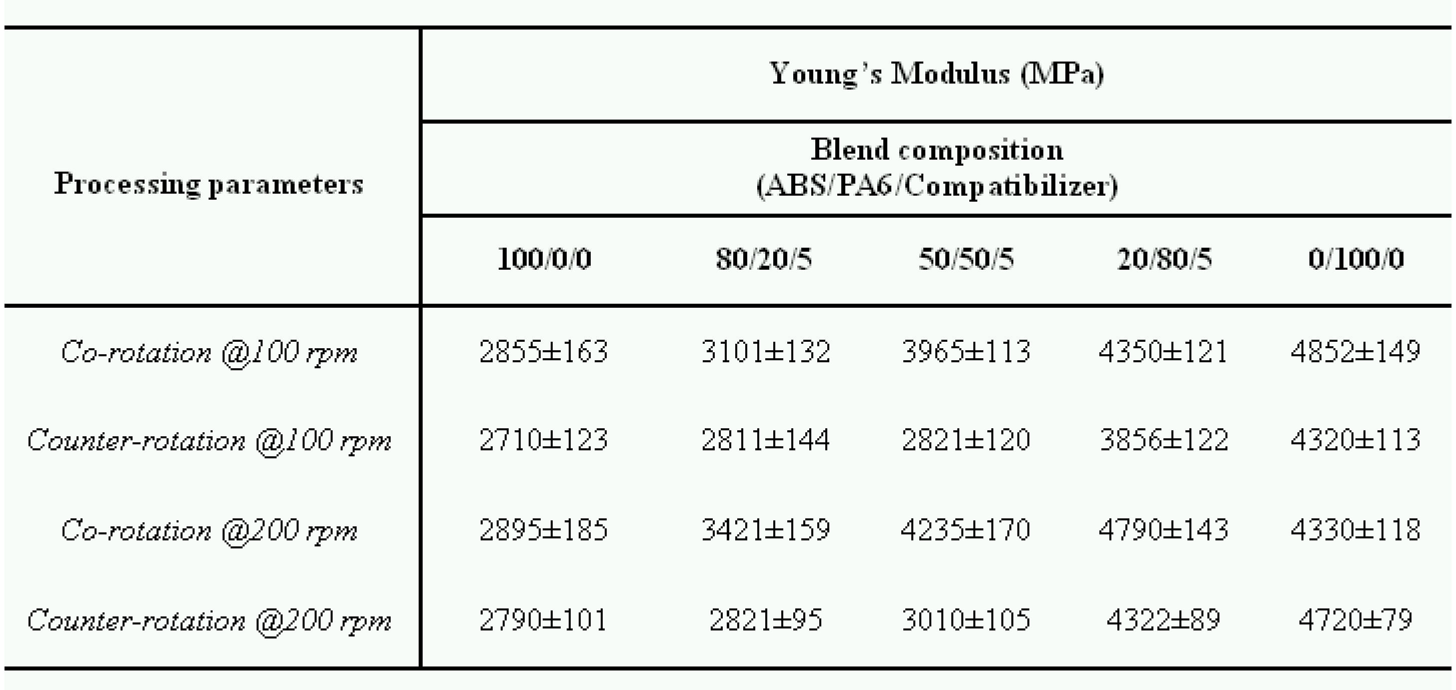

Processing parameters	**Young's Modulus (MPa)**				
	Blend composition (ABS/PA6/Compatibilizer)				
	100/0/0	**80/20/5**	**50/50/5**	**20/80/5**	**0/100/0**
Co-rotation @100 rpm	2855±163	3101±132	3965±113	4350±121	4852±149
Counter-rotation @100 rpm	2710±123	2811±144	2821±120	3856±122	4320±113
Co-rotation @200 rpm	2895±185	3421±159	4235±170	4790±143	4330±118
Counter-rotation @200 rpm	2790±101	2821±95	3010±105	4322±89	4720±79

Table D.11 Young Modulus of 50/50/5 blend based nanocomposites as the function of screw speed, screw rotation mode and clay loading

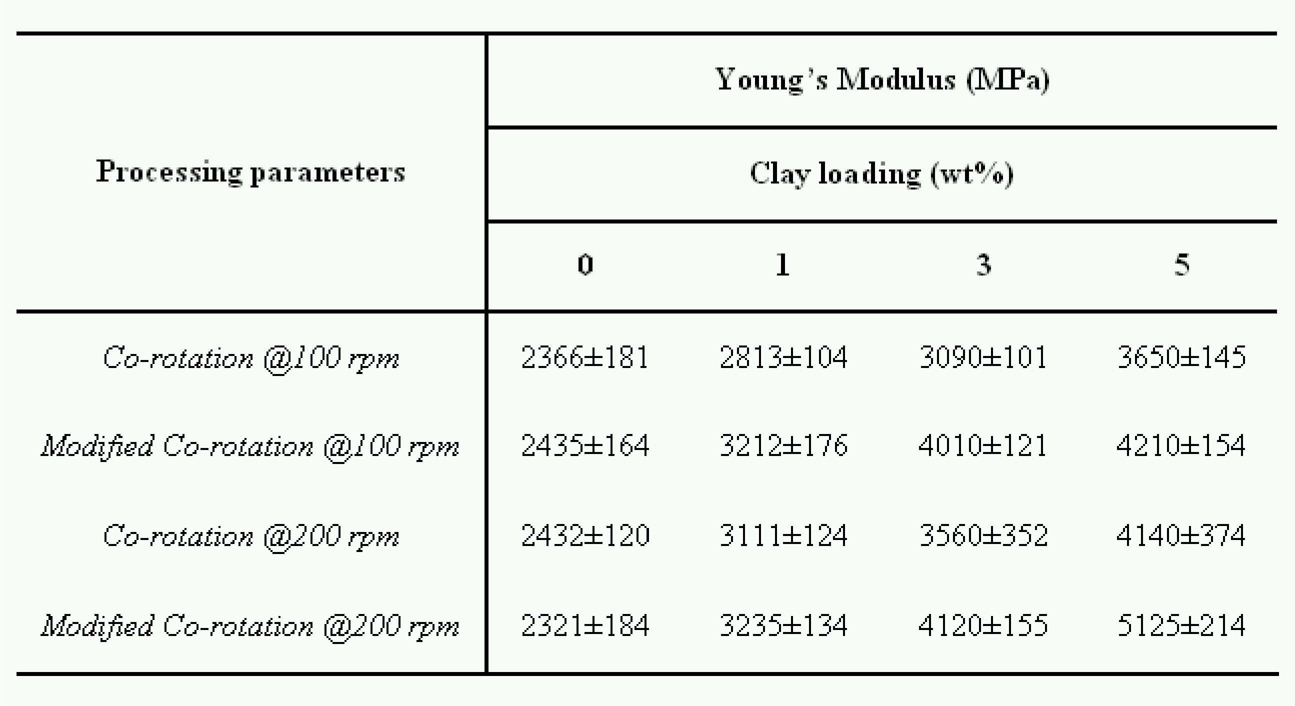

Processing parameters	**Young's Modulus (MPa)**			
	Clay loading (wt%)			
	0	**1**	**3**	**5**
Co-rotation @100 rpm	2366±181	2813±104	3090±101	3650±145
Modified Co-rotation @100 rpm	2435±164	3212±176	4010±121	4210±154
Co-rotation @200 rpm	2432±120	3111±124	3560±352	4140±374
Modified Co-rotation @200 rpm	2321±184	3235±134	4120±155	5125±214

CURRICULUM VITAE

PERSONAL INFORMATION

Name & Surname: Güralp Özkoç
Nationality: Turkish
Date and Place of Birth: 19.02.1979 - Sinop

EDUCATION

Degree	**Institution**	**Year**
M.Sc.	METU, Polymer Science and Technology	2004
B.Sc.	Gazi Unv., Chemical Engineering	2001
High School	Sinop Anadolu Lisesi	1997
Conservatory	Sinop Municipality Conservatory	1997

WORK EXPERIENCE

Place	**Position**	**Year**
METU, Dept. of Polym. Sci. Tech.	Teaching Assistant	2002- Now
TÜPRAŞ, İzmir	Intern Process Engineer	Summer, 1999
TÜPRAŞ, İzmir	Intern Process Engineer	Summer, 2000

ABROAD EXPERIENCE

Place	**Project**	**Year**
DSM Research, The Netherlands	Microcompounding of ABS/PA6 based nanocomposites	Nov. 2005 – Jan.2006

FOREIGN LANGUAGES

Advanced English, Basic German

HONORS

Institution	**Award**	**Years**
Gazi Unv. Faculty of Eng. & Arch.	Honor Certificates	1997-2001
Gazi Unv. Faculty of Eng. & Arch	Graduation Honor Certificate (3rd Degree)	2001

PUBLICATIONS

Book:

1. S. Kiralp, P. Camurlu, G. Ozkoc, M. Dogan, T. Baydemir, S. Erdogan, “Plastikler”, ODTU Yayincilik (2006).

Book Papers:

1. G. Ozkoc, G. Bayram, E. Bayramli, Annual Meeting of Metarials Research Society,”*Processing and Characterization of Short Glass Fiber/ABS/Polyamide-6 Composites*”, Boston/USA (2004).

2. G. Bayram, G. Ozkoc, P. Kurkcu, "Improvement of Adhesion Between Poly(tetrafluoroethylene) and Poly(ethylene terephthalate) Films" in Polymer Surface Modification: Relevance to Adhesion, K.L. Mittal (Ed.) , VSP, The Netherlands, vol.4 (2007).

Periodicals:

1. G. Ozkoc, G. Bayram, E. Bayramli, *“Effects of polyamide 6 incorporation to the short glass fiber reinforced ABS composites: an interfacial approach”*, Polymer, 45, 8957-8966 (2004)

2. G. Ozkoc, G. Bayram, E. Bayramli, "*Short glass fiber reinforced ABS and ABS/PA6 composites: Processing and characterization*", Polymer Composites, 26, 745-755 (2005).

3. G. Bayram and G. Ozkoc, *"Processing and Characterization of multilayer films of PET and surface modified PTFE",* Journal of Adhesion Sci. and Tech., Submitted Article, (2007).

4. G. Ozkoc, G. Bayram, E. Bayramli, "*Effects of Olefin-Based Compatibilizers on the Morphology, Thermal and Mechanical Properties of ABS/Polyamide-6 Blends",* Journal of Appl. Polymer Sci., 104, 926-935 (2007).

5. G. Ozkoc, G. Bayram, J. Tiesnitsch, "*Microcompounding of ABS/Polyamide-6 based nanocomposites*", Polymer Composites, Article in Press, (2007).

6. G. Ozkoc, G. Bayram, M. Quaedflieg, "*Effects of microcompounding conditions on the morphology and mechanical properties of ABS/PA6 blends and their nanocomposites*", Journal of Applied Polymer Science, Submitted Article, (2007).

7. G. Ozkoc, G. Bayram, E. Bayramli, *"Impact fracture toughness of ABS/Polyamide-6 blends"*, Polymer Testing, Submitted Article, (2007).

Oral Presentations:

1. G. Ozkoc, G. Bayram, E. Bayramli, SPE Annual Technical Conference, *"A study on processing and characterization of short glass fiber reinforced ABS/PA6 blends"*, Chicago/USA (2004).

2. G. Ozkoc, G. Bayram, E. Bayramli, 6. Ulusal Kimya Mühendisliği Kongresi, *"Kısa cam elyaf takviyeli ABS 'de arayüzeydeki yapışmanın poliamit katkısı ile arttırılamsı"*, İzmir (2004).

3. G. Ozkoc, G. Bayram, E. Bayramli, Annual Meeting of Polymer Processing Society, *"Short glass fiber reinforced ABS/PA6 blends based composites"*, Leibzig/Germany (2005).

4. G. Bayram, G. Ozkoc, P. Kurkcu, Fifth International Symposia on Polymer Surface Modification: Relevance to adhesion, *"Improvement of Adhesion Between Poly(tetrafluoroethylene) and Poly(ethylene terephthalate) Films",* Toronto/Canada (2005).

5. G. Ozkoc, G. Bayram, E. Bayramli, SPE Annual Technical Conference, *"Compatibilization of ABS/PA6 using olefin based polymers"*, Charlotte/USA, (2006).

6. G. Ozkoc, G. Bayram, E. Bayramli, 1. Ulusal Polimer Bilimi ve Teknolojisi Kongresi, *"ABS/PA6 karışımlarının morfolojilerinin ve mekanik özelliklerinin incelenmesi",* Ankara, (2006).

7. G. Ozkoc, G. Bayram, J. Tiesnitsch, M. Quaedflieg, Annual Meeting of Polymer Processing Society, *"Micro-compounding of ABS/PA6 Blends Based Nanocomposites: The effects of screw geometry and processing conditions"*, Yamagata/Japan (2006).

8. G. Ozkoc, G. Bayram, E. Bayramli, 7. Ulusal Kimya Mühendisliği Kongresi, *"ABS/PA6 karışımları ve nanokompozitleri"*, Eskişehir (2006).

9. G. Ozkoc, G. Bayram, E. Bayramli, Kompozit Sempozyumu ve Sergisi, "*ABS/PA6 karışımlarının kısa cam elyaf ile takviye edilmes*i", İzmir (2006).

10. G. Ozkoc, G. Bayram, M. Quaedflieg, Interactive Workshop on Micro-compounding of Polymer Nanocomposites, *"Lecture on Microcompounding of ABS/PA6 blends based nanocomposites",* ITIR, Taipei/Taiwan (2006).

Poster Presentations:

1. G. Ozkoc, G. Bayram, E. Bayramli, The Third Eastern Mediterranean Chemical Engineering Conference, "*An alternative processing method for short glass fiber reinforcement of thermoplastics*", Selanik/Greece (2003).

HOBBIES:

Playing music instruments, Cooking, Flight Simulator, Photographing, Soccer